VOLUME 77 NOVEMBER 8, 1973 NUMBER 23

JPCHAx

THE JOURNAL OF PHYSICAL CHEMISTRY

PUBLISHED BIWEEKLY BY THE AMERICAN CHEMICAL SOCIETY

THE JOURNAL OF

PHYSICAL CHEMISTRY

AMERICAN CHEMICAL SOCIETY, *1155 Sixteenth St., N.W., Washington, D. C. 20036*

Books and Journals Division

JOHN K CRUM *Director*
RUTH REYNARD *Assistant to the Director*

CHARLES R. BERTSCH *Head, Editorial Processing Department*
D. H. MICHAEL BOWEN *Head, Journals Department*
BACIL GUILEY *Head, Graphics and Production Department*
SELDON W. TERRANT *Head, Research and Development Department*

 Published biweekly by the American Chemical Society at 20th and Northampton Sts., Easton, Pa. 18042. Second-class postage paid at Washington, D. C., and at additional mailing offices.

All manuscripts should be sent to *The Journal of Physical Chemistry*, Department of Chemistry, University of Minnesota, Minneapolis, Minn. 55455.

Additions and Corrections are published once yearly in the final issue. See Volume 76, Number 26 for the proper form.

Extensive or unusual alterations in an article after it has been set in type are made at the author's expense and it is understood that by requesting such alterations the author agrees to defray the cost thereof.

The American Chemical Society and the Editor of *The Journal of Physical Chemistry* assume no responsibility for the statements and opinions advanced by contributors.

Correspondence regarding accepted copy, proofs, and reprints should be directed to Editorial Processing Department, American Chemical Society, 20th and Northampton Sts., Easton, Pa. 18042. Head: CHARLES R. BERTSCH. Assistant Editor: EDWARD A. BORGER. Editorial Assistant: JOSEPH E. YURVATI.

Advertising Office: Centcom, Ltd., 142 East Avenue, Norwalk, Conn. 06851.

Business and Subscription Information

Send all new and renewal subscriptions *with payment* to: Office of the Controller, 1155 16th Street, N.W., Washington, D. C. 20036. Subscriptions should be renewed promptly to avoid a break in your series. All correspondence and telephone calls regarding changes of address, claims for missing issues, subscription service, the status of records, and accounts should be directed to Manager, Membership and Subscription Services, American Chemical Society, P.O. Box 3337, Columbus, Ohio 43210. Telephone (614) 421-7230.

On changes of address, include both old and new addresses with ZIP code numbers, accompanied by mailing label from a recent issue. Allow four weeks for change to become effective.

Claims for missing numbers will not be allowed (1) if loss was due to failure of notice of change in address to be received before the date specified, (2) if received more than sixty days from date of issue plus time normally required for postal delivery of journal and claim, or (3) if the reason for the claim is "issue missing from files."

Subscription rates (1973): members of the American Chemical Society, $20.00 for 1 year; to nonmembers, $60.00 for 1 year. Those interested in becoming members should write to the Admissions Department, American Chemical Society, 1155 Sixteenth St., N.W., Washington, D. C. 20036. Postage to Canada and countries in the Pan-American Union, $5.00; all other countries, $6.00. Single copies for current year: $3.00. Rates for back issues from Volume 56 to date are available from the Special Issues Sales Department, 1155 Sixteenth St., N.W., Washington, D. C. 20036.

Subscriptions to this and the other ACS periodical publications are available on microfilm. Supplementary material not printed in this journal is now available in microfiche form on a current subscription basis. For information on microfilm or microfiche subscriptions, write Special Issues Sales Department at the address above.

Notice to Authors last printed in the issue of June 21, 1973

THE JOURNAL OF

PHYSICAL CHEMISTRY

Volume 77, Number 23 November 8, 1973

JPCHAx 77(23) 2713–2822 (1973)
ISSN 0022-3654

■ Supplementary material for this paper is available separately, in photocopy or microfiche form. Ordering information is given in the paper.

* In papers with more than one author, the asterisk indicates the name of the author to whom inquiries about the paper should be addressed.

AUTHOR INDEX

THE JOURNAL OF
PHYSICAL CHEMISTRY

VOLUME 77, NUMBER 23 NOVEMBER 8, 1973

Shock Tube Study of Sulfur Hexafluoride and Sulfur Chloride Pentafluoride Equilibrium Decomposition

A. P. Modica

Avco Systems Division, Wilmington, Massachusetts 01887 *(Received April 30, 1973)*

Publication costs assisted by the Space and Missile Systems Organization, U.S. Air Force Systems Command

Measurements of SF_6 and SF_5Cl decomposition were conducted in argon shock waves at total pressures of 1–3 atm and temperatures from 1700 to 2300°K. Similar experiments of SF_6 decomposition were carried out with hydrogen. A Bendix time-of-flight mass spectrometer was used to identify the important reaction products behind reflected SF_6–argon shock waves at 1800°K. Equilibrium ultraviolet absorption of SF_4 at 2660 Å was monitored in the SF_6, SF_5Cl, and SF_6–H_2 decomposition studies. Thermochemical shock tube calculations are fitted to experimental SF_4 equilibrium concentrations. Data analyses suggest a $\Delta H_f°(SF_5)$ of −241.7 kcal mol^{-1}, and bond energies of (SF_5–F) 65.2 and (SF_4–F) 87.9 kcal mol^{-1} for the SF_6 molecule.

I. Introduction

A shock tube and a thermochemical equilibrium shock wave computer program have been used in previous studies to determine band system oscillator strengths of the C_2 and CF radicals from fluorocarbon decomposition[1] and to evaluate the chemical kinetics of the CF_2 radical in fluorocarbon chemistry.[2] Currently, there is interest in the high-temperature chemistry of sulfur hexafluoride because of its application to electron attachment processes in air plasmas[3,4] and its stable source of fluorine atoms for shock-induced laser experiments with hydrogen.[5] Studies of the chemical kinetics of SF_6 and SF_4 dissociation have recently yielded probable bond energies from limiting first-order dissociation rate constants.[6,7] The present investigation deals with the thermal decomposition of SF_6 molecules, SF_5Cl molecules, and SF_6–H_2 mixtures studied in argon shock waves. A Bendix time-of-flight mass spectrometer coupled to a shock tube allowed the important decomposition products of shock heated SF_6 to be identified for the chemistry input to the thermochemical equilibrium program. The SF_5Cl molecule provided a source of SF_5 radicals in the study. Mixtures of SF_6 and hydrogen were used to generate HF in the SF_6 decomposition chemistry. In the three sets of experiments, the equilibrium ultraviolet absorption of 2660 Å of the SF_4 decomposition produce was monitored behind the shock wave. The infrared emission of the HF vibrational band of 2.5 μ was measured to determine the HF concentration in the shocked gas for comparison with the thermochemical calculation.

II. Experimental Procedure

Shock Tube. The SF_6 decomposition experiments were conducted behind incident shock waves in an optical spectroscopy shock tube and behind reflected shock waves in a shock tube coupled to a time-of-flight mass spectrometer. The optical shock tube is a 1.5 in. i.d. stainless steel tube with a 3.5 ft driver section and a 10 ft driven section. The mass spectrometer shock tube apparatus is constructed from 1 in. i.d. Pyrex glass pipe and has a 5 ft driver section and a 15 ft driven section. A Bendix (Model 14-206) time-of-flight mass spectrometer is attached to the glass driven section through the "fast reaction chamber." The shock velocity in the two facilities was measured with a series of platinum heat transfer gauges. The output of these gauges was displayed on a time-mark folded oscilloscope sweep, operated by a Radionics (Model N-2A) triangular wave and marker timing generator. Transit times between stations were measured to within ±1 μsec. The maximum error in the shock velocity was about ±0.3% and introduced an uncertainty of less than ±15°K in the calculated incident shock temperature. The

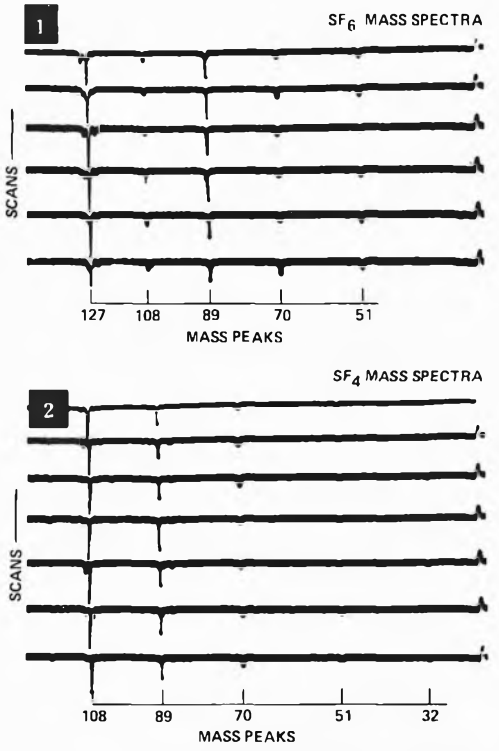

Figure 1. Mass spectra of SF_6 and SF_4 molecules: time between spectral scans, 25 μsec; sample temperature, 298°K; electron beam voltage, 50 eV; ion peaks, SF_5^+ (127), SF_4^+ (108), SF_3^+ (89), SF_2^+ (70), SF^+ (51), and S^+ (32).

error in the reflected shock temperature could have been about ±40°K based on ideal reflected shock calculations for a chemically relaxed gas. Schematics of the optical and mass spectra facilities may be found in previous reports.[8]

Reagents. The SF_6 and SF_5Cl test gases were diluted separately in 1:100 mole ratios with research grade argon. Mixtures of SF_6 and hydrogen were prepared in mole ratios of 1:0.5:100, 1:1:100, and 1:5:100 SF_6–H_2–argon for study. A 1:5:100 HF–H_2–argon mixture was used to calibrate the 2.5 μ infrared radiometer signals with known shock concentrations of HF molecules. Ultraviolet absorption measurements of SF_4 were made in 1:100 SF_4–argon shock heated samples. All reagents were obtained from commercial suppliers and used without further purification. The stated purities of the test gases were Matheson SF_6 (98% purity), SF_4 (94% purity), H_2 (99.98% purity), HF (99.9% purity), and argon (99.999% purity). Sulfur chloride pentafluoride, SF_5Cl, was obtained from Peninsular Chemresearch, Inc. Samples of SF_6 were analyzed for ultraviolet absorption with a Bausch & Lomb Spectronic 505 spectrometer and were found to be optically pure in the wavelength region 2000–3200 Å, indicating virtual absence of any SF_4 or possibly thionyl fluoride, SOF_2, impurity. Commercial samples of SF_5Cl showed ultraviolet absorption bands at 2880 and 2400 Å similar to SF_4 spectra.

III. Mass Spectrometer Measurement

Mass spectral recordings were taken of room temperature samples of SF_6 and SF_4 to identify their respective positive ion mass cracking patterns (Figure 1). The time-resolved ion peaks, taken at 25-μsec scan intervals, were displayed on a Tektronix 535A oscilloscope in combination with a Type CA preamplifier and multiscan generator. The positive ion spectra correspond to mass peaks of SF_5^+ (127), SF_4^+ (108), SF_3^+ (89), SF_2^+ (70), SF^+ (51), and S^+ (32). In the SF_6 spectra the parent positive ion peak SF_6^+ (146) does not appear because of a more favorable ionization mechanism, namely, the electron resonance

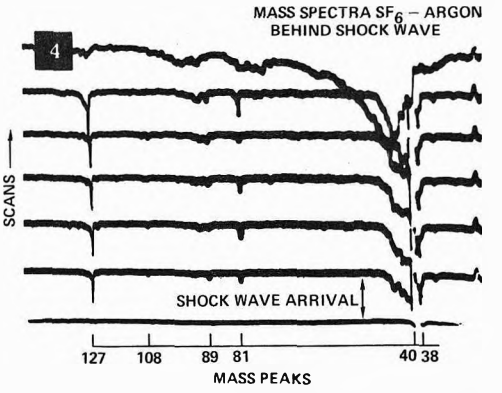

Figure 2. Mass spectra of SF_6 decomposition behind 1:100 SF_6–argon reflected shock wave: time between spectral scans, 25 μsec; electron beam voltage, 30 eV; ion peaks, SF_5^+ (127), SF_4^+ (108), SF_3^+ (89), SO_3^+ (80) impurity, Ar^+ (40) off scale, Ar^+ (38) isotope; sample pressure 0.33 atm; sample temperature 1860°K.

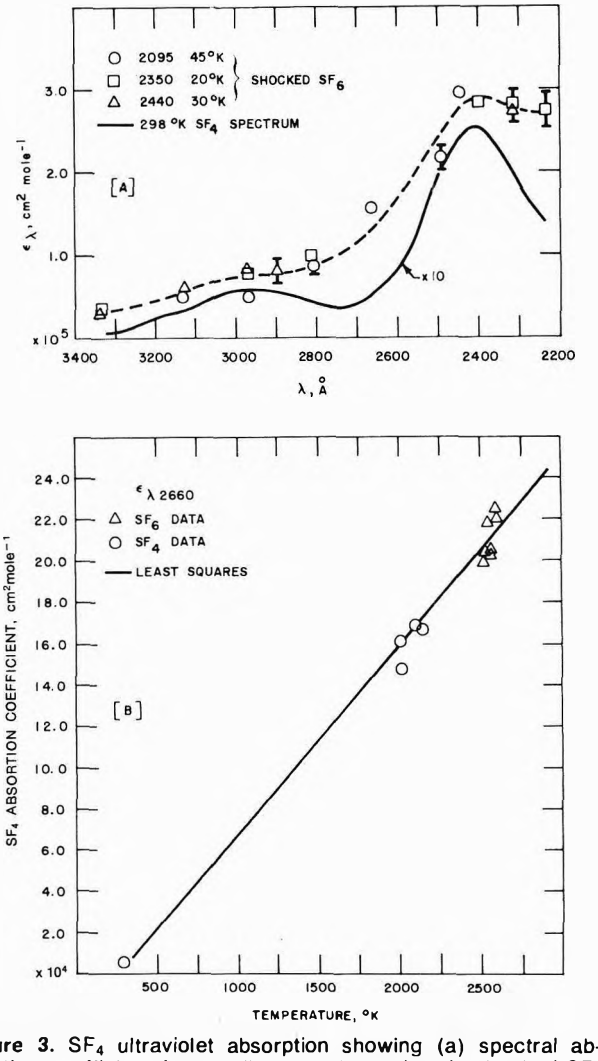

Figure 3. SF_4 ultraviolet absorption showing (a) spectral absorption coefficient from radiometer data taken in shocked SF_6 decomposition mixtures and from SF_4 spectrophotometer absorption spectra and (b) temperature dependence of SF_4 absorption coefficient at 2660 Å.

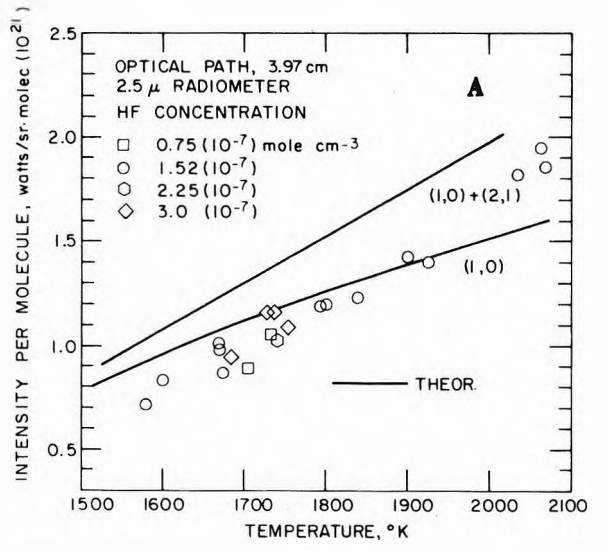

Theoretical curves are based on line intensity calculations for the 0-1 and 1-2 fundamental transitions (Meredith and Kent, BAMIRAC 4613-125-T, U. Michigan, 1966).

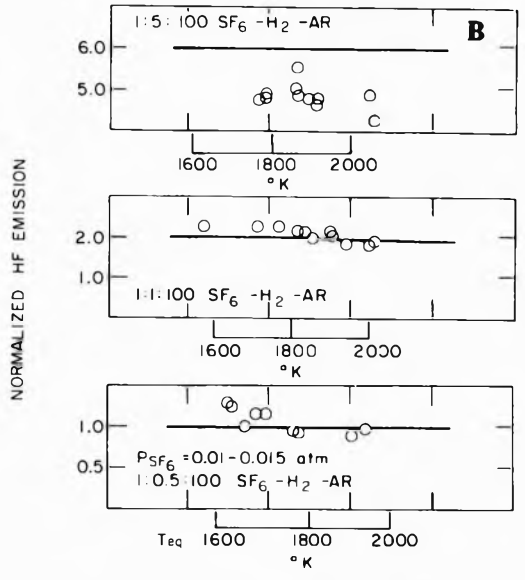

Figure 4. Infrared emission of the HF fundamental vibrational band of 2.5 μ behind argon shock waves showing (a) comparison of experimental and theoretical absolute intensities from shocked 1:5:100 HF–H_2–argon mixtures and (b) 2.5-μ emission normalized to mole ratio of HF and iritial SF_6 concentration in shocked SF_6–H_2–argon reaction mixtures: O, ir experimental data; solid lines, thermochemical calculation.

capture reaction forming SF_6^- ions, and the electron dissociative attachment of SF_6 ($SF_6 + e \rightarrow SF_5^- + F$) above electron accelerating voltages near 0.01 eV.[9] The dominant ion peak in the SF_6 mass spectra is the SF_5^+ (127) positive ion. The SF_3^+ mass peak is observed to be greater than the SF_4^+ ion peak characteristic of the parent cracking pattern of SF_6. For SF_4, the normal parent SF_4 positive ion peak dominates the spectra with decreasing abundance of the SF_3^+, SF_2^+, and SF^+ cracking pattern ions.

A mass spectral record of SF_6 decomposition at 1860°K behind a reflected argon shock wave is shown in Figure 2. The electron beam voltage of the experiment was adjusted to 30 eV low enough so that the cracking patterns were reduced to essentially mass peaks of parent molecules in the reaction mixture. The dominant ion peak of the SF_6 decomposition mixture is found to be that of the SF_5^+ ion.

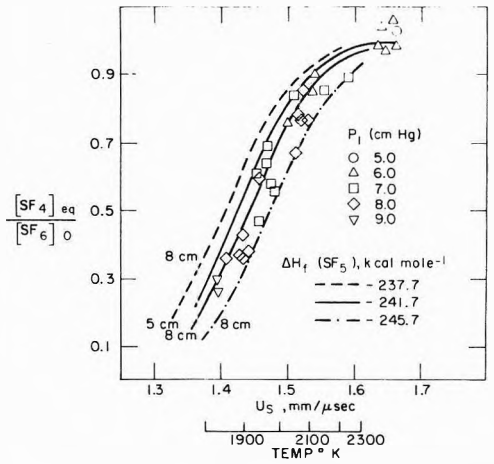

Figure 5. Experimental and thermochemical SF_4 equilibrium concentrations behind chemically relaxed 1:100 SF_6–argon shock waves.

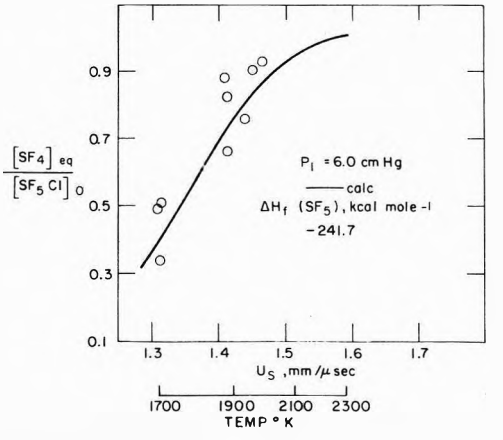

Figure 6. Experimental and thermcchemical SF_4 equilibrium concentrations behind chemically relaxed 1:100 SF_5Cl–argon shock waves.

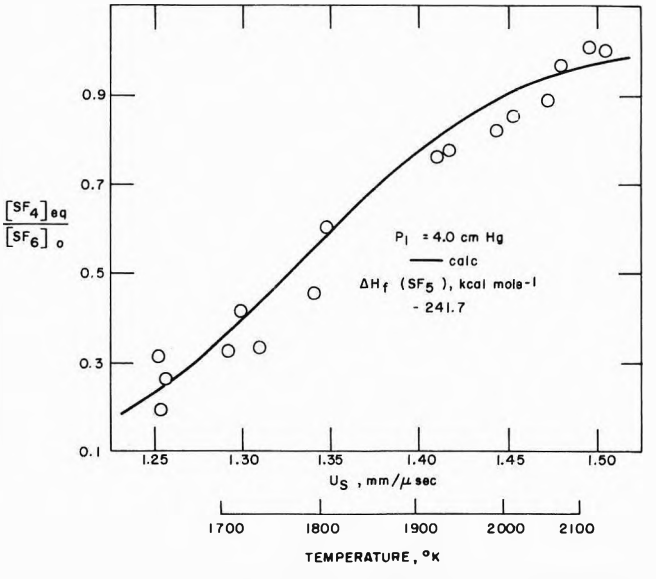

Figure 7. Experimental and thermochemical SF_4 equilibrium concentrations behind chemically relaxed 1:0.5:100 SF_6–H_2–argon shock waves.

Minor ion peaks for SF_4^+ and SF_3^+ are discernable. A mass peak near 80 appears in the background spectra and is believed to be SO_3^+ formed by an ion-molecule reac-

TABLE I: Shock Tube Equilibrium Calculation for 1:100 SF_6–Argon Mixture[a]

US[b]	T2	T2/T1	P2	P2/P1	RHO2	RHO2/RHO1	H2	H2/H1	U2
1.381520 00	1.800000 03	6.040270 00	2.608870 00	2.478430 01	7.154200-04	4.055290 00	1.804390-01	-5.342490 00	1.040850 00

INCIDENT NORMAL WAVE SPECIES
MEAN MOLECULAR WEIGHT OF MIXTURE = 4.050360 01 Z = 1.012120 00

MOLE FRACTION	PARTICLES / CC	SPECIE	MOLE FRACTION	PARTICLES / CC	SPECIE	MOLE FRACTION	PARTICLES / CC	SPECIE
1.196890-02	1.273690 17	F	5.168120-06	5.499740 13	F2	1.418250-04	1.509250 15	SF6
2.339630-03	2.489760 16	SF4	7.300000-03	7.766420 16	SF5	9.782440-01	1.041020 19	A

US	T2	T2/T1	P2	P2/P1	RHO2	RHO2/RHO1	H2	H2/H1	U2
1.436670 00	1.900000 03	6.375840 00	2.836500 00	2.694680 01	7.351130-04	4.166920 00	1.986760-01	-5.882450 00	1.091890 00

INCIDENT NORMAL WAVE SPECIES
MEAN MOLECULAR WEIGHT OF MIXTURE = 4.040530 01 Z = 1.014590 00

MOLE FRACTION	PARTICLES / CC	SPECIE	MOLE FRACTION	PARTICLES / CC	SPECIE	MOLE FRACTION	PARTICLES / CC	SPECIE
1.436950-02	1.575110 17	F	4.498140-06	4.930510 13	F2	4.925830-05	5.399300 14	SF6
4.670420-03	5.119350 16	SF4	5.038010-03	5.522270 16	SF5	9.758680-01	1.069670 19	A

US	T2	T2/T1	P2	P2/P1	RHO2	RHO2/RHO1	H2	H2/H1	U2
1.489130 00	2.000000 03	6.711410 00	3.060000 00	2.907000 01	7.516640-04	4.260740 00	2.166260-01	-6.413920 00	1.139630 00

INCIDENT NORMAL WAVE SPECIES
MEAN MOLECULAR WEIGHT OF MIXTURE = 4.031310 01 Z = 1.016910 00

MOLE FRACTION	PARTICLES / CC	SPECIE	MOLE FRACTION	PARTICLES / CC	SPECIE	MOLE FRACTION	PARTICLES / CC	SPECIE
1.662000-02	1.867030 17	F	3.819510-06	4.290700 13	F2	1.458130-05	1.638010 14	SF6
6.906720-03	7.758760 16	SF4	2.814130-03	3.161290 16	SF5	9.736410-01	1.093750 19	A

US	T2	T2/T1	P2	P2/P1	RHO2	RHO2/RHO1	H2	H2/H1	U2
1.535420 00	2.100000 03	7.046980 00	3.258610 00	3.095680 01	7.611980-04	4.314780 00	2.328200-01	-6.893400 00	1.179570 00

INCIDENT NORMAL WAVE SPECIES
MEAN MOLECULAR WEIGHT OF MIXTURE = 4.025310 01 Z = 1.018420 00

MOLE FRACTION	PARTICLES / CC	SPECIE	MOLE FRACTION	PARTICLES / CC	SPECIE	MOLE FRACTION	PARTICLES / CC	SPECIE
1.808770-02	2.040750 17	F	2.978980-06	3.393970 13	F2	3.720560-06	4.238860 13	SF6
8.375320-03	9.542060 16	SF4	1.342620-03	1.529650 16	SF5	9.721890-01	1.107620 19	A

US	T2	T2/T1	P2	P2/P1	RHO2	RHO2/RHO1	H2	H2/H1	U2
1.576310 00	2.200000 03	7.382550 00	3.433930 00	3.262230 01	7.651120-04	4.336970 00	2.473650-01	-7.324180 00	1.212850 00

INCIDENT NORMAL WAVE SPECIES
MEAN MOLECULAR WEIGHT OF MIXTURE = 4.022310 01 Z = 1.019180 00

MOLE FRACTION	PARTICLES / CC	SPECIE	MOLE FRACTION	PARTICLES / CC	SPECIE	MOLE FRACTION	PARTICLES / CC	SPECIE
1.882900-02	2.137840 17	F	2.195840-06	2.516480 13	F2	9.052370-07	1.037420 13	SF6
9.114720-03	1.044570 17	SF4	6.007300-04	6.884490 15	SF5	9.714550-01	1.113310 19	A

US	T2	T2/T1	P2	P2/P1	RHO2	RHO2/RHO1	H2	H2/H1	U2
1.613900 00	2.300000 03	7.718120 00	3.595960 00	3.416160 01	7.661250-04	4.342710 00	2.609850-01	-7.727320 00	1.242260 00

INCIDENT NORMAL WAVE SPECIES
MEAN MOLECULAR WEIGHT OF MIXTURE = 4.020940 01 Z = 1.019530 00

MOLE FRACTION	PARTICLES / CC	SPECIE	MOLE FRACTION	PARTICLES / CC	SPECIE	MOLE FRACTION	PARTICLES / CC	SPECIE
1.915810-02	2.199220 17	F	1.595210-06	1.831190 13	F2	2.293400-07	2.632670 12	SF6
9.440040-03	1.083650 17	SF4	2.707750-04	3.106310 15	SF5	9.711280-01	1.114790 19	A

[a] Heat of formation of sulfur–fluorine species in calculation ΔH_f (0°K), SF_6 −288.4 kcal/mol, SF_5 −241.7 kcal/mol, SF_4 −172.2 kcal/mol. [b] Shock quantities are US shock velocity in mm/μsec, T2 shock temperature (°K), TS/T1 temperature ratio across shock, RHO2 shock density in gm/cm^3, RHO2/RHO1 density ratio across shock, H2 shock enthalpy in kcal/gm, U2 gas velocity in mm/μsec.

tion of oxygen and sulfur impurities trapped in the drift tube of the mass spectrometer. The SF_5^+ peak is believed to be that of SF_5 radicals in the reaction mixture, since SF_6 decomposition experiments in the infrared and thermochemical equilibrium calculations show that the SF_6 molecule at 1860°K is dissociated.[6] However, the presence of the SF_5^+ ion as the dominant peak and the SF_4^+ ion as a minor peak in the spectra of shock-heated SF_6 is in complete discord with the thermochemical calculation reported by Bott and Jacobs (ref 6). Their thermochemical calculation shows that for a 0.5% SF_6–99.5% Ar mixture between 1600 and 1850°K, SF_4 is the dominant chemical species at equilibrium and that its concentration is nearly constant over the temperature range. The SF_6 concentration initially is about one-third of SF_4 at 1600°K and decreases monotonically by a factor of 40 below SF_4 at 1750°K. The SF_5 concentration begins about an order of magnitude lower than SF_4 and continues to decrease by another factor of 10 near 1775°K. The Bott–Jacobs thermochemical calculation also included the SF_3 species and shows that its concentration at around 1850°K increases to about one-third of SF_4. In the present study, the mass spectrometer data (Figure 2) indicated only a very minor response to the SF_3^+ ion peak for decomposed SF_6 at 1860°K.

IV. Ultraviolet Absorption Measurements

Spectral absorption coefficients of the SF_4 molecule were obtained over the wavelength region 3400–2400 Å from photometric measurements of dissociated samples of SF_6, analyzed according to Beer's law. The ultraviolet radiometer consisted of an Engis SO502 grating monochromator (30-Å triangular band pass at half-peak-height), an xenon–mercury continuous ultraviolet light source (Hano-

TABLE II: Shock Tube Equilibrium Calculation for 1:100 SF_5Cl–Argon Mixture

US	T2	T2/T1	P2	P2/P1	RHO2	RHO2/RHO1	H2	H2/H1	U2
1.311880 00	1.700000 03	5.704700 00	1.747850 00	2.213940 01	5.102700-04	3.841300 00	1.681120-01	-7.118780 00	9.703590-01

INCIDENT NORMAL WAVE SPECIES
MEAN MOLECULAR WEIGHT OF MIXTURE = 4.072470 01 Z = 1.010630 00

MOLE FRACTION	PARTICLES / CC SPECIE	MOLE FRACTION	PARTICLES / CC SPECIE	MOLE FRACTION	PARTICLES / CC SPECIE
5.452230-03	4.114330 16 CL	1.595770-03	1.204640 16 CLF	5.195680-09	3.922170 11 SCLF5
1.374930-03	1.037920 16 CL2	2.093660-03	1.580480 16 F	2.041670-07	1.541240 12 F2
3.988510-05	3.010890 14 SF6	3.729720-03	2.815530 16 SF4	6.026250-03	4.549160 16 SF5
9.796900-01	7.395590 18 A				

LS	T2	T2/T1	P2	P2/P1	RHO2	RHO2/RHO1	H2	H2/H1	U2
1.368490 00	1.800000 03	6.040270 00	1.914910 00	2.425550 01	5.266710-04	3.964770 00	1.859430-01	-7.873830 00	1.023330 00

INCIDENT NORMAL WAVE SPECIES
MEAN MOLECULAR WEIGHT OF MIXTURE = 4.062350 01 Z = 1.013140 00

MOLE FRACTION	PARTICLES / CC SPECIE	MOLE FRACTION	PARTICLES / CC SPECIE	MOLE FRACTION	PARTICLES / CC SPECIE
6.659240-03	5.201500 16 CL	1.444090-03	1.127980 16 CLF	2.702630-08	2.111010 11 SCLF5
8.341050-04	6.515160 15 CL2	4.036420-03	3.152830 16 F	4.314290-07	3.369880 12 F2
2.043530-05	1.596200 14 SF6	5.501810-03	4.297440 16 SF4	4.249290-03	3.319110 16 SF5
9.772550-01	7.633300 18 A				

US	T2	T2/T1	P2	P2/P1	RHO2	RHO2/RHO1	H2	H2/H1	U2
1.423060 00	1.900000 03	6.375840 00	2.082200 00	2.637450 01	5.411920-04	4.074080 00	2.038020-01	-8.630090 00	1.073760 00

INCIDENT NORMAL WAVE SPECIES
MEAN MOLECULAR WEIGHT OF MIXTURE = 4.052260 01 Z = 1.015670 00

MOLE FRACTION	PARTICLES / CC SPECIE	MOLE FRACTION	PARTICLES / CC SPECIE	MOLE FRACTION	PARTICLES / CC SPECIE
7.674650-03	6.175260 16 CL	1.082320-03	8.708700 15 CLF	1.158150-08	9.318830 10 SCLF5
4.951340-04	3.984010 15 CL2	4.175560-03	3.360550 16 F	6.098460-07	4.907010 12 F2
7.627580-06	6.137390 13 SF6	7.266720-03	5.847030 16 SF4	2.472880-03	1.989760 16 SF5
9.748260-01	7.843750 18 A				

LS	T2	T2/T1	P2	P2/P1	RHO2	RHO2/RHO1	H2	H2/H1	U2
1.472350 00	2.000000 03	6.711410 00	2.235850 00	2.832080 01	5.510390-04	4.148210 00	2.203820-01	-9.332200 00	1.117410 00

INCIDENT NORMAL WAVE SPECIES
MEAN MOLECULAR WEIGHT OF MIXTURE = 4.044680 01 Z = 1.017570 00

MOLE FRACTION	PARTICLES / CC SPECIE	MOLE FRACTION	PARTICLES / CC SPECIE	MOLE FRACTION	PARTICLES / CC SPECIE
8.453870-03	6.938990 16 CL	6.961100-04	5.713710 15 CLF	4.113400-09	3.376300 10 SCLF5
2.893140-04	2.375200 15 CL2	7.831270-03	6.427950 16 F	6.198320-07	5.085970 12 F2
2.134820-06	1.752270 13 SF6	8.530800-03	7.002130 16 SF4	1.196700-03	9.822590 15 SF5
9.730020-01	7.986450 18 A				

US	T2	T2/T1	P2	P2/P1	RHO2	RHO2/RHO1	H2	H2/H1	U2
1.515580 00	2.100000 03	7.046980 00	2.372370 00	3.005000 01	5.562340-04	4.187320 00	2.353520-01	-9.966110 00	1.153940 00

INCIDENT NORMAL WAVE SPECIES
MEAN MOLECULAR WEIGHT OF MIXTURE = 4.040330 01 Z = 1.018660 00

MOLE FRACTION	PARTICLES / CC SPECIE	MOLE FRACTION	PARTICLES / CC SPECIE	MOLE FRACTION	PARTICLES / CC SPECIE
8.975120-03	7.444290 16 CL	4.086240-04	3.389280 15 CLF	1.313770-09	1.089690 10 SCLF5
1.673320-04	1.387910 15 CL2	8.790750-03	7.291360 16 F	5.122720-07	4.248960 12 F2
5.117390-07	4.244550 12 SF6	9.201510-03	7.632060 16 SF4	5.219170-04	4.328960 15 SF5
9.719400-01	8.061620 18 A				

via arc lamp, type D-901B01), and a 1P-28 photomultiplier. The light beam was collimated perpendicular to the shock tube axis by two sets of slits, each 1 mm in width. SF_4 concentrations in the shocked reaction mixtures were calculated from absorption data taken at 2660 Å (wavelength of optimum signal-to-noise ratio). The spectral absorption coefficient for SF_4 and the temperature dependence of the 2660-Å absorption coefficient are shown in Figure 3. Measurements with SF_6 near 2100°K were corrected for incomplete dissociation (85% SF_6 dissociated). The absorption coefficient at 2660 Å was determined both from shocked sample of SF_4 and from SF_6 samples considered to be completely dissociated to SF_4. The spectral absorption data at room temperature were obtained from a Bausch & Lomb spectrophotometer SF_4 spectra.

V. Infrared Measurements

An indium antimonide detector (Philco Type ISC-301) was filtered at 2.5 μ to monitor the HF fundamental emission band in shock-heated HF samples and shocked reaction mixtures of SF_6 and hydrogen. The infrared radiation from the high-temperature test gases was viewed through barium fluoride windows, orthogonal to the shock tube axis. The 2.5-μ radiometer was calibrated against a standard black body source (Barnes Engineering Model 11-201-1) for absolute intensity measurements. A Tektronix 555 dual-beam oscilloscope displayed the radiometer signals. Absolute intensities of the HF fundamental band in emission were measured in shocked 1:5:100 HF–H_2–argon gas samples and were compared to theoretical estimates based on HF line intensities for the (1,0) and (2,1) fundamental transitions.[10] Steady-state infrared emission from HF molecules formed by the reaction of SF_6 with hydrogen was observed and normalized in terms of the mole ratio of HF to initial SF_6 behind the shock wave. The results of the HF absolute intensity measurements and the normalized HF emission data in the SF_6–hydrogen reaction study are given in Figure 4.

TABLE III: Shock Tube Equilibrium Calculation for 1:0.5:100 SF_6–H_2–Argon Mixture

US	T2	T2/T1	P2	P2/P1	RHO2	RHO2/RHO1	H2	H2/H1	U2
1.234340 00	1.600000 03	5.369130 00	9.957150-01	1.891860 01	3.073790-04	3.501130 00	1.345000-01	-4.110820 00	8.817870-01

INCIDENT NORMAL WAVE SPECIES

MEAN MOLECULAR WEIGHT OF MIXTURE = 4.052970 01 Z = 1.006730 00

MOLE FRACTION	PARTICLES / CC	SPECIE	MOLE FRACTION	PARTICLES / CC	SPECIE	MOLE FRACTION	PARTICLES / CC	SPECIE
1.781780-03	8.141380 15	F	9.794150-03	4.475180 16	HF	1.759360-07	8.038930 11	F2
8.357330-05	3.818660 14	SF6	1.105080-12	5.049390 06	H	7.598620-14	3.471990 05	HS
4.142490-16	1.892800 03	H2	2.284840-19	1.044000 00	H2S	1.875640-03	8.570240 15	SF4
7.825000-03	3.575430 16	SF5	9.786400-01	4.471640 18	A			

US	T2	T2/T1	P2	P2/P1	RHO2	RHO2/RHO1	H2	H2/H1	U2
1.291050 00	1.700000 03	5.704700 00	1.099110 00	2.088300 01	3.187790-04	3.630970 00	1.513190-01	-4.624860 00	9.354840-01

INCIDENT NORMAL WAVE SPECIES

MEAN MOLECULAR WEIGHT OF MIXTURE = 4.045880 01 Z = 1.008490 00

MOLE FRACTION	PARTICLES / CC	SPECIE	MOLE FRACTION	PARTICLES / CC	SPECIE	MOLE FRACTION	PARTICLES / CC	SPECIE
3.530240-03	1.675810 16	F	9.777010-03	4.641150 16	HF	3.650230-07	1.732760 12	F2
4.308940-05	2.045450 14	SF6	6.635780-12	3.151000 07	H	3.050860-12	1.448240 07	HS
2.243810-15	1.065140 04	H2	-1.057060-17	5.017880 01	H2S	3.583980-03	1.701310 16	SF4
6.140030-03	2.914670 16	SF5	9.769280-01	4.636480 18	A			

US	T2	T2/T1	P2	P2/P1	RHO2	RHO2/RHO1	H2	H2/H1	U2
1.348180 00	1.800000 03	6.040270 00	1.209130 00	2.297340 01	3.304770-04	3.764220 00	1.691590-01	-5.170140 00	9.900240-01

INCIDENT NORMAL WAVE SPECIES

MEAN MOLECULAR WEIGHT OF MIXTURE = 4.036470 01 Z = 1.010720 00

MOLE FRACTION	PARTICLES / CC	SPECIE	MOLE FRACTION	PARTICLES / CC	SPECIE	MOLE FRACTION	PARTICLES / CC	SPECIE
5.723300-03	2.822770 16	F	9.755470-03	4.811460 16	HF	5.476890-07	2.701240 12	F2
1.712370-05	8.445540 13	SF6	3.680760-11	1.815370 08	H	1.326130-10	6.540580 08	HS
1.295640-14	6.340880 04	H2	5.911900-16	2.915790 03	H2S	5.751410-03	2.836630 16	SF4
3.977040-03	1.961500 16	SF5	9.747750-01	4.807650 18	A			

US	T2	T2/T1	P2	P2/P1	RHO2	RHO2/RHO1	H2	H2/H1	U2
1.401790 00	1.900000 03	6.375840 00	1.315570 00	2.499580 01	3.399820-04	3.872470 00	1.864460-01	-5.698480 00	1.039800 00

INCIDENT NORMAL WAVE SPECIES

MEAN MOLECULAR WEIGHT OF MIXTURE = 4.029110 01 Z = 1.012690 00

MOLE FRACTION	PARTICLES / CC	SPECIE	MOLE FRACTION	PARTICLES / CC	SPECIE	MOLE FRACTION	PARTICLES / CC	SPECIE
7.659080-03	3.893720 16	F	9.736470-03	4.949830 16	HF	5.926670-07	3.013000 12	F2
9.946650-06	2.514780 13	SF6	1.970700-10	1.001860 09	H	6.882240-09	3.498800 10	HS
8.160160-14	4.148460 05	H2	4.434590-14	2.254460 05	H2S	7.675040-03	3.901840 16	SF4
2.046620-03	1.040460 16	SF5	9.728770-01	4.949910 18	A			

US	T2	T2/T1	P2	P2/P1	RHO2	RHO2/RHO1	H2	H2/H1	U2
1.449000 00	2.000000 03	6.711410 00	1.409880 00	2.678770 01	3.457300-04	3.937950 00	2.020070-01	-6.174110 00	1.081040 00

INCIDENT NORMAL WAVE SPECIES

MEAN MOLECULAR WEIGHT OF MIXTURE = 4.024400 01 Z = 1.013870 00

MOLE FRACTION	PARTICLES / CC	SPECIE	MOLE FRACTION	PARTICLES / CC	SPECIE	MOLE FRACTION	PARTICLES / CC	SPECIE
8.824710-03	4.567510 16	F	9.724670-03	5.033310 16	HF	4.961460-07	2.567960 12	F2
1.116280-06	5.777640 12	SF6	1.016360-09	5.261480 09	H	4.011580-07	2.076320 12	HS
5.536970-13	2.865830 06	H2	4.071350-12	2.107260 07	H2S	8.834540-03	4.572600 16	SF4
8.806180-04	4.557920 15	SF5	9.717350-01	5.029520 18	A			

US	T2	T2/T1	P2	P2/P1	RHO2	RHO2/RHO1	H2	H2/H1	U2
1.491480 00	2.100000 03	7.046980 00	1.495190 00	2.840860 01	3.489810-04	3.974980 00	2.162880-01	-6.610580 00	1.116260 00

INCIDENT NORMAL WAVE SPECIES

MEAN MOLECULAR WEIGHT OF MIXTURE = 4.022040 01 Z = 1.014470 00

MOLE FRACTION	PARTICLES / CC	SPECIE	MOLE FRACTION	PARTICLES / CC	SPECIE	MOLE FRACTION	PARTICLES / CC	SPECIE
9.434300-03	4.931830 16	F	9.701320-03	5.071420 16	HF	3.718620-07	1.943930 12	F2
2.375820-07	1.241970 12	SF6	4.790380-09	2.504200 10	H	2.036840-05	1.064770 14	HS
3.552520-12	1.857100 07	H2	3.316100-10	1.733510 09	H2S	9.337480-03	4.881220 16	SF4
3.582360-04	1.872700 15	SF5	9.711530-01	5.076750 18	A			

VI. Thermochemical Data Analysis

Concentrations of the SF_4 decomposition product from SF_6, SF_5Cl, and SF_6–hydrogen shocked experiments were determined from the measured steady-state ultraviolet absorption behind the shock wave and the SF_4 absorption coefficient, $\epsilon_{\lambda 2660}$, in Figure 3 at the equilibrium shock temperature. A shock tube thermochemical equilibrium computer program[11] was used to calculate the equilibrium composition of the shocked gas mixtures. The computer program in general couples the Rankine–Hugoniot equations with a Newton–Raphson iteration procedure to minimize the Gibbs free energy of the shocked gas composition. The free-energy functions for the sulfur fluorine species were taken from the Aerospace thermochemical tables[12] mentioned in ref 6. Free-energy functions of all other species considered in the equilibrium calculations were obtained from JANAF thermochemical tables.[13] The results of equilibrium calculations with the Aerospace tables for the sulfur fluorine species predicted that over the shocked temperature range of the study (1600–2400°K), the SF_6 and SF_5Cl molecules would be virtually dissociated completely to the SF_4 final decomposition product. However, in the present study, measured ultraviolet SF_4 concentrations and the mass spectrometer data showing the dominant ion peak to be SF_5^+ in shock-heated SF_6

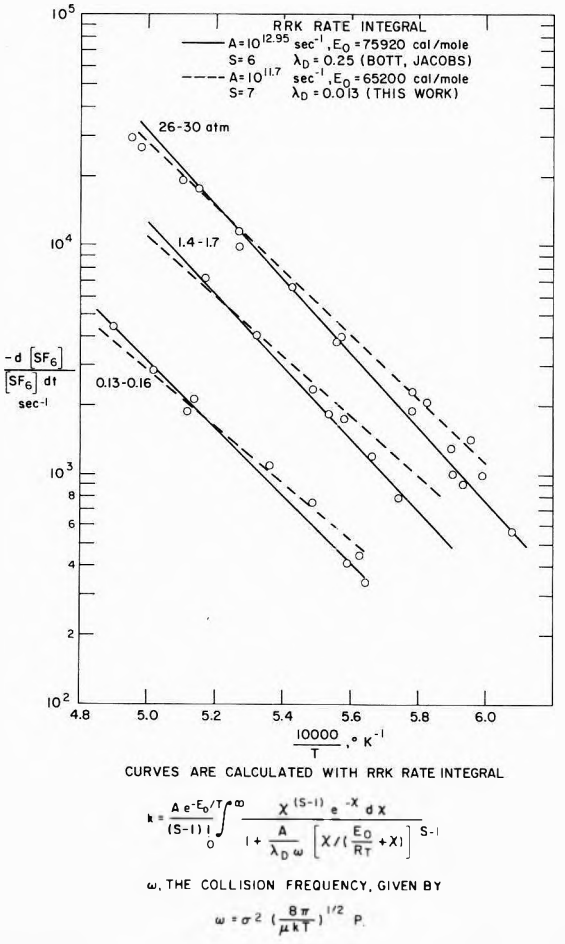

Figure 8. Theoretical curve fits to Bott–Jacobs experimental limiting first-order rate constants for SF_6 dissociation.

TABLE IV: Comparison of Thermochemical Heats of Formation for Sulfur Fluorine Species

Ref		Heat of Formation (0°K), kcal/mol	Bond energy, kcal/mol
Bott–Jacobs[a] (ref 6)	SF_6	−289.0	$D_0(SF_5–F)$ 74.9
	SF_5	−232.5	$D_0(SF_4–F)$ 65.7
	SF_4	−185.1	
This work[b]	SF_6	−288.4	$D_0(SF_5–F)$ 65.2
	SF_5	−241.7	$D_0(SF_4–F)$ 87.9
	SF_4	−172.2	

[a] Based on ref 12. The $\Delta H_f°(SF_4)$ value has been adopted in the second edition of the JANAF Tables, ref 13. [b] The $\Delta H_f°(SF_5)$ value is obtained by curve fitting the equilibrium SF_4 ultraviolet absorption data. The $\Delta H_f°(SF_4)$ value is taken from the first edition of the JANAF Tables.

were in disagreement with Aerospace thermochemical data. Assuming SF_4 was the final product of SF_6 and SF_5Cl decomposition reactions, shock tube equilibrium calculations were repeated varying the heat of formation of the SF_5 radical in the Aerospace free-energy function until calculated SF_4 concentrations were in agreement with experiment. Also the Aerospace free-energy function for SF_4 was modified to the original JANAF table SF_4 heat of formation $\Delta H_f°(SF_4)$, −172.2 kcal/mol. Typical shock tube equilibrium computer output for the SF_6, SF_5Cl, and SF_6–hydrogen mixtures tested in the study are presented in Tables I, II, and III. A comparison of experimental and calculated SF_4 concentrations for the shocked mixtures shows that the data independently are best fitted with a SF_5 heat of formation taken to be $\Delta H_f°(SF_5)$, −241.7 kcal/mol (Figures 5, 6, and 7).

VII. Discussion

Mass spectrometer and ultraviolet absorption data on SF_6 decomposition have indicated for the temperature interval of the present study an equilibrium reaction between the SF_5 radical and SF_4 molecule. Thermochemical shock tube calculations with the proposed equilibrium mechanisms are also found to fit the experimental steady-state SF_4 absorption data of the SF_5Cl thermal decomposition reactions. Infrared emission measurements on the formation of HF from the SF_6 reaction with hydrogen showed that the hydrogen atoms were reacted stoichiometrically with equal numbers of SF_6 fluorine atoms. Equilibrium SF_4 and HF concentrations were thermochemically calculated for shock SF_6–hydrogen mixtures and were comparable to the experimental SF_4 ultraviolet absorption and HF infrared emission data. The SF_5 heat of formation, $\Delta H_f°(SF_5)$ = −241.7 kcal/mol, and the SF_4 heat of formation, $\Delta H_f°(SF_4)$ = −172.2 kcal/mol, taken from the first edition of the JANAF Table were found to give a best fit to all the data of the present study. A comparison of the heats of formations used in Bott–Jacobs thermochemical calculation and those used in the calculations of this work are given in Table IV. The first and second bond dissociation energies in SF_6 are derived from the appropriate heats of formation in both studies and are also presented. It is also shown here that the value of $D_0(SF_5–F)$ = 65.2 kcal/mol can yield good equivalent RRK integral curve fits to the Bott–Jacobs limiting first-order SF_6 dissociation rate constants (Figure 8).

References and Notes

(1) J. A. Harrington, A. P. Modica, and D. R. Libby, *J. Chem. Phys.*, **44**, 3380 (1966).
(2) A. P. Modica and S. J. Sillers, *J. Chem. Phys.*, **48**, 3233 (1968).
(3) A. J. Carswell and G. G. Cloutier, *Phys. Fluids*, **7**, 602 (1964).
(4) K. E. Starner, *AIAA J.*, **7**, 2357 (1964).
(5) D. J. Spencer, T. A. Jacobs, H. Mirels, and R. W. F. Gross, *Int. J. Chem. Kinet.*, **1**, 493 (1969).
(6) J. F. Bott and T. A. Jacobs, *J. Chem. Phys.*, **50**, 3850 (1969).
(7) J. F. Bott, *J. Chem. Phys.*, **54**, 181 (1971).
(8) A. P. Modica and J. E. LaGraff, *J. Chem. Phys.*, **43**, 3383 (1965).
(9) W. M. Hickam and R. E. Fox, *J. Chem. Phys.*, **25**, 642 (1956).
(10) L. E. Young (Avco Everett Research Lab), private communication.
(11) R. Courang and K. O. Friderichs. "Supersonic Flow and Shock Waves," Interscience, New York, N. Y., 1948; R. D. Gillespie and J. Warga, "A Program for Computing Thermochemical Equilibrium Behind a Moving Shock Wave," Avco Report No. RAD TM-63-65 (Sept 1963); J. Warga, *J. Soc. Ind. Appl. Math.*, **11**, 594 (1963).
(12) R. L. Wilkins, "Thermodynamics of SF_6 and Its Decomposition and Oxidation Products," The Aerospace Corporation, TR-0158 (3240-20)-19 (1968).
(13) "JANAF Thermochemical Tables," D. R. Stull, Ed., Dow Chemical Co., Midland, Mich., 1961–1966.

Photopolymerization Mechanisms. II. Rates of Ionic Dark Addition of Benzenesulfinate Ions to Acrylic Monomers

J. D. Margerum,* R. G. Brault, A. M. Lackner, and L. J. Miller

Hughes Research Laboratories, Malibu, California 90265 *(Received December 15, 1972; Revised Manuscript Received June 11, 1973)*

Publication costs assisted by Hughes Research Laboratories

The reaction rates for sulfone formation by the ionic dark addition of benzenesulfinate ions to acrylic monomers are compared with the quantum efficiency of monomer free-radical polymerization initiated by dye-triplet redox reaction with benzenesulfinate ions. In aqueous solutions both ionic addition rates and photopolymerization yields are decreased by electron-withdrawing para substituents on benzenesulfinate. A Hammett equation correlation for the rate constants of ionic addition to acrylamide shows a ρ value of -1.23. Steric effects of using ortho in place of para groups decrease the dark reaction rates three to four times as much as they do the photopolymerization yields for a particular substituent. The temperature dependence for the rate constant (M^{-1} sec^{-1}) of benzenesulfinate ion addition to acrylamide is $k \cong 2.2 \times 10^7 \exp(-17.5 \text{ kcal}/RT)$. The rate constants for the ionic addition of *p*-toluenesulfinate ions to different acrylic monomers vary over five orders of magnitude, while the photopolymer quantum yields change by only one order of magnitude. Steric and electronic effects in the monomer structure decrease the ionic dark reaction rates with methacrylic structures and with diacetoneacrylamide. Fast addition rates are obtained with acrylic acid and hydroxyethyl acrylate. *N*-Methylolacrylamide, acrylic acid, and diacetoneacrylamide are polymerized more efficiently than acrylamide. Aqueous solutions of diacetoneacrylamide containing *o*-toluenesulfinate ions and Methylene Blue have long-term dark stability as well as good sensitivity for high photopolymer yield.

Introduction

We are studying the reaction mechanisms in photopolymerizable solutions, particularly those in which dye-sensitized reactions with benzenesulfinate ions initiate the free-radical polymerization of acrylic monomers.[1] These reactions are of interest in rapid-access imaging processes,[2] including high-resolution holographic recordings.[3,4] In the first paper of this series[1] we investigated the reactions of photoexcited Methylene Blue with para-substituted benzenesulfinate ions and the resulting free-radical polymerization of acrylamide solutions. Sulfinic acids are also known to add to unsaturated compounds to form sulfones.[5,6] Benzenesulfinate ions react similarly[7] with acrylic monomers in an ionic dark reaction (eq 1) which

$$\text{X-C}_6\text{H}_4\text{SO}_2^- + \text{CH}_2{=}\text{CHY} + \text{H}_2\text{O} \xrightarrow{k} \text{X-C}_6\text{H}_4\text{SO}_2\text{CH}_2\text{CH}_2\text{Y} + \text{OH}^- \quad (1)$$

(where Y = CONH_2, COO^-, COOH, CN, etc.)

can be considered as a Michael-type addition.[8] The sulfones are unreactive with photoexcited dyes as compared to sulfinates. Thus the dark reaction limits the shelf life of the photopolymerizable solutions because high monomer concentrations gradually use up sulfinate ions and decrease the photosensitivity. In this paper ortho and para substituents on benzenesulfinate ions as well as differences in monomer structure are studied to determine electronic and steric effects on the dark reaction (eq 1) as compared to the photopolymerization efficiency. In brief, our goal was to find structures which would decrease the rate of the dark ionic addition of benzenesulfinates to acrylic monomers without decreasing the free-radical polymerization efficiency initiated by dye-triplet redox reactions with these benzenesulfinate ions. Our studies are in aqueous solutions, mainly in the pH range of 6 to 8 where efficient photopolymerization can occur by Methylene Blue sensitization. Acrylamide is used as the monomer with which to compare the effects of ortho and para substituents on benzenesulfinate ions; and *p*-toluenesulfinate ions are used to compare the effects of different acrylic monomer structures.

Schjänberg[5] measured the rate constant for the addition of benzenesulfinic acid to acrylic acid in the low pH range (about 1.1 to 1.7) where the sulfinic acid would be partly ionized and the acrylic acid would be essentially all in the acid form. Ogata, *et al.*,[7] studied the addition of para-substituted benzenesulfinate ions to acrylonitrile; in buffered aqueous solutions at 50° they found a Hammett ρ value of -1.15. Kinetic studies also have been made of sulfone formation by benzenesulfinate ions reaction with other substrates; substituent effect correlations were reported by Ogata, *et al.*,[9] on the addition to *p*-benzoquinone, by Ritchie, *et al.*,[10] on the addition to diazonium salts, and by Lindberg[11] on the displacement reaction with bromoacetamide and bromoacetate. In general, the rates of these reactions were accelerated by electron-releasing substituents; the reported ρ values ranged between -1.55 and -0.712. Lindberg[11] also studied the bromide displacement reaction with ortho-substituted benzenesulfinates and found that they reacted more slowly than the corresponding para-substituted ions.

Experimental Section

Kinetics of Ionic Addition Reactions. The dark reaction rate was followed by measuring the OH^- liberated as sulfone is formed (eq 1), using aqueous solutions in which no dye was added. The monomer solution (45 ml) was adjusted to the desired pH, mixed with the sodium salt of the

TABLE I: Ultraviolet Peaks of Sulfones

Sulfone	λ_{max}, nm	$10^{-2}\epsilon_{max}$
$C_6H_5SO_2CH_2CH_2CONH_2$	272	9.1
	265	10.6
	258	7.6
p-$CH_2C_6H_4SO_2CH_2CH_2CONH_2$	273	6.5
	264	7.7
	262	7.9
p-$CH_3CONHC_6H_4SO_2CH_2CH_2CONH_2$	261	184
p-$CH_3C_6H_4SO_2CH_2CH_2COOCH_3$	273	6.3
	262	7.7
p-$CH_3C_6H_4SO_2CH_2CH_2COOH$	273	6.2
	263	7.5

benzenesulfinate solution (5 ml of 0.1 N), and placed in a constant temperature bath. In most runs the pH was maintained constant within ±0.05 units by the addition of 0.25 N HCl added from an automatic titration instrument connected to the electrodes of an expanded scale pH meter. The pH was recorded continuously, showing each addition of acid. Usually the reactions were followed to about 70% completion, and at the end of each run the total volume of acid added was used to calibrate the average volume of each droplet. The rate of acid addition was assumed equal to the rate of sulfone formation. Generally the initial reaction mixture was 1 to 5 N in acrylic monomer and 0.01 N in sulfinate ions, so that the monomer concentration was essentially constant and the reaction rate followed *pseudo*-first-order kinetics. Corrections were made when lower concentrations of monomer were used.

Manual titrations with a microburet were used to follow the addition reactions with the barium, strontium, and potassium acrylate monomers, and for the slow reactions with methacrylic monomers. The electrodes were placed in the reaction mixture only during the titrations, and the pH did not vary more than ±0.2 units.

The addition rate of p-toluenesulfinate to acrylic acid was followed spectrophotometrically using a Cary 14R. Equal volumes of 0.2 N solutions were mixed, adjusted to the desired pH with a small volume of acid, and held in a thermostated bath. Aliquots were transferred to a fused silica cell at regular intervals and the absorbance at 270 nm was measured to follow the sulfone formation. The reaction followed second-order kinetics.

Photopolymerization. The quantum yields of bleaching and polymerization were measured as previously described.[1] N_2-bubbled 1 N acrylic monomer solutions were used at pH 7. They contained 20% by volume of phosphate buffer (Beckman) and had concentrations of either 4×10^{-3} N or 1×10^{-2} N sodium p-toluenesulfinate, and 8×10^{-6} M Methylene Blue. They were exposed with a narrow band of light passed by a 367-nm interference filter in front of a 100-W Zr arc lamp. The incident light intensity was about 5×10^{14} photons cm^{-2} sec^{-1}. The method of analyzing the polymerization yield varied with the monomer being studied. The photopolymers from acrylamide and barium acrylate were isolated by precipitation in methanol, filtering, drying, and weighing. Poly(diacetoneacrylamide) was precipitated in water, filtered, dried, and weighed. The polymer yields from solutions of acrylic acid, potassium acrylate, N-methylolacrylamide, and methacrylamide were determined by monomer analysis before and after exposure, using a bromine addition method.[12]

Materials. Sodium benzenesulfinate and sodium o-aminobenzenesulfinate (Eastman), sodium p-toluenesulfinate (Aldrich), and p-acetamidobenzenesulfinic acid (Aldrich) were used as received. The sodium salts of p-chloro-, p-bromo-, p-nitro-, o-methyl-, and 2,4,6-trimethylbenzenesulfinic acid were synthesized from the corresponding sulfonyl chlorides by reduction with sodium sulfite.[13] They were purified by precipitation as the ferric sulfinates[14] and converted to aqueous sodium sulfinate solution. p-Aminobenzenesulfinic acid was prepared by the hydrolysis of p-acetamidobenzenesulfinic acid with sodium hydroxide by the method of Lindberg[15] (neutralization equivalent: calcd 157, found 156). Sulfinate purity was checked by uv spectra,[16] and when possible by potentiometric titration.[17]

Acrylamide (J. T. Baker), methacrylamide (Rohm and Haas), and diacetoneacrylamide (Lubrizol) were purifed by recrystallization. Acrylic acid and ethyl acrylate (J. T. Baker) and acrylonitrile (Eastman) were purified by vacuum distillation. 2-Hydroxyethyl acrylate and 2-methoxyethyl acrylate (Polyscience) and 2-hydroxyethyl methacrylate (Rohm and Haas) were vacuum distilled after treatment with barium hydroxide and drying. N-Methylolacrylamide (American Cyanamid) and hydroxymethyldiacetoneacrylamide (Lubrizol) were used as received. Metal acrylate solutions (K, Ba, Sr) were made by neutralization of acrylic acid with the metal hydroxides.

Sulfones. The addition of benzenesulfinic acid to acrylic monomers (as in eq 1) has been used to produce the corresponding sulfones with yields in the 70–90% range.[6,18,19] We prepared several sulfones in this manner and recorded their ultraviolet spectra, which are summarized in Table I. Three sulfones were made from acrylamide. Aqueous solutions of the sulfinate (25 ml, 0.5 M) and acrylamide (5 ml, 5 M) were mixed and allowed to stand 1 week at room temperature, then neutralized with HCl. 3-(p-Tolylsulfonyl)propionamide (recrystallized from aqueous ethanol, mp 176–177°; lit.[6] 175–177°) crystallized out readily, whereas 3-phenolsulfonylpropionamide (flakes, recrystallized from aqueous ethanol, mp 125–126°; lit.[6] 126–127°) and 3-(p-acetamidophenylsulfonyl)propionamide (needles, recrystallized from anhydrous ethanol, mp 189–190°; lit.[6] 190–191°) crystallized only after removal of some of the solvent and refrigeration for 3 weeks. Methyl 3-(p-tolylsulfonyl)propionate was prepared by treating 10 g of sodium p-toluenesulfinate with 35 g of methyl acrylate in 500 ml of a water–methanol solution (1:2) at 50° for 8 hr. Water was added and on cooling an oil separated out, which was crystallized from water: mp 72–73° (lit.[6] 73.5–75°). Hydrolysis of this methyl ester with 6 N HCl was used to obtain the 3-(p-tolylsulfonyl)propionic acid, which was recrystallized from water: mp 112–113° (lit.[6] 112–113°).

Nonradical Nature of Sulfinate Addition Reaction. The following experiments were conducted to show that the dark reaction was not a free-radical process, which has been suggested as an alternative mechanism.[20] (a) The reaction products from addition reaction of benzenesulfinates with acrylamide were dumped into excess methanol. No precipitate of polyacrylamide was observed. (b) The dark reaction rate of p-toluenesulfinate addition to acrylamide was observed to be the same in the presence or absence of 0.1% p-methoxyphenol, a free-radical reaction inhibitor, when studied by the automatic titration method outlined above. (c) The rate of pH change from the addition reaction was observed to be the same in the presence or absence of oxygen. Reactants mixed after vacuum evac-

uation (freeze–thaw technique with solutions in side arms) showed the same rate of color change from a pH indicator as solutions exposed to air. In each case 0.5 ml of 0.1 *N* sodium *p*-toluenesulfinate was mixed with 4.5 ml of 40% acrylamide containing 0.1% *p*-methoxyphenol and a few drops of *m*-Cresol Purple. (d) A quantitative comparison of the *p*-toluenesulfinate ion concentration remaining in evacuated *vs.* open solutions of acrylamide was made 19 hr after mixing solutions as in c (but without an indicator). In each case a 0.25-ml aliquot of the reaction solution was added to 2.25 ml of 4.0 *N* barium acrylate and 0.25 ml of 6×10^{-3} *M* Methylene Blue. The induction periods and rates of barium acrylate photopolymerization[21] were identical within experimental error. This showed that after 19 hr the sulfinate ion concentration in the acrylamide was the same whether oxygen had been present or absent.

Stability of Sulfinate Solutions. Potentiometric titrations[17] of 0.1 *N* sodium benzenesulfinate and sodium *p*-toluenesulfinate solutions stored at room temperature showed no change in sulfinate concentration over periods of several years. Air oxidation of these sulfinate solutions is negligible[22] compared to the ionic addition reactions, even at 80°.

Results

Sulfinate Ion Addition to Acrylamide. The rate of the thermal addition of various benzenesulfinates to acrylamide was measured by following the rate of OH^- liberation as in eq 1. (No dye was present and no polymerization occurred.) A typical rate constant plot is shown in Figure 1, where the *p*-toluenesulfinate ion concentration at each point was calculated from the initial value minus the acid added to maintain the pH at 7. *Pseudo*-first-order kinetics were followed, as expected due to the large excess of monomer. Table II shows a summary of various rate constants calculated from the slope of the line in plots similar to Figure 1. A given set of standardized reactant solutions showed good reproducibility for the calculated rate constant (better than ±10%). However, considerably wider variations (10–30%) were observed between some individual rate constant values measured at different times with different standardized reactant solutions. Such variations are shown in the *p*-toluenesulfinate data in the first row of Table II. We do not know the source of these variations. However, they may have been partly due to differences in the pick-up of carbon dioxide by the monomer solutions during the kinetic runs. Nitrogen-bubbled solutions consistently gave slightly higher rate constants, *e.g.*, 7.4×10^{-6} M^{-1} sec^{-1} for the *p*-toluenesulfinate addition. The second row shows that the average rate constants were not significantly different over the pH range 6–9. The third row in Table II shows that somewhat higher rate constants were obtained using 1.0 and 2.5 *M* monomer as compared to the highly concentrated 5.1 *M* acrylamide solutions. The next two rows show the effect of temperature on a series of kinetic runs made with *p*-toluenesulfinate and with benzenesulfinate. Each series was run with the same sulfinate and acrylamide solutions. Arrhenius equation plots of these rate constants (in M^{-1} sec^{-1}) gave $\log k_{CH_3} = (-17.1 \pm 0.7)/2.3RT + 7.3 \pm 0.5$ and $\log k_H = (-17.5 \pm 0.4)/2.3RT + 7.3 \pm 0.3$, respectively. The last two rows in Table II show the average reaction rate constants for other para- and ortho-substituted benzenesulfinate ionic addition reactions.

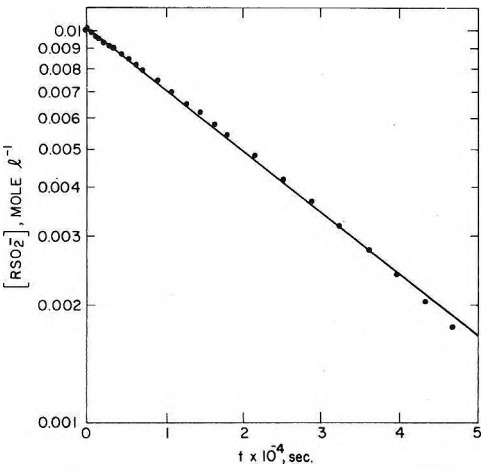

Figure 1. Kinetic plot for addition of *p*-toluenesulfinate ions to 5.06 *N* acrylamide, pH 7, 25° ($k = 7.4 \times 10^{-6}$ M^{-1} sec^{-1}).

TABLE II: Rate Constants for Ionic Addition to Acrylamide

$X-C_6H_4SO_2^-$	Variable condition[a]	Obsd rate constants,[b] 10^6k
X = *p*-CH_3		(6.8, 6.6, 6.4, 8.0, 7.4) = 7.0 av
p-CH_3	pH	7.9 (pH 6), 7.0 (pH 7), 6.5 (pH 8), 7.4 (pH 9)
p-CH_3	[Acrylamide]	7.0 (5.1 *M*), 9.1 (2.5 *M*), 8.8 (1.0 *M*)
p-CH_3	Temp	3.3 (20°), 6.4 (25°), 8.8 (30°), 15.2 (35°), 22.2 (40°)
H	Temp	2.1 (20°), 3.5 (25°), 5.3 (30°), 9.6 (35°), 13.9 (40°)
p-X		16.4 (NH_2), 3.5 (CH_3CONH), 1.8 (Br), 1.7 (Cl), 0.3 (NO_2)
o-X		5.3 (NH_2), 1.6 (CH_3), 0.03 (NO_2), 0.3 (2,4,6-CH_3)

[a] When not varied; 5.07 *M* acrylamide, 0.01 *M* sulfinate, 25°, pH 7. [b] Average values from different reactant solutions, except for temperature runs where the same solutions were compared.

Photopolymerization of Acrylamide. When a dye such as Methylene Blue was added to acrylamide solutions containing benzenesulfinate ions, exposure to light caused photopolymerization to occur much more rapidly than the ionic dark reaction. We have shown[1] that this polymerization is initiated by free radicals generated from the sulfinate ion redox reaction with the triplet state of the dye (eq 2). The efficiency of photopolymerization is related to

$$X\text{-}C_6H_4SO_2^- + {}^3D^+ \xrightarrow{k^*} X\text{-}C_6H_4SO_2\cdot + D\cdot \qquad (2)$$

the rate of this dye-triplet reaction with the sulfinate ions. We compared the effects of ortho- and para-substituted benzenesulfinate ions by measuring the quantum yields of dye bleaching (Φ_B) and acrylamide polymerization (Φ_M) under the same conditions. These results are summarized in Table III.

p-Toluenesulfinate and Acrylic Monomers. The effect of the monomer structure on the rate of the sulfinate ionic dark addition reaction was studied by using *p*-toluenesulfinate with various acrylic monomers in the absence of dye. The results are shown in Table IV. Whenever possible, 1 *N* aqueous monomer solutions were used at pH 7. Methylene Blue was added and dye-sensitized polymerization quantum yields were measured for many of these monomer solutions.

TABLE III: Photopolymerization of Acrylamide[a]

	Φ_B		Φ_M	
$X-C_6H_4SO_2^-$	*o*-X	*p*-X	*o*-X	*p*-X
X = NH_2	0.13	0.12	1250	1180
CH_3	0.13	0.15	1740	1740
CH_3CONH		0.09		1260
H		0.14		1730
Cl		0.07		930
Br		0.05		730
NO_2	0.004	0.02	85	280
Mesitylene	0.09		1100	

[a] Quantum yields from 4×10^{-3} *M* sulfinate and 8×10^{-6} *M* Methylene Blue in 1 *M* acrylamide, pH 7, 25°, 4×10^{14} photons cm^{-2} sec^{-1} incident intensity.

TABLE IV: Dark Reaction Rates of *p*-Toluenesulfinate Ion Addition to Monomers Compared with Dye-Sensitized Photopolymerization Yields

	Ionic addition rate[b]	Dye-sensitized photopolymerization[c]	
Monomer[a]	10^6k	$10^{-3}\Phi_M$	Φ_B
2-Hydroxyethyl acrylate[d]	1.1×10^3		
Acrylic acid[e]	9.1×10^2	2.2	0.07
Ethyl acrylate[d]	1.9×10^2		
Hydroxymethyldiacetoneacrylamide	6.2×10		
Acrylonitrile	5.2×10		
Barium acrylate	2.6×10	1.5	
Strontium acrylate	2.6×10		
Potassium acrylate	2.0×10	0.64	0.13
Methoxyethyl acrylate[d]	1.9×10		
N-Methylolacrylamide	1.5×10	5.4	0.12
Acrylamide	8.8	1.3	0.13
Diacetoneacrylamide	0.80	2.0	
2-Hydroxyethyl methacrylate[d]	0.08		
Methacrylamide	0.02	0.31	0.15

[a] 1.0 *N* monomer, 10^{-2} *M* *p*-toluenesulfinate, and pH 7 except where specified. [b] At 25°, *k* in M^{-1} sec^{-1}. [c] 8×10^{-6} *M* Methylene blue and 5.2×10^{14} photons cm^{-2} sec^{-1} intensity. [d] 0.25 *M* monomer. [e] Monomer 0.1 *M* for addition reaction and 1 *M* for photopolymerization, pH 2.5.

Discussion

Effect of Conditions. The rate of the *p*-toluenesulfinate ion dark addition to acrylamide was independent of pH (in the 6–9 range) and the presence or absence of oxygen. The kinetics of the dark reaction are consistent with the nucleophilic addition of the sulfinate ion to the double bond being the rate-determining step, as has been assumed by others[7] for similar reactions. However, eq 1 should be considered a reversible reaction in which the equilibrium is far to the right under the experimental conditions. The reversibility of Michael-type additions is well known,[8,23] and the elimination of arylsulfinic acids from aryl ethyl sulfones under strongly basic conditions has been clearly established.[24-28] For example, benzenesulfinate ions are produced from 3-phenylsulfonylpropionic acid in water in the pH 11–13 range.[29] However, at lower pH's the reactants in eq 1 give an almost quantitative yield of the sulfone addition product.[6,18,19] Arrhenius equation plots of temperature effects on the rate constants (for benzenesulfinate and *p*-toluenesulfinate addition to acrylamide) showed that the reactions had an activation

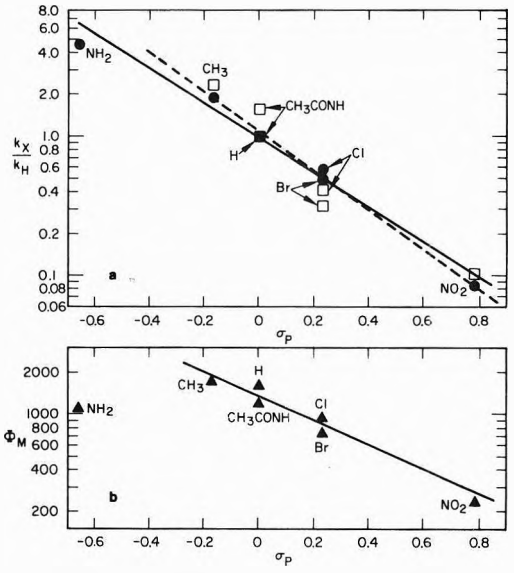

Figure 2. Hammett equation correlations for para-substituted benzenesulfinate ion reactions in pH 7 aqueous acrylamide solutions: (a) ratio of rate constants, (●) ionic dark addition reaction in 5 *M* monomer, (□) dye-triplet redox reaction in 1 *M* monomer; (b) (▲) quantum yield of monomer polymerized in 1 *M* monomer, using 4×10^{-3} *M* sulfinate and 8×10^{-6} *M* dye.

energy of about 17 kcal/mol and a frequency factor with log $A \cong 7.3$. This low-frequency factor may be related to the ambident nucleophilicity[9] of the benzenesulfinate ion, but the frequency factors of other Michael-type addition reactions vary over a wide range and both higher and lower *A* values have been reported.[7,30-33]

Effect of Para Substituents. The rates of ionic addition of para-substituted benzenesulfinate ions to acrylamide increased with the electron-releasing character of the substituent. Figure 2a shows a Hammett equation plot of the rate constant ratios (solid points) at 25°. This gives a ρ value of −1.23 when the amino substituent is included, as shown by the solid line. This is very close to the ρ value of −1.15 found by Ogata, *et al.*,[7] for similar reactions with aqueous acrylonitrile at 50°, and it falls in the general range of ρ values reported for other reactions of para-substituted benzenesulfinate ions.[9-11]

We previously used plots of quenching-corrected quantum yields of Methylene Blue bleaching in acrylamide to determine the relative rate constants for eq 2, which is the reaction of the dye-triplet state with para-substituted benzenesulfinate ions.[1] These calculated triplet redox rate constant ratios (k_X^*/k_H^*) are shown by the open squares in Figure 2a. We did not previously study the *p*-NH_2 substituent. If the *p*-NH_2 data point is excluded from our present studies, then the broken line in Figure 2a shows the least-squares plot for the ionic dark addition reaction (eq 1) by the other six substituents (solid points). The dye-triplet state redox reaction (eq 2) substituents (open squares) also fit the broken line correlation in Figure 2a, with a ρ value of −1.44. Thus, while the photopolymerizable solutions are made more thermally stable by using benzenesulfinate ions with electron-withdrawing para substituents, these groups cause a corresponding decrease in the rate constants for the generation of free radicals from the dye-triplet redox reaction.

The photopolymer yields from monomer solutions at a particular light intensity and sulfinate concentration (Table III) also varied with the para substituents, but not as sharply as the rate constants in reactions 1 and 2. Ex-

cluding the p-NH_2 substituent, the slope of a Hammett equation plot had a ρ value of -0.88 as shown in Figure 2b for the quantum yields of acrylamide polymerization. Many factors affect these quantum yields, including sulfinate ion quenching of the photoexcited dye, and the relative rates of free-radical initiation and termination. Quenching of the excited dye decreased the free-radical yield from all of the substituted sulfinates as compared to benzenesulfinate.[1] Also, the polymerization quantum yield is inversely proportional to the square root of the light intensity when benzenesulfinate is used with Methylene Blue. This is typical of photopolymerizations in which the propagation reaction is proportional to the radical concentration while the termination reaction is proportional to the square of the radical concentration. Similarly, the electron-withdrawing para-substituted benzenesulfinates give a lower concentration of free-radical initiators so that the photopolymer quantum yield is decreased, but not as much as the relative rate of free-radical formation. If this was the only factor involved, then the photopolymer quantum yields would be proportional to the square root of the initiator concentration,[34] so that (Φ_X/Φ_H) would equal $(k_X^*/k_H^*)^{1/2}$ and the Hammett equation constant for polymerization would be $\rho = -1.44/2 = -0.72$. This is not far from the observed value of -0.88 shown in Figure 2b.

In the para-substituted series, the unsubstituted benzenesulfinate is the most useful dye-sensitized initiator for acrylamide polymerization. At high concentrations it causes less quenching of the dye and provides the highest polymer yield.[1] It has an intermediate rate of thermal deactivation (ionic addition) with the monomer. Electron-donating groups cause a faster dark reaction and due to quenching effects do not give higher photopolymer yields, while electron-withdrawing groups slow down both the dark reaction and the photopolymerization.

Effect of Ortho Substituents. We expected ortho-substituted benzenesulfinate ions to undergo sulfone formation more slowly[11] than the corresponding para compounds due to steric hindrance. This was indeed the case for all the ortho derivatives we studied. The dark reactions of the o-nitro-, o-methyl-, and o-aminobenzenesulfinates were between one-tenth and one-third as fast as their para isomers. As shown in Table V, the dye-sensitized photopolymerization and bleaching reactions were much less affected by the use of ortho in place of para substituents. We found less excited state dye quenching by the o-amino- than the p-aminobenzenesulfinate, and this is partly responsible for the improved polymer yield from this ortho derivative. The o-toluenesulfinate gave as high a polymer yield ($\Phi_M = 1740$) as was obtained with p-toluenesulfinate and benzenesulfinate, and its rate constant for ionic addition ($1.6 \times 10^{-5}\ M^{-1}$ sec) was slower than either of these other two sulfinates. The additional steric hindrance in sodium 2,4,6-trimethylbenzenesulfinate further decreased the rate of ionic addition ($k = 3 \times 10^{-7}\ M^{-1}$ sec), but also decreased the photopolymer yield ($\Phi_M = 1100$).

Both electronic and steric effects control the reactivity of ortho-substituted benzenesulfinates. Compared to the same para group, the steric hindrance of an ortho group slows down appreciably the rate of ionic addition to the monomer. There is a much smaller steric effect on the dye-sensitized formation of free radicals (eq 2) and subsequent polymerization. The net result of electron-releasing and steric hindrance effects in the o-toluenesulfinate ion

TABLE V: Effect of Ortho and Para Substituents on Benzenesulfinate Ion Reaction Rates with Acrylamide

	Thermal addition[a] sulfone formation	Photopolymerization[b]	
		Dye bleaching	Polymerization
$X\text{-}C_6H_4SO_2^-$	k_o/k_p	$(\Phi_B)_o/(\Phi_B)_p$	$(\Phi_M)_o/(\Phi_M)_p$
X = NH_2	0.32	1.1	1.1
CH_3	0.23	0.88	1.0
NO_2	0.10	0.20	0.31

[a] Rate constants in 5 M acrylamide. [b] Polymerizations in 1 M acrylamide.

is that a high photopolymerization efficiency is obtained while the rate of thermal deactivation (ionic addition) is decreased as compared to the benzenesulfinate or p-toluenesulfinate ions. Thus, o-toluenesulfinate is the most effective of these structures for dye-sensitized polymerization.

Effect of Monomer Structure. The results summarized in Table IV show that differences in monomer structure caused the ionic addition reaction rates to vary by five orders of magnitude, while the polymerization quantum yield changed by only one order of magnitude. In the acrylic series $CH_2{=}CH\text{-}Y$, the rate constant of the ionic addition reaction varied with Y in the following order: COOH > COOEt > CN > COO^- > $CONH_2$. Although electron-withdrawing substituents on the olefin generally tend to accelerate the rate of Michael-type addition reactions, it is difficult to separate inductive, resonance, and steric effects. The effect of the acrylic Y substituents on the relative rates of other Michael-type addition reactions do not always fall in the same order. Our results are in good agreement with the results of Friedman, *et al.*,[35,36] who found that the rate constants for Y groups were in the order COOMe > CN > $CONH_2$ for the addition of glycine and for the addition of mercaptopropionic acid to the acrylic structures. However, studies on the addition of alcohols[37,38] have shown a different sequence of relative rates where CN > COOMe > $CONH_2$. The resonance interaction in the transition state is probably affected by the reactant being added to the double bond. The hydroxyl groups in 2-hydroxyethyl acrylate, hydroxymethyldiacetoneacrylamide, and N-methylolacrylamide increased the relative rate of sulfinate addition. This may be due to intramolecular hydrogen bonding between hydroxyl groups and the carbonyl group, which would favor the formation of the anion intermediate as illustrated in eq 3.

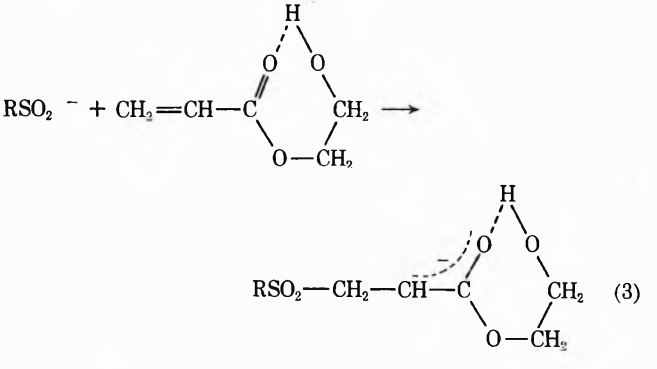

(3)

The ionic addition to methacrylic structures was several orders of magnitude slower than to the corresponding

acrylic monomers. The α-methyl acrylic substituent makes the β carbon relatively more negative and thus decreases the rate of nucleophilic attack by the sulfinate ion. α-Methyl substituents generally retard Michael-type addition reactions,[36-38] and while both electronic and steric effects are involved, Friedman and Wall[36] concluded that the effect is primarily electronic.

The ionic addition rate to diacetoneacrylamide appeared to be unusually slow as compared to acrylamide. However, molecular models indicate that its *tert*-butyl type of substituent has a steric effect that may reduce the coplanarity of the acrylic carbonyl with the double bond or that may hinder the approach of the sulfinate ion to the β carbon when these groups are coplanar. This would decrease the carbonyl resonance interaction and could be responsible for the slower rate of sulfinate ion addition. Similar effects have been reported[38] for the addition of alcohols to *N*-alkylacrylamides, where the reaction with *N*-*tert*-butylacrylamide was too slow to be determined.

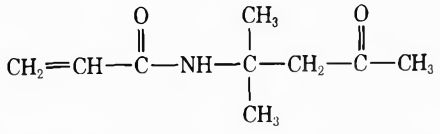

In the photopolymerizations, the initial free radical yield from the dye-triplet reaction with *p*-toluenesulfinate should be approximately the same for all the runs at pH 7. The differences in the quantum yield of bleaching (Table IV) were small, so that main differences in the polymer yields are due to the efficiency of radical capture, propagation, and termination. The photopolymer yields did not vary with monomer structure at all like the rates of the ionic dark reaction. For example, the ratio of the photopolymer quantum yield divided by the dark reaction rate constant is 2.4×10^6 for acrylic acid, 1.5×10^8 for acrylamide, 3.6×10^8 for *N*-methylolacrylamide, 2.5×10^9 for diacetoneacrylamide, and 1.6×10^{10} for methacrylamide. These last three monomers are of interest for photopolymerization imaging. The methacrylamide dark reaction is 400 times slower than acrylamide, while its photopolymer yield is only four times lower. Methacrylamide has a slower free-radical propagation rate and a faster termination rate than acrylamide,[39] which accounts for the lower photopolymer yield. *N*-Methylolacrylamide gave four times better photopolymer yield than acrylamide, while its dark reaction rate constant was only twice as fast. It gives a gel-type polymer and it is of interest as a monomer component to increase the sensitivity of photopolymerization imaging systems. The *p*-toluenesulfinate ionic addition rate to diacetoneacrylamide is ten times slower than to acrylamide, and it gave a higher photopolymer yield. This is a very favorable combination of monomer properties, although poly(diacetoneacrylamide) is insoluble and gives a light scattering image which is suitable for direct readout but not for holography. We found that added steric retardation of the ionic addition dark reaction with diacetoneacrylamide was obtained with *o*-toluenesulfinate ions, without any significant decrease in the photopolymer yields; pH 7 buffered samples of this monomer and the sulfinate remained highly photosensitive for a month at room temperature.

Acknowledgment. We are indebted to the Directorate of Chemical Sciences, Air Force Office of Scientific Research, Contract No. F44620-68-C-0043, for partial support of these studies.

References and Notes

(1) Paper I: J. D. Margerum, A. M. Lackner, M. J. Little, and C. T. Petrusis, *J. Phys. Chem.*, **75**, 3066 (1971).
(2) R. G. Brault, J. A. Jenney, J. D. Margerum, L. J. Miller, and J. B. Rust, *Image Technol.*, **13** (3), 13 (1971); *cf.* "Applications of Photopolymers," R. J. Povinelli, Ed., Society of Photographic Scientists and Engineers, Washington, D. C., 1970, pp 113–132.
(3) J. A. Jenney, *J. Opt. Soc. Amer.*, 60, 1155 (1970).
(4) J. A. Jenney, *Appl. Opt.*, **11**, 1371 (1972).
(5) E. Schjånberg, *Berichte*, **76B**, 287 (1943).
(6) O. Achmatowicz and J. Michaiski, *Rocz. Chem.*, **30**, 243 (1956); *Chem. Abstr.*, **51**, 1064 (1957).
(7) Y. Ogata, Y. Sawaki, and M. Isono, *Tetrahedron*, **26**, 3045 (1970).
(8) J. March, "Advanced Organic Chemistry: Reactions, Mechanism, and Structure," McGraw-Hill, New York, N. Y., 1968, p 568.
(9) Y. Ogata, Y. Sawaki, and M. Isono, *Tetrahedron*, **26**, 731 (1970).
(10) C. D. Ritchie, J. D. Saltiel, and E. S. Lewis, *J. Amer. Chem. Soc.*, **83**, 4601 (1961).
(11) B. Lindberg, *Acta Chem. Scand.*, 17, 393 (1963).
(12) N. D. Cheronis and T. S. Ma, "Organic Functional Group Analysis by Micro and Semimicro Methods," Wiley-Interscience, New York, N. Y., 1964, pp 522–525.
(13) S. Smiles and C. M. Vure in "Organic Synthesis," Collect. Vol. 1, 2nd ed, Wiley, New York, N. Y., 1944, p 7.
(14) C. G. Overberger and J. J. Godfrey, *J. Polym. Sci.*, **40**, 179 (1959).
(15) B. J. Lindberg, *Acta Chem. Scand.*, **20**, 1843 (1966).
(16) M. Kobayashi and N. Koga, *Bull. Chem. Soc. Jap.*, **39**, 1788 (1966).
(17) B. Lindberg, *Acta Chem. Scand.*, **17**, 383 (1963).
(18) V. Mikhailova, N. Borisova, and D. Stankevich, *Zh. Org. Chim.*, **2**, 1437 (1966); *Chem. Abstr.*, **66**, 104778*p* (1967).
(19) I. K. Fel'dman and V. N. Mikhailova, *Zh. Obshch. Khim.*, **33**, 2111 (1963); *Chem. Abstr.*, **59**, 12682*f* (1963).
(20) Private communication from a reviewer.
(21) J. B. Rust, L. J. Miller, and J. D. Margerum, *Polym. Eng. Sci.*, 9, 40 (1969).
(22) J. B. Rust, L. J. Miller, and J. D. Margerum, *Polym Prepr.*, **10**, 294 (1969).
(23) E. D. Bergmann, D. Ginsberg, and R. Pappo in "Organic Reactions," Vol. 10, R. Adams, Ed., Wiley, New York, N. Y., 1959, Chapter 3, pp 187–191.
(24) G. W. Fenton and C. K. Ingold, *J. Chem. Soc.*, 3127 (1928); 2338 (1929); 705 (1930).
(25) C. K. Ingold, *Proc. Chem. Soc.*, 265 (1962).
(26) J. E. Hofmann, T. J. Wallace, P. A. Argabright, and A. Schriesheim, *Chem. Ind. (London)*, 1243 (1963).
(27) O. Achmatowicz, E. Maruszewska-Wieczorkowska, and Y. Michaiski, *Rocz. Chem.*, **29**, 1029 (1955); *Chem. Abstr.*, **50**, 12046*h* (1956).
(28) L. F. Cason and C. C. Wanser, *J. Amer. Chem. Soc.*, **73**, 142 (1951).
(29) (a) L. J. Miller, J. D. Margerum, J. B. Rust, R. G. Brault, and A. M. Lackner, manuscript in preparation; (b) B. Holmberg and E. Schjanberg, *Ark. Kemi, Mineral. Geol.*, A15, No. 20 (1942); *Chem. Abstr.*, **38**, 2943 (1944).
(30) H. W. Johnson, Jr., E. Ngo, and V. A. Pena, *J. Org. Chem.*, **34**, 3271 (1969).
(31) M. J. Kamlet and D. J. Glover, *J. Amer. Chem. Soc.*, **78**, 4556 (1956).
(32) M. Friedman and J. S. Wall, *J. Amer. Chem. Soc.*, **86**, 3735 (1964).
(33) S. T. McDowell and C. J. M. Stirling, *J. Chem. Soc.*, **13**, 351 (1967).
(34) F. W. Billmeyer, Jr., "Textbook of Polymer Science," Wiley-Interscience, New York, N. Y., 1962, p 274.
(35) M. Friedman, J. F. Cavins, and J. S. Wall, *J. Amer. Chem. Soc.*, **87**, 3672 (1965).
(36) M. Friedman and J. S. Wall, *J. Org. Chem.*, **31**, 2888 (1966).
(37) B. A. Feit and Z. Bigon, *J. Org. Chem.*, **34**, 3942 (1969).
(38) R. N. Ring, G. C. Tesoro, and D. R. Moore, *J. Org. Chem.*, **32**, 1091 (1967).
(39) J. Ulbricht in "Polymer Handbook," J. Brandrup and E. H. Immergut, Ed., Wiley-Interscience, New York, N. Y., 1966 Chapter II-2.

The Mechanism of CO Laser Emission from the CH + NO Reaction

M. C. Lin

Naval Research Laboratory, Washington, D. C. 20375 *(Received April 24, 1973)*

Publication cost assisted by the Naval Research Laboratory

CO laser emission at 5 μm was observed in the flash photolysis of the mixtures of NO and $CHBr_3$ in vacuum uv, in the presence of a large amount of SF_6. About 32 transitions ranging from 6 → 5 to 3 → 2 were identified. The dependence of laser intensity upon the total pressures of various mixtures, the partial pressure of NO, and flash energy have been examined. These observations plus the results of gas analysis allow us to conclude that the primary pumping process in the $CHBr_3$–NO system is the following four-centered reaction: CH + NO → CO† + NH (4a), $\Delta H°_{4a} = -105$ kcal/mol. The possibility of occurrence of other side reactions was also discussed.

Introduction

We have recently reported the observation of very strong CO stimulated emissions at 5 μm from both the $O(^3P)$ + CH[1,2] and the CH + O_2[3] reactions. The primary pumping processes in these two systems are respectively

$$O(^3P) + CH \longrightarrow CO^\dagger + H \qquad \Delta H°_1 = -176 \text{ kcal/mol} \quad (1)$$

$$CH + O_2 \longrightarrow CO^\dagger + OH \qquad \Delta H°_2 = -159 \text{ kcal/mol} \quad (2)$$

In the CH–O_2 system, stimulated CO_2 emission at 10 μm, resulting from the (001) → (020) transition in the range of P(58)–P(70), was also detected.[3] It was attributed to the reaction

$$CH + O_2 \longrightarrow H + CO_2^\dagger \qquad \Delta H°_3 = -184 \text{ kcal/mol} \quad (3)$$

In these studies, $CHBr_3$ was used as the CH radical source *via* the successive removal of three Br atoms in a vacuum uv flash above 165 nm. We have found, on the basis of our gas analysis, that the conversion of $CHBr_3$ increased linearly with flash energy,[2] and also that about 30% of $CHBr_3$ was decomposed in a single flash at 1.6 kJ. These observations will be further verified later. The high CH radical concentration as well as the intrinsically high population inversions are probably the primary reasons of strong laser outputs in both O–CH and CH–O_2 systems.

In our detailed mechanistic study of the O + CH reaction,[2] we found that the addition of a small amount of NO to an SO_2–$CHBr_3$–He mixture quenched the CO laser emission very drastically; these results are shown in Figure 1. Introduction of 1 Torr of NO to a 20 Torr 1:1:20 SO_2:$CHBr_3$:He mixture, for example, reduces the laser power by as much as 68%. At higher NO concentrations, however, the intensity of CO emission decreases at a much slower rate. The initial steep decline in power upon the addition of NO is believed to be caused by the inhibition reaction

$$CH + NO \longrightarrow \text{products} \quad (4)$$

which is probably very fast. The slower decrease in laser output at higher NO concentrations indicates that reaction 4 itself might contribute, albeit less efficiently, to laser action after reaction 1 is nearly terminated. An experiment with a 2:1:20 NO:$CHBr_3$:SF_6 mixture showed that laser oscillation indeed occurred.

In this note, we report in some detail the results of our parametric study of this new reaction through CO laser emission measurements, including frequency identification, the effects of pressure and flash energy, and the results of product analysis. The mechanism of this reaction will be discussed on the basis of these results. CO laser emissions at 5 μm were also detected in the flash photolysis of mixtures of $CHBr_3$ and NO_2, $CHBr_3$ and O_3, and $CHBr_3$ and N_2O, in the presence of excess amounts of diluent (SF_6, He, or Ar); the emissions in these systems can be attributed to the combination of the elementary reactions mentioned above, with a possible contribution from the $O(^1D)$ + CH reaction. The $O(^1D)$ + CF reaction was found to produce stimulated CO emission.[4]

Experimental Section

The vacuum uv flash laser apparatus employed in this study has been described in detail previously.[1] A Suprasil laser tube (1 m long, 2.2 m i.d.), fitted with replaceable high-transmission ir windows at the Brewster angle, was positioned in an optical cavity formed by gold-coated mirrors at a separation of about 1.2 m. One of the mirrors had a 1-mm coupling hole at its center. Two 40-cm long quartz flash lamps were concentrically sealed, at about 2 cm apart, to the laser tube. The laser tube was directly connected, *via* the space between the two flash lamps, to the all-glass, greaseless vacuum system.

The flash output had a 15-μsec risetime and 50-μsec half-width. About 30 Torr of a 1% Xe–Ar mixture was used as the flash light source. Laser emissions were analyzed by a 0.5-m Minuteman Model 305M13 monochromator fitted with a kinematically mounted 150 line/mm grating blazed at 6 μm, and were observed by a Ge:Au detector, maintained at 77°K, in conjunction with an oscilloscope.

All chemicals used in this work were obtained from the Matheson Gas Products Co., except $CHBr_3$ which was purchased from Aldrich Chemical Co. Before use, the condensable chemicals were subjected to trap-to-trap distillation using different temperature baths. The noncondensables were delivered under high pressure after repeated purging and were used without further purification. All experiments were carried out at room temperature.

Results and Discussion

Figure 2 shows a typical CO laser emission trace taken from 20 Torr of 2:1:20 NO:$CHBr_3$:SF_6 mixture flashed with a 1.6-kJ energy. The intensity of this emission is con-

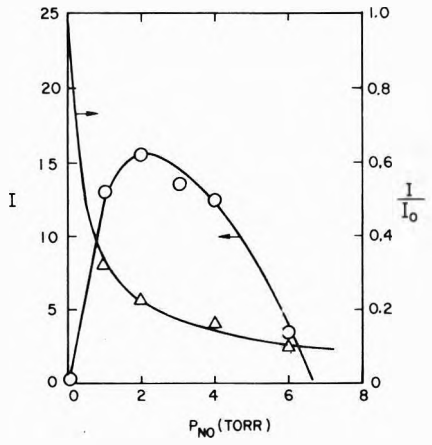

Figure 1. Dependence of CO laser intensity on the partial pressure of NO: circles, NO added to 20 Torr of 1:20 $CHBr_3$:SF_6 mixtures, E_λ = 1.6 kJ; triangles, NO added to 20 torr of 1:1:30 SO_2:$CHBr_3$:He mixtures, E_λ = 1.6 kJ (these data are taken from ref 2).

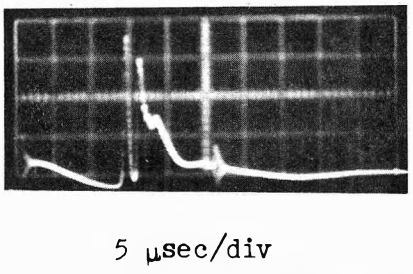

Figure 2. A typical CO laser emission trace: 25 Torr of 2:1:20 NO:$CHBr_3$:SF_6, E_λ = 1.6 kJ.

siderably weaker than that of the CH–O_2 system.[3] SF_6 dilution was found to be essential for laser action; no oscillation was detected when He or Ar was used instead of SF_6, contrary to that observed in the CH–O_2 system.

1. Partial and Total Pressure Dependence. The dependence of peak power on the partial pressure of NO is shown in Figure 1. These runs were carried out by adding different amounts of NO to 20 Torr of 1:20 $CHBr_3$:SF_6 mixture, flashed with 1.6-kJ energy. The laser intensity rises very rapidly as the pressure of NO increases; it reaches a maximum when 2 Torr of NO is present and begins to decrease rapidly at higher NO concentrations. The reduction in laser output at higher NO concentrations is believed to be due to primarily the vibrational relaxation of CO† by NO, since NO is known to quench CO† at higher vibrational levels very effectively.[5] Contrary to this, O_2 does not exhibit this inhibition effect in the O_2–$CHBr_3$ system.[3] The intensity of the CO laser emission in the O_2–$CHBr_3$ system still rises steadily when 20 Torr of O_2 was added to the same 1:20 $CHBr_3$:SF_6 mixture. The results shown in Figure 1 confirm the effectiveness of CO† quenching by NO reported by Hancock and Smith.[5]

The emission intensity as a function of total pressure for three different mixtures with the following compositions, NO:$CHBr_3$:SF_6 = 2:1:10, 2:1:20, and 2:1:50, respectively, is shown in Figure 3. The NO:$CHBr_3$ ratio and flash energy were maintained constant in these runs. The results indicate that a higher SF_6 dilution is favored. The maximum laser output increases by a factor of 3 when the SF_6 concentration is doubled from 2:1:10 to 2:1:20. A further increase from 2:1:20 to 2:1:50, however, leads to a less drastic improvement. The strong SF_6 dilution effect clearly indicates that the rise in rotational translational temperature during the reaction is significant. On account of this and the lower gain of the present system, no laser oscillation was detected when a less effective diluent such as He or Ar was used.

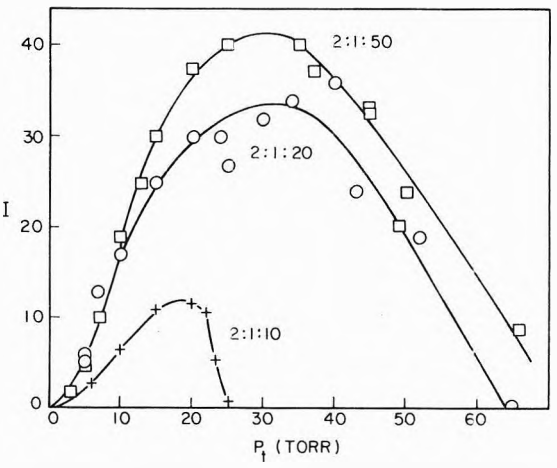

Figure 3. Dependence of CO laser intensity as a function of total pressure. The composition given for each mixture is for NO, $CHBr_3$, and SF_6 respectively; E_λ = 1.6 kJ for all flashes.

TABLE I: Observed CO Laser Transitions and Their Relative Intensities from the CH + NO Reaction[a]

Transition		Intensity	Transition		Intensity
6 → 5	P(18)	S[b]	5 → 4	P(12)	M
	P(17)	S	4 → 3	P(23)	W
	P(16)	M		P(22)	M
	P(15)	S		P(21)	S
	P(14)	M		P(20)	S
5 → 4	P(23)	W		P(19)	S
	P(22)	M		P(18)	W
	P(21)	W		P(17)	S
	P(20)	W		P(16)	S
	P(19)	M		P(15)	S
	P(18)	S		P(14)	M
	P(17)	S	3 → 2	P(23)	W
	P(16)	S		P(22)	S
	P(15)	S		P(21)	S
	P(14)	M		P(20)	S
	P(13)	M		P(19)	W

[a] Laser mixture: 20 Torr of NO:$CHBr_3$:SF_6 = 2:1:20; Σ_λ = 1.6 kJ. [b] S = strong, M = medium, and W = weak; the emission was focused with an ir lens onto the 300-μm entrance slit; the exit slit width = 50 μm.

2. Identification of Transitions. The individual CO vibration–rotational transitions were identified with the 0.5-m monochromator. A 20-Torr 2:1:20 NO:$CHBr_3$:SF_6 mixture was flash photolyzed with 1.6 kJ of energy. A total of about 32 lines ranging from 6 → 5 to 3 → 2 were identified; these transitions are summarized in Table I. The absence of the transitions above v' = 6 is most likely due to the NO relaxation mentioned previously. The relatively high J's observed in this system in comparison with those observed in the CH–O_2 system also implies that the present system has a relatively lower gain. The intensities of most bands in the CH–O_2 system were found to peak at $J \approx 13$–14, whereas in the present system they occurred at $J \geq 15$ as shown in the table.

3. Reaction Mechanism. A. Product Analysis. The chemistry of the flash-initiated $CHBr_3$–NO system is not

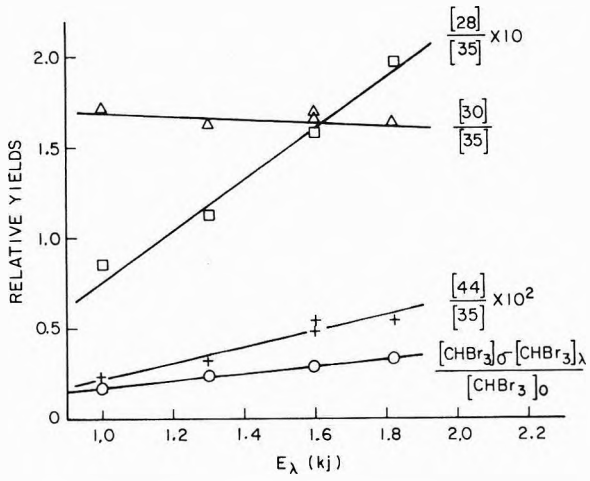

Figure 4. Relative yields *vs.* flash energy plots: laser mixture, 30 Torr of 2:1:20 NO:$CHBr_3$:SF_6.

known. In view of this, we have carried out product analysis employing a CEC-620 mass spectrometer.

Figure 4 represents the relative peak heights of different masses (m/e) as functions of flash energy. The lasing mixture, NO:$CHBr_3$:SF_6 = 2:1:20 (30 Torr), was used in these runs. The peak height of SF_2^{2+} (m/e = 35) was used as an internal standard. The conversion of $CHBr_3$ by a single flash at energy E_λ, $([CHBr_3]_0 - [CHBr_3]_\lambda)/[CHBr_3]_0$, was determined by the observed peak height of mass 92 ($CH^{79}Br^+$) in the unflashed and flashed samples. The conversion was found to increase linearly with flash energy, in accordance with the results given in Figure 5 ($I \propto E_\lambda$) and those observed in the O_2–$CHBr_3$ system.[3] The conversion of $CHBr_3$ at E_λ = 1.6 kJ is about 28% in the present system.

Similar to $CHBr_3$, the relative peak heights of mass 30 (NO), 28 (CO + N_2), and 44 (presumably N_2O) also vary linearly with E_λ within the experimental errors. The measurement for mass 28 was subjected to a greater uncertainty due to a comparable N_2 background in the mass spectrometer. In addition to these major products, several small peaks appeared at m/e 25–27, 80, and 82 in the flashed samples. They are probably due to C_2H_2 (m/e 25, 26), HCN (m/e 26, 27), and HBr (m/e 80, 82). These minor peaks are, however, too small to be measurable under these conditions.

Figure 6a shows the dependence of the relative yields of various products on NO concentration. The experiments were carried out by adding different amounts of NO to a 1:1 $CHBr_3$:Ar mixture to a total pressure of about 7 Torr. The flash energy was 1.6 kJ for all runs. In these runs, the peak height of ^{40}Ar was used as an internal standard. Ar was used to avoid the complicated cracking pattern of SF_6. Under these conditions, the partial pressure of $CHBr_3$ was significantly higher than that in a lasing mixture. The peak heights of those minor products mentioned above can now be reliably measured.

The yield of C_2H_2 (m/e 25), which is probably produced by the recombination of CH radicals,[3] diminishes rapidly as the concentration of NO increases. The yield of HCN (m/e 27) rises steadily as [NO] increases, and it starts to level off when more than 40% of NO is present. Since HCN is most likely produced from CH + NO, and C_2H_2 from CH + CH, the ratio $[HCN]/[C_2H_2]^{1/2}$ should vary linearly with NO concentration. The results presented in Figure 6b indeed establish this relationship within the

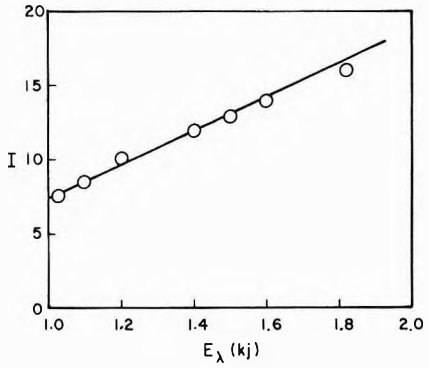

Figure 5. Intensity of CO laser emission as a function of flash energy: laser mixture, 20 Torr of 2:1:20 NO:$CHBr_3$:SF_6.

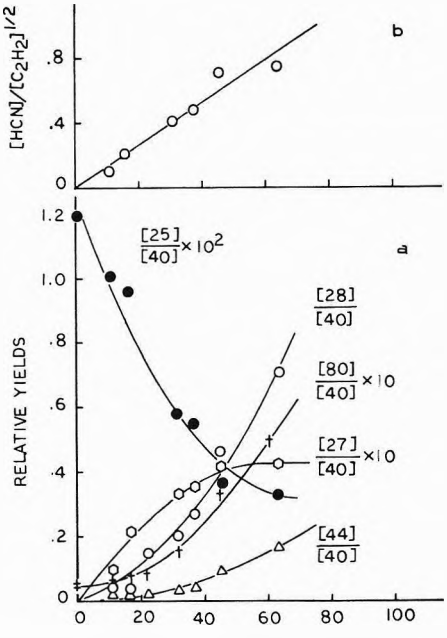

Figure 6. Relative yields *vs.* NO concentration plots.

scatter of our results. This finding further supports our previous conclusion that the CH radical is present in the photodissociation of $CHBr_3$ above 165 nm.[3]

The dependence of HBr (m/e 80) yield on NO concentration is interesting and worth discussing. In our O_2–$CHBr_3$ work,[3] we have concluded that HBr detected in the photolysis of $CHBr_3$ above 165 nm was produced predominantly from the direct photoelimination reaction, $CHBr_3 + h\nu \rightarrow HBr + CBr_2$, with probably some minor contributions from radical recombination-elimination reactions such as $CHBr_2 + CHBr_2 \rightarrow C_2H_2Br_4\dagger \rightarrow HBr + C_2HBr_3$, etc. The present observation again supports this contention. If HBr were generated exclusively from the unimolecular decomposition of vibrationally excited $CHBr_2$ radical, as was proposed by Simons and Yarwood,[6] NO would either inhibit or not change the yield of HBr. Since the direct photoelimination reaction $CHBr_3 + h\nu \rightarrow HBr + CBr_2$ can not be affected by the presence of NO, the observed acceleration effect indicates that NO is capable of partially intercepting the free radical intermediates, $CHBr_2$ and CHBr, yielding HBr, probably *via* the following paths

$$CHBr_2 + NO \rightleftharpoons CHBr_2NO \longrightarrow CBr_2{=}N{-}OH\dagger \longrightarrow HBr + BrCNO$$

$$CHBr + NO \rightleftarrows CHBrNO \longrightarrow BrC{=}N{-}OH^{\dagger} \longrightarrow HBr + CNO$$

The analogous reactions $CH_2F + NO$ and $CHF + NO$ have been shown to generate HF laser emissions.[7]

The major products in these runs are again CO ($+N_2$) and N_2O. Both peaks increase continually with NO pressure.

B. Pumping Mechanism. On the basis of our gas analysis results discussed in the preceding section and our previous CO laser emission studies in the SO_2–$CHBr_3$[2] and O_2–$CHBr_3$[3] systems, the formation of vibrationally excited CO in the present system can be best accounted for by the CH + NO reaction. This reaction may take place *via* several possible routes: (a) direct four-centered reaction

$$CH + NO \longrightarrow CO^{\dagger} + NH \quad \Delta H^{\circ}_{4a} = -105 \text{ kcal/mol} \quad (4a)$$

(b) short-chain reactions; there are two possibilities

(i) $CH + NO \longrightarrow HCN + O \quad \Delta H = -72$ kcal/mol (4b)

followed by reaction 1

$$O + CH \longrightarrow CO^{\dagger} + H \quad \Delta H^{\circ}_{1} = -176 \text{ kcal/mol} \quad (1)$$

(ii) $CH + NO \longrightarrow HCO + N \quad \Delta H^{\circ}_{4c} = -44$ kcal/mol (4c)

and

$$N + NO \longrightarrow N_2 + O \quad \Delta H^{\circ}_{5} = -75 \text{ kcal/mol} \quad (5)$$

followed by reaction 1. These three different mechanisms are all consistent with the observed linear relationship between the laser intensity (I) and flash energy (E_λ), as shown in Figure 5. In the present system, only $CHBr_3$ absorbs strongly above 165 nm. The photodissociation of NO above 165 nm is unimportant under the present flash conditions, although electronically excited NO up to the $D(^2\Sigma^+)$ state can be produced in the present flash.[8] The role of the excited NO molecule in the present system can not be evaluated, but it is probably insignificant in view of the fact that $I \propto E_\lambda$ and also that the CH + NO reaction is so fast (see Figure 1) that the presence of a small fraction of NO* would not affect the kinetics of the present system. If the CH + NO* reaction were the principal pumping step, one would expect the $I \propto E_\lambda^2$ dependence. The photodissociation of NO can be ruled out under the present conditions, since no detectable amount of N_2 was produced when a 5% NO–SF_6 mixture was flashed at 1.8 kJ. One would also expect the $I \propto E_\lambda^2$ dependence, if NO + $h\nu \rightarrow$ N + O were one of the laser iniation processes.

The yield of HCN in comparison with that of CO ($+N_2$) or N_2O suggests that reaction 4b is only a minor path; so is probably the analogous reaction 4c. Further indirect evidence supporting this contention is the absence of laser emission from the flash photolysis of a $CFBr_3$–NO–SF_6 mixture under the same experimental conditions. Since CO laser emission resulting from the $O(^3P)$ + CF reaction has been detected in the SO_2–$CFBr_3$ system under similar conditions,[4] the absence of laser action in the CF–NO system implies that the analogous reactions of (4b), CF + NO → FCN + O, and (4e), CF + NO → FCO + N, are probably unimportant. On the basis of this observation and our gas analysis results mentioned above, we arrive at the conclusion that the four-centered reaction 4a is the primary pumping step in the $CHBr_3$–NO laser system.

The production of the NH radical in reaction 4a can also account for the appearance of mass 44, which is most likely due to N_2O generated by the reaction

$$NH + NO \longrightarrow N_2O + H \quad \Delta H^{\circ}_{6} = -41 \text{ kcal/mol} \quad (6)$$

N_2O might also be produced from the combination of HNO, which may be formed by the slow termolecular recombination of NO and H. The H atom can be generated either from reaction 6 or the reaction of NH radicals, NH + NH → N_2 + 2H.

The four-centered reaction between CH and NO can take place *via* two different paths due to two possible combinations: H–C–O–N and H–C–N–O, yielding CO + NH ($\Delta H^{\circ}_{4a} = -105$ kcal/mol) and CN + OH ($\Delta H^{\circ}_{4d} = -45$ kcal/mol), respectively. The relative importance of the two processes is not known and can not be determined in the present study. No CN stimulated emission was detected in the present system. The absence of C_2N_2 (m/e 52), according to our gas analysis, should not be interpreted as due to absence of reaction 4d, CH + NO → CN + OH, because the CN radical may disappear rapidly *via* the path, CN + NO → N≡C–N=O → products.

References and Notes

(1) M. C. Lin, *Int. J. Chem. Kinet.*, **5**, 173 (1973). The use of $CHBr_3$ and CH_2Br_2 as the sources of CH and CH_2 radicals, respectively, was first reported by the author in the Third Conference on Chemistry and Molecular Lasers, May 1972, St. Louis, Mo.

(2) M. C. Lin, "Chemical Lasers Produced from $O(^3P)$ Atom Reactions. III. 5-μm CO Laser Emission from the O + CH Reaction," International Conference on Chemiluminescence, Oct 1972, Athens, Ga., to be published.

(3) M. C. Lin, "Chemical CO and CO_2 Lasers from the CH + O_2 Reaction," International Conference on Chemiluminescence, to be published.

(4) M. C. Lin, to be submitted for publication; 5-μm CO laser emission was detected when $CFBr_3$ was flashed with O_3 and SO_2, in the presence of a diluent. The pumping reactions were concluded to be $O(^1D)$ + CF and $O(^3P)$ + CF, respectively.

(5) G. Hancock and I. W. M. Smith, *Appl. Opt.*, **10**, 1827 (1971).

(6) J. P. Simons and A. J. Yarwood, *Trans. Faraday Soc.*, **57**, 2167 (1961); **59**, 90 (1962).

(7) M. C. Lin, unpublished work.

(8) M. C. Lin, "1-μm NO Laser Emissions Resulted from the $C(^2\pi) \rightarrow A(^2\Sigma^+)$ and $D(^2\Sigma^+) \rightarrow A(^2\Sigma^+)$ Transitions," International Conference on Chemiluminescence, Oct 1972, Athens, Ga., to be published.

Application of the Mechanical Stability Condition to the Prediction of the Limit of Superheat for Normal Alkanes, Ether, and Water[1]

J. G. Eberhart* and H. C. Schnyders

Chemical Engineering Division, Argonne National Laboratory, Argonne, Illinois 60439 *(Received March 29, 1973)*

Publication costs assisted by Argonne National Laboratory

If a liquid is in contact only with immiscible solid or liquid phases which it wets completely, then the liquid can be heated isobarically until it reaches its limit of superheat where it vaporizes explosively. The liquid phase can likewise be "stretched" isothermally to this same limit, which is sometimes called the tensile strength of the liquid. A kinetic limit of superheat can be predicted from homogeneous nucleation theory. A thermodynamic limit of superheat can also be predicted from the liquid-phase spinodal which is that curve in PVT space which separates metastable states from unstable states at densities larger than the critical density. Along this spinodal the equation of state satisfies the conditions $(\partial P/\partial V)_T = 0$ and $(\partial^2 P/\partial V^2)_T > 0$. Liquid spinodals for the normal alkanes from methane through nonane and for ether were derived from a variety of equations of state, including those of van der Waals, Berthelot, a modified Berthelot equation, and a generalized van der Waals equation based on scaled particle theory for rigid, convex molecules. Good agreement is obtained between experimental limits of superheat for these liquids and the liquid-phase spinodals calculated from the generalized van der Waals equation of state for rigid, cylindrical molecules with a size based on the molecular structure which they represent. Our estimate of the limit of superheat of water, based on significant structure theory, is 305° at atmospheric pressure. This exceeds superheatings observed thus far by 25°. Spinodals describing the limits of supersaturation of vapors and supercooling of liquids are briefly discussed.

Introduction

The saturation or vapor pressure curve for a fluid represents the states where liquid and vapor are in two-phase equilibrium and the chemical potentials of the two phases, μ^l and μ^v, are equal. This curve separates the equilibrium, one-phase, liquid field, where $\mu^l < \mu^v$, from the equilibrium, one-phase, vapor field, where $\mu^v < \mu^l$. A variety of experiments show that it is not only possible to superheat a liquid to pressures and temperatures in the vapor field, but that there is a well-defined limit to the extent of this metastable liquid state which is called the limit of superheat. This limit is approached experimentally either by heating a liquid at constant pressure P to its upper temperature limit T_l, or by "stretching" a liquid at constant temperature T to its lower pressure limit, P_l. The same limiting pressure–temperature relationship is defined by either experiment.

Heating a liquid isobarically to its limit of superheat can be accomplished with an apparatus of a type first used by Moore[2a] and Wakashima and Takata[2b] and later modified by other investigators.[3-12] This apparatus is essentially a vertical glass tube which is filled with a liquid heating medium which is immiscible with the liquid to be superheated. The tube is surrounded by a heater which produces an upward-increasing temperature gradient in the medium. A droplet of the liquid to be superheated is introduced in the bottom of the tube and, since the heating medium is more dense, the droplet rises in the tube, and its temperature increases as it moves upward. If the superheated droplet completely wets the liquid heating medium and also any solid impurities or motes which may be present in the droplet, then the droplet can be raised in temperature to its limit of superheat, T_l, and vaporizes explosively with a sharp "ping."

With a stabilized temperature gradient within the heating medium, a series of small droplets of the same substance sent up the tube will explode at essentially the same level in the tube, and the limit of superheat can be determined by moving the junction of a thermocouple to that level. The precision obtained in these measurements is of the order of 0.5–1.0°. Complete wetting of the liquid medium by the droplet permits the homogeneous nucleation of vapor bubbles within the body of the droplet, rather than heterogeneous nucleation at the superheated droplet–heating medium interface.[2a,13,14] The majority of the experiments performed to date have been with hydrocarbons in a medium of either sulfuric acid, glycerin, or ethylene glycol. Results which are independent of medium provide a strong indication that nucleation is homogeneous and that maximum superheating has been achieved.

A variety of techniques have also been developed for the isothermal stretching of liquids into these metastable states. These methods have been recently reviewed by Hayward.[15] Typically the experiments are done in glass tubes near room temperature. At these temperatures metastable liquids can sustain large tensile stress or negative pressure. Lower pressure limits measured isothermally in the negative pressure regime are usually referred to as the tensile strength of the liquid. Experiments performed with the superheated liquid in direct contact with glass give more erratic results than those described above, presumably because of the difficulty of obtaining complete wetting. Recently Apfel[9,10,16] devised an acoustical technique for producing negative pressures in systems comprised of liquid droplets in a liquid heating medium, and has thus extended the range of these more reliable measurements of the limit of superheat.

The scientific literature on superheating suggests two approaches to the prediction of the limit of superheat of a

liquid. One approach is that of homogeneous nucleation theory.[17-20] Here the probability of bubble nucleation is considered and an expression is derived for the nucleation rate as a function of temperature T and pressure P. From a knowledge of the vapor pressure, the density, and the surface tension, the temperature at which the nucleation rate becomes significant, T_l, can be calculated. Because the nucleation rate increases very rapidly with temperature near the experimental limit of superheat (several orders of magnitude per degree at 1 atm), T_l is relatively insensitive to the effects of variance in the volume of the droplet and its heating rate. Homogeneous nucleation theory has been used with notable success by a number of authors[2-11] to predict the limit of superheat of various hydrocarbons.

The second approach that has been suggested for the prediction of the limit of superheat is based on the mechanical stability condition of classical thermodynamics.[21-24] According to this analysis the stable ($\mu^l < \mu^v$) and the metastable ($\mu^l > \mu^v$) liquid states are those which satisfy the mechanical stability condition $(\partial P/\partial V)_T < 0$. The superheated liquid states are found on that portion of the P–V isotherm between the saturated liquid and the minimum in the van der Waals "loop." In this region, small density fluctuations of long wavelength will be compensated by an appropriate pressure fluctuation that will tend to restore the system to its initial state. On the other hand, a large local (superposition of short-wavelength components) density fluctuation such as a bubble of critical size will tend to grow at a finite rate to produce more of the stable phase.[25] Similarly the unstable states of the fluid, *i.e.*, those for which $(\partial P/\partial V)_T > 0$, are located between the minimum and the maximum of the van der Waals loop of the isotherm. For these states density fluctuations continue to grow rather than damp out. The states between the isotherm maximum and the saturated vapor represent metastable, supersaturated vapor states where $(\partial P/\partial V)_T < 0$. These states are similar to the metastable liquid in their response to fluctuations in density. The locus of all the maxima and all the minima in the fluid isotherms is the spinodal, which separates the metastable and unstable fluid states. The condition $(\partial P/\partial V)_T = 0$ is satisfied along the entire length of the spinodal which has two branches. The locus of the minima of all the isotherms, along which $(\partial^2 P/\partial V^2)_T > 0$, provides the upper bound to the limit of superheat for the liquid as a function of ambient pressure, while the locus of the maxima, with $(\partial^2 P/\partial V^2)_T < 0$, provides the upper bound to the limit of supersaturation of the vapor as a function of temperature.

As a consequence, the predictions of the limit of superheat from mechanical stability considerations are expected to lie above the predictions of nucleation theory. In fact, if both theories were without flaw we would expect nucleation theory limits to approach stability theory limits as the droplet volume decreased and the heating rate increased.

In the past, stability considerations have been applied to superheating limits only for such rudimentary equations of state as those of van der Waals[21-23] and Berthelot,[24] with qualitative rather than quantitative agreement being obtained with experiment. We have therefore applied this approach with other equations of state including a modified Berthelot equation, an augmented van der Waals equation based on scaled particle theory, and a generalized van der Waals equation of state based on an extension of scaled particle theory to nonspherical, rigid, convex molecules. We are encouraged by the close accord which exists between our predictions and experiment and believe that stability theory is a valuable approach which is complementary to that provided by homogeneous nucleation theory. In situations where a knowledge of the dependence of T_l on droplet volume and heating rate is required, the approach of homogeneous nucleation theory is indispensable. On the other hand, since T_l is, in fact, fairly insensitive to changes in either the droplet volume or the heating rate, a reliable estimate of T_l can be made by the application of stability considerations to good equations of state. Furthermore, if the surface tension data required for a nucleation theory estimate are not available, mechanical stability considerations may be the only way to estimate the limit of superheat.

Limit of Superheat from Empirical Equations of State

The most complete data presently available for comparison with spinodals are that of Skripov and his coworkers[3-8] who have measured the pressure dependence of the limit of superheat for the liquids *n*-pentane, *n*-hexane, *n*-heptane, diethyl ether, and benzene. In addition Apfel has determined the temperature dependence of the tensile strength of ether[9] and *n*-hexane.[10] An interesting feature of these measurements, which was pointed out by Skripov and Ermakov[5] for their positive pressure data, is that if the experimental limits of superheat, T_l *vs.* P, are plotted on reduced scales, then the data for these five liquids are nearly superimposed. This is shown in Figure 1 where the reduced limit of superheat, $\theta_l = T_l/T_c$, is plotted against the reduced ambient pressure, $\pi = P/P_c$, where T_c and P_c are the critical temperature and pressure. Although small, systematic differences can be seen in the normal alkanes in the direction of increasing θ_l with increasing molecular length, the near coincidence of the data provides a simple way of estimating the reduced limit of superheat of other liquids. This result also suggests that a two-parameter equation of state can provide a spinodal curve which represents the data reasonably well.

The two most familiar two-parameter equations of state are those of van der Waals (vdW) and Berthelot (Ber) which can be represented in the combined form

$$\left(P + \frac{a}{T^n \tilde{V}^2}\right)(\tilde{V} - b) = RT \qquad (1)$$

where $\tilde{V}$ is the molar volume, R is the gas constant, and a and b are constants. The vdW equation is then obtained for $n = 0$ and the Ber equation for $n = 1$. The two equations are combined in this fashion in anticipation of a value of n intermediate between 0 and 1. If the usual conditions of $(\partial P/\partial V)_T = 0$ and $(\partial^2 P/\partial V^2)_T = 0$ are applied at the critical point then eq 1 can be put in the reduced form

$$\left(\pi + \frac{3}{\theta^n \phi^2}\right)\left(\phi - \frac{1}{3}\right) = \frac{8}{3}\theta \qquad (2)$$

where $\pi = P/P_c$, $\theta = T/T_c$, and $\phi = \tilde{V}/\tilde{V}_c$ are the reduced pressure, temperature, and volume, respectively. Everywhere along the spinodal $(\partial\pi/\partial\phi)_\theta = 0$, and applying this condition to eq 2, we find the relation

$$\theta_l^{n+1} = (3\phi - 1)^2/4\phi^3 \qquad (3)$$

The spinodal can then be calculated parametrically by assuming a series of values for ϕ, calculating θ_l from eq 3, and then calculating the associated value of π from eq 2.

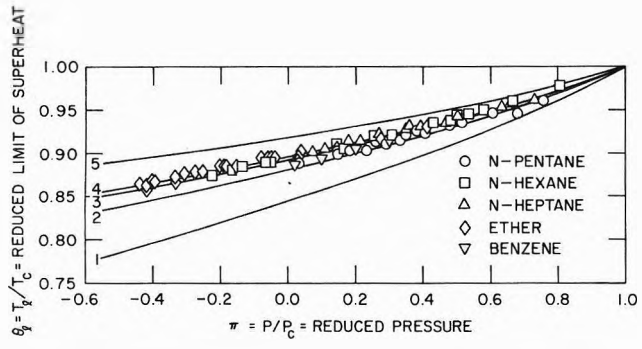

Figure 1. Reduced limit of superheat *vs.* the reduced pressure for *n*-pentane, *n*-hexane, *n*-heptane, diethyl ether, and benzene compared with reduced spinodols derived from the following equations of state: (1) van der Waals, (2) augmented van der Waals for spherical molecules (γ = 3), (3) modified Berthelot (n = ½), (4) generalized van der Waals for regular tetrahedral molecules (γ = 6.704), and (5) Berthelot (n = 1).

Spinodals generated in this fashion for the vdW and the Ber equations of state are shown in Figure 1 as curves 1 and 5. By comparing these curves with the experimental data, it is clear that the vdW spinodal is too low, whereas the Ber spinodal is too high. It was found that a value of n = ½ gives a good empirical representation of the data, within the approximation that the limits of superheat of all these liquids coincide when reduced variables are used. The spinodal for this modified Berthelot equation of state (mBer) is shown in Figure 1 as curve 3.

The reduced limit of superheat at zero pressure, $\theta_l^0 = T_l^0/T_c$, represents the upper bound to reduced temperatures at which it is possible to achieve negative pressures for a liquid. Equations 2 and 3 yield the particularly simple result of

$$\theta_l^0 = (27/32)^{1/(n+1)} \tag{4}$$

The zero pressure value of θ_l is a convenient comparison point for the spinodals of various equations of state. For the vdW (n = 0), mBer (n = ½), and Ber (n = 1) equations, θ_l^0 is 0.844, 0.893, and 0.919, respectively.

Limit of Superheat of Normal Alkanes and Ether from a Generalized van der Waals Equation of State

From a theoretical point of view, it is interesting that the reduced experimental data plotted in Figure 1 fall between the spinodal curves derived from the classical van der Waals equation of state and the Berthelot equation of state. Clearly, the only distinction between these two equations of state is the assumed value of the exponent n in eq 1. Let us rearrange this equation into a convenient form for discussion

$$Z = \frac{P\tilde{V}}{RT} = \frac{\tilde{V}}{\tilde{V} - b} - \frac{a}{RT^{n+1}\tilde{V}} \tag{5}$$

where Z is the compressibility factor. The first term on the right-hand side of eq 5 represents the effects of volume exclusion due to the infinite repulsive force which acts between hard spheres at contact, and the second term on the right-hand side represents the effect of the constant average attractive potential in which the hard spheres move. Van der Waals assumed this average attractive potential was inversely proportional to the molar volume $\tilde{V}$ with a constant of proportionality, a, which is independent of temperature. Berthelot chose to correct the defects in the van der Waals model by merely assigning an arbitrary temperature dependence to a, namely, $a_B = a/T$. This choice is not justified theoretically and is more or less a camouflage for a primary defect in the van der Waals model at high densities, namely, the inaccurate description of volume exclusion effects given by the first term on the right-hand side of eq 5.

The term $\tilde{V}/(\tilde{V} - b)$ in eq 5 is an oversimplification of excluded volume effects at high densities where the overlap of exclusion spheres of volume b (equal to four times the rigid sphere volume per sphere for a pair of rigid spheres) becomes significant. In the spirit of the augmented van der Waals (AvdW) theory of Longuet-Higgins and Widom[26] and Alder and Hecht,[27] we replace this term in eq 5 by the far more accurate compressibility factor, Z_0, for the rigid-sphere fluid given by scaled-particle theory[28]

$$Z_0 = \left(\frac{P\tilde{V}}{RT}\right)_0 = \frac{1 + y + y^2}{(1 - y)^3} \tag{6}$$

where $y = N_0 v_h/V$, N_0 is Avogadro's number and v_h is the rigid-sphere volume. For our present purposes, we shall continue to assume with van der Waals that a is constant and set n equal to zero. The reduced spinodal corresponding to the AvdW equation of state is represented by curve 2 in Figure 1. Agreement with the experimental data in reduced form is decidedly improved over the results of classical van der Waals theory (curve 1).

Recently, scaled-particle theory has been extended to fluids of arbitons, *i.e.*, hard particles of arbitrary convex shape.[29,30] Since it seems likely that all of the molecules for which experimental data are given in Figure 1 are better represented by something other than a sphere, we decided to test the effect of molecular shape on the spinodal. We now replace eq 6 by the more general equation of state for arbitons[29]

$$Z_0 = \left(\frac{P\tilde{V}}{RT}\right)_0 = \frac{1}{1 - y} + \frac{\gamma y}{(1 - y)^2} + \frac{\gamma^2 y^2}{3(1 - y)^3} \tag{7}$$

where the molecular shape factor γ is given by

$$\gamma = \bar{R}S/v_h \tag{8}$$

and $\bar{R}$ is a mean radius of curvature for the arbiton,[31,32] S is its surface area, and v_h is its volume. The resulting family of equations of state

$$Z = \frac{P\tilde{V}}{RT} = \frac{1}{1 - y} + \frac{\gamma y}{(1 - y)^2} + \frac{\gamma^2 y^2}{3(1 - y)^3} - \frac{ay}{N_0 v_h RT} \tag{9}$$

we choose to call the generalized van der Waals (GvdW) equations of state. Rigby has explored these equations of state with virial coefficient,[33] compressibility, and vapor pressure[34] calculations, using a prolate spherocylinder shape. Eq 9 has a corresponding family of reduced spinodal curves, two of which are displayed in Figure 1 as curves 2 and 4. The parameter γ has a minimum value of 3 for the shape of maximum symmetry, the rigid sphere. The spinodal (curve 2) corresponding to the AvdW equation of state is identical with that derived from eq 9 with γ = 3. Curve 4 corresponds to the GvdW equation of state for rigid regular tetrahedra (γ = 6.704).

At least qualitatively, the remaining discrepancy between the experimental data and the AvdW spinodal (curve 2) of Figure 1 is explained by the "departure" of the basically cylindrical molecular shapes of these compounds from spherical symmetry as is manifested by in-

creasing values of γ. In fact, if the data are examined closely, a fairly systematic ordering of increasing reduced limits of superheat with increasing length of the molecule can be seen at any fixed reduced pressure. Such a trend can be explained by GvdW theory for rigid cylinders of radius R and length L. As the ratio of L to R, τ, increases (corresponding to increasing length of saturated hydrocarbons), γ increases and the spinodal shifts to higher reduced temperatures. This is the apparent trend in the experimental data as one goes from n-pentane to n-heptane. This trend suggests that estimates of γ be made for each molecule from molecular structure data in order to compare the corresponding GvdW spinodal with the reduced experimental limit of superheat for that molecule. To illustrate the variation in the spinodal which is possible through variation in γ, Figure 2 shows the reduced limit of superheat at zero pressure, θ_l^0, plotted as a function of $3/\gamma$, which varies from one to zero as γ varies from its minimum value of 3 to infinity. As γ approaches ∞, θ_l^0 approaches a limit of 0.928.

For the purpose of exploring the rigid cylinder approximation, we will consider only the normal alkanes. It is assumed that the rigid cylinder, whose length-to-radius ratio, τ, increases systematically as the length of a normal hydrocarbon increases, is a fair approximation to the structure of these molecules. The angle between adjacent carbon–carbon bonds in these molecules is close to 109.5°. Assuming the usual chain structure for the molecule, which we approximate by a zig-zag configuration of carbon atoms in a plane, one finds for a cylinder whose surfaces contain the nuclear centers of all the carbon atoms

$$\tau = 2(n - 1) \tan \phi \qquad (10)$$

$$\gamma = (1 + \tau)(\pi + \tau)/2\tau \qquad (11)$$

where n is the number of carbon atoms in the normal alkane molecule and ϕ is one-half the angle between adjacent carbon–carbon bonds in the molecule. This geometrical assumption is called the nuclear cylindrical envelope for the molecule. Connolly and Kandalic[35] have used this cylindrical envelope to estimate the distance of closest approach between the rigid cores in the Kihara potentials for the n-alkanes. The second virial coefficients were calculated with these Kihara potentials and found to be in good agreement with experimental data.

Another choice of a rigid body which approximates the impenetrable volume of the n-alkane molecule is a cylinder whose surface is tangent to the outer edges of the carbon atoms, which are assigned a radius of one-half of the carbon–carbon bond distance in the molecule. We refer to this cylinder as the molecular envelope and corresponding values of γ are found by substituting

$$\tau = [2(n - 1) \sin \phi + 2]/(\cos \phi + 1) \qquad (12)$$

into eq 11. For both of these choices the hydrogen atoms are ignored.

Calculation of the spinodals for the normal alkanes from propane through nonane was performed for both of these representations (nuclear and molecular cylindrical envelopes) of the hard-core volumes of the n-alkane molecules. An ethane spinodal was only calculated in the molecular-envelope representation and the methane spinodal was calculated assuming the molecule to be a rigid sphere ($\gamma = 3$ in eq 9). These predicted limits of superheat are shown in Figure 3, along with the experimental results of Skripov, *et al.*,[3-8] Apfel,[10] and Eberhart, Kremsner, and Hathaway.[36] In Figure 4, a further comparison is made of the reduced limit of superheat at 1 atm pressure for the two envelopes with the observed values of Eberhart, *et al.*,[36] as a function of the number of carbon atoms in the n-alkane molecule. Finally, Figure 5 shows the diethyl ether spinodals for both the nuclear and molecular cylindrical envelopes, along with the measurements of Skripov[7,8] and of Apfel[9] on this system. The γ values for ether were taken as being identical with those of n-pentane. In all three figures the agreement between theory and experi-

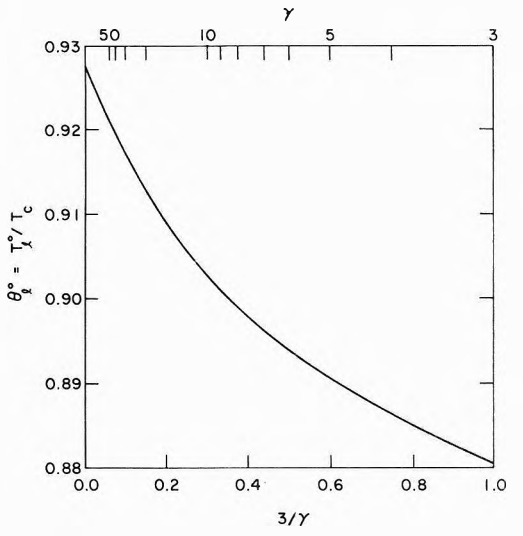

Figure 2. Reduced limit of superheat at zero pressure as a function of the molecular shape factor γ.

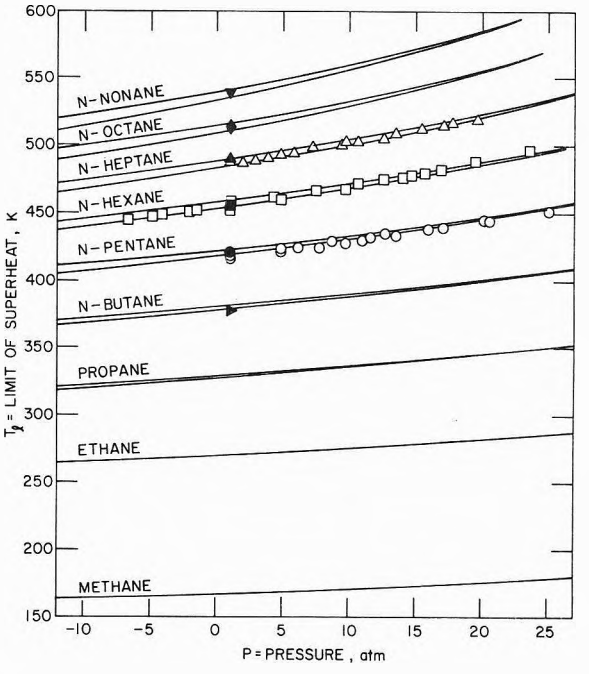

Figure 3. Pressure dependence of the limit of superheat for the normal alkanes. For propane through nonane, the upper curve is the calculated spinodal for the nuclear envelope representation, and the lower curve is the spinodal calculated for the molecular envelope representation. Only the molecular envelope representation is used to calculate the single spinodal for ethane and the methane molecule is treated as a hard sphere in the calculation of its spinodal: open points at positive pressures, Skripov, *et al.*;[3-8] open points at negative pressures, Apfel;[10] filled points at 1 atm, Eberhart, *et al.*[36]

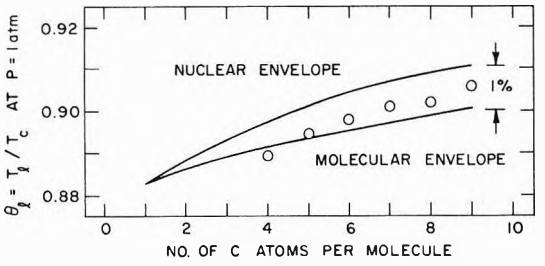

Figure 4. Reduced limit of superheat at 1 atm *vs.* the number of carbon atoms per molecule for both the nuclear and molecular envelopes. Data of Eberhart, *et al.*[36]

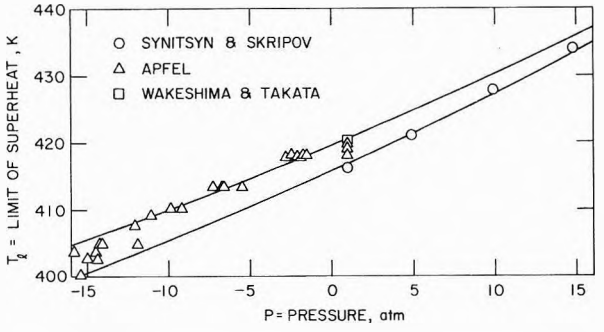

Figure 5. Pressure dependence of the limit of superheat of diethyl ether: positive pressure data, Skripov, *et al.*;[7,8] negative pressure data, Apfel.[9]

ment is excellent (generally within several degrees), with the spinodals for the nuclear envelope somewhat higher in temperature than the experimental data and the spinodals for the molecular envelope somewhat lower. Since the mechanical stability arguments used in this paper naturally lead to an *upper* bound to the limit of superheat obtained experimentally, we favor the nuclear envelope representation.

Limit of Superheat of Water from Significant Structure Theory

Hydrogen bonding in water makes it inappropriate to treat this substance as a generalized van der Waals fluid as we have done for the normal alkanes. Significant structure theory (SST)[37,38] has been successfully applied to water[39] over its normal liquid range. However, the predicted critical properties are considerably in error, probably owing to the failure to account for gas imperfection in the gas-phase part of the SST partition function. For this reason, we have chosen to reduce the SST equation of state for water[39] with the critical properties derived from it and calculate the reduced SST liquid spinodal for water. The results are shown in Figure 6. Using the experimental data on the critical properties of water and this reduced SST liquid spinodal, we estimate the limit of superheat for pure water at an ambient pressure of 1 atm to be 305°. This is somewhat higher than Apfel's[14] estimate of 298° and lower than Blander's[40] estimate of 310°, both of which are based on homogeneous nucleation theory. These theoretical estimates should be compared to the highest vaporization temperatures achieved experimentally for water, namely, 280° by Blander, *et al.*,[11] and 279.5° by Apfel.[41] However, it is possible that the true limit of superheat for pure water was not achieved in these experiments due to some miscibility of the heating medium (silicone oil,[11] benzyl benzoate[41]) with the water droplets or imperfect wetting at the interface between the droplet

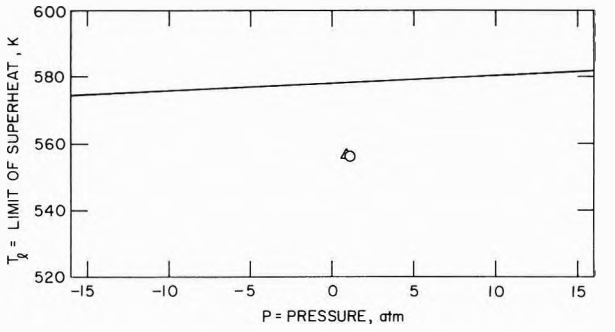

Figure 6. Pressure dependence of the limit of superheat of water. Data of Blander, *et al.*,[11] and Apfel.[41]

and the medium. Incomplete wetting lowers the attainable temperature by favoring nucleation at the interface rather than in the bulk liquid.[2a,13,14]

Another property of liquids that has long been of interest is their tensile strength.[15,16] Since significant structure theory predicts the properties of liquid water quite well in its normal liquid range, we have calculated the tensile strength of water at 300°K to be −6000 bars from the SST equation of state. The largest measured tensile strength of water is −270 bars.[42] This large disparity may in part be the result of a number of difficulties in the experimental measurement of the tensile strength of liquids.[43]

Critical Supersaturation Spinodal

If P_s is the maximum pressure sustained by the pure vapor phase in the absence of the liquid phase and P_e is the equilibrium saturated vapor pressure of the system, then $S = P_s/P_e$ is the critical supersaturation ratio. The upper bound to P_s is that point on the P–V isotherm at which $(\partial P/\partial V)_T$ is zero and $(\partial^2 P/\partial V^2)_T$ is negative. The locus of these values of P_s as a function of temperature is the vapor-phase spinodal (or critical supersaturation spinodal) for the system. Unfortunately, the upper bound values of P_s so determined for a variety of equations of state are larger than the experimental values[44,45] by as much as a factor of 10^2 at temperatures near the triple point of the substance considered. Benson and Gerjuoy[24] have shown that the van der Waals equation of state gives *apparently* reasonable agreement with experiment only because the predicted saturated vapor pressures for this equation of state are much too high. This is not so surprising since the "constants" in these equations of state were fixed at the critical temperature by reducing the equation of state with the critical properties, whereas the measurements of critical supersaturation are usually carried out at temperatures near the triple point of the substance. Of course, these "constants" are only truly constant over limited ranges of temperature and are likely to be considerably in error at the triple point when they have been "fixed" at the critical point.

Another probable cause for this large overestimation of P_s is the inadequate description of the metastable vapor states by the model equations of state we have chosen. It is clearly desirable to investigate the metastable regions of model fluids with more realistic interaction potentials. The equation of state of a fluid of particles, interacting *via* the widely used Lennard-Jones potential,[46] has been obtained by means of perturbation theories of fluids and has been found to reproduce the PVT properties of fluid argon[46,47] (including its vapor pressure) quite well. Sig-

nificantly, this equation of state for the Lennard-Jones fluid agrees well with the direct calculation of the *PVT* properties of this model fluid by molecular dynamics[48,49] and Monte Carlo[50] techniques. There is little uncertainty in our knowledge of the *PVT* states of this model fluid, even in its metastable regions.[51] A comparison of the upper bounds to the critical supersaturation pressure for the Lennard-Jones fluid with appropriately reduced experimental data is likely to distinguish whether the existing gross disparities between experiment and the predictions of empirical equations of state and the model equations of state considered in this paper are in fact due to their inaccurate description of the metastable regions of the *PVT* surface in the vicinity of the supersaturation spinodal or not. This comparison is necessary in order to isolate the major cause for the discrepancies from other possibilities which include the sufficiently rapid decay of metastable supersaturated states at pressures much lower than the upper bound to P_s and, possibly, unsuspected experimental difficulties in measuring the actual homogeneous nucleation of the liquid phase from the supersaturated vapor as opposed to some form of heterogeneous nucleation. These calculations for the Lennard-Jones fluid will be the subject of a future publication by one of us (H.C.S.).

Supercooling of Liquids and Superheating of Solids

We have seen how the limit of superheat of a liquid and the critical supersaturation ratio of a vapor can be calculated from the minimum and maximum, respectively, in the van der Waals loop of the *P–V* isotherm. It is well known that liquids can also be supercooled below their freezing point, *e.g.*, liquid water has been observed at temperatures as low as −50°.[52] Furthermore, despite statements to the contrary in some discussions of nucleation phenomena, it is also possible to significantly superheat a solid above its melting point.[53-56] Thus it is interesting to speculate whether a single equation of state which describes the entire *PVT* surface of a substance can have two van der Waals loops in its isotherms (one describing the first-order solid-to-liquid or solid-to-vapor transition and the other the first-order liquid-to-vapor transition). If equations of state can be found which contain this second loop, they would provide a means of estimating the limit of superheat of the solid (from the locus of the minima) and the limit of supercooling of the liquid (from the locus of the maxima). The minima would also provide the tensile strength of the solid if it were free from certain types of defects such as dislocations.

We have found that in some instances SST provides part of the second loop for a substance; the maximum is present but not the minimum. This local maximum in the SST isotherm is found at liquid molar volumes approximately 6–10% greater than that of the solid along its melting curve. This local maximum for argon[57] achieves a value of +1 atm at about 10° below the normal melting point. However, we have also found that the existence of these positive local maxima in isotherms at temperatures below the melting point depends on the specific set of parameters chosen to fit a certain substance. For example, two sets of SST parameters are given for carbon tetrachloride, both of which predict the properties of this liquid between its triple point and its normal boiling point with good accuracy. Nevertheless, for one of these sets of parameters,[58] the local positive maximum at densities near that of the solid does not exist at temperatures below the normal melting point of carbon tetrachloride. However, the other set[59] does lead to a positive maximum of 1 atm at about 7.5° below the normal melting point. Similar inconsistencies have been found for methane[59,60] and cyclohexane[58,60] It remains an open question as to whether or not this feature of the SST isotherm is an artifact. Second, Fulinski[61-64] has recently shown that the summation of certain infinite subsets of diagrams within the Ursell-Mayer virial expansion can lead to an approximate equation of state which has two first-order phase transitions,[65,66] and which displays two corresponding van der Waals-type loops. For quantitative accuracy a number of additional subsets of diagrams must be carefully selected, summed, and included in higher approximations to this equation of state. It remains to be seen whether or not in these higher approximations both loops persist and give accurate results in agreement with experiment.

Conclusions

We would conjecture that when a single equation of state is developed which describes accurately all features of the *PVT* diagram of a substance including its thermodynamically metastable regions, the application of the mechanical stability condition will accurately set boundaries to the metastable solid, liquid, and gaseous regions of *PVT* space. We have demonstrated that over a limited portion of *PVT* space generalized van der Waals equations of state give reliable estimates of the boundary of the metastable superheated liquid phase. In the future we would expect the quantitative prediction of the limit of supercooling of liquids and the limit of superheating of solids to be possible, using equations of state which predict not only the liquid–vapor transition, but also the solid–liquid and solid–vapor transitions as well.

Acknowledgment. The authors express their gratitude to M. Blander of Argonne National Laboratory for helpful discussions.

References and Notes

(1) This work was supported by the U. S. Atomic Energy Commission.
(2) (a) G. R. Moore, Ph.D. Thesis, University of Wisconsin, 1956; *AIChE J.*, **5**, 458 (1959); (b) H. Wakashima and K. Takata, *J. Phys. Soc. Jap.*, **13**, 1398 (1958).
(3) V. P. Skripov and V. I. Kukushkin, *Russ. J. Phys. Chem.*, **35**, 1393 (1961).
(4) V. P. Skripov and G. B. Ermakov, *Russ. J. Phys. Chem.*, **37**, 1047 (1963).
(5) V. P. Skripov and G. V. Ermakov, *Russ. J. Phys. Chem.*, **38**, 208 (1964).
(6) V. P. Skripov and E. N. Sinitsyn, *Sov. Phys. Usp.*, **7**, 887 (1964–1965).
(7) V. P. Skripov and E. N. Sinitsyn, *Russ. J. Phys. Chem.*, **42**, 167 (1968).
(8) E. N. Sinitsyn and V. P. Skripov, *Russ. J. Phys. Chem.*, **42**, 440 (1968).
(9) R. E. Apfel, *J. Acoust. Soc. Amer.*, **49**, 145 (1971).
(10) R. E. Apfel, *Nature (London), Phys. Sci.*, **233** (41), 119 (1971).
(11) M. Blander, D. Hengstenberg, and J. L. Katz, *J. Phys. Chem.*, **75**, 3613 (1971).
(12) J. G. Eberhart, W. Kremsner, and E. Hathaway, Argonne National Laboratory Report No. ANL-7878, 7 (1971).
(13) J. C. Fisher, *J. Appl. Phys.*, **19**, 1062 (1948).
(14) R. E. Apfel, *J. Chem. Phys.*, **54**, 62 (1971).
(15) A. T. J. Hayward, *Amer. Sci.*, **59**, 434 (1971).
(16) R. E. Apfel, *Sci. Amer.*, **227** (6), 58 Dec (1972).
(17) W. Döring, *Z. Phys. Chem.*, **B36**, 371 (1937); **B38**, 292 (1937–1938).
(18) M. Volmer, "Kinetic der Phasenbildung," Steinkopff, Dresden, 1939.
(19) Ya. B. Zeldovich, *Zh. Eksp. Teor. Fiz.*, **12**, 525 (1942).
(20) Yu. Kagen, *Russ. J. Phys. Chem.*, **34**, 42 (1960).
(21) J. Larmor, *Proc. Math. Soc. London*, **15**, 182 (1916).
(22) K. L. Wismer, *J. Phys. Chem.*, **26**, 301 (1922).
(23) H. N. V. Temperley, *Proc. Phys. Soc.*, **59**, 199 (1947).

(24) S. W. Benson and E. Gerjuoy, *J. Chem. Phys.*, **17**, 914 (1949).
(25) W. B. Strickfaden and L. deSobrino, *Can. J. Phys.*, **48**, 2507 (1970).
(26) H. C. Longuet-Higgins and B. Widom, *Mol. Phys.*, **8**, 549 (1964).
(27) B. J. Alder and C. E. Hecht, *J. Chem. Phys.*, **50**, 2032 (1969).
(28) H. Reiss, *Advan. Chem. Phys.*, **9**, 1 (1965).
(29) R. M. Gibbons, *Mol. Phys.*, **17**, 81 (1969).
(30) G. R. Dowling and H. T. Davis, *J. Stat. Phys.*, **4**, 1 (1972).
(31) A. Isihara and T. Hayashida, *J. Phys. Soc. Jap.*, **6**, 46 (1951).
(32) J. O. Hirschfelder, C. F. Curtiss, and R. B. Bird, "Molecular Theory of Gases and Liquids," Wiley, New York, N. Y., 1954, p 184.
(33) M. Rigby, *J. Chem. Phys.*, **53**, 1021 (1970).
(34) M. Rigby, *J. Phys. Chem.*, **76**, 2014 (1972).
(35) J. F. Connolly and G. A. Kandalic, *Phys. Fluids*, **3**, 463 (1960).
(36) J. G. Eberhart, W. Kremsner, and E. Hathaway, Argonne National Laboratory Report No. ANL-7923, 15 (1972).
(37) H. Eyring and M. S. Jhon, "Significant Liquid Structures," Wiley New York, N. Y., 1969.
(38) H. Eyring and R. P. Marchi, *J. Chem. Educ.*, **40**, 562 (1963).
(39) M. S. Jhon, J. Grosh, T. Ree, and H. Eyring, *J. Chem. Phys.*, **44**, 1465 (1966).
(40) M. Blander, private communication, 1973.
(41) R. E. Apfel, *Nature (London), Phys. Sci.*, **238**(82), 63 (1972).
(42) L. J. Briggs, *J. Appl. Phys.*, **21**, 721 (1950).
(43) L. J. Briggs, *J. Appl. Phys.*, **24**, 488 (1953).
(44) J. L. Katz, *J. Chem. Phys.*, **52**, 4733 (1970).
(45) G. M. Pound, *J. Phys. Chem. Ref. Data*, **1**, 119 (1972).
(46) R. M. Gibbons, *J. Phys. Chem.*, **76**, 1479 (1972).
(47) J. A. Barker and D. Henderson, *J. Chem. Phys.*, **47**, 4714 (1967).
(48) J. Hansen, *Phys. Rev. A*, **2**, 221 (1970).
(49) L. Verlet, *Phys. Rev.*, **159**, 98 (1967).
(50) I. R. McDonald and K. Singer, *J. Chem. Phys.*, **50**, 2308 (1969).
(51) J. P. Hansen and L. Verlet, *Phys. Rev.*, **184**, 151 (1969).
(52) G. A. Kozlov and A. A. Ravdel', *Kolloid-Z.*, **33**, 847 (1971).
(53) I. Karutz and I. N. Stranski, *Z. Anorg. Allg. Chem.*, **292**, 330 (1957).
(54) E. Roedder, *Science*, **155**, 1413 (1967).
(55) M. Blackman, S. J. Peppiatt, and J. R. Sambles, *Nature (London), Phys. Sci.*, **239**, 61 (1972).
(56) J. R. Asay and B. M. Butcher, *Bull. Amer. Phys. Soc., Ser. II*, **17**, 1105, Abstract ID5 (1972).
(57) E. J. Fuller, T. Ree, and H. Eyring, *Proc. Nat. Acad. Sci. U.S.*, **45**, 1594 (1959).
(58) K. Liang, H. Eyring, and R. P. Marchi, *Proc. Nat. Acad. Sci. U.S.*, **52**, 1107 (1964).
(59) D. R. McLaughlin and H. Eyring, *Proc. Nat. Acad. Sci. U.S.*, **55**, 1031 (1966).
(60) J. Grosh, M. S. Jhon, T. Ree, and H. Eyring, *Proc. Nat. Acad. Sci. U. S.*, **58**, 2196 (1967).
(61) A. Fulinski, *Acta Phys. Polon.*, **A37**, 177 (1970).
(62) A. Fulinski, *Acta Phys. Polon.*, **A37**, 185 (1970).
(63) A. Fulinski, *Acta Phys. Polon.*, **A39**, 181 (1971).
(64) A. Fulinski, *Acta Phys. Polon.*, **A40**, 221 (1971).
(65) A. Fulinski, *Phys. Lett.*, **31A**, 176 (1970).
(66) A. Fulinski and M. Jurkiewicz, *Phys. Lett.*, **32A**, 126 (1970).

Ion–Water Interactions in the Gas Phase[1]

P. P. S. Saluja and H. A. Scheraga*

Department of Chemistry, Cornell University, Ithaca, New York 14850 *(Received June 4, 1973)*

A quasi-experimental potential function for ion–water interactions in the gas phase is derived from mass-spectrometric and crystallographic data. Since *ab initio* computations on large ion–water complexes are not yet available, except for only a few systems, an attempt was made to use a semiempirical molecular orbital method to compute the energies of such complexes to obtain a theoretical basis for the potential function. Because the agreement between the values calculated by the molecular orbital method and the observed ones is poor, we rely on an empirical procedure to obtain a potential function for the interaction between an ion and the surrounding water molecules.

Introduction

For an understanding of the properties of dilute aqueous solutions of electrolytes it is essential to know the mutual effects of the ion and the surrounding water molecules on each other. Thus, it is logical to consider first the strong interactions of the ion with the nearest solvent molecules and then examine the influence of the ion on the structure and energies of the water molecules at greater distances. Therefore, in this paper, we compute the interaction energies between an ion M and those n water molecules next to it in the gas phase. The modification of such $M(H_2O)_n$ complexes by the surrounding water molecules in the liquid phase is a separate problem, which is presently under investigation in our laboratory.

Since *ab initio* computations[2-4] on large hydrated complexes have been carried out thus far[5,6] for only a few monohydrate complexes, a comparison of *ab initio* results with experiment[7-11] is not yet possible. Because of this, we used a semiempirical molecular orbital method[12,13] (CNDO/2) to compute the energy of $M(H_2O)_n$ complexes of varying n for several cations and anions. While a few calculations have been reported in the literature for several of the complexes treated here, the present paper extends these to other complexes not considered heretofore. Our calculations are summarized elsewhere.[14] The poor agreement between the calculated[14] and observed values[7-11] is discussed in light of the inadequacies of primarily the CNDO/2 method, and an empirical procedure is presented to obtain potential functions for the interaction between an ion and the surrounding water molecules.

Potential Function from Experimental Data

Ion–water interaction energies have recently[7-11] become available from mass-spectrometric experiments on the energetics of ion–water equilibria in the gas phase. A combination of these results[14] with equilibrium ion–water distances, taken from crystal ionic radii,[15] is used here to deduce a potential function (*e.g.*, $A_n/r^p - B_n/r^q$), the coefficients of which may be determined provided that the form (*i.e.*, p and q) is obtainable from theoretical considerations. In the following section, we use an approximate molecular orbital method to determine the values of p and q, and then deduce empirical values of A_n and B_n for various hydrated ions.

Molecular Orbital Theory

The method used here is the CNDO/2 procedure of Pople and coworkers.[12,13] The detailed hydration models and geometrical parameters for the ion–water complexes investigated here are given in the supplementary microfilm edition of this journal.[14]

For any complex $M(H_2O)_n$, the energy is calculated as a function of r (the same value of r being kept for each water molecule for a particular value of n), and the minimum-energy values $(r_0)_n$ and $(E_0)_n$ determined. The computed values of $(E_0)_n$ are augmented by the dispersion energy[16,17] (to take account of correlation effects); the dispersion energy is calculated for all pairs (*i.e.*, ion–H_2O and H_2O–H_2O) in each complex, using London's formula[18] and experimental values of polarizabilities[19] and ionization potentials.[20] In any event, the dispersion energy is very small compared to $(E_0)_n$, being approximately 0.4 kcal/mol per pair interaction. In the remainder of this paper, $(E_0)_n$ includes the dispersion energy. Then $\Delta E_{n-1,n}$ for the equilibrium

$$M(H_2O)_{n-1} + H_2O \rightleftharpoons M(H_2O)_n \qquad (1)$$

is computed as

$$\Delta E_{n-1,n} = (E_0)_n - (E_0)_{n-1} - E_{H_2O} \qquad (2)$$

for $n = 1, 2, 3, \ldots$. The values of E_{H_2O} and $(E_0)_0$ (*i.e.*, for $n = 0$) are those of Table I of the supplementary material.[14] While there is no vibrational excitation of an H_2O molecule at room temperature, we have no information about the intermolecular vibrational excitation in the complex; in the absence of this knowledge, we shall assume that there is none, and hence that the computed values of $\Delta E_{n-1,n}$ pertain to 0°K. Since the experimental values[7] of $\Delta H_{n-1,n}$ are independent of temperature in a range which includes room temperature, we assume that the observed values also pertain to 0°K. Thus, since the $\Delta(pV)$ term is small compared to $\Delta H_{n-1,n}$, we may compare the computed values of $\Delta E_{n-1,n}$ directly with the experimental values of $\Delta H_{n-1,n}$.

Results

The results for $\Delta E_{n-1,n}$ and r_0 obtained here are given in Tables III–V as supplementary material in the microfilm edition of this journal.[14] Table III contains results for complexes of Li^+ and Na^+ containing one to six water molecules; Table IV contains the same information for complexes of F^- (with one to four water molecules), Cl^- (with one to four water molecules), and CN^- (with one water molecule); Table V contains data for complexes of Be^{2+}, Mg^{2+}, and Al^{3+} (all with one to four water molecules). The computed values of $\Delta E_{n-1,n}$ become less negative with increasing n. This indicates that the binding of water molecules in the hydrated complex becomes weaker as n increases. Although the results for stabilization energies, $\Delta E_{n-1,n}$, are in qualitative agreement with experiment, the magnitudes are somewhat overestimated by the CNDO/2 method. For example, the computed values of $\Delta E_{n-1,n}$ for $Li^+(H_2O)_n$ with n varying from 1 to 6 are −45.7, −42.3, −40.7, −37.0, −27.8, and −27.6 kcal/mol, respectively; and the corresponding experimental values[9] are −34.0, −25.8, −20.7, −16.4, −13.9 and −12.1 kcal/mol. Thus, the computed values are on the average 17, 15, 15, and 9 kcal/mol more negative than the experimental values for the hydrated complexes $Li^+(H_2O)_n$, $Na^+(H_2O)_n$, $F^-(H_2O)_n$, and $Cl^-(H_2O)_n$, respectively. The most likely explanation for the overestimation of the ion–water interaction energy by the CNDO/2 method is given in the Discussion section.

TABLE I: Coefficients A_n and B_n in the Empirical Potential $A_n/r^{12} - B_n/r^6$ Obtained from Experimental Data[a]

System	n	$A_n \times 10^{-6}$, kcal Å^{12}	$B_n \times 10^{-3}$, kcal Å^6	$A_n/n \times 10^{-6}$, kcal Å^{12}	$B_n/n \times 10^{-3}$, kcal Å^6
$Li^+(H_2O)_n$	1	0.139	4.352	0.139	4.352
	2	0.245	7.654	0.122	3.827
	3	0.330	10.304	0.110	3.435
	4	0.397	12.403	0.099	3.101
	5	0.454	14.182	0.091	2.836
	6	0.503	15.731	0.084	2.622
$Na^+(H_2O)_n$	1	0.681	8.084	0.681	8.084
	2	1.243	14.754	0.621	7.377
	3	1.691	20.076	0.564	6.692
	4	2.082	24.725	0.521	6.181
	5	2.431	28.868	0.486	5.774
	6	2.735	32.472	0.456	5.412
$F^-(H_2O)_n$	1	4.553	20.599	4.553	20.599
	2	7.796	35.274	3.898	17.637
	3	10.473	47.386	3.491	15.795
	4	13.111	59.321	3.278	14.830
	5	15.690	70.990	3.138	14.198
$Cl^-(H_2O)_n$	1	15.679	28.699	15.679	28.669
	2	30.880	56.452	15.440	28.226
	3	44.884	82.052	14.961	27.351
	4	58.170	106.340	14.543	26.585
$CN^-(H_2O)_n$	1	61.161	58.104	61.161	58.104

[a] The values of r_0 are taken from crystal ionic radii.[15] and the experimental data on the equilibrium energy are taken from ref 7–11.

Discussion

The computed values of $\Delta E_{n-1,n}$ and r_0 agree with those from the CNDO/2 calculations of some workers,[21-23] but not with the results obtained for a few systems by *ab initio* treatments.[2-4,24-27]

The computed values of $\Delta E_{n-1,n}$ are more negative than the experimental ones in all cases. This overestimation of the stabilization energies, $\Delta E_{n-1,n}$, of the hydrated complexes by the CNDO/2 procedure arises from the approximations in the method, the values assigned to the parameters,[21] and also to some extent on the size of the basis set used. First, no attempt was made to optimize the program parameters at this stage. For example, in a study of heats of formation of hydrocarbons and their cations, Wiberg[28] achieved better agreement with experiment after reparameterization. This was not attempted here because the parameterization (particularly in orbital exponents) for ions is probably different from that for neutral species, and no criteria are available for assessing the validity of the orbital exponents for ions. Second, the basis sets used for the CNDO/2 method are small (valence basis set), *i.e.*, the 1s and 3d orbitals were omitted from the second row atomic basis sets (Li, Be, O, C, N). Lastly, the detailed *ab initio* results for monohydrated complexes of Li^+, Na^+, and K^+ obtained by Kistenmacher, *et al.*,[3] indicate that the neglect of three- and four-center integrals in the CNDO/2 approximation[13] gives rise to an overestimation of two-center terms. A breakdown[3] of the total energy of the hydrated complex into one-, two-, three-, and four-center contributions shows that three-center terms are mainly responsible for the repulsion in

$Li^+(H_2O)$ and $Na^+(H_2O)$ for ion–water distances in the range of 2–3 Å. Thus, the use of the CNDO/2 method appears to lead to spurious attraction at such short ion–water distances in the hydrated complexes studied here. In order to account for these higher terms explicitly, it would be necessary to modify the CNDO/2 method and use a larger basis set.[17] But, if one is going to use a larger basis set (requiring more computer time), one might as well use a more exact *ab initio* method. However, *ab initio* calculations on large complexes are prohibitively expensive,[5] and have thus far been carried out extensively[2,3] only for the species $Li^+(H_2O)$, $Na^+(H_2O)$, and $K^+(H_2O)$; thus, a comparison of *ab initio* results with experiment will not be possible until the computations on higher ion–water complexes become available.

As can be seen from Tables III-V of the supplementary material,[14] the computed values of r_0 are larger for cations and smaller for anions than the experimental values of r_0. This discrepancy is attributed to the same shortcoming of the CNDO/2 procedure, which led to discrepancies between the calculated and observed energies.

Since the trend in $\Delta E_{n-1,n}$ with n appears to be similar in both the theoretical and experimental results, we may resort to an empirical method to obtain the dependence of $\Delta E_{n-1,n}$ on r.

We assume that the functional form for the dependence of the CNDO/2 values of $\Delta E_{n-1,n}$ on r is correct, even though the absolute values are not, and represent this function as

$$\sum_n \Delta E_{n-1,n} = A_n/r^p - B_n/r^q \qquad (3)$$

Equation 3 represents the total interaction energy of the hydrated complex $M(H_2O)_n$ when n water molecules are brought into the first hydration shell of, and equidistant from, the central ion. Using the CNDO/2 results, A_n and B_n can be expressed in terms of p, q, $(r_0)_n$, and $\Sigma_n(\Delta E_0)_{n-1,n}$. Then optimization of p and q for all of the CNDO/2 data gives the best values as 12 and 6, respectively.

Having determined p and q from the CNDO/2 results, we can compute empirical values of $\Delta E_{n-1,n}$, *i.e.*, of A_n and B_n by requiring that the empirical curve agree with the experimental values of $\Delta E_{n-1,n}$ of Kebarle, *et al.*,[7-11] and of r_0 from crystal ionic radii.[15] The resulting values of A_n and B_n are shown in Table I. It can be seen that $(A_n/n - A_1/1)$ and $(B_n/n - B_1/1)$ become more negative as n increases, *i.e.*, the stabilization energies are nonadditive, probably because of the combined effects of $H_2O\cdots H_2O$ interactions in the first hydration layer and the increased shielding of the ionic charge[29] as H_2O molecules are added stepwise to the first hydration layer of the ion. These empirical functions will be of use in considering the effect of additional hydration layers when the $M(H_2O)_n$ complexes are placed in liquid water.

Acknowledgment. We are indebted to Dr. Frank A. Momany for helpful discussion.

Supplementary Material Available: A listing of the experimental data on interaction energies, the hydration models, geometrical parameters, and results of the computations will appear following these pages in the microfilm edition of this volume of the journal. Photocopies of the supplementary material from this paper only or microfiche (105 × 148 mm, 20× reduction, negatives) containing all of the supplementary material for the papers in this issue may be obtained from the Journals Department, American Chemical Society, 1155 16th St., N.W., Washington, D. C. 20036. Remit check or money order for $5.00 for photocopy or $2.00 for microfiche, referring to code number JPC-73-2736.

References and Notes

(1) This work was supported by research grants from the National Institute of General Medical Sciences of the National Institutes of Health, U. S. Public Health Service (GM-14312), and from the National Science Foundation (GB-28469X2).
(2) E. Clementi and H. Popkie, *J. Chem. Phys.*, **57**, 1077 (1972).
(3) H. Kistenmacher, H. Popkie, and E. Clementi, *J. Chem. Phys.*, **58**, 1689 (1973).
(4) W. P. Kraemer and G. H. F. Diercksen, *Theor. Chim. Acta*, **27**, 265 (1972).
(5) *Ab initio* computations on large complexes are prohibitively expensive. However, Clementi[6] has recently pointed out that these computations for higher ion–water complexes, such as $M(H_2O)_6$, can now be carried out more rapidly and thus less expensively with a revised version of his computer program. Such *ab initio* results have not yet been reported in the literature, and therefore we have resorted to an approximate molecular orbital method.
(6) E. Clementi, *Proc. Nat. Acad. Sci. U. S.*, **69**, 2942 (1972).
(7) P. Kebarle in "Ions and Ion Pairs in Organic Reactions," Vol. I, M. Szwarc, Ed., Wiley-Interscience, New York, N. Y., 1972, Chaper 2.
(8) I. Dzidic and P. Kebarle, *J. Phys. Chem.*, **74**, 1466 (1970).
(9) M. Arshadi, R. Yamdagni, and P. Kebarle, *J. Phys. Chem.*, **74**, 1475 (1970).
(10) J. D. Payzant, R. Yamdagni, and P. Kebarle, *Can. J. Chem.*, **49**, 3308 (1971).
(11) S. K. Searles and P. Kebarle, *Can. J. Chem.*, **47**, 2619 (1969).
(12) J. A. Pople and G. A. Segal, *J. Chem. Phys.*, **44**, 3289 (1966).
(13) J. A. Pople and D. L. Beveridge, "Approximate Molecular Orbital Theory," McGraw-Hill, New York, N. Y., 1970.
(14) See paragraph at end of paper regarding supplementary material.
(15) L. Pauling, "The Nature of the Chemical Bond," 3rd ed, Cornell University Press, Ithaca, N. Y., 1960, pp 260 and 518
(16) D. Hankins, J. W. Moskowitz, and F. H. Stillinger, *J. Chem. Phys.*, **53**, 4544 (1970).
(17) B. R. Lentz and H. A. Scheraga, *J. Chem. Phys.*, **58**, 5296 (1973).
(18) F. London, *Trans. Faraday Soc.*, **33**, 1 (1936).
(19) J. R. Tessman, A. H. Kahn, and W. Shockley, *Phys. Rev.*, **92**, 890 (1953).
(20) G. W. Castellan, "Physical Chemistry," Addison-Wesley, Reading, Mass., 1964.
(21) R. E. Burton and J. Daly, *Trans. Faraday Soc.*, **66**, 1281 (1970).
(22) P. Russegger, H. Lischka, and P. Schuster, *Theor. Chim. Acta*, **24**, 191 (1972).
(23) R. E. Burton and J. Daly, *Trans. Faraday Soc.*, **67**, 1219 (1971).
(24) P. Schuster and H. W. Preuss, *Chem. Phys. Lett.*, **11**, 35 (1971).
(25) G. H. F. Diercksen and W. P. Kraemer, *Theor. Chim. Acta*, **23**, 387 (1972).
(26) W. P. Kraemer and G. H. F. Diercksen, *Theor. Chim. Acta*, **23**, 393 (1972).
(27) G. H. F. Diercksen and W. P. Kraemer, *Chem. Phys. Lett.*, **5**, 570 (1970).
(28) K. B. Wiberg, *J. Amer. Chem. Soc.*, **90**, 59 (1968).
(29) L. B. Magnusson, *J. Chem. Phys.*, **39**, 1953 (1963).

Electron Spin Resonance Study on the Acrylic Acid Anion Radical and Its Protonation in Some Irradiated Frozen Solutions

Machio Iwasaki,* Mitsuharu Fukaya, Shigetada Fujii, and Hachizo Muto

Government Industrial Research Institute, Nagoya, Hirate, Kita, Nagoya, Japan *(Received September 28, 1972; Revised Manuscript Received June 22, 1973)*

Publication costs assisted by the Government Industrial Research Institute, Nagoya

An esr study has been carried out for reactions of electrons with acrylic acid (AA) in a variety of irradiated frozen solutions. The electron adducts of acrylic acid $[CH_2{=}CH{-}COOH]^-$ were found to be formed in some matrices, such as 2-methyltetrahydrofuran (MTHF), triethylamine (TEA), and 3-methylhexane (MHX). The hyperfine couplings to the end CH_2 protons ($a_0 \simeq 13$ G) are consistent with the INDO MO calculation made for the delocalized anion π radical. The post-irradiation thermal annealing of the frozen MTHF–AA solutions at 97°K resulted in protonation of the electron adducts to form the hydrogen addition radical $[CH_3{-}\dot{C}H{-}COOH]$. The same conversion was also observed in the TEA matrices at around 115°K, while no conversion was observed in the MHX matrices. The radical conversion seems to be associated with the molecular reorientations in the matrices which were found from the sudden change of the line width in the wide-line nmr measurements of frozen MTHF. On the other hand, the hydrogen addition radicals were found immediately after irradiation in some matrices containing polar protons such as alcohols and alkaline aqueous solutions. It is concluded that the electron adducts of acrylic acid can be stabilized either in a molecular anion or in its protonated form, depending upon the nature of the matrix molecules and that the hydrogen addition radicals are formed from the polar proton transfer to the electron adducts. A model of proton transfer from protonated cations *via* the hydrogen bond is proposed for protonation of the electron adducts in the MTHF and TEA matrices.

Introduction

It is well known from the esr studies that organic unsaturated compounds subjected to ionizing radiations give radicals formed from addition of hydrogen to the unsaturated bond.[1] We have reported that the hydrogen addition radicals are formed from protonation of the radical anions in irradiated single crystals of fumaric acid-doped succinic acid,[2] in which ejected electrons are captured selectively by fumaric acid forming its molecular anion. In some organic frozen solution containing unsaturated compounds,[3,4] the radical anions of the solute molecules are postulated as precursors of the hydrogen addition radicals, although the esr spectral evidence for the anionic species is not clear. Recent studies on irradiated aqueous solutions containing unsaturated compounds have also suggested that the protonation of radical anions forms hydrogen addition radicals.[5] In the case of vinyl monomers, the hydrogen addition radicals have been considered to initiate radiation-induced polymerization.[6] In this sense, the mechanism of the formation of the hydrogen addition radicals in vinyl monomers have been of considerable interest and the origin of the added hydrogen atoms has been a matter of concern for a long time. Protonation of radical anions is considered to play an important role in solid-state radiation chemistry. In the present study we have found clear esr evidence for the anion formation of acrylic acid and its protonation in some irradiated frozen solutions.

Experimental Section

The materials used were of the purest grade commercial reagents. The further purification of acrylic acid was made by a similar manner employed for methacrylic acid in our previous work.[7] All the solvents were carefully purified by the usual means employed in work with trapped electrons in frozen glasses.[8] Irradiations were made with ^{60}Co γ-rays at 77°K in the dark and the subsequent esr measurements were carried out at 77°K with a JEOL 3BS spectrometer operated at the X-band, the spectra being recorded as first derivatives with the 100-kHz modulation. The thermal annealing of the esr samples was made in a low-temperature bath controlled by the flow of nitrogen gas from a liquid nitrogen dewar. The wide-line nmr measurements were carried out with a JEOL spectrometer at 30 MHz in the temperature range from 77 to 110°K.

Results

In order to examine reactions of radiation produced electrons with acrylic acid forming molecular anions and their subsequent protonation, the experiments were performed using the two types of frozen solutions. The one consists of the solvents having no polar proton such as 2-methyltetrahydrofuran (MTHF), triethylamine (TEA), and 3-methylhexane (MHX). The other consists of the solvents having polar protons such as alcohols, alkaline ice, and propionic acid.

Acrylic Acid Anion in MTHF, TEA, and MHX. Figure 1a and 1b shows the spectra obtained from frozen pure MTHF and a frozen solution containing ~1.5 mol % of acrylic acid. It is seen that the signal of the trapped electron (the sharp single line at the center in Figure 1a) is replaced by the three-line spectrum which is attributable to the solute radical. The overlapping seven-line spectrum is from the familiar MTHF radical. Figure 1c shows the spectrum obtained by subtracting the seven-line spectrum of the MTHF radical from the spectrum in Figure 1b. Similar three-line spectra were also obtained in the TEA

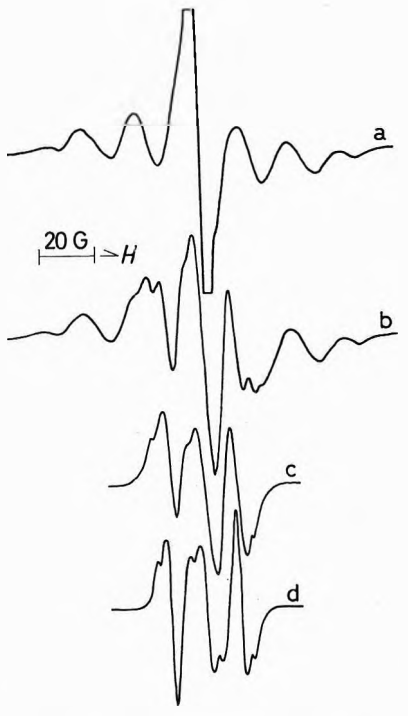

Figure 1. Esr spectra of frozen MTHF solutions containing (a) no additives, (b) 2 mol % acrylic acid: dose, 1.2 × 10^5 rads at 77°K; modulation amplitude, 2 G; microwave power, 0.10 mW; observation temperature, 77°K; gain, the same for a and b. (c) Difference spectrum obtained by subtracting the spectrum of the solvent radical from b. (d) Simulated spectrum for the $\dot{C}H_2$ π radical having ρ_C = 0.5. The hyperfine tensor elements used are −20.0, −12.5, and −6.5 G. The isotropic g factor is assumed.

and MHX matrices as shown in Figure 2. In all cases, the signal of the trapped electron is replaced by a similar three-line spectrum so that the most plausible species responsible for this spectrum is the solute anion radical I.

$$[CH_2{=}CHCOOH]^-$$
I

Competitive electron scavenging in the CH_3I-AA-MTHF system showed that the intensity of the three-line spectrum of I is diminished by addition of CH_3I (1 mol %) and that the three-line spectrum is completely replaced by the four-line spectrum of $\dot{C}H_3$ at a concentration ratio of CH_3I (10 mol %)/AA(1 mol %). These results indicate that the anion formation is depressed by dissociative electron attachment to CH_3I.

It is expected that the acrylic acid anion is a delocalized π radical having the resonance structures II, where the

$$CH_2{=}CH{-}\dot{C}\begin{matrix}O^-\\ \diagdown\\ \diagup\\ OH\end{matrix} \longleftrightarrow \dot{C}H_2{-}CH{=}C\begin{matrix}O^-\\ \diagdown\\ \diagup\\ OH\end{matrix}$$
II

unpaired electron mainly occupies the p orbital of the end CH_2 and COOH carbon atoms. The 1:2:1 three-line feature of the spectrum indicates that the spectrum is responsible for the species having two equivalent protons. The outer two lines of the three-line spectrum exhibit the familiar line shape arising from the hyperfine anisotropy of α proton couplings. Figure 1d shows the simulated spectrum for the $-\dot{C}H_2$ π radical assuming the typical anisotropy of α proton coupling with the spin density of 0.5 on the radical carbon atom. The computer program developed by Lefebvre and Maruani[9] was used for the simulation. The principal values of the hyperfine tensor are assumed to be −20.0, −12.5, and −6.5 G[10] for both the protons, the HCH bond angle to be 120°, and the component line width to be 3 G. The isotropic g factor is also assumed. The isotropic hyperfine component is obtained to be −13 G, which gives ρ_C = 0.5 using Q_{CH} = −26 G.[11] The feature of the observed three-line spectrum is fairly well reproduced. The slight discrepancy, especially in the central line, may be attributed to the omission of the effect arising from the torsional motion as well as small g anisotropy. It is well known that the central line is sharpened when the rapid motion around the C-C bond takes place,[9] although the motion is fairly restricted in our radical.

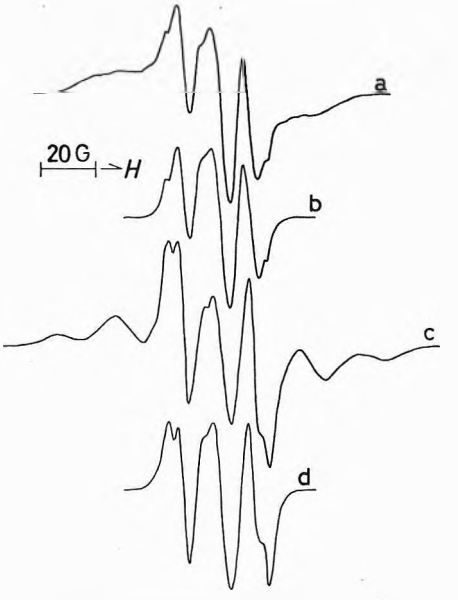

Figure 2. (a) Esr spectrum of a frozen TEA solution containing 4 mol % acrylic acid; (b) difference spectrum obtained by subtracting the spectrum of the solvent radical from a: dose, 5 × 10^5 rads at 77°K; modulation amplitude, 1.5 G; microwave power, 0.11 mW; observation temperature, 77°K. (c) Esr spectrum of frozen MHX solution containing 1 mol % acrylic acid; (d) difference spectrum obtained by subtracting the spectrum of the solvent radical from c: dose, 1.6 × 10^5 rads at 77°K; modulation amplitude, 2 G; microwave power, 0.11 mW; observation temperature, 77°K.

Thus, the three-line hyperfine coupling is reasonably attributable to the CH_2 protons and the spin density, 0.5, on the CH_2 carbon atoms is quite reasonable for our delocalized anion. Structure II predicts the small coupling to the CH proton, which may only contribute to the line width. The OH proton in such carboxylic anions, even in localized ones,[12] usually does not give a resolvable coupling in solid esr, if the OH proton sits in the COOH plane.[13,14] In order to confirm these expectations, the INDO MO calculation[15] has been performed for the acrylic acid anion assuming the molecular geometry (see Figure 3) determined by X-ray analysis.[16] The results are given in Table I. The isotropic coupling constant for the CH_2 protons and the p_π spin density on the CH_2 carbon atom are obtained to be −11 G and 0.50, respectively, in reasonable agreement with the observation. The CH and OH couplings are obtained to be −0.72 and −0.55 G, respectively, so that these couplings are too small to be resolved. As far as the author's knowledge is concerned, the detection of the acrylic acid anion by esr has not been made so far. Usually acrylic acid gives only the neutral radicals formed from addition of X (H or other groups having no appreciable couplings) to the double bond.[5a,6]

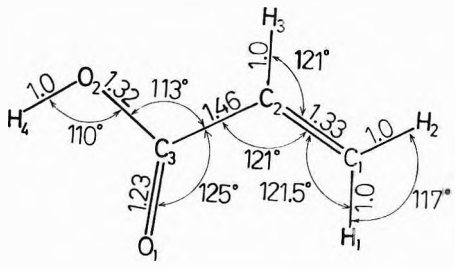

Figure 3. Molecular geometry assumed in the INDO MO calculation for the acrylic acid anion.

TABLE I: Spin Densities and Isotropic Hyperfine Splittings Obtained from INDO MO Calculations for the Acrylic Acid Anion Radical

Atom[a]	Spin densities s	Spin densities p_π	Isotropic hyperfine splittings, G
C_1	0.024	0.500	19.5
C_2	−0.002	0.062	−1.9
C_3	0.005	0.150	4.2
O_1	0.006	0.268	5.2
O_2	0.000	0.018	0.0
H_1	−0.021		−11.4
H_2	−0.020		−10.8
H_3	−0.001		−0.7
H_4	−0.001		−0.5

[a] The atomic numbering refers to that in Figure 3.

Protonation of the Acrylic Acid Anion. In order to see if the protonation of the acrylic acid anion takes place to form the hydrogen addition radical (III), the irradiated

$$CH_3\text{-}\dot{C}H\text{-}COOH$$
III

frozen solutions of MTHF, TEA, and MHX were annealed at elevated temperatures and then the esr spectra were measured at 77°K. The annealing of the MTHF solution at 90°K (liquid oxygen temperature) did not give any significant change in the spectral features and the prolonged annealing for 1–16 hr resulted in the mere decay of the anion and the MTHF radicals. However, when the samples were annealed at 97°K for 2 min, the sudden change of the three-line spectrum into the one attributable to the hydrogen addition radical III was observed as shown in Figure 4. Figure 4d shows the spectrum obtained from the pure acrylic acid (irradiated at 77°K) in which the hydrogen addition radical III is known to be formed.[6] The spectral feature is consistent with the reported hyperfine couplings to the three equivalent β protons and one α proton.[6,17] The spectrum in Figure 4c clearly indicates the formation of radical III from the anion.

The radical conversion from I to III was also observed in the TEA matrices when the samples were annealed at 115–117°K for 1–2 min, although the spectral change was less clear than that in the MTHF matrices, because of the overlapping of the spectrum due to the solvent radical. The spectrum of the TEA radical changed into the one having the resolvable structures at the positions close to those of radical III after annealing at 115–117°K. For these reasons, we have carried out similar experiments using methacrylic acid (MAA) as the solute. In this case, the gradual change of the anion into the hydrogen addition

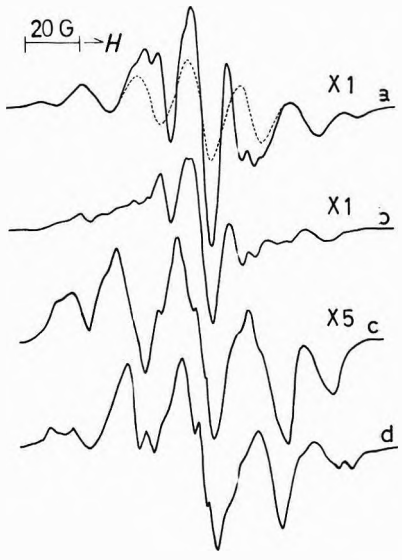

Figure 4. Esr spectra of frozen MTHF solutions containing 2 mol % acrylic acid: (a) immediately after irradiation; (b) after annealing at 97°K for 1 min; (c) after annealing at 97°K for 2 min; dose, 1.2×10^5 rads at 77°K; modulation amplitude, 2 G; microwave power, 0.10 mW; observation temperature, 77°K; gain, the same for a and b and ×5 for c. (d) Esr spectrum of pure acrylic acid: dose, 1.5×10^5 rads at 77°K; modulation amplitude, 1.0 G; microwave power, 0.10 mW; observation temperature, 77°K.

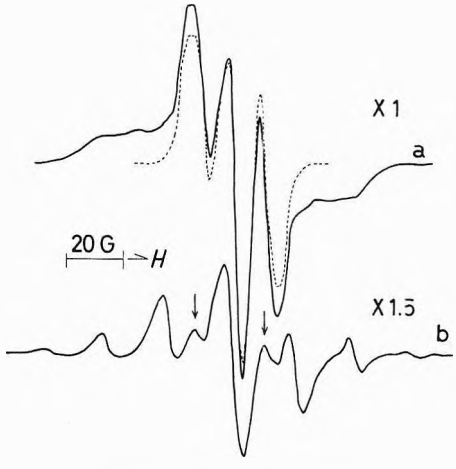

Figure 5. Esr spectra of frozen TEA solutions containing 4 mol % methacrylic acid: (a) immediately after irradiation; (b) after annealing at 117°K for 1 min. The dotted line in a indicates the difference spectrum. The peaks indicated by the arrows in b are due to the remaining anion: dose, 5.8×10^5 rads at 77°K; modulation amplitude, 3 G; microwave power, 0.11 mW; observation temperature, 77°K; gain, ×1.5 for b.

radical $CH_3\dot{C}(CH_3)COOH$ was clearly observed after the samples were annealed at 110°K for 5–50 min. Annealing at 117°K for 1 min resulted in the very rapid conversion as shown in Figure 5. (Since annealing for 1 min is insufficient to maintain the thermal equilibrium, the actual sample temperature may be slightly lower than 117°K.) The spectrum of the hydrogen addition radical of MAA is well characterized[7] so that the spectral interpretation is quite clear in this case.

We have also examined the conversion of the MAA anion to the hydrogen addition radical in the MTHF matrices and found that the conversion takes place at 97°K. It is also to be added that the spectrum of the anionic species of MAA is essentially the same as that of the

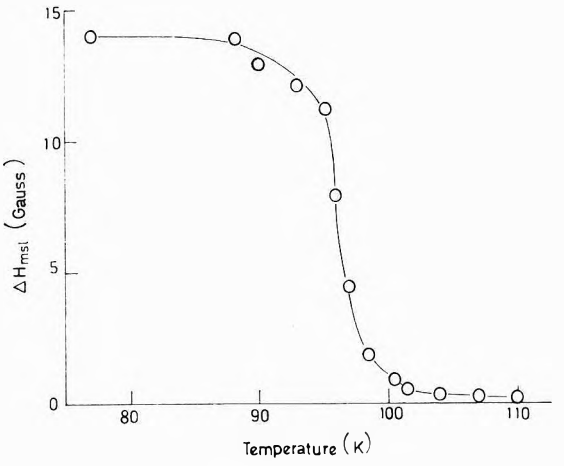

Figure 6. Temperature change of the maximum slope line width of the wide-line nmr spectra of frozen MTHF.

acrylic acid anion as shown in Figure 5a. This is reasonably expected from the electronic structure of the anion described in the previous section.

These results clearly indicate that the protonation of the electron adducts takes place at preferable temperatures which are characteristic of the matrices. This hints that the radical conversion temperature may be related to the molecular motions of the matrices, therefore, we have measured the temperature change of the line width of the wide-line nmr spectra of frozen MTHF. As shown in Figure 6 the sudden narrowing of the line width was found at the radical conversion temperature, that is, 97°K. These results suggest that the protonation reaction is associated with the molecular reorientations in the matrices.

In contrast to the MTHF and TEA matrices, thermal annealing of the MHX matrices resulted in the mere decay of the anions and the MHX radicals in the wide range of annealing temperatures up to the melting point. The difference will be discussed in the later section.

Matrices Having Polar Protons. The frozen methanol solution containing 5% water and ~2 mol % acrylic acid did not give a signal from the solute anion I nor from the trapped electron. Instead of these, the spectrum of the hydrogen addition radical III appeared with the solvent radical as shown in Figure 7a. Replacement of the trapped electron with the solute radical indicates that radical III originates from the electron adduct of the solute. The ethanol solution containing 3–7 mol % acrylic acid also gave a similar result suggesting that alcoholic protons are easily transferred to the electron adducts.

Shown in Figure 7b is the spectrum obtained from alkaline ice (8 *N* NaOH) containing ~3 mol % acrylic acid. The spectrum is essentially the same as that of pure acrylic acid indicating the efficient yield of the hydrogen addition radical. In this case, the species is considered to have the basic form IV. Recently Neta and Fessenden[5a]

$$\underset{\text{IV}}{\dot{C}H_2CHCO_2^-}$$

have reported that the basic form has similar esr parameters to those of the acidic form III.

Polycrystalline samples of propionic acid containing ~3 mol % acrylic acid gave a considerable amount of radical III together with the ethyl and other radicals originating from propionic acid. This suggests that electrons are efficiently captured by the small amount of acrylic acid and

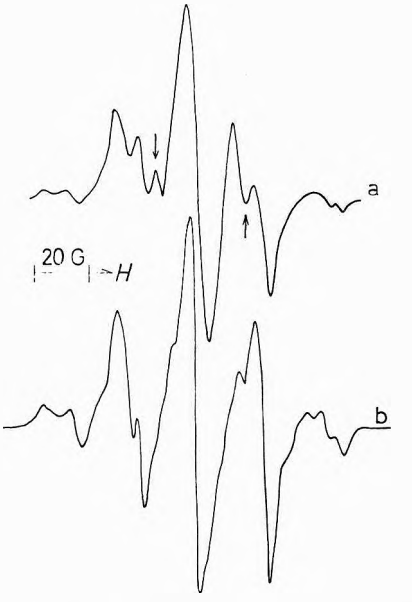

Figure 7. Esr spectra of (a) a frozen methanol solution containing 5 mol % water and 2 mol % acrylic acid; (b) a frozen alkaline (8 *N* NaOH) aqueous solution containing 3 mol % acrylic acid: dose, (a) 2×10^5 rads, (b) 1×10^5 rads at 77°K; modulation amplitude, 1.5 G; microwave power, 0.12 mW; observation temperature, 77°K. The origin of the lines indicated by the arrows in a is not clear. The spectrum of pure methanol also gave the high-field line when the modulation amplitude of 1.5 G is used. The same extra lines are observed for uv-irradiated methanol by Sullivan and Koski (*J. Amer. Chem. Soc.*, **85**, 384 (1963)). However, larger modulation amplitudes gave the familiar spectrum for γ-irradiated methanol.

rapid protonation of the electron adducts takes place in these mixed crystals.

These results obtained from the matrices having polar protons indicates that protonation of the electron adducts more easily takes place in these matrices.

Discussion

Our studies demonstrate that the electron adducts of acrylic acid can be stabilized in some solutions having less possibilities of donating H^+ to the adducts, while the hydrogen addition radicals are formed immediately after irradiation by rapid protonation of the electron adducts in some solutions having larger possibilities of donating H^+. The quite analogous results have been obtained for α-methylstyrene in MTHF and ethanol matrices by Lin, Tsuji, and Williams.[4] They have observed the anionic species in MTHF and immediate protonation in ethanol. The conversion from the anion to the hydrogen addition radical was also observed in the MTHF matrices during post-irradiation annealing at 96°K. It is to be noted that protonation of the entirely different anionic species takes place at exactly the same temperature as that in our case. On the other hand, protonation of the same acrylic acid anion takes place at different temperatures in the MTHF and TEA matrices. In addition, the nmr measurements indicate that the conversion temperature is related to the molecular motions in the matrices. These results suggest that the protonation reaction is more predominantly governed by the molecular reorientations in the matrices rather than the nature of the anionic species.

The rapid decrease of the nmr line width from 11 to only 1.5 G in the temperature range 95–99°K suggests that the motions of the MTHF molecules involve overall rotations. The further decrease at 100–110°K from 1.5 G to the

very narrow line width characteristic of the liquid phase suggests the onset of the rapid self-diffusion. These behaviors are quite analogous to those in the plastic crystals of cyclopentane and cyclohexane.[18,19] These results may suggest that radical conversion takes place before the onset of rapid self-diffusion and it is associated with the overall rotations of the matrix molecules which are supposed to provide the preferable orientation for proton transfer.

On the other hand, the temperature change of the nmr line width of pure TEA glasses reported by Tsujikawa, Fueki, and Kuri shows a gradual decrease from about 9 to 3 G at 90–110°K and an irreversible abrupt increase at 113°K.[8c] The gradual decrease was interpreted as resulting from the onset of molecular motions and the irreversible increase from a phase transition. Since it has been reported[8c] that the pure TEA sample becomes opaque with the irreversible phase change and that no trapped electron spectrum is obtained with this opaque sample, the phase transition may be associated with the crystallization of the sample. The radical conversion in our irradiated TEA–AA and TEA–MAA systems was initiated around 110°K and became very rapid around 112–115°K, which agrees with the crystallization temperature of the pure TEA glasses. However, it is to be noted that our samples remain transparent after completing radical conversion. In addition, we have observed the softening of the samples at slightly higher than radical conversion temperature. The deep needle-shape hole on the surface of the frozen sample gradually disappeared to become a flat surface by annealing at 117°K for about 5 min although this change was not observed during radical conversion. Since this temperature is very much lower than the melting point (160°K) of pure TEA, our samples seem to become supercooled liquids in this temperature range. These observations indicate that the addition of small amounts of additives or some other causes prevent the crystallization of our samples. We presume that the radical conversion is initiated by the molecular motions associated with the narrowing of the nmr line width in this temperature region rather than the reported abrupt increase at 113°K.

It is hard to believe that the protonation reaction occurs by the direct proton transfer from the neutral MTHF or TEA solvents. The rapid protonation in the matrices having the OH protons such as alcohol and alkaline ice indicates that the polar protons are more easily transferred to the anion. The radiation induced positive ion in the MTHF glasses is generally considered to be a protonated species formed from the following ion–molecule reaction

$$MTHF^+ + MTHF \longrightarrow \text{(protonated MTHF)} \quad (1)$$

A similar protonated cation may be formed in the TEA glasses.

$$TEA^{\cdot+} + TEA \longrightarrow (Et)_3\overset{+}{N}\text{-}H \quad (2)$$

The OH or NH proton in these protonated cation can be a candidate for the origin of the proton transferred to the anion. In fact, protonation of the anion was not observed in the MHX matrices which has no hetero atom and thus less possibility to form such a protonated species.

Now, an important point is in the fact that rapid protonation is always observed in the hydrogen-bonded system. This may suggest that the intermolecular hydrogen bond may play an important role in proton transfer from the surroundings to the electron adducts. The proton transfer model proposed in our previous work[2,20-22] with some hydrogen-bonded crystals might be applicable to these glasses. Although MTHF and TEA glasses do not have strong intermolecular hydrogen bonds, the protonated cation $>O^+-H$ or $>N^+-H$ may be able to form hydrogen bonds with the oxygen or nitrogen atom in a neighboring molecule, if the reorientation of the molecules is allowed by thermal annealing. This may ease proton transfer through the hydrogen bond to the oxygen or nitrogen atom in the neighboring molecule

$$\text{>}\overset{+}{X}\text{-H}\cdots X \longrightarrow X\cdots H\text{-}\overset{+}{X}\text{<} \quad (3)$$

where X represents the oxygen or nitrogen atom. The proton may be successively transferred from molecule to molecule by changing the partner of the intermolecular hydrogen bond during the molecular reorientations. The proton migration may discontinue when the protonated cation encounters the electron adduct forming the hydrogen addition radical by the charge neutralization reaction. However, the contribution of the diffusion of the protonated cation may not be completely excluded from the present results.

On the other hand, rapid protonation in the alcohol and alkaline ice matrices may be interpreted by the two alternative mechanisms: one is direct proton transfer from the surrounding solvent molecule and the other is proton transfer from the protonated cation of the solvent. In the alcohol matrices

$$[CH_2{=}CHCOOH]^- + ROH \longrightarrow CH_3\dot{C}HCOOH + RO^- \quad (4)$$

$$[CH_2{=}CHCOOH]^- + H^+ \text{ from } [ROH_2]^+ \longrightarrow CH_3\dot{C}HCOOH + ROH \quad (5)$$

In the alkaline ice matrices

$$[CH_2{=}CHCOO]^{2-} + H_2O \longrightarrow CH_3\dot{C}HCOC^- + OH^- \quad (6)$$

$$[CH_2{=}CHCOO]^{2-} + H^+ \text{ from } H_2O^+ \text{ or } H_3O^+ \longrightarrow CH_3\dot{C}HCOO^- \quad (7)$$

At the present moment, the direct protonation mechanism is generally accepted by many workers.[4,5,23] However, the possibility of the alternative mechanism may not be ignored, because these matrices are the hydrogen bond system, in which proton transfer *via* the hydrogen bridge is considered to easily take place when protonated cations are formed.

Acknowledgment. One of the authors (M. I.) is grateful to Professor McDowell for his invitation to the University of British Columbia, where the essential part of this manuscript has been written.

References and Notes

(1) For example, see reviews by M. Iwasaki, *MTP Int. Rev. Sci., Phys. Chem. Ser.*, **4**, 317 (1972).
(2) M. Iwasaki, H. Muto, and K. Toriyama, *J. Chem. Phys.*, **55**, 1894 (1971).
(3) C. Chachaty, *J. Chim. Phys.*, **64**, 614 (1967).
(4) J. Lin, K. Tusji, and F. Williams, *Trans. Faraday Soc.*, **64**, 2896 (1968).
(5) (a) P. Neta and R. W. Fessenden, *J. Phys. Chem.*, **76**, 1957 (1972); (b) I. S. Ginns and M. C. R. Symons, *Chem. Commum.*, 893 (1971).
(6) Y. Shioji, S. Ohnishi, and I. Nitta, *J. Polym. Sci., Part A-1*, 3373 (1963).
(7) Y. Sakai and M. Iwasaki, *J. Polym. Sci., Part A-1*, **7**, 1749 (1969).

(8) (a) D. R. Smith and J. J. Pieroni, *Can. J. Chem.*, **42**, 2209 (1964); (b) S. Fujii and J. E. Willard, *J. Phys. Chem.*, **74**, 4313 (1970); (c) H. Tsujikawa, K. Fueki, and Z. Kuri, *J. Chem. Phys.*, **47**, 256 (1967).
(9) R. Lefebvre and J. Maruani, *J. Chem. Phys.*, **42**, 1480 (1965).
(10) The hyperfine tensor for the α proton coupling is well established. For example, CH_2COOH in malonic acid gives the principal elements of −32.9, −20.1, and −10.8 G with the isotropic component of −22.2 G. [A. Horsfield, J. R. Morton, and D. H. Whiffen, *Mol. Phys.*, **1**, 475 (1961).] The three tensor elements obtained from the simulation for our radical are reduced by factors of 0.61, 0.62, and 0.60, respectively, because of larger delocalization of the spin density in our radical.
(11) J. R. Bolton, "Radical Ions," E. T. Kaiser and L. Kevan, Ed., Interscience, New York, N. Y., 1968, p 10.
(12) J. W. Wells, *J. Chem. Phys.*, **52**, 4062 (1970).
(13) The carboxyl anion in an irradiated single crystal of alanine[14] has an exceptionally large OH coupling ($a_0 \simeq 15$ G). However, our recent study by ENDOR has made it clear that this is due to the conformation of the OH bond, which is out of the COO plane (*J. Chem. Phys.*, in press).
(14) (a) A. Minegishi, Y. Shinohara, and G. Meshitukɛ, *Bull. Chem. Soc. Jap.*, **40**, 1549 (1967); (b) I. Miyagawa, N. Tamura, and J. W. Cook, Jr., *J. Chem. Phys.*, **51**, 3520 (1969); (c) J. W. Sinclair and M. W. Hanna, *J. Phys. Chem.*, **71**, 84 (1967); (d) J. W. Sinclair and M. W. Hanna, *J. Chem. Phys.*, **50**, 2125 (1969).
(15) J. A. Pople and D. L. Beveridge, "Approximate Molecular Orbital Theory," McGraw-Hill, New York, N. Y., 1970, p 136.
(16) Y. Chatani, Y. Sakata, and I. Nitta, *J. Polym. Sci., Part B-1*, 419 (1963).
(17) H. Fischer, *Z. Naturforsch. A*, **19**, 866 (1964).
(18) (a) F. A. Rushworth, *Proc. Roy. Soc., Ser. A*, **222**, 526 (1954); (b) J. G. Aston, "Physics and Chemistry of the Organic Solid State," D. Fox, Ed., Wiley, New York, N. Y., 1963, p 564.
(19) E. R. Andrew, *J. Phys. Chem. Solids*, **18**, 9 (1961).
(20) B. Eda and M. Iwasaki, *J. Chem. Phys.*, **55**, 3442 (1971).
(21) M. Iwasaki, K. Minakata, K. Nunome, and K. Tagami, *J. Chem. Phys.*, **57**, 3187 (1972).
(22) K. Minakata and M. Iwasaki, *J. Chem. Phys.*, **57**, 4758 (1972).
(23) T. Shida and W. H. Hamill, *J. Chem. Phys.*, **44**, 4372 (1966); S. Arai and L. M. Dorfman, *ibid.*, **41**, 2190 (1964); M. C. Sauer, S. Arai, and L. M. Dorfman, *ibid.*, **42**, 708 (1965).

Ultraviolet and Electron Spin Resonance Spectra of Nitropyridines and Nitropyridine *N*-Oxides

Aldo Gamba, Vincenzo Malatesta, Gabriele Morosi, Cesare Oliva, and Massimo Simonetta*

C. N. R. Center for the Study of Structure/Reactivity Relations and Institute of Physical Chemistry, University of Milan, Milan, Italy
(Received February 9, 1973)

The esr and uv spectra of 2-, 3-, and 4-nitropyridine and 2-, 3-, and 4-nitropyridine *N*-oxide anion radicals in solution have been measured as well as the uv spectra of 2-, 3-, and 4-nitropyridine *N*-oxide neutral molecules in the same solvent. The results have been interpreted by application of a number of semiempirical quantum mechanical methods. By comparison of experimental and calculated data an assignment of visible and ultraviolet absorption bands to electronic transitions and of hyperfine splitting (hfs) coupling constants to magnetic nuclei is proposed.

Introduction

The electronic structure of the ground and excited states of pyridine, pyridine *N*-oxide, their mononitro derivatives, and the corresponding anion radicals has been the subject of several investigations, both experimental and theoretical (see ref 1–10 and references therein), the most frequently used techniques being uv and esr spectroscopy.

However, the esr spectra of some of these radicals had never been measured, and the same is true for the uv spectra. It seems worthwhile collecting esr and uv spectra of all of these radicals in the same conditions, particularly in the same solvent, together with the uv spectra of the parent neutral molecules.

Many theoretical methods are available for the interpretation of these experimental data, some of which are unfortunately of no practical use for our systems, due to their complexity. We tried some of the most well-established semiempirical approaches including the σ/π approximation.

The aim of the present work is to verify the possibility of obtaining for each anion radical a good correlation between experimental data for all the measured observables, that is hfs coupling constants, electronic transition energies and probabilities, and the corresponding theoretical results obtained by solution of just one eigenvalue–eigenvector problem. Also transition energies and probabilities for the neutral molecules were calculated in each method by using the same approximations and parametrization as for the corresponding anions.

The numbering and reference axes for the neutral molecules are shown in Figure 1. The corresponding radicals will be identified with the same numbers primed.

Methods of Calculation and Parameters

Anion Radicals. Calculations were carried out by means of semiempirical methods based on the σ/π approximation and by means of the INDO method,[11] which includes all valence electrons.

Owing to the lack of experimental data, geometries for ions were assumed equal to those of parent neutral molecules. The experimental (planar) geometries were used for the heavy atom skeletons in pyridine[12] and pyridine *N*-oxide. In the case of pyridine *N*-oxide the suggested weighted average[13] for bond lengths and bond angles of the two crystallographically independent molecules, contained in the unit cell, was used: N–O = 1.35 Å; N–C_2 = 1.34 Å, C_2–C_3 = C_3–C_4 = 1.37 Å; $C_5C_4C_3$ = 118°; $C_4C_3C_2$

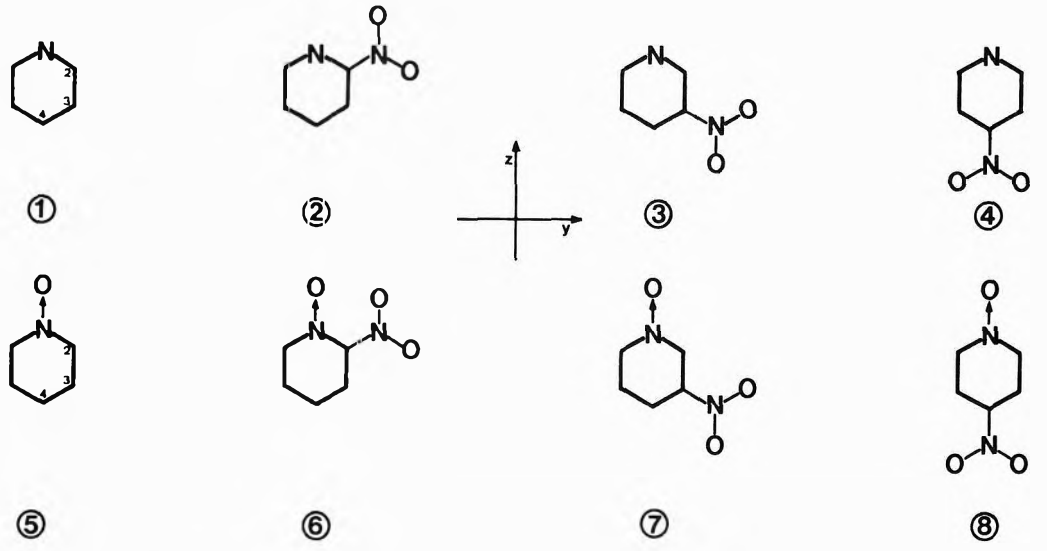

Figure 1. Numbering of molecules and reference axes.

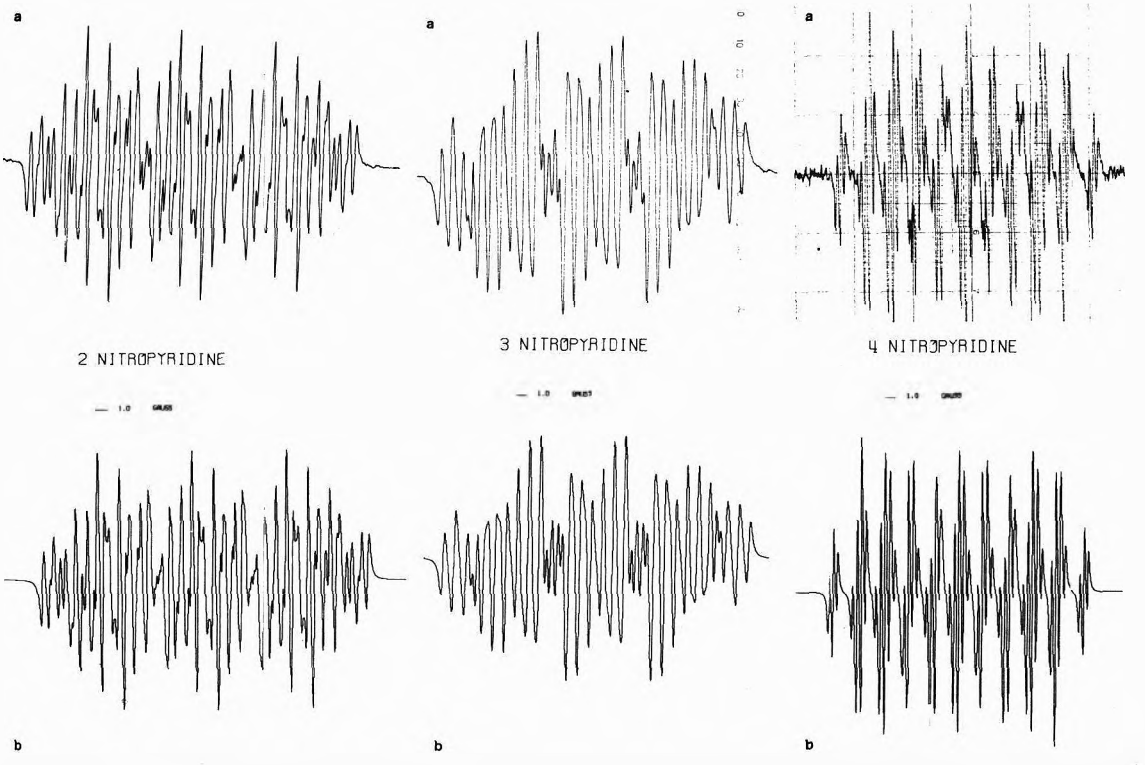

Figure 2. Experimental (a) and simulated (b) (J. Heinzer, "Least Squares Fitting of Isotropic Multiline Esr Spectra," Quantum Chemistry Program Exchange (QCPE), Indiana University, Bloomington, Ind.) esr spectra of anion radicals of nitropyridine isomers. The modulation amplitude produces negligible distortion as fields between 0.75×10^{-4} and 5×10^{-4} G were used for widths between 0.2 and 0.4 G (C. P. Poole, Jr. "Electron Spin Resonance," Chapter 10-E, Interscience, New York, N. Y., 1967).

TABLE I: Polarographic Data

Molecule	$-E_{1/2}$ (V) *vs.* sce
2-Nitropyridine	1.08
3-Nitropyridine	1.06
4-Nitropyridine	0.92
2-Nitropyridine *N*-oxide	0.96
3-Nitropyridine *N*-oxide	0.83
4-Nitropyridine *N*-oxide	0.87

= 120°30′; C_3C_2N = 119°30′. All C–H bonds were assumed in the ring plane bisecting external ring angles, with a bond length equal to 1.08 Å. For nitro derivatives the same geometries of the rings as for unsubstituted compounds were used. The nitro group was assumed coplanar with the ring, with the following geometry: ONO = 124°; N–O = 1.21 Å; C–N = 1.48 Å,[14] and bisecting external ring angle.

In the scope of a σ/π approximation, restricted LCI-SCF methods, in versions given by Pople and Longuet-Higgins (P)[15] and by Roothaan (R)[16] were taken into consideration, as well as the McLachlan (M) method.[17]

Starting HMO's were evaluated with the parametrization suggested by Rieger and Fraenkel[18] and that adopted by Janzen and Happ for the N → O group;[9] for the ring

TABLE II: Calculated (P and R Methods) Spin Densities and Proton Hfs Constants and Experimental Coupling Constants[a]

		Theoretical				
		P method		R method		
Anion radical	Position	ρ_i	a_i[c]	ρ_i	a_i[d]	Exptl[b]
1′	N	0.34553		0.34572		6.28[e]
	2	0.10727	−2.496	0.10659	−2.526	3.55
	3	0.00835	−0.194	0.00868	−0.206	0.82
	4	0.42324	−9.849	0.42374	−10.042	9.70
2′	N	0.19238		0.18476		1.893
	3	0.07615	−1.772	0.07804	−1.849	2.728
	4	−0.01015	0.236	−0.00714	0.169	0.591
	5	0.15542	−3.616	0.14908	−3.533	3.777
	6	−0.06210	1.445	−0.05302	1.257	0.866
	N($-NO_2$)	0.35847		0.37170		8.184
3′	N	−0.03899		−0.03403		1.313
	2	0.09704	−2.258	0.09831	−2.330	3.183
	4	0.20719	−4.821	0.19934	−4.724	4.433
	5	−0.06758	1.572	−0.05469	1.296	1.091
	6	0.20404	−4.748	0.19098	−4.526	3.643
	N($-NO_2$)	0.38375		0.40151		9.327
4′	N	0.18351		0.17080		2.473
	2	−0.03064	0.713	−0.02392	0.567	0.451
	3	0.13348	−3.106	0.13355	−3.165	3.033
	N($-NO_2$)	0.34948		0.36318		7.817
5′	N($N\rightarrow O$)	0.23120		0.23074		10.91[f]
	2	0.13761	−3.202	0.13656	−3.236	3.01
	3	−0.01131	0.263	−0.01054	0.250	0.44
	4	0.38087	−8.862	0.38243	−9.063	8.51
6′	N($N\rightarrow O$)	0.12892		0.14196		3.76
	3	0.03996	−0.930	0.03237	−0.767	1.43
	4	−0.03053	0.710	−0.01911	0.453	1.13
	5	0.08615	−2.005	0.07883	−1.868	3.76
	6	−0.06652	1.548	−0.04675	1.108	2.65
	N($-NO_2$)	0.23426		0.17631		7.30
7′	N($N\rightarrow O$)	−0.01815		−0.01888		0.915
	2	0.08022	−1.867	0.09317	−2.208	3.354
	4	0.19986	−4.650	0.19243	−4.560	4.322
	5	−0.06193	1.441	−0.04845	1.148	2.767
	6	0.19034	−4.429	0.17990	−4.263	3.501
	N($-NO_2$)	0.42714		0.44466		7.752
8′	N($N\rightarrow O$)	0.13495		0.13663		4.380
	2	−0.03967	0.923	−0.03247	0.770	1.180
	3	0.10438	−2.429	0.10582	−2.508	3.187
	N($-NO_2$)	0.30542		0.30325		6.240

[a] In gauss. [b] In acetonitrile (present work) except when otherwise stated. [c] $a^H = -23.3\ \rho_C^{\pi}$ (G). [d] $a^H = -23.7\ \rho_C^{\pi}$ (G). [e] In liquid NH_3.[36] In dimethylformamide.[5]

nitrogen in nitropyridines the following parameters were assumed: $\delta = 0.5$ and $\gamma_{CN} = 1.0$.[19]

Energy parameters adopted through PPP calculations are available.[20] Two-center Coulomb repulsion integrals were calculated adopting the Pariser and Parr approximation.[21] Prescriptions to evaluate the integrals at distances less than 2.80 Å were given elsewhere.[22]

In CI calculations we considered interaction of ground configuration with all singly excited configurations of types A, B, C_α and C_3, according to the definitions reported in ref 23. For details on the calculation of energy and oscillator strength matrix elements for doublets, based on Longuet-Higgins and Pople and Roothaan procedures, see ref 21 and 23.

INDO calculations were performed using the program by Dobosh,[24] modified to include the calculation of the spin densities and hfs coupling constants from wave functions purified of the quartet component.[25,26]

Neutral Molecules. Singlet-singlet excitation energies and probabilities were evaluated by means of the standard PPP method with the same parameters used for ions, including all singly excited configurations in the CI treatment.

For better confidence in the assignment of bands to electronic transitions, it seemed worthwhile comparing PPP excitation energies and probabilities with those obtained by the "Molecules in Molecules" (MIM) method.[27] The results for nitropyridines can be found in the literature.[2] MIM calculations for nitropyridine *N*-oxides were performed following the same prescriptions as given in ref 2 for nitropyridine derivatives. Geometry, two-center Coulomb integrals, and β resonance integrals are the same as used in PPP calculations. All the starting data necessary for MIM calculations are available.[20]

To verify if the transition energies obtained by the two different methods are consistent and to interpret the re-

TABLE III: Calculated (M Method) Spin Densities and Hfs Coupling Constants and Experimental Values[a]

Anion radical	Position	Spin density	Calculated coupling constant[b]	Measured coupling constant[c]
1′	N	0.34694	6.36[e]	6.28[d]
	2	0.13049	−3.52	3.55
	3	−0.01403	0.38	0.82
	4	0.42015	−11.34	9.70
2′	N	0.16380	2.12[e]	1.893
	3	0.08966	−2.42	2.728
	4	−0.01334	0.36	0.591
	5	0.14685	−3.96	3.777
	6	−0.05094	1.38	0.866
	N(−NO_2)	0.21834	7.34[f]	8.184
3′	N	−0.04393	−1.52[e]	1.313
	2	0.11259	−3.04	3.183
	4	0.16222	−4.38	3.643
	5	−0.05222	1.41	1.091
	6	0.18832	−5.08	4.433
	N(−NO_2)	0.23389	9.10[f]	9.327
4′	N	0.16834	1.95[e]	2.473
	2	−0.01819	0.49	0.451
	3	0.11821	−3.19	3.033
	N(−NO_2)	0.20635	6.86[f]	7.817
5′	N(N→O)	0.28693	8.72;[g] 10.14[h]	10.91[i]
	2	0.13809	−3.73	3.01
	3	−0.01720	0.46	0.44
	4	0.38393	10.37	8.51
6′	N(N→O)	0.13603	4.66;[g] 4.78[h]	3.76
	3	0.10120	−2.06	2.65
	4	−0.02438	0.66	1.13
	5	0.14578	−3.94	3.76
	6	−0.05222	1.41	1.48
	N(−NO_2)	0.21369	7.50[f]	7.30
7′	N(N→O)	−0.03419	−3.05;[g] −1.19[h]	0.915
	2	0.12369	−3.34	3.354
	4	0.16164	−4.36	3.501
	5	−0.05062	1.37	2.767
	6	0.19074	−5.15	4.322
	N(−NO_2)	0.23456	9.14[f]	7.752
8′	N(N→O)	0.14624	5.19;[g] 5.14[h]	4.38
	2	−0.02777	0.75	1.18
	3	0.11730	−3.17	3.19
	N(−NO_2)	0.20419	7.14	6.24

[a] Coupling constants in gauss. [b] $a^H = -27.0\rho_C^{\pi}$.[9] [c] In acetonitrile except when otherwise stated. [d] In liquid NH_3.[36] [e] $a^N = \pm 13.1\rho_N^{\pi} \pm 6.96(\rho_{C2}^{\pi} + \rho_{C6}^{\pi})$. [f] $a^{N(NO_2)} = \pm 99.0\rho_N^{\pi} \mp 35.8(2\rho_O^{\pi})$.[18] [g] $a^{N(N\rightarrow O)} = 42.57\rho_N^{\pi} - 18.98\rho_O^{\pi} - 6.66(\rho_{C2}^{\pi} + \rho_{C6}^{\pi})$.[5] [h] $a^{N(N\rightarrow O)} = 35.61\rho_N^{\pi} - 0.93\rho_O^{\pi}$ from P. B. Ayscough and F. P. Sargent *J. Chem. Soc. B*, 907 (1966). [i] In dimethylformamide.[5]

sults of PPP calculations directly in the language of locally excited and charge-transfer configurations, a configurational analysis[28] was carried out.

Experimental Section

Materials. 2-Nitropyridine was prepared by oxidation of 2-aminopyridine (Fluka);[29] mp 71° (ethanol); (lit.[29] 71°). *3-Nitropyridine* was obtained by oxidation of 3-aminopyridine[30] and separated on a silica column; mp 36° (ethane–ethyl acetate); (lit.[30] 35–36°). *4-Nitropyridine* was prepared by reduction of 4-nitropyridine *N*-oxide (Fluka);[31] mp 47.5° (ligroin); (lit.[31] 47.5°). *2-Nitropyridine N-oxide* was prepared by oxidation of 2-aminopyridine (Fluka);[32] mp 86° (ethanol); (lit.[32] 85–86°). *3-Nitropyridine N-oxide* was prepared by oxidation of 3-aminopyridine (Fluka);[33] mp 173° (ethanol); (lit.[33] 172–173°). *4-Nitropyridine N-oxide* was a Fluka product, purified from acetone; mp 159°. Acetonitrile was Merck UVASOL 16/66. It was further purified following a previously described procedure.[34] *Tetraethylammonium perchlorate* (TEAP) was a Carlo Erba product for polarography.

Preparation and Measurements for Anion Radicals. Anion radicals were prepared in vacuum cells by controlled potential electrolysis following external generation (EG) technique.[22,35] Technical details and the vacuum apparatus have been described previously.[22,34] The EG technique presents the advantage of reaching almost complete reduction and allows the measurements in parallel of esr and uv spectra of radicals, which give more confidence on the assignment of observed electronic spectra to anion radicals.

Reduction potentials for each compound were evaluated from polarographic curves recorded in acetonitrile at room temperature, and the half-wave potentials are collected in Table I. A multipurpose AMEL Model 463 polarograph was used.

Esr spectra were obtained with a Varian 4502 X-band spectrometer with a 100-kHz field modulation. Elec-

TABLE IV: Spin Densities and Hfs Coupling Constants Calculated by INDO Method, and Experimental Values for Magnetic Nuclei in Pyridine, Nitropyridines, and Pyridine *N*-Oxide

Anion radical	Position	Calcd [A][a]		Calcd [B][a]		Exptl[b]	
		ρ_i	a_i	ρ_i	a_i		
		$\langle S^2 \rangle = 0.7862$		$\langle S^2 \rangle = 0.7503$			
1′	N	0.0211	8.022	0.0071	8.024	6.28[c]	6.28[d]
	2	−0.0070	−3.759	−0.0023	−1.643	3.14[c]	3.55[d]
	3	0.0007	0.365	0.0002	0.161	0.88[c]	0.82[d]
	4	−0.0162	−8.739	−0.0054	−3.816	9.10[c]	9.70[d]
		$\langle S^2 \rangle = 0.7815$		$\langle S^2 \rangle = 0.7506$			
2′	N	0.0076	2.876	0.0025	2.860	1.893	
	3	−0.0049	−2.641	−0.0016	−1.158	2.728	
	4	0.0027	1.437	0.0009	0.632	0.591	
	5	−0.0062	−3.323	−0.0020	−1.456	3.777	
	6	0.0031	1.671	0.0010	0.736	0.866	
	$N(-NO_2)$	0.0194	7.349	0.0065	7.342	8.184	
		$\langle S^2 \rangle = 0.7770$		$\langle S^2 \rangle = 0.7504$			
3′	N	−0.0040	−1.535	−0.0013	−1.516	1.313	
	2	−0.0052	−2.781	−0.0017	−1.219	3.183	
	4	−0.0063	−3.384	−0.0021	−1.481	4.433	
	5	0.0033	1.785	0.0011	0.785	1.091	
	6	−0.0056	−3.028	−0.0019	−1.327	3.643	
	$N(-NO_2)$	0.0234	8.876	0.0079	8.880	9.327	
		$\langle S^2 \rangle = 0.7871$		$\langle S^2 \rangle = 0.7506$			
4′	N	0.0096	3.660	0.0032	3.641	2.473	
	2	0.0022	1.210	0.0007	0.533	0.451	
	3	−0.0060	−3.225	−0.0021	−1.781	3.033	
	$N(-NO_2)$	0.0172	6.526	0.0058	6.514	7.817	
		$\langle S^2 \rangle = 0.7796$		$\langle S^2 \rangle = 0.7504$			
5′	$N(-N\rightarrow O)$	0.0270	10.261	0.0091	10.278	10.91[e]	
	2	−0.0053	−2.883	−0.0018	−1.261	3.01[e]	
	3	0.0009	0.472	0.0003	0.209	0.44[e]	
	4	−0.0126	−6.827	−0.0042	−2.985	8.51[e]	

[a] Calcd [A]: INDO wave function; calcd [B]: INDO wave function after quartet spin component annihilation. [b] In acetonitrile except when otherwise stated. [c] In hexamethylphosphoramide.[1] [d] In liquid NH_3.[36] [e] In dimethylformamide.[5]

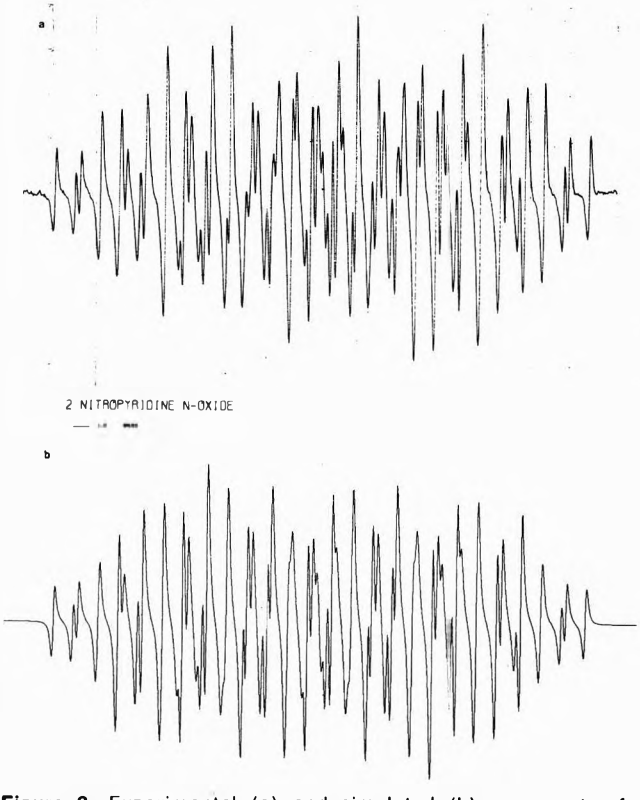

Figure 3. Experimental (a) and simulated (b) esr spectra for 2-nitropyridine *N*-oxide.

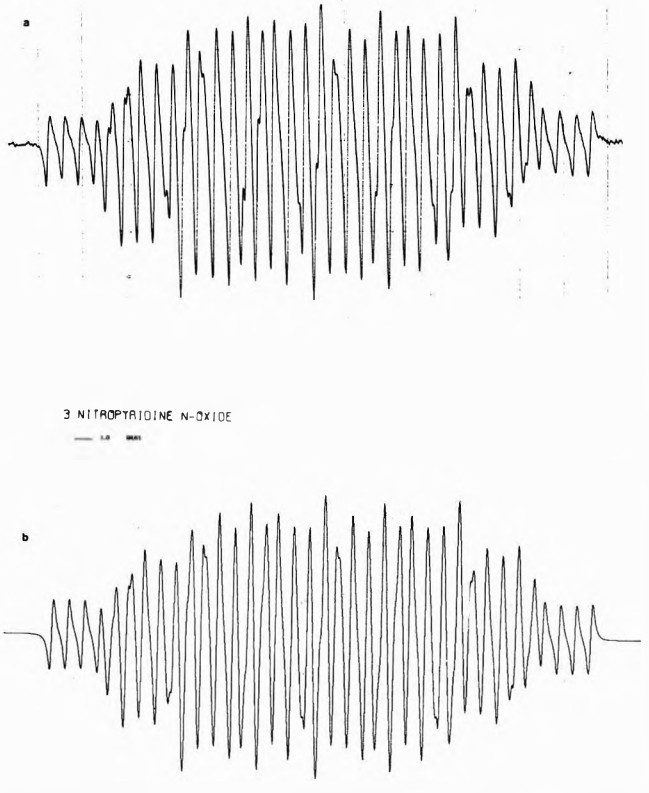

Figure 4. Experimental (a) and simulated (b) spectra for 3-nitropyridine *N*-oxide.

TABLE V: Doublet–Doublet Transition Energy, Oscillator Strength, and Polarization for Electronic Bands in Pyridine, Pyridine *N*-Oxide, and Their Nitro Derivatives Anion Radicals

Anion radical	Calcd (R method) ΔE, eV	f	Pol.	Exptl[a] ΔE, eV	
1′	0.555	$<10^{-3}$	y		
	2.827	0.046	z		
	4.436	0.009	z		
	5.180	0.005	y		
	6.110	0.411	y		
2′	1.741	0.024		2.25	
	2.544	0.112		2.79	
	3.899	0.010			
	4.131	0.206		4.00	
	4.832	0.016			
	5.234	0.008			
	5.462	0.141		5.18 (?)[b]	
3′	1.464	0.023		2.10	
	2.270	0.106		2.69	2.69[c]
	4.037	$<10^{-3}$			
	4.348	0.216		4.00	4.04[c]
	4.965	0.010		4.96 (?)[b]	
	5.383	0.028			
	5.445	0.006			
	5.645	0.108			
4′	2.259	0.001	y	1.75	1.90[c]
	2.311	0.145	z	2.76	2.81[c]
	3.975	0.061	y	3.94	4.00[c]
	4.000	0.053	z	4.27	
	4.254	0.127	z	4.92	
	5.308	0.050	y		
5′	0.935	$<10^{-3}$	y		
	2.508	0.052	z		
	3.213	0.116	z		
	4.187	0.060	y		
	5.279	0.182	y		
6′	1.131	0.043		1.88	
	2.263	0.090		2.95	
	3.172	0.024			
	3.892	0.076		3.99	
	4.502	0.014			
	5.251	0.275			
7′	1.368	0.030		1.91	
	1.696	0.001			
	2.586	0.105		2.56	
	3.791	0.026		3.19	
	4.149	0.147		3.82 (?)[b]	
	4.265	0.126		4.85 (?)[b]	
	4.949	0.099			
	5.182	0.300			
8′	1.353	0.010	z	1.96	
	2.681	$<10^{-3}$	y		
	2.822	0.461	z	2.53	
	3.934	0.033	y	3.06	
	4.320	0.002	z		
	4.627	0.050	y		
	4.820	0.012	z		
	5.487	0.033	y		

[a] In acetonitrile except when otherwise stated. [b] A band of the parent neutral molecule falls in the same region. [c] Radical obtained by reduction of the parent compound with potassium metal in 1,2-dimethoxyethane.[3,4]

tronic absorption spectra were measured with a Beckman DK-2A spectrophotometer. Acetonitrile was used as solvent in esr and uv measurements.

Uv Spectra of Neutral Molecules. The electronic absorption spectra of nitropyridine *N*-oxides were measured with a Beckman DK-2A spectrophotometer using acetonitrile, *n*-hexane, and *n*-pentane as solvents. Recording was carried out in a purified nitrogen stream (oxygen content <0.2 ppm).

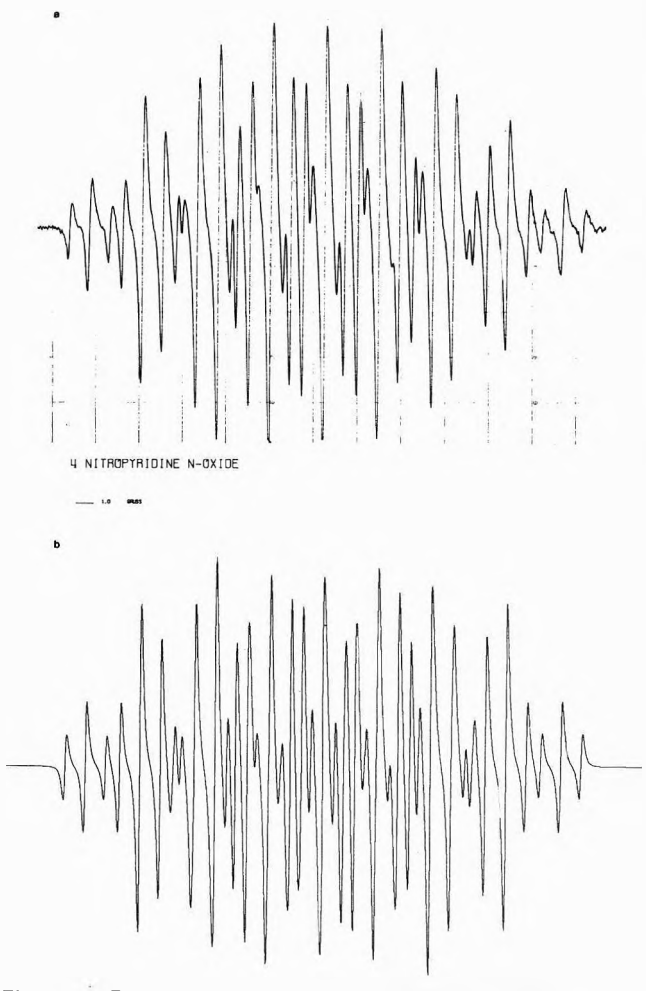

Figure 5. Experimental (a) and simulated (b) spectra for 4-nitropyridine *N*-oxide.

Results and Discussion

Esr Spectra. The esr spectra of 2-nitropyridine and 2- and 3-nitropyridine *N*-oxides were unknown. They have been measured in acetonitrile and are shown in Figures 2–5 together with the spectra of remaining isomers measured by us in the same solvent. The coupling constants for pyridine in liquid ammonia, and pyridine *N*-oxide in dimethylformamide, are taken from the literature.[1,5,36]

The interpretation of the esr spectra by means of a simulation process has led to the determination of the coupling constants for all magnetic nuclei. The assignment of hfs coupling constants to specific nuclei is a quite difficult task in the case of nonsymmetric molecules because the corresponding radicals contain four nonequivalent hydrogens and two nonequivalent nitrogens. It is evident from Tables II and III that both signs and magnitude ratio of spin densities of nitrogen nuclei in each molecule are uniquely predicted by the P, R, and M methods, and the substantial difference in magnitude of measured coupling constants for the two different nitrogens in each molecule seems an encouraging preliminary for the assignments reported in Tables II and III. Moreover, for 4-nitropyridine and 4-nitropyridine *N*-oxide the assignment of the coupling constants of nitrogen nuclei, based on isotope substitu-

TABLE VI: Singlet–Singlet Transition Energy, Oscillator Strength, and Polarization for Electronic Bands of Pyridine, Pyridine *N*-Oxide, and Their Nitro Derivatives

	PPP			MIM			Exptl[a]			
Molecule	ΔE, eV	f	Pol.	ΔE, eV	f	Pol.	ΔE, eV	f	ΔE, eV	f
1	4.895	0.067	y				4.75[b]	0.04 (y)[c]		
	5.366	0.004	z				6.17[b]	0.10[c]		
	7.269	1.043	y				6.82[b]	1.30[c]		
	7.357	1.173	z				6.99[b]			
	8.333	0.002	y							
2	4.903[d]	0.064		4.729	0.09		4.57		4.70	0.08[e]
	4.888	0.204		5.519	0.14		5.28		5.43	0.24[e]
	6.061	0.038								
	6.381	0.562		6.452	0.23		6.07		6.53	0.56[e]
	6.677	0.870		6.681	0.48					
	7.623	0.730								
3	4.674	0.156		4.863	0.08		4.60		4.66	0.11[e]
	4.989	0.118		5.336	0.22		5.04		5.25	0.34[e]
	6.162	0.171								
	6.311	0.578		6.512	0.63		6.05			
	6.821	0.657		6.712	0.10					
	7.603	0.603								
4	4.280	0.136	y	4.504	0.04	y	4.31		4.44	0.03[e]
	4.981	0.116	z	5.888	0.07	z	5.44		5.51	0.22[e]
	6.199	0.223	y	6.005	0.13	y				
	6.274	0.829	z	6.500	0.72	z			6.48	0.24[e]
	6.563	0.055	y							
	7.657	1.112	y							
5	4.028	0.004	y				3.87	0.012 (y)[f]		
	3.969	0.321	z				4.40	0.205[g]		
	5.569	0.453	y				5.72	0.196[g]		
	6.306	0.389	z				6.60	0.246[g]		
	7.387	0.128	z							
	7.647	0.714	z							
6	3.241	0.190		3.088	0.081		3.40	0.013		
	3.974	0.040		4.042	0.183		4.27–4.35	Sh		
	4.843	0.586		4.985	0.374		4.76	0.160		
	5.293	0.212		5.733	0.364		5.90			
	5.936	0.034		6.279	0.469					
	6.526	0.195		7.580	0.011					
7	2.927	0.045		3.447	0.009		3.26	0.012	3.26[h]	
	3.948	0.255		4.282	0.286		4.31	0.13	4.25[h]	
	5.016	0.569		5.434	0.548		4.93	0.21	4.98[h]	
	5.281	0.293		6.043	0.283		5.24	Sh		
	5.724	0.087								
	6.334	0.167		6.393	0.283		>6.20		6.32[h]	
	6.899	0.549		7.503	0.064					
8				3.758	0.001	y				
	3.698	0.649	z	3.881	0.430	z	3.59	0.41		
	3.927	0.038	y							
	5.084	0.248	y	5.191	0.521	y	5.10	0.19		
	5.403	0.051	z	6.299	0.103	z				
	6.180	0.082	z	6.512	0.256	z	>6.20			

[a] In acetonitrile except when otherwise stated. [b] Under vacuum: L. W. Pickett, M. E. Corning, M. Wieder, D. A. Semenow, and J. M. Buckley, *J. Amer. Chem. Soc.*, **75**, 1618 (1958). [c] K. K. Innes, J. P. Birne, and I. G. Ross, *J. Mol. Spectrosc.*, **22**, 125 (1967). [d] The inversion of the first two transitions is justified by means of the analysis of the excited states wave functions, see Table VII. [e] In *n*-hexane. [f] Polarization and Stark effect measurements on the electronic origin of the transition (at 3.87 eV) show that the transition is polarized in the molecular plane along the short axis;[40] the first two calculated transitions are predicted in the inverse order. [g] Reference 6. [h] In *n*-pentane.

tion,[3] is in perfect agreement with our assignments. Nitrogen coupling constants were evaluated from M spin densities using well known relationships given as footnotes in Table III. Since we could not find in the literature a generally accepted relationship between P and R spin densities and coupling constants for the different kinds of nitrogen atoms present in our molecules and we had few experimental data to obtain significant values of the necessary constants through a correlation, we did not calculate nitrogen coupling constants from spin densities obtained by the P and R methods.

In the case of proton nuclei the coupling constants were assigned on the basis of calculated spin densities. The calculated proton coupling constants were obtained by means of the McConnell relationship. When P and R spin densities were used, the constant Q was evaluated through a linear regression procedure on the experimental a_H values. The best Q's are equal to −23.3 and −23.7 G, re-

TABLE VII: Major Contributing (%) Configurations[a] in PPP and MIM Wave Functions of Nitropyridines and Nitropyridine *N*-Oxides for Excited States[b] Experimentally Found According to Our Assignments

	PPP			MIM		
	ΔE, eV	f	Configurations	ΔE, eV	f	Configurations
2	4.903	0.06	$T_2^A(43.5); L_1(28.0); L_2(11.6)$	4.729	0.09	$L_1(83.0); T_3^A(13.2)$
	4.888	0.20	$T_3^A(44.5); L_2(22.5); L_1(8.4)$	5.519	0.14	$T_3^A(57.0); L_2(22.6); L_1(12.5)$
	6.381	0.56	$L_3(66.0); L_4(7.0)$	6.452	0.23	$L_3(31.4); T_2^A(29.7); L_4(19.6)$
3	4.674	0.16	$L_1(57.0); T_3^A(13.2)$	4.863	0.08	$L_1(89.1); T_3^A(8.7)$
	4.989	0.12	$L_2(42.5); L_1(13.6); T_3^A(10.5); T_2^A(9.5)$	5.336	0.22	$T_3^A(58.2); L_2(16.1); T_2^A(12\ 7); L_1(6.1)$
	6.311	0.58	$L_2(26.2); T_3^A(18.5)$	6.512	0.63	$T_2(38.4); L_4(26.4); L_3(21.6); L_2(6.8)$
4	4.280	0.14	$L_1(62.0); T_3^A(22.0)$	4.504	0.04	$L_1(82.1); T_3^A(17.6)$
	4.981	0.12	$L_2(54.0); T_2^A(17.4); L_3(7.3)$	5.888	0.07	$L_2(52.3); T_2^A(38.6); L_3(7.9)$
	6.274	0.83	$L_2(31.2); T_2^A(23.0); L_3(14.5)$	6.500	0.72	$L_2(46.1); T_2^A(32.3); L_3(20.6)$
6	3.241	0.19	$T_4^A(38.8); L_1(24.8)$	3.088	0.09	$L_1(54.0); T_4^A(35.4)$
	3.974	0.04	$L_2(41.8); L_1(16.9)$	4.042	0.18	$L_2(52.1); L_1(32.0)$
	4.843	0.59	$L_2(20.0); T_4^A(15.4); L_3(13.0); L_1(12.0)$	4.985	0.37	$L_2(37.6); T_4^A(36.4); L_3(16.7); L_1(9.2)$
	5.293	0.21	$L_1(23.6); L_3(18.5); T_4^A(15.8); T_3^A(14.6)$	5.733	0.36	$L_3(54.0); T_4^A(15.5); L_4(13.7); T_3^A(11.8)$
7	2.927	0.05	$L_1(48.8); T_4^A(30.3)$	3.447	0.01	$L_1(89.0); T_4^A(9.3)$
	3.948	0.26	$L_2(75.5)$	4.282	0.29	$L_2(96.8)$
	5.016	0.57	$T_4^A(17.5); T_3^A(15.4); L_1(14.0); L_3(11.0)$	5.534	0.55	$L_3(66.0); T_4^A(23.8); L_1(2.8); T_3^A(2.5)$
	5.281	0.29	$T_4^A(26.2); T_3^A(21.3); L_1(17.1)$	6.043	0.28	$L_4(38.1); T_4^A(27.4); T_3^A(25\ 0); L_1(3.6)$
	6.334	0.17	$L_3(52.1); T_2^A(14.0); T_4^A(3.6)$	6.393	0.28	$T_4^A(35.0); L_3(27.7); L_4(24.0)$
8	3.698	0.65	$L_2(57.2); T_4^A(19.3)$	3.881	0.43	$L_2(86.5); T_4^A(13.0)$
	5.084	0.25	$L_3(49.5); T_3^A(15.6)$	5.191	0.52	$L_3(85.5); T_3^A(13.2)$
	6.180	0.08	$L_4(16.4)$	6.512	0.26	$L_4(92.5)$

[a] Configurations with weight less than 10% in both calculations, or with weight less than 1%, have been omitted. [b] L_j for molecules 2, 3, and 4 from ref 2; L_j for molecules 6, 7, and 8 from ref 20.

spectively. The corresponding plots of the proton coupling constants as a function of the spin density on contiguous carbon atom are shown in Figure 6. When M spin densities were used the Q constant was assumed equal to -27 G.[9]

Spin densities and coupling constants for pyridine, nitropyridines, and pyridine *N*-oxide calculated by the INDO method, before and after annihilation of the quartet component, are shown in Table IV. Calculations for nitropyridine *N*-oxides gave unsatisfactory results; for example in the case of 4-nitropyridine *N*-oxide the coupling constants of the two different nitrogens are predicted in reverse order with respect to experimental evidence.[3,37] It is probably due to the fact that too many heteroatoms, and in different bonding situations, are present in these molecules: an *ad hoc* parametrization would be needed, but it would not be justified here owing to the paucity of available data.

For considered pyridines INDO calculations without projection are in fair agreement with experiment. Annihilation of quartet components preserves the correct order of the proton constants, but the absolute values are generally worse.

On the whole the values calculated by the different methods (up to five in some cases) allow the prediction of the coupling constants with confidence, since all the methods agree almost in all cases. The only exceptions are found for the M method; in 3-nitropyridine $a_{H6} > a_{H4}$ according to the M method, while $a_{H4} > a_{H6}$ according to the INDO, P, and R methods; in 2-nitropyridine *N*-oxide $a_{H3} > a_{H6}$ according to the M method, while $a_{H6} > a_{H3}$ according to the P and R methods, and in 3-nitropyridine *N*-oxide $a_{H4} > a_{H6}$ according to the R and P methods, while $a_{H6} > a_{H4}$ according to the M method.

Uv Spectra. We measured visible and uv spectra in acetonitrile for the same six radicals for which esr spectra were taken. The results are shown in Table V together

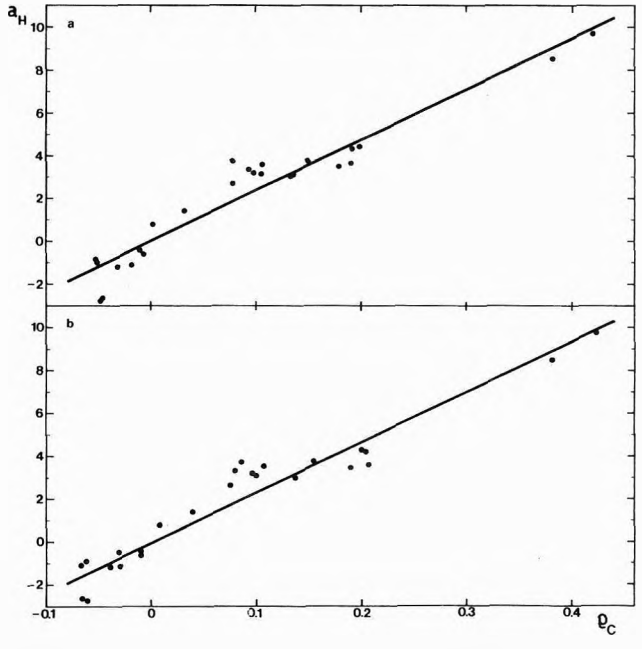

Figure 6. Regression of theoretical spin densities at carbons on observed coupling constants of adjacent protons: a, spin densities calculated by R method: $r = 0.929$, $n = 26$; b, spin densities calculated by P method: $r = 0.932$, $n = 26$.

with transition energies, oscillator strength, and polarizations, calculated by the R method for the same six radicals as well as for pyridine and pyridine *N*-oxide anions, for which no experimental data are available. The experimental data for 3- and 4-nitropyridine anions obtained by metal reduction are also shown for the sake of comparison. The assignment of experimental bands to electronic transitions was made taking into account both calculated

energies and intensities. Unfortunately with the technique used in the present work it is not possible to measure intensities. The agreement for the transition energies is satisfactory but not excellent as may be expected for open shell systems. In all cases, however, the appearance of absorption in the visible region is correctly predicted. The differences in solvents and methods of preparation do not significantly influence the measured spectra (see the last column in Table V).

In Table VI our experimental data (in one or two solvents) for the parent neutral molecules of the six nitro-substituted anions are reported together with the results of PPP and MIM calculations. Experimental data from the literature and our PPP calculations for pyridine and pyridine *N*-oxide are also reported.

For pyridine and pyridine *N*-oxide the interpretation by PPP calculations of the electronic bands in the uv region is correct if the fact is taken into account that this method (without an *ad hoc* parametrization) systematically underestimates the energy of the second transition of azines.[38,39] As a consequence, in the case of pyridine *N*-oxide, owing to the smaller energy difference, the first two transitions are predicted in reverse order. In this case, indeed, polarization measurements show that the first band is polarized in the molecular plane along the short axis.[40] The same situation occurs with 2-nitropyridine and this fact can be confirmed by the configurational analysis of excited states calculated by the PPP method in terms of MIM configurations, as shown in Table VII. For the other molecules shown in the same table, a complete correspondence between PPP and MIM wave functions for excited states can be observed.

On the whole MIM calculations agree better with experiment than PPP calculations as far as transition energies and oscillator strengths are concerned. The data reported in Table VII put into evidence the following points. In general no band can be classified as a pure charge-transfer or locally excited bands, but a mixing of configurations of the two types is always present to a different extent. The lowest energy locally excited configuration Λ_1 (Λ_2 in the case of 4-nitropyridine *N*-oxide) and the lowest energy charge-transfer configuration (T_3^A in nitropyridines and T_4^A in nitropyridine *N*-oxides, respectively) give the major contribution to the first excited state for all molecules.

We have assigned the first band of nitropyridine *N*-oxides to a $\pi^* \leftarrow \pi$ transition on the basis of the values of oscillator strengths (0.013, 0.012, and 0.413 for 2-, 3-, and 4-nitropyridine *N*-oxides, respectively), which are rather high for a $\pi^* \leftarrow$ n transition.[41] The uv spectra of the three isomers recorded in a protic solvent (methanol) show a blue shift for all the bands, as is usual for the $\pi^* \leftarrow \pi$ bands of aromatic *N*-oxides,[6] so that in this case the solvent effect cannot distinguish a $\pi^* \leftarrow \pi$ from a $\pi^* \leftarrow$ n transition.

In conclusion, it may be said that semiempirical methods (for example, the PPP method) with one parametrization can be used for the description of the electronic structure of a series of molecules and radical anions in ground and excited states.

Acknowledgment. The authors are indebted to Dr. G. F. Tantardini for the configurational analysis program.

Supplementary Material Available. Parameters for PPP and MIM calculations will appear following these pages in the microfilm edition of this volume of the journal. Photocopies of the supplementary material from this paper only or microfiche (105 × 148 mm, 20× reduction, negatives) containing all of the supplementary material for the papers in this issue may be obtained from the Journals Department, American Chemical Society, 1155 16th St., N.W., Washington, D. C. 20036. Remit check or money order for $3.00 for photocopy or $2.00 for microfiche, referring to code number JPC-73-2744.

References and Notes

(1) J. Chaudhuri, S. Kume, J. Jagur-Grodzinski, and M. Szwarc, *J. Amer. Chem. Soc.*, **90**, 6421 (1968).
(2) G. Favini, A. Gamba, and I. R. Bellobono, *Spectrochim. Acta, Part A*, **23**, 89 (1967).
(3) M. Itoh, T. Okamoto, and S. Nagakura, *Bull. Chem. Soc. Jap.*, **36**, 1665 (1963).
(4) M. Itoh and S. Nagakura, *Bull. Chem. Soc. Jap.*, **38**, 825 (1965).
(5) T. Kubota, K. Nishikida, H. Miyazaki, K. Iwatani, and Y. Oishi, *J. Amer. Chem. Soc.*, **90**, 5080 (1968).
(6) M. Yamakawa, T. Kubota, and H. Akazawa, *Theoret. Chim. Acta*, **15**, 244 (1969).
(7) S. Kobinata and S. Nagakura, *Theoret. Chim. Acta*, **14**, 415 (1969).
(8) D. M. Hirst, *Theoret. Chim. Acta*, **20**, 292 (1971).
(9) E. G. Janzen and J. W. Happ, *J. Phys. Chem.*, 73, 2335 (1969).
(10) P. T. Cottrell and P. H. Rieger, *Mol. Phys.*, **12**, 149 (1967).
(11) J. A. Pople, D. L. Beveridge, and P. A. Dobosh, *J. Chem. Phys.*, **47**, 2026 (1967).
(12) B. Bak, L. Hansen, and J. R. Rastrup-Andersen, *J. Chem. Phys.*, **22**, 2013 (1954).
(13) D. Ülkü, B. P. Huddle, and J. C. Morrow, *Acta Crystallogr., Sect. B*, **27**, 432 (1971).
(14) J. Trotter, *Acta Crystallogr.*, **12**, 884 (1959).
(15) H. C. Longuet-Higgins and J. A. Pople, *Proc. Phys. Soc., London, Sect. A*, **68**, 591 (1955).
(16) C. C. J. Roothaan, *Rev. Mod. Phys.*, **32**, 179 (1960).
(17) A. D. McLachlan, *Mol. Phys.*, **3**, 233 (1960).
(18) P. H. Rieger and G. K. Fraenkel, *J. Chem. Phys.*, **39**, 609 (1963).
(19) G. Favini and A. Gamba, *Ric. Sci., A*, **6**, 3 (1964).
(20) See paragraph at end of paper regarding supplementary material.
(21) R. Pariser and R. G. Parr, *J. Chem. Phys.*, **21**, 466, 767 (1953).
(22) A. Gamba, V. Malatesta, G. Morosi, and M. Simonetta, *J. Phys. Chem.*, **76**, 3960 (1972).
(23) R. Zahradník and P. Čársky, *J. Phys. Chem.*, **74**, 1235 (1970).
(24) P. A. Dobosh, "CNDO and INDO Molecular Orbital Program," Quantum Chemistry Program Exchange (QCPE), No. 141, Indiana University, Bloomington, Ind.
(25) T. Amos and L. C. Snyder, *J. Chem. Phys.*, **41**, 1773 (1964).
(26) D. L. Beveridge and P. A. Dobosh, *J. Chem. Phys.*, **48**, 5532 (1968).
(27) H. C. Longuet-Higgins and J. N. Murrell, *Proc. Phys. Soc., London, Sect. A*, **68**, 601 (1955).
(28) H. Baba, S. Suzuki, and T. Takemura, *J. Chem. Phys.*, **50**, 2078 (1969).
(29) A. Kirpal and W. Bohm, *Chem. Ber.*, **65**, 680 (1932).
(30) O. von Schickh, A. Binz, and A. Schulz, *Chem. Ber.*, **69**, 2593 (1936).
(31) E. Ochiai, *J. Org. Chem.*, **18**, 534 (1953).
(32) E. V. Brown, *J. Amer. Chem. Soc.*, **79**, 3565 (1957).
(33) E. C. Taylor and J. S. Driscoll, *J. Org. Chem.*, **25**, 1716 (1960).
(34) S. Wawzonek and M. E. Runner, *J. Electrochem. Soc.*, **99**, 457 (1952).
(35) G. Panzone, Thesis, University of Milan, 1969.
(36) C. L. Talcott and R. J. Myers, *Mol. Phys.*, **12**, 549 (1967).
(37) T. Kubota, Y. Oishi, K. Nishikida, and H. Miyazaky, *Bull. Chem. Soc. Jap.*, **43**, 1622 (1970).
(38) G. Favini, I. Vandoni, and M. Simonetta, *Theoret. Chim. Acta*, **3**, 45 (1965).
(39) G. Favini, I. Vandoni, and M. Simonetta, *Theoret. Chim. Acta*, **3**, 418 (1965).
(40) R. M. Hochstrasser and D. A. Wiersma, *J. Chem. Phys.*, **55**, 5339 (1971).
(41) J. N. Murrell, "The Theory of the Electronic Spectra of Organic Molecules," Methuen, London, 1963, p 188.

Reduction of Dyes by Free Radicals in Solution. Correlation between Reaction Rate Constants and Redox Potentials

P. S. Rao[1] and E. Hayon*

Pioneering Research Laboratory, U. S. Army Natick Laboratories, Natick, Massachusetts 01760 *(Received June 11, 1973)*

Publication costs assisted by Natick Laboratories

The reactions of some free radicals (RH·) with a number of organic dyes (D) have been examined in aqueous solutions using the fast-reaction technique of pulse radiolysis. The radicals studied include $\cdot CH_2OH$, $(CH_3)_2\dot{C}OH$, $NH_2\dot{C}HCOO^-$, ·C-OH (C = cytosine), ·TH (TH_2 = dihydrothymine), and $\cdot CH_2^-$ and were produced by reaction of the substrates with OH radicals. The dyes used were Crystal Violet, Safranine T, Phenosafranine, Indigo Di- and Tetrasulfonate, Methylene Blue, Thionine, Indophenol and 2,6-Dichloroindophenol. The electron transfer reaction, RH· + D → R + $\cdot D^-$ + H^+ (k_1), were determined by following the bleaching kinetics of the dyes at the wavelengths where they absorb. The rates were found to increase monotonically with increase in the redox potential E_m of the dyes examined. Similarly the efficiencies (expressed in percentage) of these reactions were obtained and found to be markedly dependent upon the E_m values of the dyes in the range from −0.357 to +0.217 V. These results are discussed and the suggestion made that this correlation represents the dependence upon ΔE_m, the difference in the redox potentials of the donor radical and the acceptor dyes.

Introduction

Organic dyes are an important class of compounds which usually can undergo both oxidative and reductive processes. Various aspects of the photochemistry[2] and radiation chemistry of dyes[3] and the role of dyes in photodynamic action and photosensitization reactions[4] have been reviewed recently. For example, the reaction which leads to the photoreduction of an excited dye molecule by a substrate usually involves an electron or hydrogen atom transfer from the reducing agent to the dye. In these cases, free radicals (or odd valent unstable species) are produced in solution and these can undergo subsequent redox reactions with the dye molecules. This work deals with the nature of these reactions in aqueous solutions.

The fast-reaction technique of pulse radiolysis was used to produce certain free radicals, under conditions such that these radicals were the only species reacting with the various dyes present in solution. From the "bleaching" kinetics of the colored dyes (D) used, it was possible to determine the reaction rate constants of process 1

$$RH\cdot + D \longrightarrow \cdot D^- + R + H^+ \quad (1)$$

$$\cdot D^- + H^+ \text{ (or } H_2O) \longrightarrow \cdot DH \text{ (+ } OH^-) \quad (2)$$

where RH· is the free radical and ·DH and $\cdot D^-$ the semiquinone radical and radical anion of the dye (D). The k_1 values obtained have been correlated with the redox properties of the various dyes studied.

Experimental Section

The pulse radiolysis set-up used has been described elsewhere.[5,6] Single pulses of 2.3-MeV electrons and ~30-nsec durations were used. Dosimetry was carried out[5] using KCNS solutions.

Fresh solutions were prepared just previous to use and considerable care was taken to minimize the exposure to light of the dyes in aqueous solutions. A synchronized shutter was used (open for ~2–5 msec) to reduce exposure of the solution to the monitoring light from the 450-W xenon lamp and, in addition, appropriate cut-off filters were employed.

Most of the dyes used were supplied by J. T. Baker Co. and the rest from Eastman Chemicals. Glycine was obtained from Calbiochem and the pyrimidines from Cyclochemicals. Solutions were buffered using perchloric acid, potassium hydroxide, and 1 mM phosphates or tetraborate.

The redox potentials of the dyes were obtained from the literature.[7] E_m values refer to the redox potential at the stated pH used.

Results and Discussion

The radiation chemistry of water produces

$$H_2O \rightsquigarrow e_{aq}^- \text{ (2.8), OH (2.8), H (0.55), } H_2O_2 \text{ (0.71), } H_2 \text{ (0.45)}$$

where the values in parentheses are the G values (yield produced per 100 eV of energy absorbed by the water). The experiments were carried out in N_2O-saturated aqueous solutions to convert the hydrated electrons into OH radicals

$$e_{aq}^- + N_2O \longrightarrow OH + N_2 + OH^- \quad (3)$$

where $k_3 = 8.0 \times 10^9\ M^{-1}\ sec^{-1}$ (ref 8). The concentrations of the dyes and substrates were also kept low such that >90% of the e_{aq}^- reacted according to reaction 3.

Organic dyes are known to polymerize in aqueous solution with increase in the concentration of the dye (see, *e.g.*, ref 9). The radiation dose was therefore kept very low, ~70–200 rads/pulse, in order not to exceed the concentration of the dyes above 25 μM, and at the same time ascertain complete reaction between the free radicals produced and the dyes. These low doses also reduced the extent of radical–radical reaction under these experimental conditions to <5%.

Five organic free radicals were studied in detail, and were produced from the reaction of the substrates with OH radicals

$$OH + CH_3OH \longrightarrow \cdot CH_2OH + H_2O \quad (4)$$

TABLE I: Reaction Rate Constants and Efficiencies (%) of One-Electron Reduction of Dyes by Free Radicals in Aqueous Solution

				Wavelength monitored,	Free radical donors[e]													
					·CH_2OH			$(CH_3)_2COH$			NH_2CHCOO^-			Cytosine ·C–OH			·TH[f]		
No.	Dyes[a]	E_m, V[b]	pH	nm	k	%	R	k	%	R	k	%	R	k	%	R	k	%	R
1.	Crystal Violet	−0.357	7	525		4	H	2.3	84	H	1.2	56	F		10	H		14	
2.	Safranine T	−0.289	7	520		12	H	2.8	86	H	1.6	60	F	1.2	17	H	0.9	22	H
3.	Phenosafranine	−0.254	7	520	1.2	22	H	3.2	82	H	1.9	66	F	*g*			1.2	57	H
4.	Indigo Disulfonate	−0.199	9	610	1.9	62	H	4.0	88	H	2.8	71	F	2.0	55	H	*g*		
4′.	Indigo Disulfonate	−0.125	7	610	2.0	75	H	4.0	88	H				1.9	81	H	2.3	77	H
5.	Indigo Tetrasulfonate	−0.046	7	610	3.0	80	H	4.2	89	H	2.6	78	F	2.0	84	H	2.7	78	H
6.	Methylene Blue[c]	+0.011	7	580	3.4	91	H	4.4	91	H	3.7	86		2.3	85	H	2.7	81	H
7.	Thionine[d]	+0.031	8	600	2.6	86	H	4.2	88	H	3.2	85	F	2.7	84		*g*		
8.	Indophenol	+0.083	9	610	3.1	92	H	4.0	86	H	*g*			2.2	88	H	*g*		
9.	2,6-Dichloroindophenol	+0.217	7	600	3.2	94	H	4.4	88	H	3.6	87		*g*			3.4	82	H

[a] Unless stated otherwise, 25 μM concentration of dyes was used. [b] From ref 7, at 25°. [c] 10 and 20 μM and doses of 70–150 rads/pulse. [d] 20 μM. [e] Rate constants, k, given in 10^{-9} M^{-1} sec^{-1} units, and reversibility, R, of the dyes are indicated as F (fully reversible) and H (half-reversible, *i.e.* 50% of the dye is regenerated). [f] Produced from reaction of OH radicals with dihydrothymine. [g] Thermal reaction between substrate and the dye apparently occurs.

$$OH + (CH_3)_2CHOH \longrightarrow (CH_3)_2\dot{C}OH + H_2O \quad (5)$$

$$OH + \overset{+}{N}H_3CH_2COO^- \longrightarrow \overset{+}{N}H_3\dot{C}HCOO^- + H_2O \quad (6)$$

$$\overset{+}{N}H_3\dot{C}HCOO^- \underset{pK_a < 1.0}{\rightleftharpoons} NH_2\dot{C}HCOO^- + H^+ \quad (7a)$$

$$NH_2\dot{C}HCOOH \underset{pK_a \sim 6.5}{\rightleftharpoons} NH_2\dot{C}HCOO^- + H^+ \quad (7b)$$

$$OH + C \longrightarrow \cdot C\text{-}OH \quad (8)$$

$$OH + TH_2 \longrightarrow \cdot TH + H_2O \quad (9)$$

where C = cytosine and TH_2 = dihydrothymine. These radicals had previously been studied: ·CH_2OH,[5] $(CH_3)_2COH$,[5] NH_2CHCOO^-,[10] ·C–OH,[11] and ·TH.[11]

The rates of reaction 1 were determined by following the "bleaching" or "disappearance" kinetics of the dyes at the appropriate wavelengths where they absorb. From the pseudo-first-order kinetics observed, dependent upon [dye], the second-order k_1 rates were calculated. These values for reaction of the free radicals with various dyes (triphenylmethane, azine, thiazine, and quinoneimine dyes) are given in Table I. These can be seen to be in the range 8.0×10^8–4.4×10^9 M^{-1} sec^{-1}.

The log k_1 values have been plotted for each radical as a function of the redox potential, E_m, of the dyes, and can be seen in Figure 1. In addition to the five radicals mentioned above, the rates of reaction of ·CO_2^- radials with various dyes, previously determined and summarized in ref 3, are plotted as a function of the E_m of the dyes in Figure 1. To these values have been added our own determined rates for these and some other dyes.

In all these cases, the log k_1 *vs.* E_m plots start levelling off at the higher redox potentials of the dyes, with k_1 values close to the expected near-diffusion-controlled rates. Similar results and dependence of the rates of electron transfer reactions from free radicals to a large number of quinones upon the redox potentials of the quinones have recently been observed.[12]

The efficiency of reaction 1, based on the extent (percentage) of bleaching of the dyes by the various radicals, was also determined. This was obtained based on 100% efficiency for the bleaching of the dyes on reaction with e_{aq}^- or ·CO_2^- radicals

$$e_{aq}^- + D \longrightarrow \cdot D^- \quad (10)$$

$$OH + HCOO^- \longrightarrow \cdot CO_2^- + H_2O \quad (11)$$

$$\cdot CO_2^- + D \longrightarrow \cdot D^- + CO_2 \quad (12)$$

with $k_{10} \sim 1$–5×10^{10} M^{-1} sec^{-1} and $k_{12} \sim 1.6$–5.0×10^9 M^{-1} sec^{-1}. These $-\Delta$OD of the dyes based on reactions 10 or 11, equivalent to 100% bleaching efficiency, were obtained immediately before the experiment under otherwise identical experimental conditions of dosimetry, pH, wavelength, and slit widths on the double monochromators. The percentage efficiencies for the transfer of an electron from the free radicals to the dyes are given in Table I. For each radical a marked dependence of the percentage efficiency for the reduction of the dyes can be observed on going from one dye to the other. These approached 100% with dyes having $E_m > 0.01$ V.

Following the bleaching of the dyes from the reaction with free radicals, the degree of reversibility of the dye was monitored on the oscilloscope about 15 sec after the electron pulse. With all the free radicals examined, except with NH_2CHCOO^-, ~50% of the concentration of the bleached dye was regenerated. This 50% reversibility is consistent with a disproportionation reaction of the dye

TABLE II: Rate Constants, k, for the Reaction of Organic Radicals with Dyes in Aqueous Solution

Dyes, D[a]	Donor radical, RH·	pH	k(RH· + D), M^{-1} sec^{-1} [b]
Fluorescein (500)	$CH_3\dot{C}HOH$	10.8	4.5×10^8
	Thymine (·T–OH)	10.8	5.7×10^8
	Uracil (·U–OH)	10.8	6.0×10^8
	Cytosine[d]	9.2	1.5×10^9
Crystal Violet (520)	$\cdot CO_2^-$	7.0	1.5×10^9 (1.7×10^9)
	Thymine (·T–OH)	10.8	1.3×10^9
	Uracil (·U–OH)	10.8	1.5×10^9 (1.7×10^9)
	Thymine[d]	5.4	2.4×10^9
Indigo Disulfonate (610)	$\cdot CO_2^-$	7.0	2.0×10^9 (2.1×10^9)
	Histidine[c]	7.0	1.1×10^9 (1.3×10^9)
	Riboflavin (·RF$^-$)	10.8	5.0×10^8
Toluidine Blue (610)	Riboflavin (·RF$^-$)	10.8	6.0×10^8
Methylene Blue (660, 580)	Riboflavin (·RF$^-$)	10.8	6.2×10^8
	Lipoate (·RSSR$^-$)	7.5	1.0×10^9
Indophenol (610)	$\cdot CO_2^-$	9.0	2.8×10^9 (2.7×10^9)
	Thymine (·T–OH)	10.8	2.0×10^9
	Histidine[c]	9.0	1.6×10^9 (1.0×10^9)
2,6-Dichloroindophenol (600)	$\cdot CO_2^-$	7.0	3.5×10^9 (3.6×10^9)
	Riboflavin (·RF$^-$)	10.8	6.2×10^8
	Histidine[c]	7.0	1.1×10^9 (1.1×10^9)

[a] Values in parentheses are wavelengths monitored (in nm). [b] Rates determined by following "bleaching" kinetics of the dye at appropriate wavelengths; values in parentheses were determined by following formation kinetics of the reduced dye semiquinone radical, usually at 400 nm. [c] OH adduct. [d] e_{aq}^- adduct.

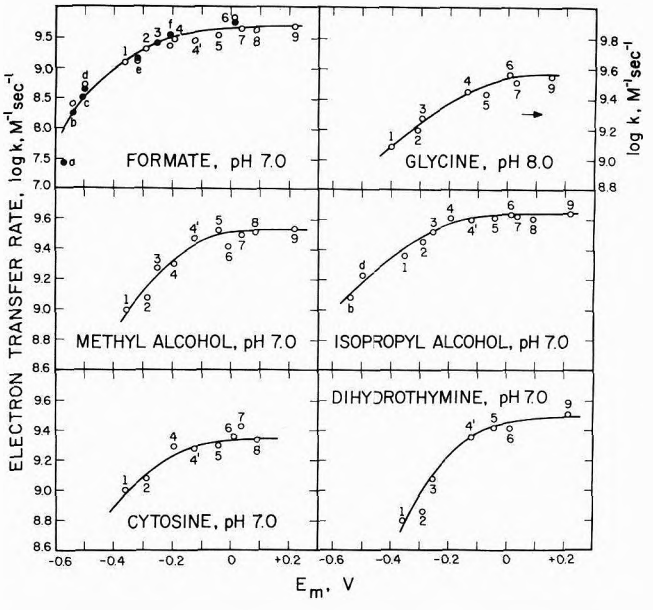

Figure 1. Dependence of log k_1, the rate of electron transfer, from free radicals to various dyes in aqueous solutions as a function of the redox potential, E_m, of the dyes. Donor radicals used are $\cdot CO_2^-$, $NH_2\dot{C}HCOO^-$, $\cdot CH_2OH$, $(CH_3)_2\dot{C}OH$, ·C–OH, and ·TH. The dyes used corresponding to the numbers are given in Table I. In addition, the letters are a, Fluorescein; b, Rhodamine B; c, Acriflavin; d, Eosin Y; e, NAD^+; and f, Riboflavin. The data represented by ● were taken from ref 3, and O symbols were determined in this work. Total dose ~200 rads/pulse, corresponding to a [radical] = 1.2 μM.

semiquinone radical (or radical anion)

$$\cdot DH + \cdot DH \longrightarrow D + DH_2 \qquad (13)$$

where DH_2 is the leuco dye. Almost complete reversibility was observed from reaction of the dyes with the $NH_2\dot{C}HCOO^-$ radical. These results are not easy to explain and would appear to indicate a reduction of the substrate by the dye semiquinone radical. Alternatively, dehydroglycine may be produced from the reaction of $NH_2\dot{C}HCOO^-$ with the dyes, and this unstable product could be reoxidized either by reaction with ·DH or with DH_2.

The rate constants for the reaction of a number of organic free radicals with some other dyes in aqueous solutions have been determined in the course of this work. These rates are presented in Table II. Most of these rates are in general agreement with the postulate that electron transfer rates increase with increase in the redox potential $\Delta E = E_D - E_{RH\cdot}$. The somewhat lower observed rate k_1 for the riboflavin radical ·RF$^-$ cannot be explained at present.

Conclusions

The above results show a strong dependence of the electron transfer reaction from free radicals, to a number of organic dyes or acceptors, upon the redox potential of the acceptors. The potential ranged from E_m values of −0.357 to +0.217 V at pH 7.0. This dependence was observed based on both the efficiencies and the rates of the electron transfer processes. While the results here have been correlated on the basis of the redox potential of the acceptor only, it is clear that such a dependence should be based on the difference between the redox potentials of the donor radical and the acceptor. Work is currently in progress[13] to determine the redox potentials of these donor free radicals in aqueous solution.

References and Notes

(1) Permanent address, Radiation Chemistry Section, C.S.M.C.R.I., Bhavnagar, India.
(2) H. Meier in "The Chemistry of Synthetic Dyes," Vol. 4, K. Venkataraman, Ed., Academic Press, New York, N. Y., 1971, p 389.
(3) L. I. Grossweiner, *Radiat. Res. Rev.*, **2**, 345 (1970).
(4) J. D. Spikes and R. Livingston, *Advan. Radiat. Biol.*, **3**, 29 (1969); A. A. Lamola, *Mol. Photochem.*, **4**, 107 (1972); L. I. Grossweiner and A. G. Kepka, *Photochem. Photobiol.*, **16**, 305 (1972).

(5) M. Simic, P. Neta, and E. Hayon, *J. Phys. Chem.*, **73**, 3794 (1969).
(6) J. P. Keene, E. D. Black, and E. Hayon, *Rev. Sci. Instrum.*, **40**, 1199 (1969).
(7) "Handbook of Biochemistry," Chemical Rubber Publishing Co., Cleveland, Ohio, 1970, p J-33; "Techniques of Chemistry," Vol. 1, Part II A, A. Weissberger and B. W. Rossiter, Ed., Wiley-Interscience, New York, N. Y., 1971, p 55; W. M. Clark, "Oxidation Reduction Potentials of Organic Systems," Williams and Wilkins, Baltimore, Md., 1960.
(8) M. Anbar and P. Neta, *Int. J. Appl. Radiat. Isotopes*, **18**, 493 (1967).
(9) L. Michaelis and S. Granick, *J. Amer. Chem. Soc.*, **67**, 1212 (1945); L. Michaelis, *Cold Spring Harbor Symp. Quant. Biol.*, **12**, 131 (1947).
(10) P. Neta, M. Simic, and E. Hayon, *J. Phys. Chem.*, **74**, 1214 (1970); **76**, 3507 (1972).
(11) E. Hayon and M. Simic, *J. Amer. Chem. Soc.*, **95**, 1029 (1973).
(12) P. S. Rao and E. Hayon, *Nature (London)*, **243**, 334 (1973).
(13) P. S. Rao and E. Hayon, *J. Amer. Chem. Soc.*, submitted for publication.

Vapor-Phase Charge-Transfer Complexes. IX. Contact Charge-Transfer Spectra for Volatile Aliphatic Hydrocarbon–Iodine Systems

S. N. Bhat, M. Tamres* and M. S. Rahaman

Department of Chemistry, University of Michigan, Ann Arbor, Michigan 48104 *(Received May 21, 1973)*

Publication costs assisted by the National Science Foundation

Spectra in the ultraviolet region of mixtures of iodine with O_2, N_2, methane, ethane, propane, *n*-butane, *n*-pentane, and neopentane were studied in the vapor phase. This extends the study of contact charge-transfer bands reported previously for mixtures of iodine with higher molecular weight saturated hydrocarbons. The CCT bands were characterized by subtracting from the total absorbance the contributions of the hydrocarbon spectrum and the maximally pressurized iodine spectrum.

Introduction

In a previous publication,[1] contact charge-transfer (CCT) bands in the vapor phase for mixtures of molecular iodine and several saturated hydrocarbons that are liquid at room temperature were reported. These were compared to similar spectra obtained in solution. In both phases, iodine shows an enhanced absorption with an extended tail in the ultraviolet region. The actual characterization of the CCT bands, in both phases, is dependent on the choice of the reference system for the "free" iodine contribution to the total absorbance.[1,2a]

The present study extends the observations on the CCT bands to mixtures of iodine with the more volatile saturated hydrocarbons from *n*-pentane down to methane, and also with N_2 and O_2 gases. The overall results support the view that the reference for "free" iodine in the vapor phase should be its maximally pressurized spectrum (called to our attention by Mulliken[2b]).

Experimental Section

The spectrophotometric measurements were made with a Cary 14 spectrophotometer using procedures described previously.[1] All experiments were run at least in duplicate. The results were considered reproducible when the absorbances matched to ~0.01 unit in the wavelength region down to 210 nm, and to ~0.02 unit at still lower wavelengths.

The desired concentration of iodine was obtained by weighing out a small quantity of iodine in a specially designed break-seal tube[1] which was then attached to an absorbance cell of approximately known volume. The actual concentration of iodine was determined spectrophotometrically from its visible absorption spectrum.[3]

The vapors and gases were introduced into the absorbance cell through a vacuum line. One end of the cell was attached to a source of the purified vapor or gas and the other end to the manifold. The cell could be isolated at both ends by closing Teflon stopcocks. The line was evacuated (10^{-4} mm) prior to introducing the sample. The vapor or gas was allowed to pass through the cell into the manifold until a desired pressure at the recorded room temperature was reached, at which point the stopcock to the source was closed. The pressure in the cell and manifold was equilibrated, and the cell isolated from the manifold by closing the stopcock. The pressure was determined by measuring the height of the meniscus levels of a mercury manometer in the vacuum line using a Wild cathetometer (readings to about ±0.02 mm). A low-temperature trap (above the boiling point of the vapor or gas) placed between the cell and the manifold prevented mercury vapor from entering the cell.

To remove the cell from the vacuum line, the hydrocarbon vapor was frozen at liquid N_2 temperature in a side arm of the cell, and the cell was sealed off at constrictions a short distance from the Teflon stopcocks. The pressure of the hydrocarbon vapor was corrected for the small change in volume due to sealing. This calculation was based on estimating the volume of the sections of tubing from the sealed points to the Teflon stopcocks from their measured lengths and diameters, and comparing its magnitude to the actual cell volume after sealing which was determined at the end of the experiment by filling the cell

with a measured quantity of water. Methane at liquid N_2 temperature has an appreciable vapor pressure (~10 mm), and this was taken into account in the correction. With N_2 or O_2 in the cell, sealing was accomplished without condensation, and no pressure correction for volume change was necessary.

The source and purification of iodine have been described.[4] All the hydrocarbons were from J. T. Baker Co. and, except for methane which was ultrapure grade, the hydrocarbons were purified in the standard way by bubbling the vapor slowly through a train of three concentrated H_2SO_4 baths and condensing the sample into a trap. The trap was connected *via* a standard tapered joint and Teflon stopcock to a U-tube type storage bulb. The other end of the U-tube, also with a Teflon stopcock, was sealed to the absorbance cell (which, in turn, was sealed to the vacuum line). The contents of the trap were transferred to the storage bulb, and air was removed through successive freezing of the sample with liquid nitrogen and pumping. The very low absorbance at wavelengths below 210 nm was used as the criterion for the purity of the vapors and gases.

Results

The vapor-phase spectrum of iodine alone and in the presence of nitrogen, oxygen, methane, ethane, propane, *n*-butane, neopentane, and *n*-pentane were recorded at several temperatures. The data for *n*-butane–iodine shown in Figure 1 are typical of the results. Data for all the hydrocarbon–iodine systems at the single temperature of 110° are shown in Figure 2. Since the iodine concentration in the different mixtures varied by several per cent, the absorption curves were all adjusted to the same iodine concentration of 9.03×10^{-5} *M* by assuming a linear dependence of absorption with iodine concentration.[1] The concentration of the hydrocarbon vapors (as well as the gases) were calculated using the ideal gas law and all were within 1% of 3.50×10^{-2} *M*. The curves in Figure 2 have been corrected for the small absorption of the free hydrocarbons. For the purpose of comparison, the earlier results with the higher molecular weight hydrocarbons, which were studied at the same hydrocarbon pressure, are included in Figure 2.

It is apparent that mixtures of iodine and hydrocarbons produce an enhanced absorbance in the ultraviolet region, and that this enhancement is progressively smaller the lower the molecular weight of the hydrocarbon. (The curve for propane–I_2, not shown in Figure 2, appears to lie between that for ethane–I_2 and *n*-butane–I_2, but the differences here begin to approach the experimental limits). With methane, the lightest member of the series, the absorbance observed with an iodine mixture appears no different from that for N_2–I_2 or O_2–I_2.

Again, as found in the earlier study,[1] the increase in absorbance with temperature for *n*-butane–I_2 in Figure 1 matches that of the temperature broadening of iodine alone, within experimental limits. Thus, for this limited temperature range, there is no apparent temperature dependence of the CCT band.[1]

Discussion

The combined results of the present and previous study give a clearer indication as to the choice of a reference system for "free" iodine in order to characterize the CCT bands. Since at comparable pressure (~1 atm) and temperature, such diverse gases as He, N_2, O_2, and CH_4, with quite different ionization potentials and polarizabilities, have about the same effect on the iodine spectrum suggests that curve 2 in Figure 2 should be the reference system for the "free" iodine absorption.[2b] The similar effect of the gases is attributed to molecular collisions which result in a broadening of the vibrational and rotational structure of the V ← N iodine transition at 182 nm to that of a smooth continuum. Further, it was shown in the previous study that, for a fixed temperature and iodine concentration, the absorbance is directly proportional to the alkane concentration. Extrapolation of the absorbance to zero alkane concentration over a range of wavelengths gave a curve which more closely corresponded to that observed for the He–I_2 system than any other, within experimental limits.

The curves in Figure 2 have already been corrected for the free hydrocarbon absorption. Therefore, subtracting curve 2 from all the other absorption curves in Figure 2, gives the contribution due only to CCT bands. These are shown in Figure 3. It is evident that no band maxima are observed, although in one or two cases there is indication of the presence of an inflection point.

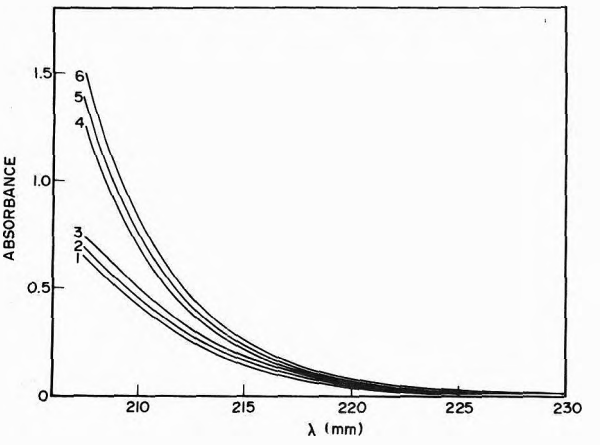

Figure 1. Temperature dependence of I_2 and of *n*-butane–I_2 in a 50.0-cm cell: $[I_2] = 9.03 \times 10^{-5}$ *M* at (1) 110°, (2) 120°, (3) 130°; and $[n\text{-butane}] = 3.50 \times 10^{-2}$ *M* + I_2 at (4) 110°, (5) 120°, (6) 130°.

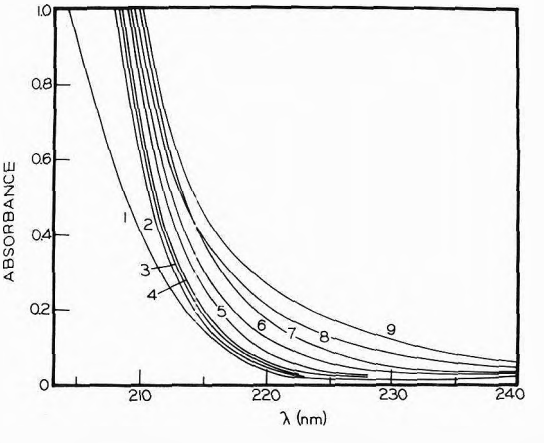

Figure 2. Ultraviolet spectra of iodine at 110° in the vapor phase: curves 1–5 for I_2 at 9.03×10^{-5} *M* in a 50.0-cm cell; curves 6–9 for I_2 at 6.50×10^{-5} *M* in a 75.0-cm cell; all gases and vapors are at 3.50×10^{-2} *M*; (1) no added gas. (2) N_2, O_2, or CH_4, (3) ethane, (4) *n*-butane, (5) *n*-pentane or neopentane, (6) *n*-hexane, (7) *n*-heptane, (8) cyclohexane, (9) methylcyclohexane. Curves 3–9 corrected for small alkane absorption.

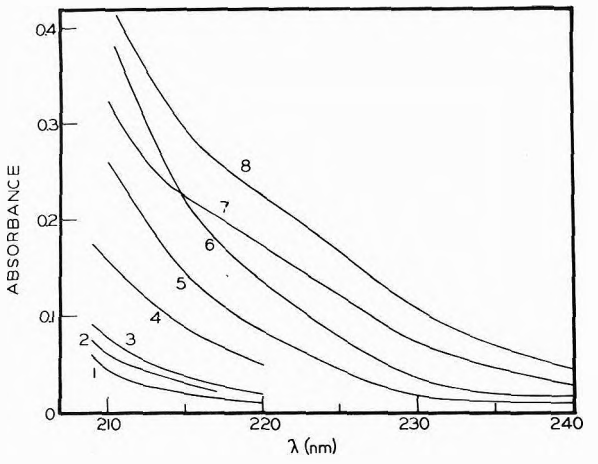

Figure 3. CCT spectra of alkane–iodine systems at 110° in the vapor phase: curves 1–4 for I_2 at 9.03×10^{-5} *M* in a 50.0-cm cell; curves 5–8 for I_2 at 6.50×10^{-5} *M* in a 75.0-cm cell; all alkanes at 3.50×10^{-2} *M*; (1) ethane–I_2, (2) propane–I_2, (3) *n*-butane–I_2, (4) *n*-pentane–I_2 or neopentane–I_2, (5) *n*-hexane–I_2, (6) cyclohexane–I_2, (7) *n*-heptane–I_2, (8) methylcyclohexane–I_2.

It has been pointed out[1] that several reports of CCT band maxima for saturated hydrocarbon–iodine systems in *solution* must be considered in error because of the choice of the reference solvent to subtract the "free" iodine contribution. Only in the study of Julien and Person,[5] who also reported distinct maxima for the CCT bands of several alkane–iodine systems, was an attempt made to correct, although qualitatively, for a CCT contribution from the reference solvent–iodine system.

Several factors may account for the trend in the CCT bands shown in Figure 3. Theory predicts that, in the absence of mixing of the CCT state with nearby excited states of donor or acceptor, the transition energy to the CCT state is approximated by the equation[1,6]

$$h\nu_{CCT} \simeq I_D^V - E_A^V - e^2/d_{12} \qquad (1)$$

where I_D^V is the vertical ionization potential of the donor, E_A^V is the vertical electron affinity of the acceptor, and e^2/d_{12} is the coulombic energy of attraction of D^+ and A^- at the intermolecular distance d_{12}.

It would be expected that d_{12} is the same for all the saturated hydrocarbon–iodine systems, being somewhat larger than the sum of the van der Waals radii for a methyl group and an iodine atom.[1,7] Thus, toward the common acceptor, iodine, the appearance of the CCT bands should correlate with the ionization potentials of the saturated hydrocarbons. As observed in Figure 3, the CCT band appears at a longer wavelength with increasing molecular weight (and decreasing ionization potential[8]) of the alkane. Equation 1 further predicts that the charge-transfer band for a saturated hydrocarbon–*atomic* halogen system should be appreciably red-shifted compared to that for the corresponding saturated hydrocarbon–*molecular* halogen system because the electron affinity of the atom is greater than that of the corresponding molecule. This has been found to be the case both in solution[9,10] and in the vapor phase.[11] Distinct CCT band maxima have been observed for the ~ ted hydrocarbons with both I and Br atoms. It is i~ ~sting that the band maxima for the halogen atom ~ystems are red-shifted in going from vapor to solution,[11] which is consistent with the solvent effect generally observed for weak complexes.[2a]

Another consideration pertinent to Figure 3 is the molar absorptivity, ϵ, of the contact pair. The concentration of contacts, which can be calculated from collision theory,[1] should be the same for all the saturated hydrocarbon–iodine systems at the same conditions, thereby giving the same "collision" equilibrium constant, *K*. The regular increase in absorbance in Figure 3, as the alkane molecular weight increases, corresponds to an increase in the $K\epsilon$ product.[1] Thus, ϵ (which is related to transition probability) may be increasing systematically with increasing polarizability of the alkane.

The CCT bands for the systems in Figure 3 were not studied much below 210 nm because the steep rise in absorbance accompanied by a rapidly increasing slit width made quantitative measurement doubtful. Without data on the CCT band maxima, no comparison can be made with the positions of the intense excited state of iodine at 182 nm and the intense excited states of the alkanes at still lower wavelength. Interaction of the CCT band with a nearby intense excited state band cannot be entirely discounted. Borrowing of intensity by the CCT band through such an interaction might contribute to the sequence observed in Figure 3.

For interactions as weak as those of contact pairs, there should be essentially no preferred orientation of the electron donor and acceptor, and the various geometries of the contact pair should be nearly equally probable.[12] However, the different orientations should have different transition probabilities.[13] The observed CCT band is then a composite due to the contributions from all orientations. Experiments on I_2 with the open-chain *n*-pentane and the ball-like neopentane, both of which have almost identical ionization potentials,[8] were run to see the effect of geometry of the pentane on the CCT band. No difference in their CCT bands was observed, within experimental limits.

Acknowledgment. This research was supported by the National Science Foundation through Grant No. GP-9216.

References and Notes

(1) M. Tamres and J. Grundnes, *J. Amer. Chem. Soc.*, **93**, 801 (1971).
(2) (a) M. Tamres in "Molecular Complexes," R. Foster, Ed., Paul Elek Ltd., London, 1973; (b) p 96.
(3) M. Tamres and S. N. Bhat, *J. Phys. Chem.*, **75**, 1057 (1971).
(4) M. Brandon, M. Tamres, and S. Searles, *J. Amer. Chem. Soc.*, **82**, 2129 (1960).
(5) L. M. Julien and W. B. Person, *J. Phys. Chem.*, **72**, 3059 (1968).
(6) R. S. Mulliken and W. B. Person, "Molecular Complexes," Wiley, New York, N. Y., 1969.
(7) R. S. Mulliken, *Recl. Trav. Chim. Pays-Bas*, **75**, 845 (1965).
(8) K. Watanabe, T. Nakayama, and J. Mottl, *J. Quant. Spectrosc. Radiat. Transfer*, **2**, 369 (1962).
(9) R. E. Bühler, *Radiat. Res. Rev.*, **4**, 233 (1972).
(10) R. E. Bühler, *J. Phys. Chem.*, **76**, 3220 (1972).
(11) V. A. Brosseau, J. R. Basila, J. F. Smalley, and R. L. Strong, *J. Amer. Chem. Soc.*, **94**, 716 (1972).
(12) O. K. Rice, *Int. J. Quantum Chem., Symp.*, **No. 2**, 219 (1968).
(13) L. E. Orgel and R. S. Mulliken, *J. Amer. Chem. Soc.*, **79**, 4839 (1957).

Molecular Weight Dependence of the Chlorine-35 Nuclear Magnetic Resonance Line Width in Polypeptides[1a]

David E. Carlstrom,[1b] Wilmer G. Miller,* and Robert G. Bryant

Department of Chemistry, University of Minnesota, Minneapolis, Minnesota 55455 *(Received July 3, 1973)*

Publication costs assisted by the U. S. Public Health Service

A random copolymer of glutamic acid and a small amount of cysteine was prepared and fractionated according to molecular weight by gel permeation chromatography. The ^{35}Cl nmr line width of the mercurated copolymer in 0.5 *M* NaCl was measured as a function of molecular weight both in the random coil and the α-helical conformations. The line width of the polymer-bound ^{35}Cl was shown to be controlled by rotational motion, and not by chemical exchange. In the random coil form the polymer ^{35}Cl line width was $3.5 \pm 0.5 \times 10^5$ Hz, and was independent of molecular weight except for very small chains. The ^{35}Cl line width could be approximately accounted for in terms of the motion of a monomeric unit plus internal rotation of the side chain-appended label. The ^{35}Cl line widths were found to be independent of the conformational state of the polymer. Thus the observed correlation times are not consistent with that expected for a rigid rod with two internal independent rotations. This discrepancy is discussed in terms of helix flexibility and of coupled internal rotation. We conclude that because of rapid internal motion the halide relaxes independently of the much slower motion of the rod to which it is attached. The implications of these results on the interpretation of halide probe experiments on biological macromolecules is discussed.

Introduction

Nuclear magnetic resonance spectroscopy has been a useful method for the study of macromolecules of biological interest under a variety of conditions.[2,3] In addition to structural information the nmr experiment may provide information about the time scales for various events such as chemical exchange, rotational diffusion, and the motion of local components with respect to the whole macromolecule.[4] The development of the quadrupole relaxation probe has provided a large gain in sensitivity as well as an almost equal gain in specificity when the spectroscopy is done in conjunction with carefully controlled chemistry.[5] Specific sites of a macromolecule may be probed using rather low macromolecule concentrations. One of these probes, the chloride ion probe, has been widely applied.[5-7] Interpretation of the data has been complicated by lack of explicit knowledge concerning the relative importance of chemical exchange and rotational diffusion in determining the correlation function for the nuclear electric quadrupole interaction which dominates the nuclear relaxation. It is generally considered that the relaxation is dominated by rotational diffusion. However, the rotational correlation times deduced from experiment are uniformly shorter than that expected for the rigid macromolecules.[5-9] The treatment of Wallach[8] for macromolecular motion with internal rotation has been used to interpret these results. Since most proteins have rotational correlation times of 10^{-8}–10^{-7} sec, and most probes have at least one or two bonds about which an internal rotation might occur, it is always possible to rationalize the experimental values in terms of the Wallach treatment of the internal rotation.

In this communication the molecular weight dependence of the ^{35}Cl line width is reported for a series of glutamic acid polymers containing a small amount of cysteine. The ^{35}Cl line widths were determined with the polypeptide as a random coil and as a helix. By this approach the rotational relaxation of the helical macromolecule can be systematically varied, while the extent of internal motion of the probe remains independent of molecular weight. In addition, the ^{35}Cl line width exhibited by the disordered random coil may be directly compared with the corresponding helical macromolecule, while variation in temperature and chloride ion concentration allows the importance of exchange relative to rotational motion to be assessed.

Theory

It is efficient to review the basic theory of the halide probe experiment. The chlorine nucleus has a spin of 3/2 and a sizable nuclear electric quadrupole moment. In most cases quadrupole nuclei relax mainly by the interaction between the electric quadrupole moment and the electric field gradients at the nucleus. As intermolecular contributions to local electrical field gradients are very weak, only intramolecular motions contribute to the relaxation. If the electric field gradient tensor is axially symmetric, which is a fairly good approximation when the chloride nucleus participates in a covalent bond, the reciprocal of the nuclear relaxation time, or line width $\Delta\nu$, is given in the limit of extreme motional narrowing by

$$\Delta\nu = (1/\pi T_1) = (1/\pi T_2) = (2\pi/5)(e^2qQ)^2\tau_c \qquad (1)$$

where q is the electric field gradient at the nucleus of quadrupolar moment Q, and τ_c is the correlation time for the reorientation of the electric field gradient with respect to the direction of the applied magnetic field. If the quadrupole nuclei exist in two kinds of sites or environments with no exchange of nuclei between the sites, the observed nmr signal would be a superposition of two signals, each characterized by a separate line width given by eq 1. In a typical experiment the halide-labeled macromolecule is placed in a solution containing halide ions. Although there is a large difference in line width of the halide in the two environments, only a composite line is observed, suggesting that exchange of halide between the two types of sites is fast compared to the reciprocal of the line width

of the wider line. Under conditions of fast exchange and extreme motional narrowing Marshall[10] has shown the composite halide line width to be

$$\Delta\nu = (2\pi/5)(e^2q_FQ)^2T_Ff_F + (2\pi/5)(e^2q_BQ)^2T_Bf_B \quad (2)$$

or

$$= \Delta\nu_Ff_F + \Delta\nu_Bf_B \quad (3)$$

where

$$1/T_F = 1/\tau^F{}_{rot} + 1/\tau^F{}_{ex} \quad (4)$$

and

$$1/T_B = 1/\tau^B{}_{rot} + 1/\tau^B{}_{ex} \quad (5)$$

Here f_B is the fraction of halide bound to the macromolecule, f_F the fraction of free halide, and τ_{rot} and τ_{ex} are appropriate rotational and exchange correlation times, respectively. Inasmuch as $\Delta\nu$, $\Delta\nu_F$, and halide concentrations can be measured, $\Delta\nu_B$ can be determined. Knowledge of the quadrupole coupling constant allows a value for T_B to be extracted from the experimental data. The observed composite line sets only a maximum on the exchange correlation time. Consequently, such a composite spectrum provides no *a priori* information as to the domination of exchange or rotational motion in effecting relaxation of the quadrupole nuclei, as can be seen from eq 5. If one can conclude that T_B is dominated by rotational relaxation, the experimentally determined $\tau^B{}_{rot}$ may be compared with that predicted from theory appropriate to the macromolecules in question, *i.e.*, to the rotational relaxation of spheres, rods, or random coils with or without internal motion.

Experimental Section

Polymer Preparation. Introduction of sulfhydryl groups into proteins by thiolation of free amine groups has been very successful.[11-13] Introduction of sulfhydryl into poly-α,L-glutamic acid (PGA) through thiolation of the N-terminal amine has been reported.[14] Our attempts to end label PGA in this manner both with *N*-acetyl-D,L-homocysteine thiolactone and with *S*-acetylmercaptosuccinic anhydride met with uniform failure. Over 25 different variations in pH, temperature, solvent, and ratio of polymer to thiolating agent failed to produce the desired product. The reported synthesis[14] used the procedure of Benesch and Benesch[11] whereby Ag^+ is used as a catalyst to aid ring opening in the thiolactone. When employing this procedure we frequently obtained a yellow, nondialyzable product which could be formed also without PGA in the reaction solution. Further study of the yellow product indicated that it was a polynuclear silver *N*-acetylhomocysteine polymer. Elemental analysis (Ag, 37.4%; S, 10.5%; C, 21.2%; H, 3.5%) was consistent only with 1:1 stoichiometry. Osmotic pressure measurements indicate it to be a polyelectrolyte with a typical molecular weight of 10,000–20,000. Viscosity measurements also show it to be a polyelectrolyte but quite compact in the presence of supporting electrolyte ($[\eta]$ = 0.018 dl g^{-1} in 1 *M* NaCl). The inability to thiolate using procedures generally successful with proteins may be due to the very large number of negatively charged carboxyl groups which surround the lone amine.

Sulfhydryl groups were successfully introduced into PGA by randomly copolymerizing 5 mol % *S*-carbobenzoxy-L-cysteine *N*-carboxyanhydride with γ-benzyl-L-glutamate *N*-carboxyanhydride. The benzylglutamate NCA was obtained from Pilot Chemicals, Inc., and the *S*-carbobenzoxy-L-cysteine NCA was prepared from *S*-carbobenzoxycysteine (Schwarz/Mann) and phosgene by the method of Berger, Noguchi, and Katchalski.[15] The NCA's were copolymerized in dioxan (purified by refluxing over sodium for 48 hr and distilling just prior to use) using triethylamine as initiator. The monomer to initiator ratio was 100. The polymerization was followed by the CO_2 evolution and was stopped after approximately 85% monomer conversion. The polymer was precipitated by pouring the reaction solution into water. The white fibrous product was filtered, washed, and vacuum dried. Since the resulting polymer was essentially polybenzylglutamate containing an occasional carbobenzoxycysteine, its molecular weight was estimated from its intrinsic viscosity in dimethylformamide[16] to be 150,000, corresponding to about 700 monomeric units per weight average molecule. The benzyl and carbobenzoxy groups were removed by bubbling dry HCl (20 min), followed by dry HBr (45 min), into a solution of the polymer dissolved in 1,2-dichloroethane.[17] After 2 hr the turbid solution was purged with N_2, poured into ether, filtered, washed, and dried. The copolymer, designated PGA–SH, was dissolved in oxygen-free water by stirring and slow addition of NaOH, exhaustively dialyzed under N_2, and recovered by lyophilization. No residual benzyl or carbobenzoxy groups could be detected from uv absorption near 260 nm. The weight average molecular weight of the deblocked polymer was estimated by viscosity[18] to be 32,000 (as acid form), indicating a weight average degree of polymerization of about 250.

Molecular Weight Fractionation. Portions of the polymer were molecular weight fractionated by gel permeation chromatography using agarose gels (Bio-Rad Laboratories) in a 2.5 × 100 cm column (type K-25, Pharmacia Fine Chemicals, Inc.) equipped with flow adaptors adjusted to give a bed volume of 400 ml. The polymer was injected into the column as a 1 wt % solution in 0.5 *M* NaCl with a total volume about 2.5% of bed volume. The eluant was degassed 0.5 *M* NaCl with a nominal pH of 6, and was pumped at a rate less than the maximum suggested rate for the gel employed. The effluent was monitored by uv absorption at 210 nm, and collected as 7-ml fractions in tubes appropriate for nmr measurements.

The column was molecular weight calibrated using previously fractionated and characterized samples of polyglutamic acid.[19,20] Each calibration sample was chromatographed individually to obtain its elution volume, taken as the center of the elution peak.

Three different fractionations were made. The first (fractionation I) was carried out using PGA–SH on Biogel A-5m, 50–100 mesh, whereas fractionation II employed Biogel A-50m, 100–200 mesh. The fractionation of PGA–SHgCl (*cf. seq*), fractionation III, also employed Biogel A-50m gel.

Sulfur and Peptide Concentrations. The sulfur content was determined at various times by several techniques. In preliminary experiments the free sulfhydryl content was determined by spectrophotometric determination with *p*-chloromercuribenzoate.[21] This proved too insensitive for use on the fractionated samples at the concentrations appropriate to the nmr measurements. In some cases ^{35}Cl nmr line width measurements were used to determine sulfhydryl concentration by titration with 0.01 *M* $HgCl_2$,[6,7] or by back titrating PGA–SHgCl with mercaptoethanol.[22]

The most important (*cf. seq*) set of sulfhydryl and peptide determinations was on the fractions from fractionation III. The mercury adduct of cysteine has a strong absorbance centered around 230 nm (ϵ_{230}^{max} 1.5 × 10^4) in 0.5 *M* NaCl. The peptide bond absorbs about 1% as strongly at this wavelength, but steadily increases as the wavelength is lowered. Each fraction was scanned from 215 to 240 nm and the sulfhydryl and peptide bond concentrations determined by a least-squares fit. Sodium polyglutamate and an equimolar mixture of $HgCl_2$ and cysteine in 0.5 *M* NaCl were used as model systems for the determination of peptide bond and mercurated cysteine molar absorptivities, respectively.

Amino acid analysis was performed on a commercial amino acid analyzer after the conversion of cysteine and any cystine to cysteic acid by the usual procedure.[23]

Nmr ^{35}Cl Line Width Measurements. The ^{35}Cl nuclear magnetic resonance measurements were made on a modified Varian DP-60 spectrophotometer equipped with a V-4210 variable radiofrequency unit operating at 5.6 MHz. The resonance signal was modulated at 500 Hz and detected as the first side band using a Princeton Applied Research Model 121 lock-in amplifier. Line widths were measured as the full width at half-height of the absorption mode signal and each reported line width is the average of at least five traces. Errors are given as the mean deviation. Line widths were calibrated from side bands of a saturated NaCl solution with the modulation frequency counted to ±0.1 Hz by a Hewlett-Packard Model 521C counter. Line width measurements were made at a nominal temperature of 27° except for one fraction in which a Varian variable temperature controller, Model E-257, was employed.

The molecular weight fractionation was designed such that the bulk of the fractions were of appropriate sulfhydryl concentration for direct nmr measurements without additional handling. With fractionations I and II the ^{35}Cl line widths were determined as a function of the quantity of added 0.01 *M* $HgCl_2$. With fractionation III the line widths were determined directly, and in several cases as a function of added mercaptoethanol by back-titration.

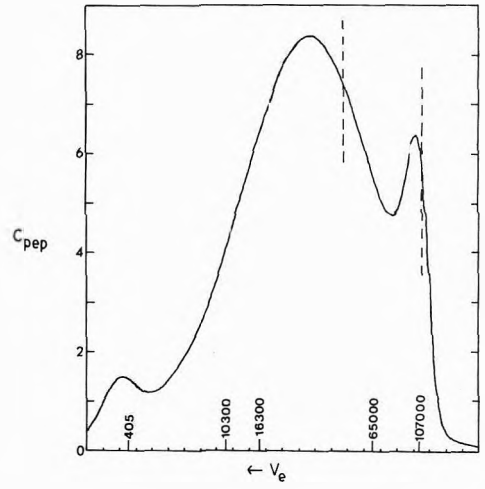

Figure 1. Fractionation I. Fractionation of PGA–SH on Biogel A-5m in 0.5 *M* NaCl, pH 6. Chromatogram indicates the peptide bond concentration (C_{pep}) as a function of elution volume (V_e). Molecular weight scale is that from PGA calibration. Between the dashed vertical lines there was sufficient signal for nmr line broadening measurements.

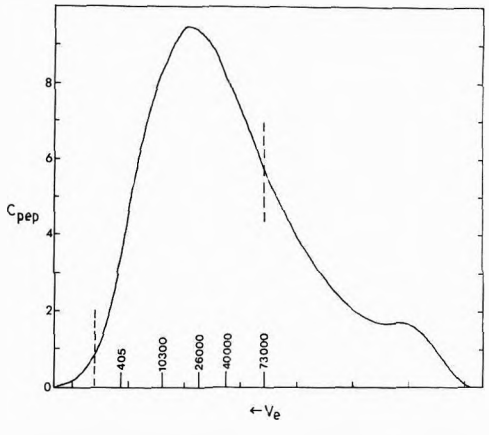

Figure 2. Fractionation II. Similar to fractionation I except Biogel A-50m was employed.

Results

The cysteine–glutamic acid copolymer recovered after side chain deblocking and lyophilization was soluble with difficulty at neutral pH. Adjustment of the pH to 11.5 clarified the solution after a few minutes, and the solution remained clear after readjustment to neutral pH. A trace of the chromatogram for PGA–SH on Biogel A-5m, fractionation I, is shown in Figure 1. The dashed lines indicate the region of sufficient sulfhydryl concentrations to give measurable nmr line broadening upon $HgCl_2$ addition to the fractions. Although Biogel A-5m has an exclusion limit of 5 × 10^6 for globular proteins, the shape of the chromatogram suggested that a substantial amount of the random coil polypeptide was being excluded from the gel. In addition the bulk of the measurable ^{35}Cl line broadening effects is in the region where fractionation is poor. For these reasons another portion of PGA–SH was solubilized and fractionated (fractionation II) on Biogel A-50m, which has an exclusion limit of 5 × 10^7 for globular proteins. The chromatogram, shown in Figure 2, indicates only a small amount of the sample is excluded from the gel. The measurable nmr effects extended over a much greater fraction of the sample. However, it was disturbing that the nmr effects were apparently shifted toward lower molecular weights compared with fractionation I. Titration of the unfractionated PGA–SH with *p*-chloromercuribenzoate indicated a free sulfhydryl content of 1.5%, in good agreement with the break in the nmr line width measured as a function of added $HgCl_2$. Amino acid analysis of the oxidized, unfractionated PGA–SH indicated a cysteic acid content of 5.2%, in good agreement with the monomer ratio used in the polymerization. The sulfur analyses suggested that some of the sulfhydryls had been oxidized to cystine, putting disulfide bridges into the polymer, or that we were apparently losing sulfur, or both. The presence of disulfide bonds is well known to alter the hydrodynamic volume of random coil peptides,[24] and gel chromatography would consequently not fractionate according to chain length. If disulfide bonds were present in the PGA–SH, the high pH treatment to facilitate solubilization could cause elimination of sulfur.[25]

To eliminate these problems 115 mg of PGA–SH was dissolved in 10 ml of 0.5 *M* NaCl, 0.3 ml of mercaptoethanol was added to reduce possible disulfide bonds, and the pH adjusted to 8.5. After 3 days the solution was dialyzed with oxygen excluded, and the dialyzate poured into 10 ml of 0.01 *M* $HgCl_2$. The resulting polymer, PGA–SHgCl, was dialyzed to remove the slight excess of $HgCl_2$, and re-

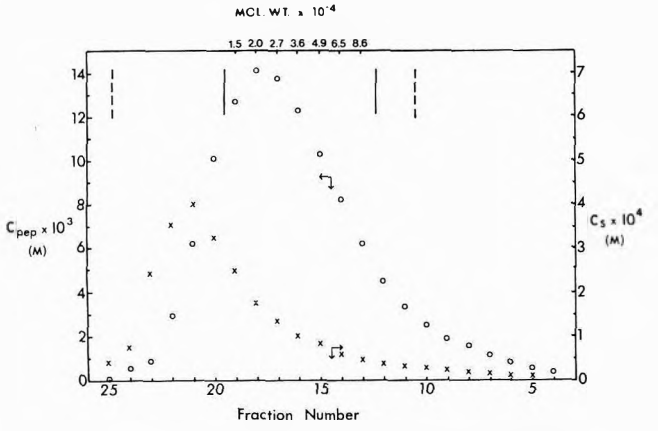

Figure 3. Fractionation III. Fractionation of PGA–SHgCl on Biogel A-50m in 0.5 *M* NaCl, pH 6. Chromatogram shown as the peptide (C_{pep}) and sulfhydryl (C_s) concentration as a function of fraction number. Dashed vertical lines indicate limits of nmr detectability, while solid vertical lines indicate limits of reliable molecular weight assignment.

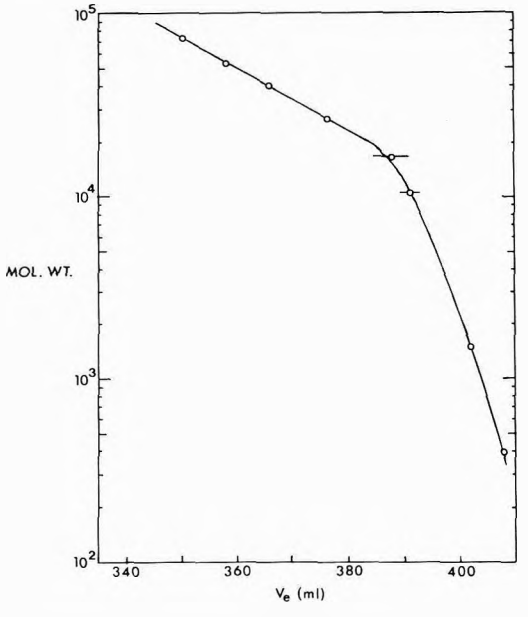

Figure 4. Molecular weight calibration of the Biogel A-50m column using fractionated PGA[19,20] in 0.5 *M* NaCl, pH 6.

covered by lyophilization. This material, which should be devoid of any oxidized sulfhydryls and hence be linear polypeptide chains, was readily soluble. It was fractionated on Biogel A-50m, and designated fractionation III. The mercurated cysteine and peptide concentrations in each fraction were determined by uv analysis, and are shown in Figure 3. Also shown in Figure 3 are the corresponding molecular weights, based on the calibration curve shown in Figure 4. The molecular weight calibration indicates that material eluting with V_e > 390 ml is poorly fractionated. Although these fractions can be assigned a molecular weight on the basis of mean elution volume, they will be broad and of unknown validity. Fractions eluting earlier than the highest calibration molecular weight may be assigned a tentative molecular weight by linear extrapolation. This should be valid until the exclusion limit is reached, at which point the calibration curve would turn sharply upward and the corresponding fractions contain poorly fractionated material. Therefore, any assignment of molecular weight <10,000 and >90,000 is only approximate. The sulfhydryl distribution is shown in more detail in Table I. ^{35}Cl nmr line width measurements on these fractions as a function of added mercaptoethanol gave sharp end points (Figure 5) and cysteine concentrations in substantial agreement with the uv analysis.

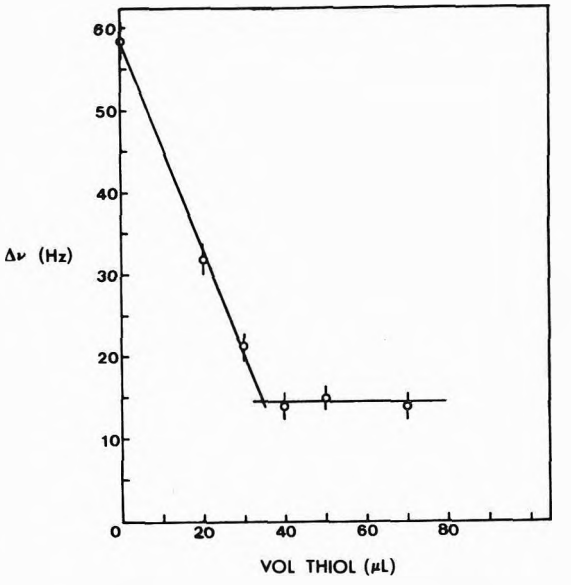

Figure 5. ^{35}Cl line width as a function of added mercaptoethanol[22] in a typical fraction from fractionation III.

TABLE I: Sulfhydryl Distribution in Fractionation III

Fraction no.	Molecular weight (acid form)	% cysteine		DP	Av no. –SH/ polymer molecule[c]
		Uv[a]	Nmr[b]		
10	>90,000	1.08			
11	>90,000	0.95			
12	>90,000	0.80	0.63		
13	86,000	0.73		670	4.9
14	65,000	0.72	0.57	500	3.6
15	49,000	0.79		380	3.0
16	36,000	0.81	0.82	280	2.3
17	27,000	0.98		210	2.1
18	20,000	1.23	1.3	160	2.0
19	15,000	1.94		115	2.2
20	<10,000	3.2	4.1 ± 0.2		
21	<10,000	6.5			
22	<10,000	12	13.6		
23	<10,000	27			

[a] Both peptide and cysteine determined by uv analysis. [b] Peptide by uv, cysteine by titration with mercaptoethanol. [c] Based on uv analysis for cysteine content.

The ^{35}Cl line width for many of the fractions was measured shortly after the fraction was collected from the column. Through application of eq 3 these were converted to $\Delta\nu_B$ and are plotted in Figure 6 (open circles) as a function of molecular weight. Approximately 6 weeks later the ^{35}Cl line width of the remaining fractions was measured. The line widths were uniformly lower, suggesting sample deterioration, even though the samples were stored in semidarkness in sealed tubes. However, if these measured line widths are each multiplied by a common factor (1.3), all values fall on a common curve. This can be seen in Figure 6 where the closed circles represent the scaled values. This agreement suggests that only the –SHgCl concentration had decreased, perhaps due to deterioration

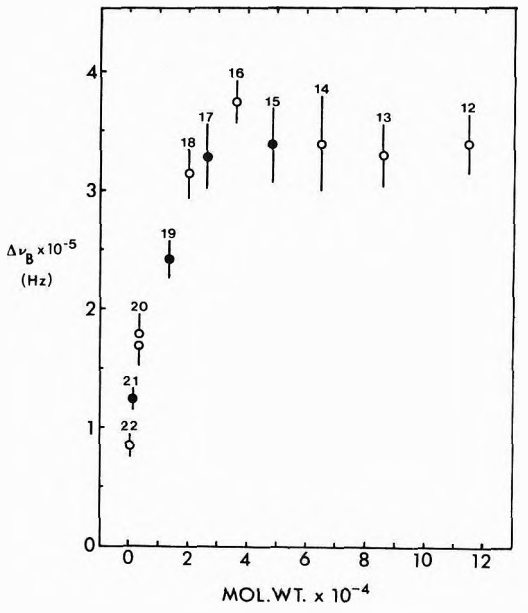

Figure 6. $\Delta\nu_B$ as a function of molecular weight (fractionation III) of PGA-SHgCl determined in 0.5 *M* NaCl, pH 6, 27°. Sulfhydryl concentration determined by uv analysis. See text for meaning of open and closed circles. Numbers above data points indicate fraction number.

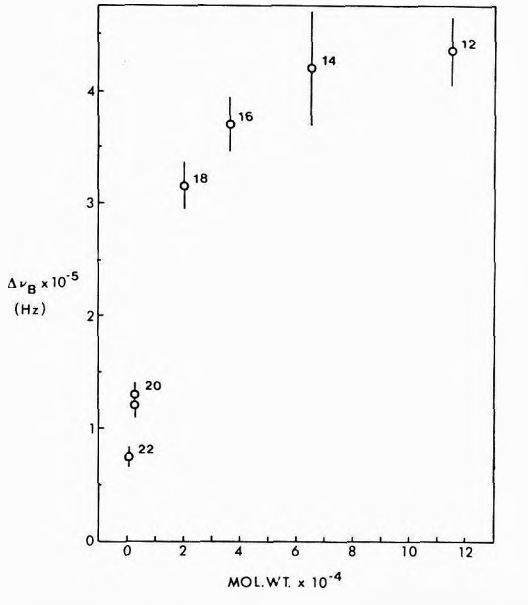

Figure 7. Analogous to Figure 6 except sulfhydryl concentration based on nmr mercaptoethanol titration.

by light. In Figure 7 the molecular weight dependence of $\Delta\nu_B$ is shown based alternatively on the limited set of mercaptoethanol titrations for cysteine content.

The temperature dependence of the ^{35}Cl line width of fraction 15 (molecular weight ~49,000) is shown in Figure 8, plotted as the dependence of $\Delta\nu - \Delta\nu_F$ on η/T. Since the mercury-chloride equilibrium constant[22] is on the order of 10^5, $f_F \approx 1$, and f_F and f_B are temperature independent, the ordinate is proportional to $\Delta\nu_B$. The linearity indicates the line width is controlled by a diffusion process. According to eq 5 this could result from either diffusion-controlled exchange, or possibly rotational motion. If a diffusion controlled τ^B_{ex} dominates eq 5, $\Delta\nu_B$ should respond linearly to changes in τ^B_{ex}. Inasmuch as the bound chloride is typically about four orders of magnitude

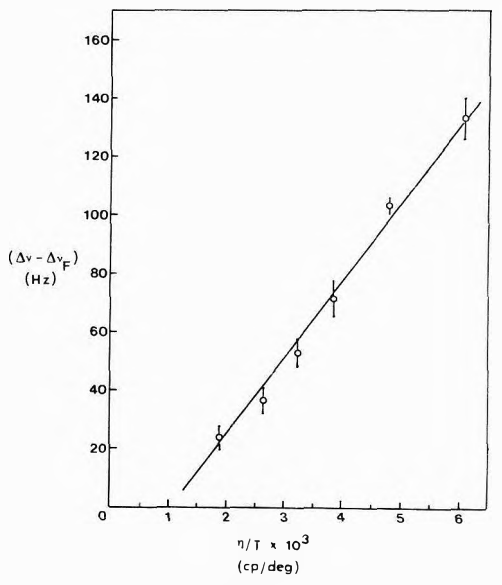

Figure 8. Dependence of the ^{35}Cl line width on η/T for fraction 15 (fractionation III) in 0.5 *M* NaCl, pH 6. η is the solvent viscosity.

TABLE II: ^{35}Cl Line Width Dependence on $[Cl^-]_{tot}$

Fraction 18 (III), pH ≈6		Fraction 17 (III), pH ≈6		Unfractionated sample, pH ≈4.5 ± 0.2	
$[Cl^-]^a$	$\Delta\nu_{obsd}$, Hz	$[Cl^-]^b$	$\Delta\nu_{obsd}$, Hz	$[Cl^-]^c$	$\Delta\nu_{obsd}$, Hz
1.0	50.9 ± 1.5			1.0	27.4 ± 1.1
0.5	54.8 ± 2.5	0.5	70.3 ± 0.8	0.5	31.2 ± 2.1
0.25	52.8 ± 5.4	0.25	67.9 ± 3.2	0.25	30.3 ± 1.6

[a] Dilution made with 1 *M* $NaNO_3$ to maintain constant ionic strength. [b] Dilution made with 0.5 *M* $NaNO_3$. [c] Dilution made with pH-adjusted 1 *M* $NaNO_3$ to maintain helical form.

lower in concentration than the free chloride, direct exchange of chloride between bound-chloride sites should be negligible compared to exchange with the large excess of free chloride ion. Therefore, the pseudo-first-order rate constant for bound chloride exchange, and hence $1/\tau^B_{ex}$, should be a linear function of free chloride ion. The effect of the chloride concentration was determined by addition of enough solid NaCl to make the solution 1 *M* in NaCl, the line width measured, followed by measurements as a function of added 1 *M* $NaNO_3$. By this procedure the ionic strength of the solution is kept constant, which should ensure that there is no change in polymer conformation. Also, the quantities f_F and f_B remain constant, and $\Delta\nu_F$ is a very weak function of chloride ion concentration. The observed line width, which is dominated by $\Delta\nu_B f_B$, is seen in Table II to remain constant within experimental error. If T_B were dominated by τ^B_{ex}, $\Delta\nu_B$ would have changed by a factor of four. It thus seems unambiguous that T_B is dominated by τ^B_{rot} and not τ^B_{ex}. Consequently, the molecular weight dependence of $\Delta\nu_B$ in Figure 6 represents the molecular weight dependence of τ^B_{rot}, assuming eq 2 and 5 are applicable.

With selected fractions the ^{35}Cl line width was measured as a function of pH, and hence of polypeptide conformation. The results, shown in part in Figure 9, show no perceptible effect of the line width on conformation; even though the conformation is changed from random coil to helix. Also shown in Figure 9 is the pH dependence of the line width of unfractionated PGA-SH.

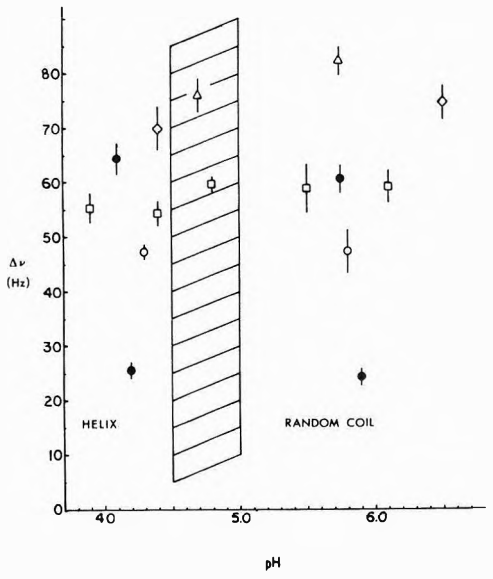

Figure 9. ^{35}Cl line width as a function of pH in 0.5 *M* NaCl: solid symbols, Fractionation III, fraction 16, upper; fraction 13, lower; unfilled symbols, unfractionated PGA-SH: (Δ) C_{pep} = 5.2 m*M*, C_{HgCl_2} = 0.17 m*M*; (□) C_{pep} = 5.0 m*M*, C_{HgCl_2} = 0.1 m*M*; (○) C_{pep} = 3.1 m*M*; C_{HgCl_2} = 0.08 m*M*; (◇) C_{pep} = 7.8 m*M*, C_{HgCl_2} = 0.15 m*M*. Hashed area indicates region of helix–random coil transition.

Discussion

Polymer Preparation, Fractionation, and Characterization. We have presented considerable detail concerning the polymer preparation and handling because of the reactive nature of sulfhydryl containing polymers. In addition to the sulfur content, the sulfur distribution is of some importance when discussing the nmr results.

The monomer reactivity ratios in the solvent and initiator system employed for the polymerization are unknown. However, the polymerization should proceed by the "strong base" initiation mechanism[26-28] whereby the molecular weight is roughly independent of the monomer conversion. Although polymers formed early in the reaction may have a different composition than those formed near the end, this mechanism, plus what is known in general concerning NCA reactivities, will assure that the sulfur distribution is nearly random in most of the molecules.

As can be seen in Table I the sulfhydryl content in PGA-SHgCl was weakly dependent on chain length, except at the small size end. Inasmuch as we feel this represents the total cysteine content, and is lower than the monomer feed, the high sulfur content molecules of small size may have formed near the termination of the reaction as the glutamate content of the unreacted monomer becomes depleted. Due to their high sulfur content any molecular weight assignment based on PGA calibration is undoubtedly meaningless when the cysteine content exceeds a few per cent. These low molecular weight molecules were of sufficient size, however, that they were not removed by dialysis. The mean sulfhydryl content of fractionation III, 2%, is only slightly higher than that found in the unfractionated material before mercaptoethanol reduction and -HgCl labeling. Except for the amino acid analysis on the unfractionated, oxidized material, all indications are that cysteine is incorporated into high molecular weight chains at a rate less than its mole fraction in the monomer feed. We are unable to explain the amino acid analysis.

A more detailed analysis of fractionation III adds further to our feeling of linear polymer chains. The side-chain deblocking with acid drops the weight average degree of polymerization from 700 to 250. This indicates main chain as well as side chain breakage, which is a rather typical result when deblocking glutamate polymers. Since the main chain scission should be random, the molecular weight distribution should approach the "most probable" distribution irrespective of the distribution before deblocking.[29] Comparison of the cumulative weight fraction distribution over the molecular weight range 10^4–10^5, which comprises 80 wt % of the polymer, with that expected for the most probable distribution, normalized to be coincident at 0.5 cumulative weight fraction, shows good agreement though the experimental distribution is slightly broader. The weight and number average molecular weights may be calculated also from the chromatogram, and their ratio compared to the "most probable" value of 2. This comparison is made somewhat difficult by the sensitivity of the averages to the molecular weight assignment at low and high elution volumes. Assigning a molecular weight of 115,000 to fractions eluting at less than 340 ml, and a value of 3000 to any fraction eluting at greater than 405 ml, results in M_w = 42,200 and M_n = 12,000. Reassigning the high elution fractions such that any $V_e > 400$ ml is assigned a molecular weight of 10,000, which does not seem unreasonable in light of the fact that all the material was nondialyzable, results in M_w = 43,400 and M_n = 23,000. A final reassignment of 90,000 to any fraction eluting less than 340 ml results in M_w = 39,800 and M_n = 22,700. The weight average molecular weight is 20–30% larger than the viscosity determined value made on the unfractionated, nonmercaptoethanol treated material, and the M_w/M_n ratios bracket the value for the most probable distribution. If there were significant intra- or intermolecular disulfide bonds, it seems unlikely that the results would agree this closely with the expected distribution and averages. We thus believe that the ^{35}Cl line width measurements were performed on linear, noncrosslinked polymer chains.

Molecular Weight Dependence of ^{35}Cl Line Width. Random Coil Polymers. The data of Figure 8 indicate that T_B in eq 2 and 5 is controlled by a diffusion process. To determine whether chemical exchange makes a significant contribution to T_B two possibilities for the exchange process must be considered since the exchange mechanism is not known. The assumption that the exchange reaction is first order in polypeptide–mercury complex only leads to the conclusion that the rate constant for association must be on the order of 10^{15} sec^{-1}. Therefore, the first-order dissociation is not considered further.

If the exchange reaction is second order, first order in chloride ion and first order in mercury complex, then τ_{ex} of eq 5 is given by

$$\tau_{ex} = 1/k_2[Cl^-] \quad (6)$$

where k_2 is the second-order rate constant. Assuming that k_2 is a diffusion-controlled constant

$$k_{2,diff} = (4\pi N/1000)R_{12}D_{12} \quad (7)$$

where k is expressed in units of M^{-1} sec^{-1}, N is Avogadro's number, R_{12} the reaction radius in cm, and D_{12} the sum of the translational diffusion coefficients for chloride ion and the mercury species. Setting $D_{12} \simeq D_{Cl} = 10^{-5}$

$cm^2\ sec^{-1}$, $R_{12} \simeq 5 \times 10^{-8}$ cm, $\tau_{ex} = (k_{2,diff}[Cl^-])^{-1} \simeq 5 \times 10^{-10}$ sec. This value may be compared with T_B calculated from eq 2, if the quadrupole coupling constant is known. In solid $HgCl_2$ (e^2qQ) is reported to be 40 MHz and Wallach suggests that it may be about 8 MHz in related compounds.[8] Using these values and the high molecular weight limit for $\Delta\nu_B$ of 3.5×10^5 Hz, the value of T_B ranges from 2×10^{-10} to 5×10^{-9} sec. The value of τ_{ex} calculated above is close to these limits; however, τ_{ex} must be inversely proportional to the chloride ion concentration which is not observed as shown in Table II. Therefore the data are entirely consistent with the conclusion that T_B is a measure of τ^B_{rot} and not τ^B_{ex}.

The data in Figures 6 and 7 indicate that the ^{35}Cl line broadening is independent of molecular weight until one reaches very small molecular weights. As can be seen from Table I, however, the falloff in $\Delta\nu_B$ might be associated with the sudden increase in sulfur content, and is not necessarily a simple molecular weight dependence. Ignoring this interpretive problem the quadrupole relaxation dominated line widths reported here show the same type of molecular weight dependence as the dipolar relaxation dominated line width in the proton magnetic resonance spectra of dilute solution random coil polymers.[30]

The segmental motion of random coil polymers is highly complex. Most of their hydrodynamic properties depend on low-frequency modes, and can be accounted for by the spring-bead treatments of Zimm[31] and Rouse.[32] Ullman,[33] utilizing the Zimm-Rouse spring-bead relaxation distribution for segmented motion, has derived the expression for proton relaxation times, where the proton is relaxed by dipolar interaction with another proton rigidly affixed to the same backbone atom. The results should be directly applicable to quadrupole relaxation except for some constant, molecular weight independent, factors. The Ullman treatment predicts the observable line width to be molecular weight dependent in the absence of hydrodynamic interaction but molecular weight independent, except for short chain lengths, in the presence of the more realistic system having hydrodynamic interaction. Our results are entirely consistent with this prediction.

In the detailed study on the molecular weight dependence of the proton line width in polyethylene oxide Liu and Ullman[34] find that at low polymer concentrations both T_1 and T_2 are molecular weight independent above a chain length of about 50 monomeric units. Rather than discuss the results in terms of Ullman's treatment of the spring-bead model, they chose instead a model based on the rotation of a single monomeric unit with respect to the coordinate system of the laboratory plus rotamer motion within the monomer unit. This is in fact similar in principle, though not in detail, to the Wallach treatment[8] except that the motion of a monomeric unit is very different from the motion of a rigid macromolecule of equivalent chain length, or radius of gyration. The analysis of Liu and Ullman, which gives results in good agreement with dielectric relaxation and infrared data, yields a relaxation time of about 10^{-8} sec for the isotropic rotational diffusion of a monomer unit in this random coil polymer.

Inasmuch as the Liu-Ullman results indicate that the mean motion of a monomeric unit at low concentration is independent of chain length above a minimal value, it seems appropriate to use a similar model in our case, though taking cognizance of the side chain habitat of the relaxing nucleus, as shown in Figure 10a. Under the assumption of fast and independent rotational motion about

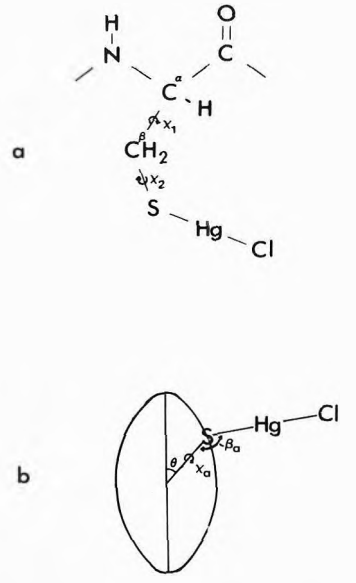

Figure 10. (a) Portion of the polypeptide chain containing the chloride nucleus; (b) ellipsoid of revolution with one internal rotation.

χ_1 and χ_2, the apparent rotational correlation time should be

$$\tau^{\beta}_{rot} = \tau_m\left[\frac{1}{2}(1 - 3\cos^2\beta_1)\right]^2\left[\frac{1}{2}(1 - 3\cos^2\beta_2)\right]^2 \quad (8)$$

where τ_m is the rotational correlation time of a monomeric unit (α carbon), β_1 is the C^α-C^β-S bond angle, and β_2 is the C^β-S-Hg bond angle. Thus τ^{β}_{rot} should be of the order of $10^{-2}\tau_m$. Although there is certain to be differences among random coil monomer unit motions, if we use 10^{-8} sec for τ_m, the value obtained by Liu and Ullman in dilute aqueous polyethylene oxide solutions, eq 8 yields rotational correlation times in the range calculated from our experimental data. Additionally, a τ_m of 10^{-8} sec also satisfies the conditions of motional narrowing, a point which will be of much concern when discussing the helical conformation results. Without both T_1 and T_2 measurements a more quantitative analysis than that given here seems unwarranted.

Molecular Weight Dependence of ^{35}Cl Line Width. Helical Polymers. As we were unable to detect any significant change in line width upon converting selected random coil fractions to the helical conformation, rotational correlation times calculated from eq 2 and 5 would be the same as in the previous section. Although the helical conformation of PGA has not been as well studied as some other synthetic polypeptides, as the pH is lowered the random coil is known to change in a cooperative fashion to the helical conformation.[35] In 0.5 *M* NaCl most of the conformational transition occurs between pH 4.5 and 5.[36,37] By pH 4 the polymer has attained maximal helical content. An additional effect with PGA is aggregation at low pH.[38-40] Recent polarization of fluorescence studies indicate that PGA becomes fully helical and rotates as an intact rod just before aggregation occurs.[41] The aggregation pH is concentration, molecular weight, and ionic strength dependent. It is likely that in at least some instances our measurements were taken on aggregated though not precipitated material.

It is of interest to contemplate the effect disulfide bonds would have when the random coil is converted to the helix, although we believe fractionation III is devoid of

such complications. Due to the unfavorable statistics for two points along a random coil to come within the same volume element, an intramolecular disulfide bond seems less likely to occur than an intermolecular one. This is analogous to the condensation polymerization of a bifunctional monomer, *e.g.*, a hydroxyacid, where linear chains are formed in great abundance compared to ring molecules. Once one intermolecular disulfide bond formed, additional ones between the same two parent molecules will again be improbable on statistical grounds. Since a closed loop is highly improbable, exposure of singly coupled molecules to helix-forming conditions should do little to impede complete helix formation. Circular dichroism spectra were recorded for selected fractions (II) at pH 4 yielding the characteristic double minimum of the helix. The residue ellipticities, $[\Theta]_{222}$, were approximately 27,000 deg cm^2/dmol in substantial agreement with the expected value.[42]

When the random coil polypeptide is converted to a helix the quadrupole probe can be described as being attacked to a rod, but with two internal rotations. The autocorrelation function for the motion of an ellipsoid of revolution with *one internal rotation* has been worked out.[43] The geometric definitions are shown in Figure 10b. In the limit of extreme narrowing the rotational correlation time to be associated with T_B in eq 2 is

$$\tau^{B}_{rot} = \frac{1}{6D_\perp} \times \left[1 + \frac{3(D_\perp - D_\parallel)}{(5D_\perp + D_\parallel)} \sin^2\Theta\left(1 + \frac{3(D_\perp - D_\parallel)}{2(D_\perp + 2D_\parallel)} \sin^2\Theta\right)\right] \times \left[\frac{1}{2}(1 - 3\cos^2\beta_a)\right]^2 + f(D, D_\perp, D_\parallel, \Theta, \beta_a) \quad (9)$$

where $D_\perp$ and D are rotational diffusion coefficients of and about the major axis, respectively, and D is the rotational diffusion coefficient associated with the bond rotation χ_a. If $D \gg D_\perp$, D , a seemingly safe assumption here, the second term in eq 9 drops out. Over most of the molecular weight range in our study $D \gg D_\perp$. In this case and with $D \gg D_\parallel$, eq 9 reduces to

$$\tau^{B}_{rot} = \frac{1}{6D_\perp}\left[1 - 3\sin^2\Theta\left(1 - \frac{3}{4}\sin^2\Theta\right)\right] \times \left[\frac{1}{2}(1 - 3\cos^2\beta_a)\right]^2 \quad (10)$$

By analogy with Wallach's treatment[8] of the autocorrelation function for a sphere with multiple, fast, independent internal rotations, the appropriate equation for *our* halide probe becomes

$$\tau^{B}_{rot} = \frac{1}{6D_\perp}\left[1 - 3\sin^2\Theta\left(1 - \frac{3}{4}\sin^2\Theta\right)\right] \times \left[\frac{1}{2}(1 - 3\cos^2\beta_a)\right]^2\left[\frac{1}{2}(1 - 3\cos^2\beta_b)\right]^2 \quad (11)$$

where β_a and β_b correspond to the C^α–C^β–S and C^β–S–Hg bond angles, respectively. The rotatory diffusion coefficients may be calculated from Perrin's[44] equations. When $D > D_\perp$, equivalent to a long, thin rod, $1/D_\perp$ becomes proportional to the cube of the major axis (rod) length. Inasmuch as Θ, β_a, and β_b are independent of polymer chain length τ^{B}_{rot} should depend on the cube of the molecular weight. Hence it should vary by at least 10^3 over the molecular weight range studied, whereas we observed no variation in line width outside the experimental variation of a few per cent.

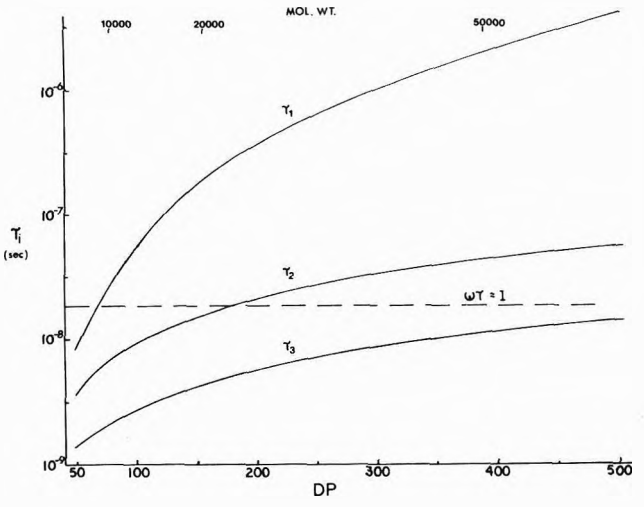

Figure 11. Molecular weight dependence of τ_1, τ_2, and τ_3 appropriate for the PGA α-helix at 300°K in water: dashed line, $\omega\tau_i = 1$.

Before considering reasons for this discrepancy, the question of motional narrowing must be considered. This is a particularly serious question when the nuclear spin is greater than 1, since a Block type equation is not obtained except in the extreme narrowing limit.[45] In order for eq 9 to be valid $(\omega\tau_i)^2$ must be much less than unity, where $\tau_1^{-1} = 6D_\perp$, $\tau_2^{-1} = D + 5D_\perp$, $\tau_3^{-1} = 4D + 2D_\perp$, the remaining τ^{-1}'s are of the order of D, and ω is 3.5×10^7 sec^{-1} in our experiment. As D and $D_\perp$ may be computed from Perrin's equations, $\tau_1 - \tau_3$ may be calculated. When calculating the hydrodynamic properties of a rod through the use of an equivalent ellipsoid, it is generally considered appropriate to use an ellipsoid equal in length to the rod and having the same volume.[46] Using this equivalency and assuming a diameter of 10 Å for the PGA α-helix, the molecular weight dependence of $\tau_1 - \tau_3$ is shown in Figure 11.

These τ values will not be changed meaningfully by a different choice of the somewhat ambiguous helix diameter. What is obvious from Figure 11 is that the condition for motional narrowing is not met for the higher molecular weight fractions, though it is for the lower molecular weights. Focusing our attention on the region where motional narrowing is valid, a factor of 2 change in the molecular weight should result in a change in line width of about a factor of 8. No such effect was observed. Although in very short chains the PGA molecule is only partially helical at low pH, the infinite chain length value is effectively reached within the motional narrowing region.[20] We are thus forced to conclude that the model of a rigid ellipsoid with two internal independent rotations cannot explain our data.

There are two aspects of the rigid ellipsoid (rod) with internal rotation model which can be further explored. Is the PGA α-helix a rigid rod? How much internal rotation is necessary before the relaxation is independent of whether or not it is attached to a rod, ellipsoid, or other "solid" particle?

The aggregation problem mentioned previously, as well as the difficulty in synthesizing material with molecular weights much in excess of 10^5, has inhibited detailed studies on the rigidity of the PGA α-helix. Its precursor, polyglutamate esters such as polybenzyl glutamate (PBLG), has, however, received considerable study with

respect to rigidity. It is well known that PBLG does not behave as a perfectly rigid rod.[47-50] Only the mean deviation from rigid rod behavior has been measured, and not the frequencies or amplitudes of the motion. Although the rigidity of PGA may differ from PBLG, it should be a matter of degree and not of kind. The effect of this type of motion on T_2 is unknown as we have been unable to find that the autocorrelation function for this type of important biological molecule, the semiflexible highly asymmetric macromolecule, has been considered. The approach of Harris and Hearst to the dynamics of semiflexible chains[51-53] might prove useful in this regard. Since, by suitable choice of flexibility, the Harris–Hearst model can treat any degree of flexibility ranging from rigid rods to Zimm–Rouse random coils, it is obvious that at some degree of rod flexibility the autocorrelation function will no longer reflect only the rotary motion of the entire macromolecule.

If the halide probe is attached to the end of a flexible chain whose other end is attached to a rigid particle, how much internal rotation is necessary before the halide relaxation is independent of the attached rigid particle? The Wallach treatment using fast, independent, internal rotations will always make the apparent rotational correlation time a function of the rotation of the rigid molecule, as each internal rotation merely multiplies the correlation time of the rigid part by a factor of $[\frac{1}{2}(1 - 3\cos^2\beta)]^2$ for each internal rotation. It seems obvious that in any real chain with more than one internal rotation, the rotational motions are correlated. Theoretical treatment of such correlated motions is difficult. The situation is made more complex by the fact that T_1 is dependent only on high-frequency motions, whereas, T_2 and hence line width depends on low-frequency motions as well.[34] Some information bearing on this point can be obtained from experimental studies. In dilute solution, dipolar relaxation of protons attached to the main chain atoms in polyethylene oxide random coils indicates that the slowest relaxation seen by the proton is 10^{-8} sec.[34] Similar studies on the side chain methyl protons in dilute solution random coil polydimethylsiloxane yields a mean correlation time of 3.6 $\times 10^{-12}$ sec, and within experimental error $T_1 = T_2$.[55,56] Carbon-13 T_1 measurements on ribonuclease yield a rotational relaxation time of 7×10^{-11} sec for the epsilon carbon of the lysines, which is effectively independent of whether the protein is in its native globular state, or denatured.[57] By contrast the main chain α-carbon atoms had correlation times characteristic of the intact globular protein when in the native state, but a much shorter correlation time when denatured. It is of interest to note that it had been suggested that internal rotation in a chain such as the lysine side chain would not be observed by this technique.[58] A correlation time of 6×10^{-10} sec is reported for segmental motion in polystyrene by carbon-13 T_1 measurements; however, it is suggested that internal rotation of phenyl groups is relatively unimportant.[59] The study of amino acids adsorbed on ion exchange resins provides some interesting results.[60] Correlation times of 0.1–2 nsec were deduced both from carbon-13 dipolar relaxed and deuterium quadrupole relaxed nuclei. The T_2 relaxation time was considerably shorter than T_1 indicating that low-frequency modes related to the resin lattice motion must contribute significantly to the line width. Finally the ^{13}C nmr spectra of polybenzylglutamate (PBLG) provide some insight into this problem.[61] In a low molecular weight sample, carbon atoms in the main chain exhibit line widths quite dependent on whether the molecule was helical or disordered. Side chain carbons show less conformational dependence, which appears to completely disappear for the carbons at the end of the side chain.

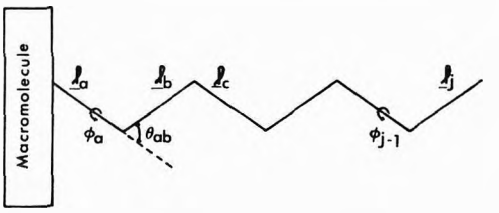

Figure 12. Side chain of macromolecule. Bond rotation angles, coordinate system, etc., are as defined in ref 62.

From the several sets of data described above it seems clear that if a nucleus is bound to a large macromolecule through a series of flexible links, it takes very few links before the nuclear motion is uncorrelated to that of the macromolecule to which it is attached. Uncorrelated in this context means the relaxing nucleus experiences effectively rapid, isotropic motion even if the particle to which it is attached is motionless. The question then arises, are two internal rotations sufficient for the ^{35}Cl nucleus to lose important correlation with the macromolecule motion, or is helix flexing important? Inasmuch as the cysteine α carbon must have a very different motion when it is part of a random coil from when it is incorporated into a helix, this motion must be unimportant or we would observe a conformational effect on line width. It hardly seems possible, however, that two internal rotations are sufficient. There is perhaps some support for this in the ^{35}Cl line width study of mercaptalbumin.[7] The halide probe was placed in a position identical with ours, *i.e.*, on the end of mercurated-cysteine side chains. The conformation was varied from the native globular state to that of a protein random coil through addition of urea, yet the equivalent of $\Delta\nu_B/f_B$ in eq 3 changed by less than a factor of 2, and at some intermediate states of denaturation was almost identical with that of the native protein.

Some additional insight into the problem of internal motion may be had through a simple calculation. Consider a macromolecule with attached side chain, shown in Figure 12 in its trans, planar conformation. If Θ_{aj} is the angle between l_a and l_j and $\langle 3\cos^2\Theta_{aj}(t) - 1\rangle$ is zero even though l_a is fixed in space, the motion of l_j will appear to be isotropic and independent of the motion of l_a. Internal rotation about single bonds is generally rapid with relaxation times of 10^{-10}–10^{-12} sec. If we assume that in the time interval of interest the side chain conformations rapidly intraconvert, then $\langle 3\cos^2\Theta_{aj}(t) - 1\rangle$ may be replaced by its statistical mechanical average, *i.e.*, the average is taken over all conformations weighted according to their probability of occurrence. Through use of the rotational isomeric state model this average is readily computed,[62] the details of which are given in the Appendix. Also given in the Appendix are the appropriate expressions for computing $\langle 3\cos^2\Theta_{Hj} - 1\rangle$, where Θ_{Hj} is the angle between the magnetic field and bond j when the "immobile" macromolecular part of the chain is in a fixed direction with respect to the magnetic field. Shown in Figure 13 is the dependence of $\langle 3\cos^2\Theta_{Hj} - 1\rangle$ on side chain length and Θ_{Ha} for a hydrocarbon (methylene) side chain for the case of free rotation and, similarly, in Figure 14 for a statistical weight matrix of interdependent bond rotations appropriate to the methylene chain.[62] It is obvious that as the

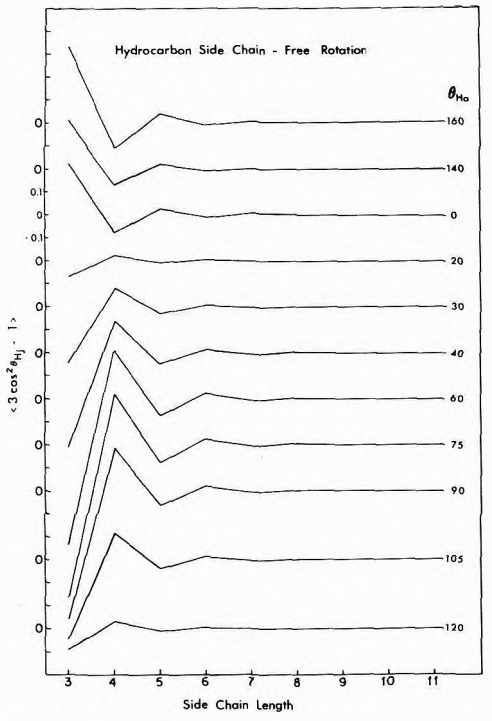

Figure 13. $\langle 3 \cos^2 \Theta_{Hj} - 1 \rangle$ for a methylene side chain as a function of side chain length and Θ_{Ha} for the case of free rotation. $\langle 3 \cos^2 \Theta_{aj} - 1 \rangle$ equals $\langle 3 \cos^2 \Theta_{Hj} - 1 \rangle$ when $\Theta_{Ha} = 0$. Ordinate markings correspond to 0.1.

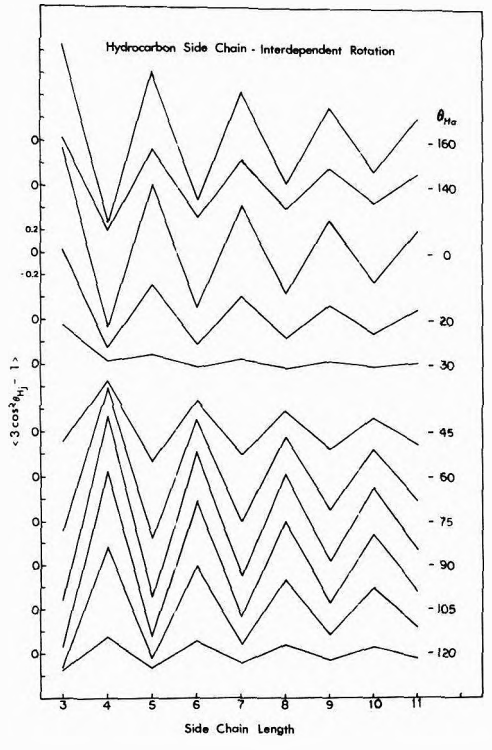

Figure 14. Same as Figure 13 except for interdependent bond rotation as given by eq A8.

length of the side chain is increased the motion of l_j rapidly loses correlation with the motion of the macromolecule to which it is attached at least for free rotation. Only when the main chain relaxation becomes comparable to the side chain relaxation is the former likely to affect the relaxation of l_j. Considering Figure 13 it is not surprising that the outlying nuclei in ribonuclease or PBLG side

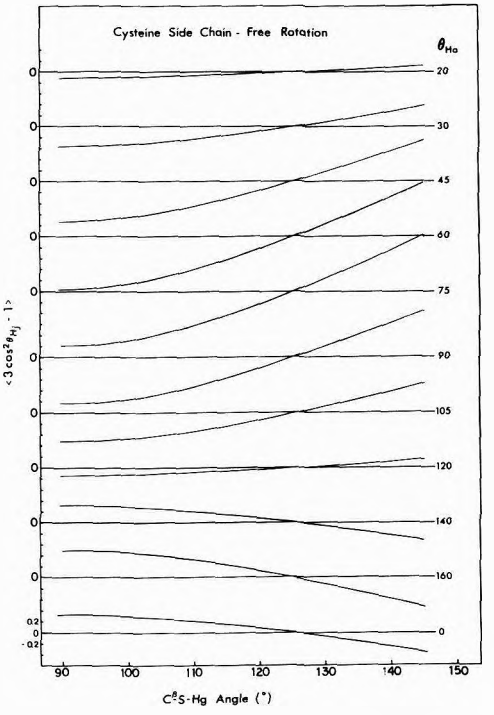

Figure 15. $\langle 3 \cos^2 \Theta_{Hj} - 1 \rangle$ for cysteine-Hg-Cl side chain as a function of C^β-S-Hg bond angle, and Θ_{Ha}. Ordinate markings correspond to 0.2.

chains relax effectively independently of the rigidity of the main chain.

The appropriate calculation for the cysteine -Hg-Cl side chain can be made by taking l_j as the -S-Hg-Cl moiety. Results of such calculations shown in Figure 15 for the case of free rotation show $\langle 3 \cos^2 \Theta_{Hj} - 1 \rangle$ to be strongly dependent on the C^β-S-Hg bond angle. The bond angle appropriate to our side chain is unknown. A value about 15° larger than generally found[63,64] for C-S-Hg bond angles would make $\langle 3 \cos^2 \Theta_{Hj} - 1 \rangle$ close to zero for all orientations of the "immobile" macromolecule with respect to the magnetic field. It is possible that the actual bond angle could accidently be close to that needed to give a zero average. In this case we would expect no molecular weight dependence until the molecular weight became low enough to give a significant main chain contribution to the relaxation, which is entirely in accord with our experimental observations.

It seems then that the rotational correlation time deduced from a typical halide probe experiment may be primarily a reflection of internal motion and not of the motion of the biological macromolecule to which it is attached. Thus, our model to explain the random coil results is equally as meaningless as that of globular, rigid particle motion with independent, internal rotations. That internal motion is responsive to changes in local environment, and thus indirectly may monitor changes in the macromolecule conformation, is not surprising, since the hydrodynamic behavior of short chains has been shown to be very different from that of long chains, and to depend on local solvent-solute interactions rather than on a model assuming continuum hydrodynamics.[65]

Appendix

If Θ_{aj} is the angle between l_a and l_j (Figure 12) in a side chain of j bonds, then $\cos^2 \Theta_{aj}$ averaged over all conformations is given by

$$\langle \cos^2 \Theta_{aj} \rangle = Z^{-1} J^*(U_a \otimes e_a{}^T \otimes e_a{}^T)(T \otimes T)_a \times [(U \otimes E_9)(T \otimes T)]^{j-2}(E_\nu \otimes e_j \otimes e_j)J \quad \text{(A1)}$$

for a chain having a maximum of ν rotational states for each ϕ. In eq A1 U_a and U are statistical weight matrices of order $\nu \times \nu$, $\otimes$ indicates the direct matrix product, and E_ν and E_9 are unit matrices of order ν and 9, respectively. The vectors $e_a{}^T$ and e_j are unit vectors associated with bonds l_a and l_j, respectively, and given by

$$e_a{}^T = (100) \quad \text{(A2)}$$

and

$$e_j = \begin{pmatrix} 1 \\ 0 \\ 0 \end{pmatrix} \quad \text{(A3)}$$

The matrices $T \otimes T$ are $9\nu \times 9\nu$ pseudodiagonal matrices whose "elements" are the matrices $T_i \otimes T_i$, one for each of the ν rotational states ϕ_{ii} associated with a particular bond, where T_i is given by

$$T_i = \begin{bmatrix} \cos \Theta_i & \sin \Theta_i & 0 \\ \sin \Theta_i \cos \phi_{ii} & -\cos \Theta_i \cos \phi_{ii} & \sin \phi_{ii} \\ \sin \Theta_i \sin \phi_{ii} & -\cos \Theta_i \sin \phi_{ii} & -\cos \phi_{ii} \end{bmatrix} \quad \text{(A4)}$$

J^* and J are vectors containing ν elements, given by

$$J^* = (10 \cdots\cdots 0) \quad \text{(A5)}$$

and

$$J = (1 \cdots\cdots 1)^T \quad \text{(A6)}$$

Z is the configurational partition function given by

$$Z = J^* U^{j-1} J \quad \text{(A7)}$$

So long as bond angles $(180 - \Theta_i)$ are known the side chain may be of any type. The rotational isomeric states may be inter- or independent.[62] If one assumes all rotational isomers are equally probable, all elements of the U matrices are equal. If in addition rotational isomers are chosen to be symmetric about the trans isomer, the resulting $\langle \cos^2 \Theta_{aj} \rangle$ will be equivalent to the free rotation result. For the case of a hydrocarbon side chain with interdependent bond rotation, U for the three state (t, g^+, g^-) model takes the form[62]

$$U = \begin{array}{c} \\ t \\ g^+ \\ g^- \end{array} \begin{array}{c} \begin{array}{ccc} t & g^+ & g^- \end{array} \\ \begin{bmatrix} 1 & \sigma & \sigma \\ 1 & \sigma & 0 \\ 1 & 0 & \sigma \end{bmatrix} \end{array} \quad \text{(A8)}$$

where $\sigma = 0.43$ at 300°K.

If a unit vector e_H in the direction of the magnetic field lies in the plane of the side chain when it is in its trans, planar conformation, and makes an angle Θ_{Ha} with e_a, then $\langle \cos^2 \Theta_{Hj} \rangle$ for the angle Θ_{Hj} between the magnetic field direction and l_j may be calculated from eq A1 by replacing $J^*(U_a \otimes e_a{}^T \otimes e_a{}^T)$ by

$$[U_a(1,1)(e_{H,1}{}^T \otimes e_{H,1}{}^T) \cdots\cdots U_a(1,\nu)(e_{H,\nu}{}^T \otimes e_{H,\nu}{}^T)] \quad \text{(A9)}$$

where

$$e_{H,i}{}^T = [\cos \Theta_{Ha} \quad \sin \Theta_{Ha} \cos \phi_{a,i} \quad \sin \Theta_{Ha} \sin \phi_{a,i}] \quad \text{(A10)}$$

References and Notes

(1) (a) This work supported in part by NIH research grants No. GM16122, GM16922, and GM18719; Research Corporation, The Graduate Schoo and the Chemistry Department, University of Minnesota. (b) The data presented in this paper is taken in part from the thesis of D. E. Carlstrom submitted in partial fulfillment of the requirements for the degree of Doctor of Philosophy, University of Iowa, Iowa City, 1972.

(2) (a) G. Roberts and O. Jardetzky, *Advan. Protein Chem.*, **24**, 447 (1970). (b) J. J. Rowe, J. Hinton, and K. L. Rowe, *Chem. Rev.*, **70**, 1 (1970).
(3) O. Jardetzky and N. G. Wade-Jardetzky, *Ann. Rev. Biochem.*, **40**, 605 (1971).
(4) B. D. Sykes and M. Scott, *Ann. Rev. Biophys. Bioeng.*, **1**, 251 (1972).
(5) T. R. Stengle and J. D. Baldeschwieler, *Proc. Nat. Acad. Sci. U. S.*, **55**, 1020 (1966).
(6) T. R. Stengle and J. D. Baldeschwieler, *J. Amer. Chem. Soc.*, **89**, 3045 (1967).
(7) R. G. Bryant, *J. Amer. Chem. Soc.*, **91**, 976 (1969).
(8) D. Wallach, *J. Chem. Phys.*, **47**, 5258 (1967).
(9) R. P. Haugland, L. Stryer, T. R. Stengle, and J. D. Baldeschwieler, *Biochemistry*, **6**, 498 (1967).
(10) A. G. Marshall, *J. Chem. Phys.*, **52**, 2527 (1970).
(11) R. Benesch and R. E. Benesch, *Biochem. Biophys. Acta.*, **63**, 166 (1962).
(12) R. Benesch and R. E. Benesch, *Proc. Nat. Acad. Sci. U. S.*, **44**, 848 (1958).
(13) I. M. Klotz and R. E. Heiney, *J. Amer. Chem. Soc.*, **81**, 3802 (1959).
(14) R. G. Bryant, *J. Amer. Chem. Soc.*, **89**, 2496 (1967).
(15) A. Berger, J. Noguchi, and E. Katchalski, *J. Amer. Chem. Soc.*, 78, 4483 (1956).
(16) H. Fujita, A. Teramoto, T. Yamashita, K. Okita, and S. Ikeda, *Biopolymers*, **4**, 781 (1966).
(17) G. D. Fasman, M. Idelson, and E. R. Blout, *J. Amer. Chem. Soc.*, **83**, 709 (1961).
(18) A. Wada, *Mol. Phys.*, **3**, 409 (1960).
(19) R. L. Snipp, Ph.D. Thesis, University of Iowa, 1964.
(20) R. L. Snipp, W. G. Miller, and R. E. Nylund, *J. Amer. Chem. Soc.*, **87**, 3547 (1965).
(21) P. D. Boyer, *J. Amer. Chem. Soc.*, **76**, 4331 (1954).
(22) R. G. Bryant, *J. Inorg. Nucl. Chem.*, **34**, 3467 (1972).
(23) S. Moore, *J. Biol. Chem.*, **238**, 235 (1963).
(24) C. Tanford, K. Kawahare, and S. Lapanje, *J. Amer. Chem. Soc.*, **89**, 729 (1967).
(25) J. W. Donovan and T. M. White, *Biochemistry*, **10**, 32 (1971).
(26) C. H. Bamford and H. Block in "Polyamino Acids, Polypeptides and Proteins," M. A. Stahmann, Ed., University of Wisconsin Press, Madison, Wisc., 1962, p 65.
(27) M. Szwarc, *Advan. Polym. Sci.*, **4**, 1 (1965).
(28) E. Scoffone, E. Peggion, A. Cosani, and M. Terbojevich, *Biopolymers*, **3**, 535 (1965).
(29) A. Charlesby, *Proc. Roy. Soc., Ser. A*, **224**, 120 (1954).
(30) F. A. Bovey and G. V. D. Tiers, *Advan. Polym. Sci.*, **3**, 139 (1963).
(31) B. H. Zimm, *J. Chem. Phys.*, **24**, 269 (1956).
(32) P. E. Rouse, *J. Chem. Phys.*, **21**, 1272 (1953).
(33) R. Ullman, *J. Chem. Phys.*, **43**, 3161 (1965).
(34) K. J. Liu and R. Ullman, *J. Chem. Phys.*, **48**, 1158 (1968).
(35) P. Doty, A. Wada, J. T. Yang, and E. R. Blout, *J. Polym. Sci.*, **23**, 851 (1957).
(36) N. Kono and A. Ikegami, *Biopolymers*, **4**, 823 (1966).
(37) O. B. Ptitsyn, T. V. Barskaya, I. A. Bolotina, and N. G. Illarionova, *Biofizika*, **12**, 386 (1967).
(38) T. M. Schuster, *Biopolymers*, **3**, 681 (1965).
(39) B. R. Jennings, G. Spach, and T. M. Schuster, *Biopolymers*, **6**, 635 (1968).
(40) G. Spach and D. Constantin, *Biopolymers*, **6**, 653 (1968).
(41) T. J. Gill, III, C. T. Ladoulis, H. W. Kung, and M. F. King, *Biochemistry*, **11**, 2644 (1972).
(42) G. Holzworth and P. Doty, *J. Amer. Chem. Soc.*, **87**, 218 (1965).
(43) D. E. Woessner, B. S. Snowden, Jr., and G. H. Meyer, *J. Chem. Phys.*, **50**, 719 (1969).
(44) F. Perrin, *J. Phys. Radium*, **7**, 497 (1934).
(45) A. Abragam, "Principles of Nuclear Magnetism," Oxford University Press, London, 1961, p 314.
(46) C. Tanford, "Physical Chemistry of Macromolecules," Wiley, 1961, p 342.
(47) N. W. Tschoegl and J. D. Ferry, *J. Amer. Chem. Soc.*, **86**, 1474 (1964).
(48) V. N. Tsvetkov, I. N. Shtennikova, E. I. Ryumtsev, and V. S. Skagka, *Vysokomol. Soedin.*, **7**, 1111 (1965).
(49) W. G. Miller and P. J. Flory, *J. Mol. Biol.*, **15**, 298 (1966).
(50) H. Fujita, A. Teramoto, K. Okita, T. Yamashita, and S. Ikeda, *Biopolymers*, **4**, 769 (1966).
(51) R. A. Harris and J. E. Hearst, *J. Chem. Phys.*, **44**, 2595 (1966).
(52) J. E. Hearst, E. Beals, and R. A. Harris, *J. Chem. Phys.*, **48**, 5371 (1968).
(53) N. Saito, K. Takahashi, and Y. Yunoki, *J. Phys. Soc. Japan*, **22**, 219 (1967).
(54) T. C. Farrar and E. D. Becker, "Pulse and Fourier Transform NMR," Academic Press, New York, N. Y., 1971, Chapter 4.
(55) K. J. Liu and R. Ullman, *Macromolecules*, **2**, 525 (1969).
(56) C. Cuniberti, *J. Polymer Sci., Part A-2*, **8**, 2051 (1970).
(57) A. Allerhand, D. Doddrell, V. Glushko, D. W. Cochran, E. Wenkert, P. J. Lawson, and F. R. N. Gurd, *J. Amer. Chem. Soc.*, **93**, 544 (1971).
(58) K. F. Kuhlmann, D. M. Grant, and R. K. Harris, *J. Chem. Phys.*, **52**, 3439 (1970).
(59) A. Allerhand and R. Hailstone, *J. Chem. Phys.*, **56**, 3718 (1972).

(60) H. Sternlicht, G. L. Kenyon, E. L. Packer, and J. Sinclair, *J. Amer. Chem. Soc.*, **93**, 199 (1971).
(61) G. Boccalon, A. S. Verdini, and G. Giacometti, *J. Amer. Chem. Soc.*, **94**, 3639 (1972).
(62) P. J. Flory, "Statistical Mechanics of Chain Molecules," Interscience, New York, N. Y., 1969.
(63) D. C. Bradley and N. R. Kunchur, *Can. J. Chem.* **43**, 2786 (1965).
(64) D. C. Bradley and N. R. Kunchur, *J. Chem. Phys.*, **40**, 2258 (1964).
(65) R. K. Devan, V. A. Bloomfield, and P. B. Berget, *J. Phys. Chem.*, **75**, 3120 (1971).

Estimation of Kinetic Isotope Effects Using Atomic Force Constants

W. T. King

Department of Chemistry, Brown University, Providence, Rhode Island 02912 *(Received April 9, 1973)*

Using atomic force constants, primary kinetic isotope effects in a series of well-studied reactions were computed by Bigeleisen's frequency moment method. It was found that the kinetic isotope ratios were predicted with sufficient accuracy to discriminate between alternative mechanisms for the same reaction. The application of atomic force constants to the analysis of secondary isotope effects is also briefly considered.

Introduction

Recently[1-3] a quantity called an atomic force constant was defined and shown to have several remarkable properties. The purpose of this paper is to show that because of these properties, it might be possible to estimate the kinetic isotope effect in a postulated reaction mechanism with sufficient accuracy to determine if that mechanism is consistent with observation.

Within the framework of transition state theory,[4] the rate constant ratio for a reaction involving a pair of isotopically substituted reactants, labeled a and a′ (a′ refers to the lighter species) is[5]

$$\frac{k_{a'}}{k_a} = \left(\frac{\nu_{a'}^*}{\nu_a^*}\right) \prod_i^{3N-7} \left[\frac{\Gamma(u_{a_i'}^\dagger)}{\Gamma(u_{a_i}^\dagger)}\right] \prod_i^{3N-6} \left[\frac{\Gamma(u_{a_i})}{\Gamma(u_{a_i'})}\right] \quad (1)$$

in which $\Gamma(u)$ is the ratio of the quantum to classical vibrational partition function for a single frequency, ν_i

$$\Gamma(u) = (u/2)/\sinh(u/2)$$
$$u = hc\nu/kT$$

Here, as is customary, the dagger distinguishes properties of a transition state species from those of the reactants (unmarked). The quantity ν^* is sometimes called the frequency of decomposition, and the ratio $(\nu_{a'}^*/\nu_a^*)$ is the classical limit of its partition function ratio.

Bigeleisen and his coworkers[6-13] base their theories of isotope effects on the (truncated) series expansion of the partition function ratios for isotopic pairs

$$\ln \prod_i \frac{\Gamma(u_{a_i})}{\Gamma(u_{a_i'})} = \sum_{j=1}^{n} \frac{\tau_j(-1)^{j+1}B_{2j}}{(2j)(2j)!} \sum_i (u_{a_i'}^{2j} - u_{a_i}^{2j}) \quad (2a)$$

$$= \frac{\tau_1}{24}\sum_i (u_{a_i'}^2 - u_{a_i}^2) - \frac{\tau_2}{2880}\sum_i (u_{a_i'}^4 - u_{a_i}^4) + \cdots \quad (2b)$$

in which the B_{2j} are the Bernoulli numbers[14] and the τ_j are the so-called modulating coefficients. These coefficients depend on temperature and the order of the series (2) defined by n, and are the result of representing $\ln \Gamma(u)$ as a finite polynomial. It can be shown that they approach unity very rapidly at high temperatures (small u) and that (2) reduces to an ordinary finite Taylor's series under this condition. The infinite Taylor's series expansion of (2) converges only if $u_i < 2\pi$ for all i, whereas a finite polynomial representation of sufficiently high order gives the desired function at any temperature.

This orthogonal expansion and the properties of the modulating coefficients have been discussed in considerable detail by Ishida and Bigeleisen.[10] Consequently, only those coefficients relevant to this paper are considered here and are defined in a subsequent section.

This paper is primarily concerned with the frequency moments in this equation. The first moment in (2), in particular, is related to atomic force constants through the Decius–Wilson sum rule[3,15,16]

$$\Sigma(u_{a_i'}^2 - u_{a_i}^2) = \left(\frac{hc}{kT}\right)^2 \sum_i (\nu_{a_i'}^2 - \nu_{a_i}^2) = N_0\left(\frac{\hbar}{kT}\right)^2 \sum_\alpha (\mu_{\alpha'} - \mu_\alpha)\nabla_\alpha^2 U \quad (3)$$

in which μ_α denotes the reciprocal mass of atom α and $\nabla_\alpha^2 U$ is the Laplacian of the molecular potential energy function, U, differentiated with respect to the coordinates of nucleus α. This particular combination of Cartesian force constants is called an atomic force constant.[1] Substitution of the appropriate ratios (2) into (1), using (3) leads to a relatively simple expression for the logarithm of the rate constants

$$\ln \frac{k_{a'}}{k_a} \simeq \ln\left(\frac{\nu_{a'}^*}{\nu_a^*}\right) + \frac{\tau_1}{24}\left(\frac{\hbar}{kT}\right)^2 N_0 \sum_\alpha (\mu_{\alpha'} - \mu_\alpha) \times (\nabla_\alpha^2 U - \nabla_\alpha^2 U^\dagger) + \cdots \quad (4)$$

where the last term summarizes the change in force constant acting upon each substituted atom α. In (4) it is seen that only isotopically substituted atoms contribute

directly to the isotope ratio. The nonsubstituted atoms might make a contribution to an isotope effect through the higher moments in eq 2 but this would normally be expected to be a small contribution in the temperature range considered here.

Usually only one kind of atom is isotopically substituted in a kinetic isotope study and eq 4 can be simplified. Define an apparent frequency for this atom as

$$\nu_\alpha \equiv [N_0\mu_\alpha\nabla_\alpha{}^2U]^{1/2}/(2\pi c) \quad (5)$$

Substituting this into (4) yields an alternative equation

$$\ln\frac{k_a'}{k_a} = \ln\left(\frac{\nu_a{}^*}{\nu_a{}^*}\right) + \frac{\tau_1}{24}\left(\frac{hc}{kT}\right)^2 n_\alpha(\nu_\alpha{}'^2 - \nu_\alpha{}^2) + \cdots \quad (6)$$

in which n_α is the number of atoms α that are isotopically substituted.

A different method, made possible by the development of appropriate computing techniques,[17] is the so-called "exact" method developed principally by Wolfsberg.[12] In this method, a model for the transition state is chosen, and force constants are assigned to it that are consistent with those for the reactants, but adjusted in such a way that the normal frequency associated with the decomposition coordinate has a null or an imaginary value. The normal frequencies for all species are computed, substituted into (1), and the kinetic isotope effect is calculated.

The "exact" method, then, yields an expression for the kinetic isotope effect directly at all temperatures. This advantage is partially negated by the necessity of introducing a large number of assumptions about the detailed geometry, structure, and potential function in the transition state. Because many of the correlations of structure and force constants are not yet satisfactorily understood, especially in the case of bending and interaction force constants, it is not clear that the greater detail obtained by the "exact" method is a genuine advantage over the frequency moment approximation, even though the "exact" methods seems to have gained in popularity in the recent literature.[18]

The moment method, on the other hand, has a number of attractive features. The dominant contribution to the kinetic isotope effect arises from the difference in force constants acting upon a substituted atom between the reactant and the transition state. This contribution is treated directly in this approximation, as seen in (4), but only indirectly in the "exact" method. This, it is felt, is a distinct advantage because assumptions about the force field acting upon the other atoms involved in the reaction are unnecessary. An even more important advantage is that it appears to be possible to obtain a usefully accurate value for the atomic force constants, $\nabla_\alpha{}^2U$, in (4) for first row compounds by a relatively simple calculation.

Such calculations are the purpose of this paper. First, the properties of atomic force constants are summarized, and a simple formula for their estimation is presented. Next, the problem of estimating the frequency moments and modulating coefficients in order to compute expanded reduced partition function ratios is outlined. The estimation of the temperature independent term, $(\nu_a{}'^*/\nu_a)$ is then briefly considered. Finally, these estimated quantities are used to compute the kinetic isotope ratios in a few well-studied reactions, and the results are compared with experiment. Wherever alternative formulations are possible, the computationally simpler one will be chosen, even at the expense of a little accuracy.

TABLE I: Contributions of Bonded Atoms X–Y Atomic Force Constants Derived from Eq 10

*n*X–Y*m*[a]	*R*(X–Y),[b] Å	X(Y),[c] mdyn/Å	Y(X), mdyn/Å
H–C4	1.09	4.94	6.07
H–C3	1.08	5.16	6.31
H–C2	1.06	5.62	6.80
H–N3	1.01	6.24	9.58
H–O2	0.96	6.50	13.23
F–C4	1.36	13.19	1.07
4C–C4	1.54	3.73	3.73
4C–C3	1.52	4.11	4.11
3C–C3	1.46	5.48	5.48
4C–N2	1.47	2.67	6.10
3C–O2	1.36	2.51	11.72
2C–O2	1.36	2.51	11.72
3C=C3	1.34	9.65	9.65
2N=N2	1.25	11.40	11.40
3C=O	1.22	6.73	22.28
2C=O	1.16	10.20	29.13
2C≡C2	1.20	18.28	18.28
2C≡N	1.16	16.34	25.48

[a] The index *n* in *n*X denotes the number of groups bonded to X, including Y. [b] Average bond lengths taken from ref 24, p 111. [c] The symbols X(Y) denotes the contribution of orbitals on Y to the force constant for X, see text.

Atomic Force Constants

The atomic force constant for an atom α in a molecule is defined as the Laplacian of the molecular potential energy function $U(R)$, $\nabla_\alpha{}^2U$, differentiated with respect to the Cartesian coordinates of nucleus α.[1] Experimentally, they are found by analysis of the frequency sum rule originally given by Decius and Wilson,[15] but expressed in a Cartesian coordinate representation[3,16]

$$\sum_i \nu_i{}^2 = [N_0/(2\pi c)^2]\sum_\alpha \mu_\alpha\nabla_\alpha{}^2U \quad (7)$$

The summations extend over all normal modes and all atoms, respectively.

A set of atomic force constants characteristic of H, C, N, O, and F atoms has been given which reproduce the sum of squared frequencies in a diverse group of compounds with good accuracy.[1] These force constants, to a good approximation, were found to be independent of bonding multiplicity or other details of molecular geometry. Consequently, the sum of squared frequencies in (7) can be computed for compounds of these elements, with a few exceptions,[1] without explicit prior knowledge of their structures.

It was also shown that atomic force constants are simply related to the molecular electron density function.[2,19-21] If the electron density is represented by an expansion in atomic orbitals centered on each atom[22]

$$\rho(r;R) = \sum_\beta\sum_\gamma\sum_{i,j} C_{\beta\gamma}{}^{ij}\beta_i\gamma_j$$

where, for instance, β_i denotes an orbital $\chi_i(r - R_\beta)$ in which β is an index identifying the nucleus and i is a quantum number index specifying the orbital, and $C_{\beta\gamma}{}^{ij}$ is the appropriate coefficient which depends only upon nuclear coordinates, then[2]

$$\nabla_\alpha{}^2U = 4\pi Z_\alpha \sum_{\beta\neq\alpha}\left[\sum_i C_{\beta\beta}{}^{ii}\beta^2(R_\alpha)\right] + \text{small terms} \quad (8)$$

where $\beta_i{}^2(R_\alpha)$ denotes the electron density at α, due to the

TABLE II: Atomic Force Constants in Millidyne/Å Units

$\nabla_\alpha^2 U$	Observed values[a] (eq 7)	CNDO values[b] (eq 8)	Estimated values (eq 10)
$\nabla_{H(C)}^2 U$	6.30 (0.02)[c]	4.96	4.94
$\nabla_{H(N)}^2 U$	7.75 (0.11)	6.45	6.24
$\nabla_{H(O)}^2 U$	8.41 (0.09)	5.77	6.50
$\nabla_{F(C)}^2 U$	11.12 (0.63)		13.19
$\nabla_C^2 U$	23.77 (0.45)	16.66	23.34 (1.19)[d]
$\nabla_N^2 U$	22.67 (2.12)	23.95	27.12 (1.64)[e]
$\nabla_O^2 U$	17.74 (0.94)	22.17	24.34 (2.09)[f]

[a] Reference 1. [b] Reference 2. [c] Standard errors in parentheses. [d] Average value, see text. [e] The average of constants for HCN and NH_3. [f] The average of constants for H_2O and H_2CO.

orbital $\chi_i(r - R_\alpha)$. For compounds of first row elements, the "small terms" have been found to be negligible to a good approximation. It is not clear that this is also the case for the heavier elements, however,[1]

Approximate Hartree–Fock calculations (CNDO) suggest that the atomic population densities in first row compounds are approximately spherically symmetric and equal to those in the isolated atoms in their valence configurations.[23,24] That is, for the 2s and 2p Slater orbitals for the first row elements

$$C_{2s}\chi_{2s}^2(R) + \sum_{i=x,y,z} C_{2p}{}^{(i)}\chi_{2p_i}{}^2(R) \simeq (Z-2)\chi_{2s}^2(R) \quad (9)$$

in which Z is the nuclear charge on the atom of interest. Because orbital "hybridization" is eliminated by forming the sum on the left side of this equation, the approximate validity of (9) provides an explanation for the observation that atomic force constants are independent of bond multiplicity in molecules.[1,2]

It also suggests that eq 8 can be further simplified. Sums like (9) above for some atom β, evaluated at $R = R_{\alpha\beta}$, represent the contribution of the orbitals of β to the atomic force constant for another atom α. Thus, by summing over all hydrogen and first row atoms to which α is bonded, using (9), yields

$$\nabla_\alpha^2 U \simeq 4\pi Z_\alpha\left[\sum_H Z_H\chi_{1s}^2(R_{H\alpha}) + \sum_{\beta\neq\alpha}(Z_\beta - 2)\chi_{2s}^2(R_{\alpha\beta})\right] \quad (10)$$

where H denotes hydrogen. The 1s electrons on first row elements are so tightly bound that they make no significant contribution to atomic force constants. In using (9) in (10) it is assumed that only orbitals in the second shell need be considered for first row elements and that contributions from any more distant nonbonded atoms can be ignored. This last assumption will be reconsidered later in the discussion of secondary isotope effects.

Using nodeless Slater orbitals

$$\chi_{1s} = (C_1^3/\pi)^{1/2}\exp(-C_1 r)$$

$$\chi_{2s} = (C_2^5/96\pi)^{1/2} r\exp(-C_2 r/2)$$

$$\chi_{2p} = (C_2^5/96\pi)^{1/2}\sqrt{3}x\exp(-C_2 r/2)$$

in which C_1 is 1.00 for hydrogen,[25] and C_2 is 3.25, 3.90, 4.55, and 5.20 for C, N, O, and F, respectively, the separate terms in (10) were computed for several cases of interest using averaged "standard" bond lengths.[24] The results are summarized in Table I. In this table, the symbol X(Y) denotes the contribution of the electron density centered on a single atom Y to the atomic force constant for X, as defined by the terms in eq 10; that is, for example, for Y ≠ H

$$X(Y) \equiv 4\pi Z_X(Z_Y - 2)\chi_{2s}^2(R_{X-Y})$$

The atomic force constant, then, is computed by summing the appropriate terms from Table I. For example, using Table I and (10), the atomic force constant, in millidyne/Å units, for carbon in a few representative compounds are found to be

$$\nabla_C^2 U = \begin{cases} 24.28 = 4 \times 6.07 & \text{in } CH_4 \\ 21.94 = (3 \times 6.07) + 3.73 & \text{in } CH_3CH_3 \\ 22.27 = (2 \times 6.31) + 9.65 & \text{in } CH_2CH_2 \\ 25.08 = 6.80 + 18.28 & \text{in CHCH} \\ 23.14 = 6.80 + 16.34 & \text{in HCN} \end{cases}$$

The averaged value for $\nabla_C^2 U$ in these cases is 23.34 ± 1.19 and is in excellent agreement with the experimental value of 23.77 ± 0.45.[1]

The results of the above calculation and others are collected in Table II, and are compared with the results of the analysis of experimental data. It is seen that the atomic force constants obtained by eq 10 agree quite closely with those derived using the electron densities found in the approximate, but more elaborate CNDO calculation, using eq 8. In view of the nature of the approximations made in reducing the Laplacian of the potential function to that given by (10), the calculated force constants are in remarkably good agreement with their experimentally determined values.

In summary, then, atomic force constants are given by an expression similar to Poisson's equation of electrostatic theory. In compounds of first row elements, these constants can be computed with reasonable, or at least useful, accuracy from this equation simply by taking the molecular electron density as that resulting from the superposition of the electron densities of the individual atoms in their valence configurations. Consequently, atomic force constants are insensitive to the rather subtle details of chemical bond formation and it is doubtful that much structural information could be obtained from them.

This lack of sensitivity can be exploited in the study of kinetic isotope effects, however. The decomposition of atomic force constants even for centrally bonded atoms, into the separate, additive contributions of individual atoms suggests that it might be possible to estimate the force constant changes for an isotopically substituted atom in a reaction quite easily by considering the atomic configuration only in the vicinity of the reactive site where bonds are broken and the electron density is changed.

Partition Function Expansion

The next problem is that of computing a sufficient number of modulating coefficients, τ_i, and frequency moments in (2) to estimate partition function ratios over a useful temperature range. As mentioned, Bigeleisen and Ishida[10,11] have quite thoroughly investigated the modulating coefficients and their theory will only be outlined here.

The logarithms of the reduced partition functions, $\Gamma(u_j)$ in (1), are equal to the following sum for all u_j[11,26]

$$\ln\prod_j \Gamma(u_j) = -\sum_j\sum_{s=1}^{\infty} \ln\left[1 + \left(\frac{u_j}{2\pi s}\right)^2\right] \quad (11)$$

TABLE III: Correlation of the Higher Moments of the Frequency Spectra of Molecules and the First Moment, Defined by the Correction, δ_N, Eq 17

	δ_2	δ_3	δ_4	Ref
CH_3F/CD_3F	0.320	0.458	0.552	32
CH_3COOH/CD_3COOH	0.300	0.429	0.519	32
CH_3OH/CD_3OH	0.319	0.456	0.552	32
C_6H_6/C_6D_6	0.249	0.340	0.408	32
C_2H_4/C_2D_4	0.217	0.297	0.355	33
CH_2O/CD_2O	0.263	0.377	0.456	32
H_2O/D_2O	0.042	0.035	0.021	32
CH_3OH/CH_3OD	0.081	0.088	0.091	32
CH_3COOH/CH_3COOD	0.099	0.115	0.128	32
C_2H_2/C_2D_2	0.005	−0.077	−0.171	32
CH_3CCH/CH_3CCD	0.003	−0.085	−0.187	32
HCN/DCN	−0.000	−0.095	−0.209	32

Bigeleisen and Ishida's theory consists of representing the logarithm terms in (11) by a finite series of orthogonal polynomials. One of the simpler expansions they considered expresses the modulating coefficients in terms of the shifted Chebyshev polynomials, $T_n^*(x)$,[27,28] and their coefficients C_n^m

$$T_n^* = \sum_{m=0}^{n} C_n^m x^m$$

where $C_n^m = (-1)^{n+m}2^{2m}n(n+m-1)!/[(n-m)!(2m)!]$. They showed that the modulating coefficients are given by

$$\tau_k = \Upsilon(n,k,R) \equiv 1 - \sum_{m=0}^{k-1} C_n^m(-1/R)^m/T_n^*(-1/R) \quad (12)$$

where R defines the internal, $[0,R]$, over which the logarithms in (11) are represented. If R is defined as

$$R = (hc\nu_{max}/2\pi kT)^2 \quad (13)$$

where ν_{max} is the highest normal frequency in the lighter isotope, then (11) is estimated by interpolation in the internal $[0,R]$ for each value of u_i.

In keeping with the spirit of this paper the modulating coefficients used here are these easily computed functions derived from the second-order Chebyshev polynomials. Specifically

$$\tau_1 = \Upsilon(2,1,R) = 1 - 1/T_2^*(-1/R) \quad (14a)$$

and

$$\tau_2 = \Upsilon(2,2,R) = 1 - (1+8/R)/T_2^*(-1/R) \quad (14b)$$

This implies that the first two terms in the expansion (2) are to be considered, even though the theory outlined in the preceding section concerns only the first term. It will be shown, however, that this theory yields an upper bound to the magnitude of the second-order term, and can be used to estimate reduced partition function ratios over a wider temperature range than that covered by a first-order term alone. This is of considerable importance in applying these approximations to the analysis of reactions involving hydrogen–deuterium exchange, for which all frequency moments are large.

Consider the second-order moment

$$\sum_i (u_{a_i'}^4 - u_{a_i}^4) = \left\{\left(\frac{\hbar}{kT}\right)^2 N_0\right\}^2 [TrG'FG'F - TrGFGF]$$

where G and F are the Wilson kinetic and potential energy matrices, respectively.[29] If Cartesian coordinates are used, then

$$Tr(GFGF) = \sum_i\sum_j \mu_{ii}\mu_{jj}F_{ij}F_{ji} - \sum_i\sum_j \mu_{ii}\mu_{jj}(F_{ii}F_{jj} - F_{ij}^2)$$

$$= [Tr(GF)]^2 - 2\sum_{i>j}\sum \begin{vmatrix} \mu_{ii} & 0 \\ 0 & \mu_{jj} \end{vmatrix} \begin{vmatrix} F_{ii} & F_{ij} \\ F_{ij} & R_{jj} \end{vmatrix}$$

which follows because the G matrix is diagonal in a Cartesian representation and because the first term, $[Tr(GF)]^2$, was added and subtracted from $Tr(GFGF)$. The last term is just the sum of second principle minors of GF and is equal to the sum of binary products of eigenvalues of GF.[16] Thus

$$\sum_i (u_{a_i'}^4 - u_{a_i}^4) = \left(\sum_i u_{a_i'}^2\right)^2 - \left(\sum_i u_{a_i}^2\right)^2 - 2\sum_{i>j}\sum [u_{a_i'}u_{a_j'} - u_{a_i}u_{a_j}]$$

Since the prime refers to the lighter isotope, then, according to a theorem by Rayleigh,[30] $u_{a_i} \geq u_{a_i} \geq 0$ for all modes (in the harmonic approximation) we may write

$$0 \leqslant \sum_i (u_{a_i'}^4 - u_{a_i}^4) \leqslant \left(\sum_i u_{a_i'}^2\right)^2 - \left(\sum_i u_{a_i'}^2\right)^2 \quad (15)$$

Usually, only one species of atom is isotopically substituted in a reaction study and the sums above can be simplified further. In this case using (3) yields an alternative form of (15)

$$\sum_i (u_{a_i'}^4 - u_{a_i}^4) = (1-\delta_2)\left[\left(\frac{\hbar}{kT}\right)^2 N_0 n_s \nabla_\alpha^2 U\right]^2 \times (\mu_\alpha'^2 - \mu_\alpha^2) \quad (16)$$

where

$$0 \leqslant \delta_2 \leqslant 1$$

is a number characteristic of the molecule considered and is introduced to replace the inequality in (15) with an equality, and n_s is the number of equivalent atoms isotopically substituted.

Thus, the atomic force constant $\nabla_\alpha^2 U$ can be used to estimate an upper limit to the second term in (2) so that the partition function ratios can be estimated over a little wider temperature range than that given by the first term alone. The corrections, δ_2, were determined for a series of isotopic pairs (mostly hydrocarbon derivatives) several of which are summarized in Table III. In addition analogous corrections for the higher moments

$$\Sigma(u_{a_i'}^{2N} - u_{a_i}^{2N}) = (1-\delta_N)(\Sigma(u_{a_i'}^2)^N - (\Sigma u_{a_i}^2)^N \quad (17)$$

are also given in this table. As might have been anticipated, the correction, δ_2 in eq 17, is about the same in similar isotopic pairs. The magnitude of this quantity is governed by the force constants around the site of isotopic substitution and the force constants and masses at other sites are less important in determining its magnitude. Apparently this correlation extends beyond the second moment, as well. It would be a little more dangerous, in spite of a strong temptation to do so, to include estimates of the higher moments using the δ_N corrections in the expansion of partition function ratios, because their signs or the bounds on their magnitudes cannot be determined before-

TABLE IV: Modulating Coefficients $\Upsilon(n,m,r)$ for $m = 1, 2$ and a Maximum Frequency of 3257 cm^{-1}

1000/T, °K^{-1}	$\Upsilon(1,1,R)$	$\Upsilon(2,1,R)$	$\Upsilon(2,2,R)$
0.25	0.9829	0.9999	0.9663
0.50	0.9350	0.9979	0.8761
0.75	0.8647	0.9908	0.7547
1.00	0.7824	0.9758	0.6270
1.25	0.6971	0.9519	0.5093
1.50	0.6151	0.9200	0.4086
1.75	0.5400	0.8817	0.3261
2.00	0.4734	0.8390	0.2602
2.25	0.4153	0.7938	0.2080
2.50	0.3652	0.7477	0.1670
2.75	0.3222	0.7018	0.1348
3.00	0.2855	0.6572	0.1094
3.25	0.2540	0.6144	0.0894
3.50	0.2269	0.5738	0.0734
3.75	0.2036	0.5356	0.0607
4.00	0.1835	0.5000	0.0505

hand, except, of course, for diatomic molecules for which $\delta_N = 0$.[31]

For the reactions discussed here, a value of 0.3 will arbitrarily be assigned to δ_2. The actual magnitude of δ_2 is most important in analyzing hydrogen–deuterium isotope effects in which large frequency differences are found, but less important in computing the isotope effects due to heavier atom substitutions because of the much smaller frequency shifts. Consequently, a value of 0.3 for δ_2 seems most appropriate here because H/D isotope effects in only nonacetylenic compounds are investigated.

In order to test the usefulness of this choice for δ_2 and to estimate the temperature range over which the partition function expansion is accurate, an effective first-order modulating coefficient was defined

$$\tau_{eff} \equiv [(24/n_s)/\Sigma(u_{a_i}'^2 - u_{a_i}^2)]\prod_i \left[\frac{\Gamma(u_{a_i})}{\Gamma(u_{a_i}')}\right] \qquad (18)$$

From eq 2, 16, and 18 it is seen that in the approximation considered

$$\tau_{eff} \simeq \tau_1 - (\tau_2/120)(1 - \delta_2)(\hbar/kT)^2 n_\alpha N_0(\mu_\alpha' + \mu_\alpha)\nabla_\alpha^2 U \qquad (19)$$

where, again, n_s denotes the number of isotopically substituted atoms. To evaluate the functions $\Upsilon(2,1,R)$ and $\Upsilon(2,2,R)$ in (14), an expansion parameter ν_{max} must be chosen. Because hydrocarbons are examined here, this parameter is defined by (13) as

$$\nu_{max} \equiv \nu_H = 3257\ cm^{-1}$$

and was computed using the averaged, observed atomic force constant from Table II in eq 5. This frequency is presumably large enough to include all of the normal frequencies of the saturated hydrocarbons and is close to the maximum frequency expected in nonsaturated hydrocarbon derivatives as well. With this choice of ν_{max}, the modulating coefficients τ_i (or $\Upsilon(2,i,R)$, eq 14) become functions of temperature only, and their values are listed in Table IV. For completeness, the first-order function $\Upsilon(1,1,R)$ is also included.

The observed effective modulating coefficient, eq 18, is compared with the second-order estimate, eq 19, in Figure 1. The experimental points in this figure are calculated points using eq 18, and complete sets of normal frequencies for several representative isotopic pairs, taken from

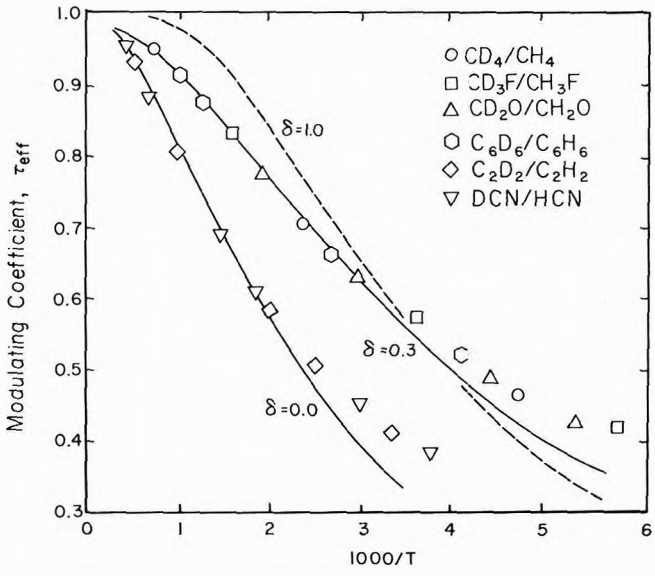

Figure 1. Comparison of observed apparent modulating coefficient, eq 18, with the calculated value, eq 19, for various values of δ_2.

the literature.[32,33] The lines in this figure are graphs of eq 19, using the averaged atomic force constant $\nabla_{H(C)}^2 U$, Table II, and different values for the second-order correction, δ_2.

Several features are noteworthy in this figure. First, the observed or "exact" values for the effective modulating coefficients for these and other CD/CH isotopic pairs (not shown) appear to fall along two distinct curves, one for acetylenic isotope pairs and the other for the other hydrocarbons and their derivatives. This illustrates the rationalization made about the correlation of frequency moments summarized in Table III and supports the hypothesis that isotope effects are determined almost completely by the environment of the sites of isotopic substitution and only weakly influenced by the remainder of the molecule. Second, the graphs of eq 19 reproduce the "exact" effective modulating coefficient quite well. This in turn illustrates the thesis of this paper that the environment of a site of isotopic substitution in a molecule is characterized by a very small number of parameters, the atomic force constant, $\nabla_{H(C)}^2 U$ in this case, and a correction, δ_2, both of which can be estimated with good accuracy without a detailed examination of the potential surface of the specific system considered. Finally, this figure demonstrates that second-order terms in the partition function expansion must be considered if H/D isotope effects are to be analyzed over a usefully wide temperature range. Clearly, the first-order approximation, $\Upsilon(1,1,R)$ in Table IV, is a poor representation of τ_{eff} in (18) below 1000°K. By including rough estimates of δ_2 here, this temperature range is lowered to about 500°K in the case of acetylenic substituted compounds, and to about 400°K for the other hydrocarbons or their derivatives.

Temperature Independent Factor

The determination of the temperature independent factor, $(\nu_a'^*/\nu_a^*)$ in (1), is the crucial step in the analysis of kinetic isotope effects. Its calculation requires that the reaction coordinate in the transition state be identified either by examination of the potential surface for the reactants and products, or, because such detailed infor-

mation is rarely available, simply by postulate. Once such a postulate is made, the limiting frequency ratio ($\nu_{a'}^*/\nu_a^*$) for motion along the reaction coordinate can be computed, atomic force constant changes estimated, and the temperature dependent factors computed as well.

Here the so-called fragment value will be used to estimate the temperature independent factor, which has been discussed extensively in the literature.[12,18] This value is simply the ratio of the normal frequencies for vibration along the reaction coordinate in the limit of vanishingly small force constants for the bonds ruptured by reaction, and is equal to the square root of the inverse ratio of the reduced masses of the resulting fragments.

Calculations

Combining eq 2, 3, 5, and 16, the final approximate, working equation for the kinetic isotope ratio is obtained

$$\ln\left(\frac{k_{a'}}{k_a}\right) \simeq \ln\left(\frac{\nu_{a'}^*}{\nu_a}\right) + \frac{\tau_1}{24}\left(\frac{hc}{kT}\right)^2 n_\alpha(\nu_{\alpha'}^2 - \nu_\alpha^2) - \frac{\tau_2(1-\delta_2)}{2880}\left(\frac{hc}{kT}\right)^4 n_\alpha(\nu_{\alpha'}^4 - \nu_\alpha^4) \quad (20)$$

where τ_1 and τ_2 are defined in (14) and tabulated in Table IV. The quantity δ_2 is arbitrarily given the value 0.3 in the cases studied here and the remaining quantities are defined in (5) and (6).

Three well-studied systems will be considered now to test these approximations. These are hydrogen–deuterium isotope effects in the reactions of fluoryl radicals with isotopically substituted hydrocarbons, the carbon isotope effects in the decomposition of malonic acid, and finally, the nitrogen isotope effects in the decomposition of various azo compounds. Two estimates for the force constant changes are tested, one using the force constants obtained from theoretically estimated electron densities, eq 10, and the other using empirically determined force constants from the analysis of eq 7, and the isotope effects computed from them are then compared with their experimental values.

A. H–D Isotope Effect. The reaction of CF_3 radicals with CHD_3 has been extensively studied by Johnston and his coworkers[5,34,35] from 300 to 4000°K, and their results provide a good test of the approximation scheme described here. The isotope effects studied are the relative rates of extraction of hydrogen to that of deuterium from CHD_3 by way of the transition state

$$CF_3 + CHD_3 \rightleftharpoons [F_3C\cdots H\cdots CD_3]^\dagger \xrightarrow{k_H} F_3CH + CD_3$$

$$CF_3 + CHD_3 \rightleftharpoons [F_3C\cdots D\cdots CHD_2]^\dagger \xrightarrow{3k_D} F_3CD + CHD_2$$

The parameter, $\nabla_H{}^2U - \nabla_H{}^2U\dagger$, for this reaction can be interpreted as the change in force constant resulting from the change in electron density at the hydrogen nucleus, caused by the removal of CD_3 and the approach of the CF_3 group. If it is assumed that in the transition state, the C···H···C internuclear distances are greater than about 1.5 Å, then according to (10) neither fragment contributes a significant charge density at the hydrogen nucleus so that $\nabla_H{}^2U\dagger \simeq 0$. Under this approximation the effective force constant difference between the transition state and reactants is $\nabla_{H(C)}{}^2U$, which may be estimated either empirically from the analysis of (7), or theoretically using (10). In this case the empirical value is 6.30 mdyn/Å, given in Table II, and the estimated theoretical value is 4.94 mdyn/Å, listed in Table I. The apparent frequencies

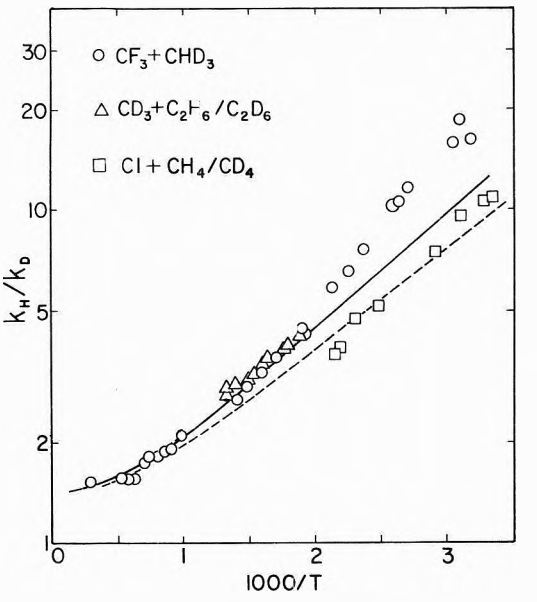

Figure 2. Kinetic isotope ratios for proton extraction from hydrocarbons. Calculated ratios from empirical atomic force constant (—) and from theoretical force constant, eq (10) (---).

for hydrogen and deuterium derived from these force constants using (5) are summarized in Table V.

The remaining parameter (ν_H^*/ν_D^*) was estimated using the familiar *F–G* matrix methods of Wilson,[29] and is also listed in Table V. Here, the ratio (ν_H^*/ν_D^*) was taken as the ratio of the square roots of the G matrix elements corresponding to the vibrational coordinates representing the motion of H or D toward the CF_3 group, taking the fragments as rigid masses in a linear configuration; that is

$$(\nu_H^*/\nu_D^*)^2 = \left[2\mu_H + \frac{1}{2}(\mu_{CF_3} + \mu_{CD_3})\right] \Big/ \left[2\mu_D + \frac{1}{2}(\mu_{CF_3} + \mu_{CHD_2})\right] \quad (21)$$

This factor gives the classical frequency ratio for displacements along the assumed reaction coordinate in the limit of a vanishing C–H force constant, and is consistent with the approximation made above that $\nabla_H{}^2U\dagger \simeq 0$.

The kinetic isotope effect for this reaction was calculated as a function of temperature, using these parameters in eq 20 and the results are graphed in Figure 2, where they are compared with experimental measurements. Two curves are shown, one derived from force constants determined empirically, Table II, and the other from force constants estimated by eq 10, Table I. In both cases the agreement between the calculated and experimental isotope ratios over the temperature range above about 450°K is quite good, especially in view of the fact that no specific assumptions were made about the properties of the transition state other than $\nabla_H{}^2U\dagger \simeq 0$, and those concerned with estimating the temperature independent factor (ν_H^*/ν_D^*).

In addition, these calculations suggest that the temperature dependence of the kinetic isotope effect for all hydrocarbon proton extractions following the same mechanism should be equal, within the fragment approximation. In this approximation the term $\nabla_H{}^2U\dagger$ vanishes, so that the temperature coefficient depends only upon the transferable atomic force constant $\nabla_H{}^2U$. Further, the temperature independent factor is approximately equal to

TABLE V: A Summary of the Parameters Used to Compute the Kinetic Isotope Effect

Reaction		Empirical values (Eq 7)	Theoretical values (Eq 10)
$CF_3 + CHD_3$	$\nabla_H{}^2U - \nabla_H{}^2U\dagger$, mdyn/Å	6.30	4.94
	υ_H, cm^{-1}	3256.8	2883.9
	υ_D, cm^{-1}	2303.8	2040.0
	$(\upsilon_H^*/\upsilon_D^*)$	1.402	1.402
$CH_2(COOH)_2$	$\nabla_C{}^2U - \nabla_C{}^2U\dagger$, mdyn/Å	5.94	4.11
	$\upsilon^{12}C$, cm^{-1}	916.6	762.4
	$\upsilon^{13}C$, cm^{-1}	880.6	732.5
	$\upsilon^{14}C$, cm^{-1}	848.6	705.9
	$(\upsilon^{12}C^*/\upsilon^{13}C^*)$	1.0026	1.0026
	$(\upsilon^{12}C^*/\upsilon^{14}C)$	1.0051	1.0051
$PhCH(CH_3)-N{=}N-X$	$\nabla_N{}^2U - \nabla_N{}^2U\dagger$, mdyn/Å	7.56	6.10
	$\upsilon^{14}N$, cm^{-1}	956.1	860.0
	$\upsilon^{15}N$, cm^{-1}	924.5	830.8

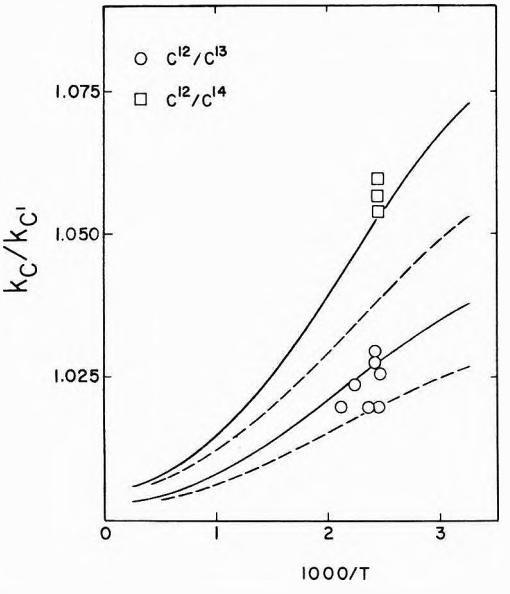

Figure 3. Kinetic isotope ratios for the decomposition of malonic acid. Calculated ratios from theoretical atomic force constant (---) and from empirical force constant (—).

$(\mu_H/\mu_D)^{1/2}$ in the majority of cases, according to (21). As a test, the kinetic isotope effect for the reaction of ethane with methyl radicals[36] is compared with the $CF_3 + CHD_3$ reactions in Figure 2. The kinetic isotope effect for these two reactions are closely equal, as predicted.

Proton extraction by halogen atoms might constitute exceptions to this rule. It has been observed that the temperature coefficient in the kinetic isotope effect for the reactions $Cl + CH_4/CD_4$ is about half that for the fluoryl radical reactions, though in fair agreement with the calculated ratios (see Figure 2) while that for the reactions $Cl + C_2H_6/C_2D_6$ shows essentially no temperature dependence at all.[37] It is possible that the approximation, $\nabla_H{}^2U\dagger \simeq 0$ is not valid, particularly for this last reaction. If, for example, the change in electron density at the proton, due to removal of the hydrocarbon radical, is partially compensated by overlapping the electron density of the halogen in the transition state, the force constant changes will be smaller than in the other reactions considered, and would display a smaller temperature coefficient.

B. $^{12}C/^{13}C$ and $^{12}C/^{14}C$ Isotope Effects. The carbon isotope effects in the decomposition of malonic acid have been fairly extensively studied and have been analyzed by a number of different methods.[8] In each, the reaction is assumed to proceed through a two fragment transition state

$$\begin{array}{l} {}^{*}\mathrm{COOH} \\ | \\ \mathrm{CH_2} \\ | \\ \mathrm{COOH} \end{array} \rightleftharpoons [\mathrm{HOOCCH_2}\cdots {}^{*}\mathrm{COOH}] \xrightarrow{k_C{}^{*}} \mathrm{CH_3COOH} + \mathrm{C^*O_2}$$

$$\mathrm{COOH} \rightleftharpoons [\mathrm{HOOC^*CH_2}\cdots \mathrm{COOH}] \xrightarrow{k_C} \mathrm{CH_3}{}^{*}\mathrm{COOH} + \mathrm{CO_2}$$

The same transition state is assumed here, and the relevant parameters needed for computing the kinetic isotope effect are summarized in Table V. The theoretical estimate of the carbon force constant was taken from Table I, while the empirical estimate is taken to be one-fourth of the observed force constant, $\nabla_C{}^2U$, given in Table II. This fraction was chosen because the transferability of the atomic force constant observed for carbon suggests that each group to which carbon is bonded contribute equally (per electron pair bond) to the magnitude of $\nabla_C{}^2U$.[2]

The kinetic isotope effects derived for this model using (20) are summarized in Figure 3. The isotope ratios computed from the empirically estimated force constants are in generally good agreement with the observed data while those given by the theoretically estimated force constants are consistently lower than the observed ratios for $^{12}C/^{14}C$. In all cases, however, the agreement with experiment seems sufficiently close to constitute a useful analysis of kinetic isotope data for systems of this kind and perhaps to reduce the number of alternative mechanisms to be considered. The negative curvature in the graphs in Figure 3 below 400°K suggest that this is just about the lower temperature limit of eq 20.

C. $^{14}N/^{15}N$ Isotope Effect. The thermal decomposition of a number of α-phenylethylazo derivatives has been extensively studied by Seltzer and his coworkers.[38-40] Primary kinetic isotope effects produced by $^{14}N/^{15}N$ and $^{12}C/^{13}C$, and secondary H/D substitutions were studied in order to distinguish between alternative mechanisms for the decomposition of these compounds, and to establish possible structures for their transition states. Because most of the reactions considered can proceed through more than one plausible transition state, a comparison of calculated kinetic isotope ratios with the observed ratios should provide a good test of the value of this approximation method.

Following the same program as in the other examples, two calculations were carried out, one using empirically

TABLE VI: Calculated Kinetic Isotope Ratios ($^{14}N/^{15}N$), ($^{12}C/^{13}C$), and (H/D) for the Thermal Decomposition of Some α-Phenylethylazo Compounds[a]

	Assumed transition state		k'/k (calcd) (empirical)	k'/k (calcd) (theoretical)	k'/k^b (obsd)
[1]	$PhCH(CH_3)\cdots N^*{=}N{-}CH_3$	434°K	1.030	1.026	
	$PhCH(CH_3)\cdots N{=}N^*{-}CH_3$		1.008	1.008	
			Mean 1.019	1.017	1.013
[2]	$PhCH(CH_3){-}N{=}N^*\cdots CH_3$	434°K	1.022	1.018	
	$PhCH(CH_3){-}N^*{=}N\cdots CH_3$		1.000	1.000	
			Mean 1.011	1.009	
[3]	$PhCH(CH_3\cdots N{=}N{-}C^*H_3$	434°K	1.008	1.008	1.007
[4]	$PhCH(CH_3){-}N{=}N\cdots C^*H_3$	434°K	1.054	1.046	
[5]	$PhCH^*(CH_3)\cdots N{=}N{-}CH_3$	434°K		1.01[c]	
				1.13[d]	
[6]	$PhCH(CH_3)\cdots N{=}N{-}CH_3{}^*$	434°K		1.02[e]	
				0.97[f]	0.97
[7]	$PhCH(CH_3)\cdots N^*{=}N\cdots(CH_3)CH{>}h$	378°K	1.020	1.018	1.023
[8]	$PhCH^*(CH_3)\cdots N{=}N\cdots(CH_3)CH^*Ph$	378°K		1.36[g]	1.27

[a] The substituted atom is denoted by an asterisk. [b] Reference 38. [c] Ratio due to removal of azonitrogen orbitals, see text. [d] Ratio due to apparent increase in C–H length to 1.105 Å, see text. [e] Fragment value, see text. [f] Ratio due to decrease of C–H distance by 0.002 Å, see text. [g] Same parameter used as in case *d*, see text.

determined atomic force constants and the other using theoretical values estimated from eq 10. The empirical value for the nitrogen atomic force constants was taken as 7.56 mdyn/Å, a value equal to one-third of the observed value given in Table II. As discussed above for carbon, this value is assumed to represent the change in $\nabla_N{}^2U$ due to the removal of charge at nitrogen by rupture of one electron pair bond. The theoretical estimates for the force constants were taken from Table I, using the appropriate bond lengths, the apparent frequencies were calculated using (5), and the results are summarized in Table V.

A major purpose in the study of isotope effects in the decomposition of azo compounds is to determine in what order the two C–N bonds are cleaved. Using the data in Table IV, and eq 20, the kinetic isotope ratios for $^{14}N/^{15}N$ and $^{12}C/^{13}C$ substitutions were computed in the fragment approximation for the assumed transition state in the decomposition of azobis-α-phenylethane,[43] and for alternative transition states in the decomposition of α-phenylethylazomethane which represent alternative patterns of bond cleavage. The calculated results are summarized in Table VI, and are compared with observed values. Because the nitrogen isotope in the azo group is assumed to be randomly substituted at either nitrogen site, the geometric mean of the two kinetic ratios is taken to represent the observed ratio.[38]

The decomposition of the azomethane compound is an interesting example of the use of both the $^{14}N/^{15}N$ and $^{12}C/^{13}C$ isotope effects. The kinetic isotope effects for transition states representing cleavage of either the phenylethyl–azo or the methyl–azo bonds in this compound were both calculated, and are listed in Table VI. It was found that the $^{14}N/^{15}N$ isotope ratios are not particularly helpful in discriminating between these two mechanisms. The kinetic isotope effect calculated for transition states [1] and [2] in Table V are roughly equal, 1.019 and 1.011, respectively, as might have been anticipated. In both transition states, an essentially equivalent C–N bond is cleaved which, according to (20), yields the same temperature dependent factor. The difference in the two, then, is determined by the relatively small difference in their temperature independent, reduced mass factors. A comparison with the experimental value of 1.007 for the $^{12}C/^{13}C$ isotope effects calculated for transition states, [3] and [4], definitely supports mechanisms [1] and [3] in which the ethylazo bond is cleaved first.

Other examples of primary isotope effects have been examined for this series of azo compounds, such as in [7], Table VI, for example, and equivalent results were found. Rather than discuss these, secondary kinetic isotope effects in some of these compounds are considered instead.

As pointed out[12,18] temperature dependent secondary isotope effects indicate a change in force constants at a site of secondary isotopic substitution. Such changes can result from the removal of electron density by the leaving group or by structural changes around the substitution site. Equation 8, or its approximation, eq 10, provide a means for estimating the magnitudes of these two effects in the analysis of secondary isotope effects.

Secondary isotope effects were studied in α-phenylethylazomethane by (H/D) substitutions at two different sites, shown in [5] and [6], Table VI. In the reactant, the ethyl C–N and the α-CH bond lengths are about 1.47 and 1.09 Å, as given in Table I, and the nonbonded distance between the α-hydrogen and nearest nitrogen is about 2.10 Å. The change in force constant $\nabla_H{}^2U - \nabla_H{}^2U\dagger$ for the α hydrogen, due to cleavage of the CN bond and removal of nitrogen atom orbitals, is about 0.01 mdyn/Å, as given by eq 10. Using this value a ratio ($k_{\alpha H}/k_{\alpha D}$) of 1.01 is found with a reduced mass fragment value of 1.0017 for the temperature independent factor in eq 20.

Clearly, this value is much too small to account for the observed value of 1.13,[38] given in Table VI. This, in turn, suggests that other structural changes have occurred in the phenylethyl fragment which further reduce the electron density at the substituted α hydrogen. Although the precise nature of these changes cannot be determined without the expenditure of a good deal of computational effort, they are equivalent in effect to an addition decrease in electron density at hydrogen by about 6%. Such a change could result from an increase in the C–H bond length from 1.09 Å to about 1.105 Å in the transition

state. At this distance the atomic force constant for hydrogen is 4.63 mdyn/Å, as given by eq 10, so that $\nabla_H{}^2U - \nabla_H{}^2U\dagger = 4.94 - 4.63 = 0.31$ mdyn/Å for the α hydrogen. Using this value in eq 20, the calculated kinetic isotope ratio is found to be 1.13. The value for both removal of N and elongation of the CH bond is given in [5], Table VI. This particular set of parameters also accounts fairly well for the observed secondary isotope effect due to the substitution of both α hydrogens in azobis-α-phenylethane. For this system eq 20 gives 1.36 for the $k_{\alpha\text{-}H_2}/k_{\alpha\text{-}D_2}$ ratio, transition state [8].

There is little evidence to support the assumption that the α-CH bond would actually be increased by 0.015 Å in the phenylethyl fragment. The CH bond lengths in the planar methyl radical are about 1.08 Å,[41] the same as in ethylene, and any reasonable argument applied to the phenylethyl radical would presumably lead to a similar conclusion regarding the α-CH bond. It is felt nonetheless that the use of atomic force constants here has been of value in equating the magnitude of an isotope effect to an equivalent structural change, and in pointing out that in this case a problem in interpretation might still exist.

The observed magnitude of the secondary isotope effect produced by deuterium substitution of the azomethyl fragment also is equivalent to a small structural change in this fragment. In the absence of any structural changes, the isotope effect predicted from the fragment [6] in Table VI is 1.023, and is significantly larger than the observed effect of 0.97. To account for the observed inverse isotope effect, the electron density at the methyl hydrogens must increase in the transition state. The magnitude of this increase is equivalent to a contraction of the CH bond by only about 0.002 Å. Using eq 10, the atomic force constant for hydrogen at 1.092 Å is about 4.98 mdyn/Å, so that $\nabla_H{}^2U - \nabla_H{}^2U\dagger = -0.04$ mdyn/Å. Using this in the appropriate equations the isotope ratio, k_{H3}/k_{D3}, is reduced to 0.97, Table VI. Again it is not clear that this small apparent decrease in the CH bond length is either real or reasonable. This magnitude is about equal to the difference in the thermally averaged bond lengths for CH and CD, and it does not seem too unreasonable to ascribe this secondary isotope effect to anharmonicity. It should also be pointed out however that force constants changes of the magnitude required to account for these secondary isotope effects are of the same order of magnitude as the uncertainty in observed atomic force constants, and that the above discussion should not be taken too literally.

One final comment will be made concerning the correlation of kinetic isotope effects and structures of transition states. Seltzer and Hamilton[38] analyzed the kinetic isotope effects in these azo compounds using the "exact" method. In the calculations on the azobis compound, the following structural differences between the reactant and transition states were assumed

$$\text{R-C}\overset{1.47\text{ Å}}{\text{---}}\text{N}_1{}^*\overset{1.24\text{ Å}}{=\!=}\text{N}_2\overset{1.47\text{ Å}}{\text{---}}\text{C-R} \quad \text{(reactant)}$$

$$\text{R-C}\overset{1.72\text{ Å}}{\text{- - -}}\text{N}_1{}^*\overset{1.17\text{ Å}}{=\!=}\text{N}_2\overset{1.72\text{ Å}}{\text{- - -}}\text{C-R} \quad \text{(transition state)}$$

and a set force constants, which appeared to be consistent with these structures were chosen or adjusted to reproduce the observed ratios. The other bond lengths and angles in the R groups were assumed to remain unchanged.

It is possible to estimate the effective atomic force constant for nitrogen and compute an isotope effect based on this structure. Changes in electron density at N_1 arise from two sources, the removal of charge density contained in orbitals centered on C by stretching the CN bond to 1.72 Å, and the adding of charge density from orbitals centered on N_2 by shortening the NN bond to 1.17 Å. Using eq 10, the density change due to C orbitals produces a force constant change at N_1 of 4.27 mdyn/Å and that due to N_2 produces a change of −5.94 mdyn/Å, so that $\nabla_N{}^2U - \nabla_N{}^2U\dagger = -1.67$ mdyn/Å, thereby predicting an inverse isotope effect for this reaction, contrary to observation. This points out a major problem in the "exact" method, in that empirical correlations between structure and valence force constants are not yet sufficiently well characterized to deduce a definitive structure for a transition state species.

Conclusions

The calculation of kinetic isotope effects using Bigeleisen and Ishida's theory and atomic force constants shows considerable promise as a means of interpreting chemical reactions and for designing kinetic experiments. These calculations suggest that primary kinetic isotope effects might be predicted with useful accuracy, merely by considering which bonds are cleaved or formed in the reaction. The calculations are quite simple and have an additional advantage over the "exact" method in that the transition state need not be overdescribed. It is not yet clear that the approximations used here are sufficiently good to account for secondary kinetic isotope effects. It should be pointed out, however, that none of the approximations made to compute atomic force constants are irreversible. If necessary, a more refined calculation of these properties can be carried out so that the method described here is only limited in principle by the accuracy with which the higher frequency moments can be estimated.

Acknowledgments. I wish to express my gratitude to Professor John O. Edwards of Brown University, for his many useful discussions on the problems described in this paper, and to Professor Jacob Bigeleisen for his very helpful comments on this manuscript.

References and Notes

(1) R. R. Gaughan and W. T. King, *J. Chem. Phys.*, **57**, 4530 (1972).
(2) W. T. King, *J. Chem. Phys.*, **57**, 4535 (1972).
(3) W. T. King and A. J. Zelano, *J. Chem. Phys.*, **47**, 3197 (1967).
(4) S. Glasstone, K. J. Laidler, and H. Eyring, "The Theory of Rate Processes," McGraw-Hill, New York, N. Y., 1941.
(5) See, for instance, H. S. Johnston, "Gas Phase Reaction Rate Theory," Ronald Press, New York, N. Y., 1966.
(6) J. Bigeleisen and M. Goeppert-Mayer, *J. Chem. Phys.*, **15**, 261 (1947).
(7) J. Bigeleisen, "Proceedings of the International Symposium on Isotope Separation," North Holland Publishing Co., Amsterdam, 1957, Chapter 9.
(8) J. Bigeleisen and M. Wolfsberg, *Advan. Chem. Phys.*, **1**, 15 (1958).
(9) J. Bigeleisen, T. Ishida, and W. Spindel, *J. Chem. Phys.*, **55**, 5021 (1951).
(10) T. Ishida, W. Spindel, and J. Bigeleisen, *Advan. Chem. Ser.*, **No. 89**, 148 (1969).
(11) J. Bigeleisen and T. Ishida, *J. Chem. Phys.*, **48**, 1311 (1968).
(12) M. Wolfsberg and M. J. Stern, *Pure Appl. Chem.*, **8**, 225 (1964).
(13) M. J. Stern and M. Wolfsberg, *J. Chem Phys.*, **39**, 2776 (1963).
(14) See, for example, C. Lanczos, "Applied Analysis," Prentice-Hall, Englewood Cliffs, N. J., 1956.
(15) J. C. Decius and E. B. Wilson, Jr., *J. Chem. Phys.*, **19**, 1409 (1951).
(16) J. Bigeleisen, *J. Chem Phys.*, **28**, 694 (1958).
(17) J. H. Schachtschneider and R. G. Snyder, *Spectrochim. Acta*, **19**, 117 (1963).
(18) See, for instance, W. A. Van Hook, "Isotope Effects in Chemical Reactions," C. J. Collins, Ed., Van Nostrand-Reinhold, New York, N. Y., 1970, Chapter 1.

(19) A. B. Anderson and R. G. Parr, *J. Chem. Phys.*, **53**, 3375 (1970).
(20) A. B. Anderson and R. G. Parr, *Theor. Chim. Acta*, **25**, 1 (1972).
(21) A. B. Anderson, *J. Chem. Phys.*, **58**, 381 (1973).
(22) See, for example, K. Rudenberg, *Rev. Mod. Phys.*, **34**, 326 (1962).
(23) J. A. Pople and G. A. Segal, *J. Chem. Phys.*, **43**, S136 (1965).
(24) J. A. Pople and D. L. Beveridge, "Approximate Molecular Orbital Theory," McGraw-Hill, New York, N. Y., 1970.
(25) These charges were taken from ref 24, p 29. The value for C_1 for hydrogen differs slightly from that used in ref 2.
(26) E. T. Whittaker and G. N. Watson, "Modern Analysis," Cambridge University Press, Cambridge, England, 1965, Section 7-5, 7-6.
(27) Reference 14, Chapter 7.
(28) M. Abramowitz and I. A. Stegun, "Handbook of Mathematical Functions," Dover Publications, New York, N. Y., 1964, Chapter 22.
(29) E. B. Wilson, Jr., J. C. Decius, and P. C. Cross, "Molecular Vibrations," McGraw-Hill, New York, N. Y., 1955.
(30) Lord Rayleigh, "Theory of Sound," Vol. I, reprint, Dover Publications, New York, N. Y., 1945.
(31) The very small, but negative value of δ_2 for the HCN/DCN isotope pair is undoubtedly due to small errors in the observed frequencies or anharmonicity.
(32) T. Shimanouchi, *Natl. Std. Ref. Data Ser., Natl. Bur. Std. (U.S.)*, **6** (1967); **11** (1967); **17** (1968).
(33) B. Crawford, Jr., J. E. Lanchaster and R. G. Inskeep, *J. Chem. Phys.*, **21**, 678 (1953).
(34) T. E. Sharp and H. S. Johnston, *J. Chem. Phys.*, **37**, 1541 (1962).
(35) H. S. Johnston and E. Tshuikow-Roux, *J. Chem. Phys.*, **36**, 463 (1962).
(36) J. R. McNesby, *J. Phys. Chem.*, **64**, 1671 (1960).
(37) G. Chiltz, R. Eckling, P. Goldfinger, G. Huybrechts, H. S. Johnston, L. Meyers, and G. Verbeke, *J. Chem. Phys.*, **38**, 1053 (1963).
(38) S. Seltzer and S. G. Mylonakis, *J. Amer. Chem. Soc.*, **89**, 6584 (1967).
(39) S. Seltzer and E. J. Hamilton, Jr., *J. Amer. Chem. Soc.*, **88**, 3775 (1966).
(40) S. Seltzer, *J. Amer. Chem. Soc.*, **83**, 2625 (1961).
(41) G. Herzberg, *Science*, **177**, 123 (1972).

A New Explanation of the Infrared and Raman ν(XH) Band Shape of Hydrogen-Bonded Complexes

J. Lascombe,* J. C. Lassegues, and P. V. Huong

Laboratoire de Spectroscopie Infrarouge, associé au CNRS, Université de Bordeaux I, 33-Talence, France
(Received July 23, 1973)

Publication costs assisted by the Université de Bordeaux

A theory is proposed to explain the width of the infrared and Raman ν(XH) stretching band of gaseous hydrogen-bonded complexes X-H···Y and to predict the effects of isotopic substitution and temperature. The calculated profiles of the $FH\cdots NCCH_3$ and $FD\cdots NCCH_3$ complexes are then compared with the experimental spectra. The model is extended to interpret the ν(XH) bandwidth of hydrogen bonds in the condensed state.

Introduction

Several theories have been proposed to explain the structure of the stretching band of an XH hydrogen-bonded group.[1-11] In general, it is agreed that the ν(XH) absorption involves many combinations and overtones whose intensities are enhanced by anharmonicity.

In particular, combinations between the ν(XH) vibration and intermolecular modes such as ν(X···Y) where Y represents the proton acceptor are frequently suggested.[2-4] For gaseous complexes between hydrogen chloride and an ether, the assignment of various submaxima in the ν(ClH) absorption to ν(ClH) ± $n\nu$(Cl···O) has recently been made on the basis of intensity measurements over a wide range of temperature.[9-10]

Nevertheless, the various bands composing the whole ν(XH) absorption are always abnormally broad and no satisfactory explanation has yet been given.[11] It seems to us that the broadening could be interpreted in terms of fluctuations. Indeed, in the absence of fluctuations, the various transitions involved would give the normal relatively narrow vibration-rotation bands.

In this paper, we propose a relatively simple model which can explain the band broadening of hydrogen bonds in the gaseous state. This model is then extended to various condensed states.

Profile of the ν(XH) Band of a Gaseous Hydrogen-Bonded Complex

Let us consider an isolated triatomic and linear system X-H···Y with r and R the distances X-H and X···Y and $V(r,R)$ its potential of the Lippincott-Schroeder type.[12] Such a system must give a discrete vibrational spectrum.

Suppose now that the complex is coupled with a thermic bath; one must take into account the coupling potential $W(r,R,\tau)$, where τ is a stochastic variable. This potential induces a broadening of the lines. In this paper only the broadening of the ν(XH) line is treated, but the result can be extended without difficulty to all the lines involving combinations with low-frequency modes, such as ν(XH) ± $n\nu$(X···Y).

In the gaseous state and under low pressures, it is natural to look for the origin of the potential $W(r,R,\tau)$ in the molecular rotations. Because of the relatively heavy mass of a hydrogen-bonded system, its rotational frequencies can be considered as continuous and the problem of band profiles may then be treated in terms of classical mechanics. Such a treatment has given satisfactory interpretation of the smooth profiles of many infrared and Raman band shapes.[13-15]

In this approximation, the total potential V_T of a linear hydrogen-bonded complex can be written as

$$V_T = V(r,R) + \frac{1}{2} I(r,R)\omega^2 \quad (1)$$

where I is the moment of inertia of the system and ω its angular rotational frequency.

At equilibrium, the following equations can be deduced

$$\frac{\partial V(r,R)}{\partial R} + \frac{1}{2}\left[\frac{\partial I(r,R)}{\partial R}\right]\omega^2 = 0 \quad (2)$$

$$\frac{\partial V(r,R)}{\partial r} + \frac{1}{2}\left[\frac{\partial I(r,R)}{\partial r}\right]\omega^2 = 0 \quad (3)$$

$$\frac{\partial^2 V(r,R)}{\partial R^2} + \frac{1}{2}\left[\frac{\partial^2 I(r,R)}{\partial R^2}\right]\omega^2 = k_{X\cdots Y} \quad (4)$$

$$\frac{\partial^2 V(r,R)}{\partial r^2} + \frac{1}{2}\left[\frac{\partial^2 I(r,R)}{\partial r^2}\right]\omega^2 = k_{X-H} \quad (5)$$

where $k_{X\ldots Y}$ and k_{X-H} are respectively the force constant of the X···Y and X–H bonds.

The assumption of relatively slow fluctuation of the vibrational frequencies ω_{XH}, according to Kubo's slow modulation model,[16] leads to a band profile totally determined by the Maxwell-Boltzmann distribution of the rotational frequencies

$$P(\omega_{XH})\ d\omega_{XH} = P(\omega)\left(\frac{d\omega}{d\omega_{XH}}\right) d\omega_{XH} \quad (6)$$

where

$$P(\omega)\ d\omega = \omega \exp\left[-\frac{I\omega^2}{2kT}\right] d\omega \quad (7)$$

The preceding equations can be simplified because the quantities $\partial I/\partial r$, $\partial^2 I/\partial r^2$, and $\partial^2 I/\partial R^2$ are negligible in the useful range of r and R values. So the following relation between the vibrational and rotational frequencies can easily be deduced from eq 2, 3, and 4

$$\omega_{XH} = \omega^0{}_{XH} + a\omega^2 \quad (8)$$

where $\omega^0{}_{XH}$ is the frequency origin corresponding to $\omega = 0$ and a is a factor having the meaning of a vibration–rotation interaction constant.[17]

Equations 6 and 8 lead directly to the distribution function of the Q branch which is Raman active

$$P(\omega_Q)\ d\omega_Q = \frac{1}{2a\omega} P(\omega)\ d\omega_Q \quad (9)$$

while the infrared absorption, due to positive and negative combinations of the vibrational and rotational frequencies (R and P branches), is characterized by the frequencies

$$\omega_R = \omega^0{}_{XH} + \omega + a\omega^2 \quad (10)$$

$$\omega_p = \omega^0{}_{XH} - \omega + a\omega^2 \quad (11)$$

and the probability densities

$$P(\omega_R)\ d\omega_R = \frac{1}{2a\omega + 1} P(\omega)\ d\omega_R \quad (12)$$

$$P(\omega_p)\ d\omega_p = \frac{1}{2a\omega - 1} P(\omega)\ d\omega_p \quad (13)$$

There are several special features of these hydrogen-bond profiles.

(a) Under the influence of the centrifugal force, the R(X···Y) distance increases and, following the Lippincott–Schroeder equation, there is a corresponding decrease of the r(X–H) distance, so the a value is always positive. This is in contrast with the usual negative value of the vibration–rotation interaction constant α of a covalent rotor.[17]

(b) This a value is high because of the unusual weakness of the hydrogen bond (bond energy of the order of one-tenth of a normal covalent bond energy) and the large dependence of the vibrational frequency ν(XH) on the R(X···Y) distance.[18,19] The quantity $a\omega^2$ is therefore usually greater than ω.

(c) A discontinuity appears in the classical spectrum when $\omega = 1/2a$ corresponding to the band head of the P lines in the quantum mechanical treatment as recently shown by Thomas and Thompson.[6] This singularity is damped by taking into account the inherent slit function of the spectrometer. Convoluting the above profiles with a rectangular slit function of width β, the calculated profile is finally given by

$$I_{(\nu)} = N\left[\int_{\nu_R - \nu^0{}_{XH} - \beta/2}^{\nu_R - \nu^0{}_{XH} + \beta/2} P(\nu_R)\ d\nu_R + \int_{\nu_p - \nu^0{}_{XH} - \beta/2}^{\nu_p - \nu^0{}_{XH} + \beta/2} P(\nu_p)\ d\nu_p\right] \quad (14)$$

where the frequencies ν are expressed in cm^{-1}.

This model leads to the following predictions.

(a) There is a slight decrease of the frequency at the maximum but a noticeable narrowing of the band width on cooling 0.07 cm^{-1}/deg as indicated by eq 12, 13, and 14. These predictions agree with the experimental data we have recently obtained by a temperature study of the ν(ClH) band of the gaseous ClH···$O(CH_3)_2$ complex.[9] Previous work has also indicated that the position of the ν(XH) band maximum of various other complexes does not vary with temperature.[20,21]

(b) The Raman band becomes narrower by a factor of $\sqrt{2}$ on deuterium substitution as indicated by eq 9. For the infrared bandwidth, the isotopic ratio is between 1 and $\sqrt{2}$, its value depends on the relative importance of ω with respect to a $a\omega^2$.

Calculation of the ν(FH) Band Profile for the Gaseous FH···$NCCH_3$ Complex and Comparison with Experimental Data

(*a*) *Experimental Infrared Spectrum.* The FH···$NCCH_3$ gaseous complex has a relatively simple spectrum in the ν(FH) stretching region[3,22,23] with only a weak and well-separated ν(FH)–ν(F···N) combination band at 3500 cm^{-1} (Figure 2A). Recently Thomas[7] has reported for the same complex another sideband at about 3850 cm^{-1}. This may be due to the HF dimer[22,23] or to the FH···FH···$NCCH_3$ complex. However, these discrepancies are not important here since we are only concerned with the profile of the main ν(FH) absorption.

(*b*) *Calculated Infrared Profile from the Proposed Model.* The gaseous FH···$NCCH_3$ complex can be taken as a linear rotor[23] to a good approximation and a Lippincott–Schroeder potential function $V(r,R)$ can be used, where $V(r,R)$ is given by

$$V(r,R) = D_0\left\{1 - \exp\left[\frac{-n(r - r_0)^2}{2r}\right]\right\} - D_0{}^* \exp\left[-\frac{n^*(R - r - r_0{}^*)^2}{2(R - r)}\right] + A\left\{\exp(-bR) - \frac{R_0}{2R}\exp(-bR_0)\right\}$$

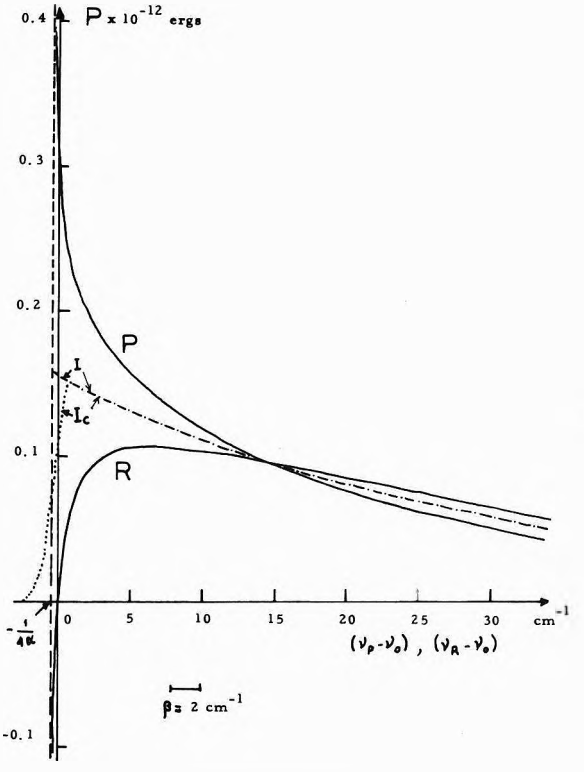

Figure 1. Distribution functions for ν(FH) profile of the FH···NCCH$_3$ gaseous complex: I is the half-sum of the P and R branches; I_c is the profile obtained after convoluting of I with a rectangular slit of 2 cm^{-1}.

TABLE I: Parameters Used in the Lippincott–Schroeder Potential of the FH···NCCH$_3$ System

Parameter		Ref
D_0, kcal/mol	135	17
$n \times 10^{-8}$, cm^{-1}	9.39	
$n^* \times 10^{-8}$, cm^{-1}	13.60	
$r_0 \times 10^8$, cm	0.9171	12
$r_0^* \times 10^8$, cm	1.014	12
$K_0 \times 10^{-5}$, dyn/cm	9.59	17
$K_0^* \times 10^{-5}$, dyn/cm	6.42	12
$b \times 10^{-8}$, cm^{-1}	4.8	12
m	1	12

The symbols are the same as in ref 12 and the parameters used are given in Table I. At equilibrium, *i.e.*, $\omega = 0$, the following set of values is obtained: $A = 2.38 \times 10^{-7}$ erg, R(F···N) = 2.695 Å, r(F–H) = 0.946 Å, and ν(F···N) = 166 cm^{-1}. The ν(FH) frequency has been chosen at the maximum of the main absorption (3652 cm^{-1}). The moment of inertia has been evaluated using the geometrical parameters of free acetonitrile[24] and the calculated values of R and r. The quantity $\partial I/\partial R$ is found equal to 17.88×10^{-31} g cm and the a value is 0.58 cm^{-1} for the hydrogenated complex and 0.427 cm^{-1} for the deuterated one.

The calculated profile and its convolution with a 2-cm^{-1} rectangular slit are shown in Figure 1 and compared with the ν(FH) experimental spectrum in Figures 2A.

Both profiles show the same intensity change on the high-frequency side in contrast with the sharp intensity change on the other side. The calculated profile is narrower than the experimental band, but only the main ν(FH)

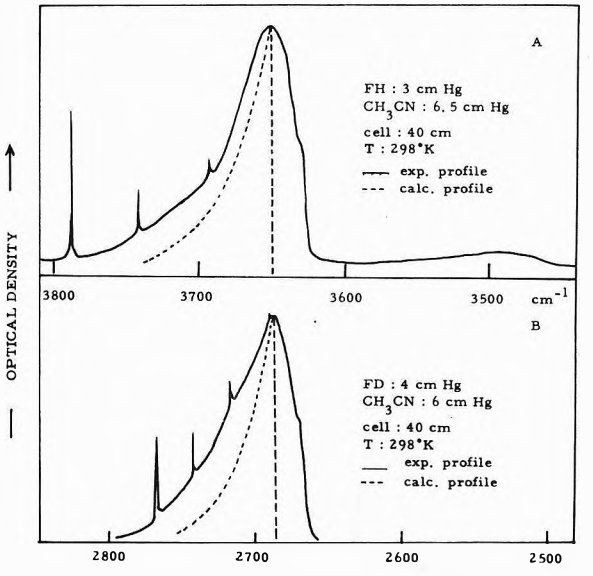

Figure 2. Experimental and calculated profiles of the absorptions ν(FH) of the FH···NCCH$_3$ gaseous complex and ν(FD) of the FD···NCCH$_3$ gaseous complex. In the experimental profile, the spectrum of free acetonitrile is cancelled.

transition is taken into account in the calculation. The fit would perhaps be improved with other values of the parameters and also by using a more general potential $V(r,R,\theta)$ where θ is the X-H···Y angle.[25] Furthermore, the whole absorption in the ν(FH) as well as in the ν(FD) region (Figure 2B) certainly involves combinations with intermolecular bending modes[5,6,26] which contribute to the broadening. Weak shoulders are observed in both experimental spectra at about 3630 and 3715 cm^{-1} for FH···NCCH$_3$ and 2670 cm^{-1} for FD···NCCH$_3$. However, the main conclusion is that the present model, based on the simple effect of the centrifugal forces on the rotating complex, gives a more basic mechanism and a larger broadening effect than any other previous proposals.

The ν(XH) Band of Hydrogen Bonded Complexes in Condensed States

In Figure 3 is shown the ν(ClH) infrared absorption of the ClH···O(CH$_3$)$_2$ complex in solution and in various solid matrices at low temperature.

In these condensed states all the spectral features are broad and no submaxima can definitively be distinguished in contrast with the appearance of ν(ClH) ± $n\nu$(Cl···O) combinations in the gas-phase spectrum. Furthermore, the frequency of the absorption maximum depends now strongly on the physical state and the temperature. Finally, the bandwidth appears to depend drastically on the processing of the sample; for example, for the complex isolated in solid SF_6, a broadening of about a factor of 2 is noticed going from the spectrum of a slowly solidified solution to that obtained by a deposit of the gas mixture on a cold window.

These results show that in the condensed state the potential of a hydrogen bond must still be represented by an expression of the type

$$V_T = V(r,R) + W(r,R,\tau)$$

where the stochastic potential W is no longer due to free molecular rotations but to the interactions with the surrounding medium, the random parameter τ representing

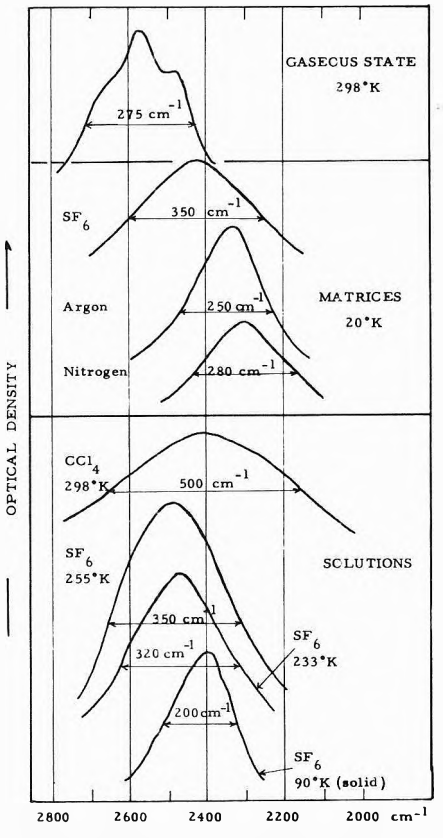

Figure 3. Infrared profile ν(ClH) of the $ClH\cdots O(CH_3)_2$ complex at various physical states and temperatures.

the configurations of the neighboring molecules. A similar formulation has recently been proposed by Hadzi, *et al.*,[27] making use of the Lippincott–Schroeder potential function and of a thermal distribution of the $R(X\cdots Y)$ distance in the liquid phase.

The wide range of experimental conditions used for the $ClH\cdots O(CH_3)_2$ complex provide qualitative but more general information. For example, the ν(ClH) frequency of this complex is higher in an SF_6 matrix than in an argon matrix at the same temperature of 20 K, in contrast with the normal decrease observed for ClH monomer.[28] This unexpected behavior of the complex is related to the different "cage effects" of the various matrices on the geometry of the hydrogen bond and particularly on the $R(X\cdots Y)$ distance. The smaller cavities of the argon matrix imply a shorter $R(X\cdots Y)$ distance and a lower ν(ClH) frequency.

The width of the ν(ClH) band, on the other hand, depends strongly on temperature in the liquid state and on the order of the surrounding molecules in the solid state. This is illustrated by the narrower bandwidth obtained in a slowly solidified SF_6 solution compared with a SF_6 gas mixture trapped on a cold window, the latter being a much less ordered medium. Nevertheless, in both cases, the broadening is large enough to smooth out the sidebands of the gas-phase spectrum. To obtain narrow bands requires highly ordered crystals.[8]

Conclusion

The large infrared and Raman bandwidth of the ν(XH) stretching vibration of a hydrogen-bonded complex has been explained on the basis of a fluctuating potential function.

For the gas-phase spectrum, the broadening is essentially due to the fluctuations of the $R(X\cdots Y)$ distance resulting from the molecular rotations of the complex considered as a nonrigid rotor.

In the condensed state, important variations both in the frequency and in the bandwidth are interpreted by means of an interaction potential between the complex and the surrounding medium. The frequency shift is due to the mean value of this potential while the bandwidth is associated with the fluctuations of the potential and therefore reflects the disorder of the surrounding medium.

References and Notes

(1) S. Bratoz, D. Hadzi, and N. Sheppard, *Spectrochim. Acta*, **8**, 249 (1956).
(2) J. E. Bertie and D. J. Millen, *J. Chem. Soc.*, 497, 514 (1965).
(3) J. Arnold and D. J. Millen, *J. Chem. Soc.*, 503, 510 (1965).
(4) Y. Marechal and A. Witkowski, *J. Chem. Phys.*, **48**, 3697 (1968).
(5) Y. Grenie, J. C. Cornut, and J. C. Lassegues, *J. Chem. Phys.*, **55**, 5844 (1971).
(6) R. K. Thomas and H. W. Thompson, *Proc. Roy. Soc., Ser. A*, **316**, 303 (1970).
(7) R. K. Thomas, *Proc. Roy. Soc., Ser. A*, **325**, 133 (1970).
(8) A. Lautie and A. Novak, *J. Chem. Phys.*, **56**, 2479 (1972).
(9) J. C. Lassegues and P. V. Huong, *Chem. Phys. Lett.*, **17**, 444 (1972).
(10) J. E. Bertie and M. V. Falk, Paper 17, International Conference on Hydrogen Bonding, Ottawa, Canada, 1972.
(11) G. N. Robertson, Thesis, Oxford, 1970.
(12) R. Schroeder and E. R. Lippincott, *J. Phys. Chem.*, **61**, 921 (1957).
(13) H. Shimizu, *J. Chem. Phys.*, **43**, 2453 (1965).
(14) S. Bratos, J. Rios, and Y. Guissani, *J. Chem. Phys.*, **62**, 439 (1970).
(15) S. Bratos and E. Marechal, *Phys. Rev. A*, **4**, 1078 (1971).
(16) R. Kubo, "Fluctuation, Relaxation and Resonance in Magnetic Systems," Ter Haar, Ed., Oliver and Boyd, Edinburg, 1962, p 23.
(17) G. Herzberg, "Infrared and Raman Spectra," Van Nostrand, New York, N. Y., 1965.
(18) K. Nakamoto, M. Margoshes, and R. E. Rundle, *J. Amer. Chem. Soc.*, **77**, 6480 (1955).
(19) W. C. Hamilton and J. A. Ibers, "Hydrogen Bonding in Solids," W. A. Benjamin, New York, N. Y., 1968.
(20) E. Osawa and Z. I. Yoshida, *Spectrochim. Acta, Part A*, **23**, 2029 (1967).
(21) S. A. Rice and J. L. Wood, *J. Chem. Soc., Faraday Trans. 2*, **69**, 87 (1973).
(22) M. Couzi, J. Le Calve, P. V. Huong, and J. Lascombe, *J. Mol. Struct.*, **5**, 363 (1970).
(23) M. Couzi and P. V. Huong, *C. R. Acad. Sci.*, **270**, 832 (1970).
(24) I. Nakagawa and T. Shimanouchi, *Spectrochim. Acta*, **18**, 513 (1962).
(25) P. V. Huong and G. Turrell, *J. Mol. Spectrosc.*, **25**, 185 (1968).
(26) P. V. Huong and A. Graja, *Chem. Phys. Lett.*, **13**, 162 (1972).
(27) A. Azman, B. Borstnik, and D. Hadzi, *J. Mol. Struct.*, **8**, 315 (1971).
(28) J. B. Davies and H. E. Hallam, *Trans. Faraday Soc.*, **67**, 3176 (1971).

Exchange Reactions of Benzene on a Fuel Cell Electrode at Cathodic Potentials

H. J. Barger, Jr.,* and A. J. Coleman

Electrochemical Division, U. S. Army Mobility Equipment Research and Development Center, Fort Belvoir, Virginia 22060
(Received June 20, 1973)

Publication costs assisted by the Fort Belvoir Technical Library

The electrochemical reactions of C_6H_6 in D_3PO_4 were studied at electrode potentials ranging from 0.15 to −0.10 V measured against the dynamic hydrogen electrode. The effects of flow rate and reaction temperature were examined. Results indicated that the adsorption potential was important in determining the amount of reduction and that flow rate has a marked effect on the isotopic distribution of benzene and cyclohexane. Readsorption of product cyclohexane was shown to occur but was not a major factor in determining isotopic distributions. The relative amount of deuteriocyclohexanes produced using C_6H_{12} as the reactant suggested two types of exchange reactions were occurring.

Introduction

In an earlier paper,[1] we examined the hydrogen–deuterium exchange of benzene on a fuel cell electrode *vs.* a dynamic hydrogen electrode[2] over the potential range 0.45–0.20 V, a region where hydrocarbon oxidation occurs. The electrode potential was shown to have a marked effect on the amount of exchange and on which deuterio isomers were produced. This paper extends the potential range into the region where reduction becomes an important reaction.

Experimental Section

Apparatus and Materials. The electrochemical cell, controlling circuitry, and reactant flow system were described earlier.[1,3] A Perkin-Elmer 154D vapor fractometer was added to the flow system down stream from the cell. The effluent gases could be diverted either into the mass spectrometer or into the gas chromatograph. The initial reactant concentrations in the carrier gas were determined by diverting the gas mixture around the cell and into the gas chromatograph where the peak area could be compared to the area from a standard. The concentration of reactant (0.93 μmol/cc was generally used for benzene and 1.06 μml/cc for cyclohexane) varied less than 1% with carrier gas flow rate. The potential of the working electrode was measured *vs.* the dynamic hydrogen electrode (dhe) and potentiostatically controlled to ±1 mV. Potentials in the text are reported *vs.* the dhe.

Deuteriobenzene, 99.5 atom %, was purchased from Bio-Rad Laboratory, Richmond, Calif. The electrolyte, 85% D_3PO_4 99 atom %, and perdeuteriocyclohexane, 99 atom %, were both purchased from Isomet, Oakland, N. J. The D_3PO_4 was preelectrolyzed prior to use. The H_3PO_4 used had been treated with H_2O_2 and preelectrolyzed.[4] Acid concentrations were maintained at 85% by bubbling helium presaturated with appropriate concentrations of D_2O or H_2O into the cell.

Experimental Procedures. The mass spectrometric and data acquisition techniques were described previously.[1] All spectra were taken at low voltage, *ca.* 9.4 V, to minimize fragmentation of the parent molecules. At this ionizing voltage, no fragmentation of the deuteriobenzenes was observed between m/e 78 and 84. Cyclohexane was observed to have small $M - 1$ peaks, approximately 3% of the parent peak. In those experiments where both C_6H_{12} and C_6D_6 were likely constituents of the cell effluent, m/e 69 was used to determine the contribution of C_6H_{12} to m/e 84. All spectra were corrected for naturally occurring ^{13}C and deuterium. Sensitivity values for C_6H_6, C_6D_6, C_6H_{12}, and C_6D_{12} were determined from pure samples or known mixtures of the compounds. Relative values were computed based on the sensitivity of C_6H_6 being equal to one. Sensitivity values for deuterated species other than perdeuterio compounds were estimated from the difference between the nondeuterated and perdeuterated compounds by assuming a linear relationship between sensitivity and the number of deuterium atoms in the molecule.[5] Fragmentation corrections for the deuteriocyclohexanes could not be determined for each species since the isomers were not available in pure form. The inlet pressure was reduced so that the contribution to the $M - 1$ or $M - 2$ peaks to a corresponding parent would be very small.

The pretreatment of the working electrode consisted of a series of potential steps to remove impurities or previous adsorbates and a galvanostatic pulse to measure the electrochemical surface area. Two slightly varying experimental procedures were followed after the electrode pretreatment. In the first, a gas mixture of reactant and carrier is passed through the cell cavity at a constant flow rate. The working electrode was potentiostated at various potentials, and a mass spectrum of the effluent was recorded at each potential. In the second method, the electrode was potentiostated at a desired value, and the flow rate was varied with a mass spectrum taken at each flow rate. The agreement of the data obtained from the two methods was within experimental error (±5%). All mass spectra were taken after the electrode reached steady state; steady state being judged to occur when the cell current became constant after a potential or flow rate change, usually 60 to 90 sec. The computer was programmed to record two mass spectra at each potential and output the average.

Results and Discussion

Preliminary experiments at electrode adsorption potentials in the range −0.10 to +0.05 V with benzene as the reactant and D_3PO_4 as the electrolyte produced mass peaks of differing magnitude at most mass numbers be-

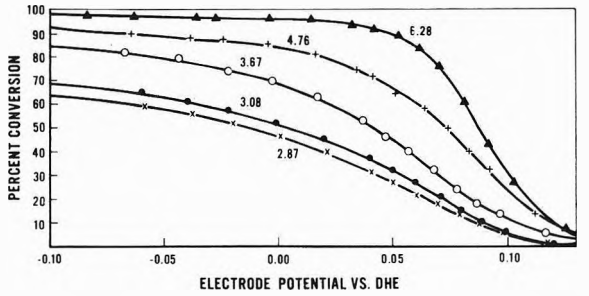

Figure 1. Per cent conversion of benzene to cyclohexane as a function of potential at several mean cavity times. Mean cavity time (m^2 sec) is defined as cell cavity volume times electrode surface area divided by flow rate.

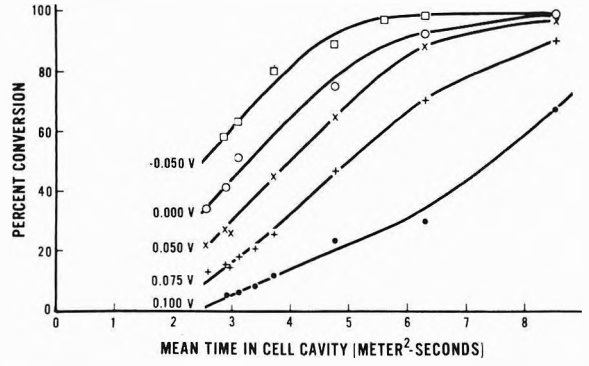

Figure 2. Per cent conversion of benzene to cyclohexane as a function of mean time in cell cavity for several adsorption potentials.

tween 78 and 96. Without knowing what the reaction products were at each potential, the task of sorting out the reaction processes seemed very formidable. Therefore we studied the reduction of benzene with H_3PO_4 as the electrolyte under conditions planned later with D_3PO_4. The effect of adsorption potential on benzene conversion to cyclohexane is shown in Figure 1 for a number of flow rates. These data were replotted to show the effect of flow rate on conversion. Figure 2 shows a number of these plots for experiments performed at 70°. Very similar plots were obtained over the temperature range 65–110°. These reactions seem to be more dependent on flow rate than on reaction temperature. The curvature of the plots in Figure 2 is probably related to flow limitations in the case of low potentials and to multiple reactant adsorption at the high potentials; readsorption would increase the probability that a reduction site on the catalyst would be reached before the molecule was swept out of the cell cavity. The most important finding from these experiments was that only cyclohexane was produced in reducing benzene. This agrees with the results of Langer and Yurchak[6] but contrasts with electrochemical reductions where solvated electrons are thought to be involved;[7] in the latter case 1,4-cyclohexadiene is produced. Thus within the limits of our experimental detectability, the mass peaks between 84 and 96 were derived from deuterio isomers of cyclohexane and not deuterio isomers of cyclohexene or cyclohexadiene.

The effect of benzene concentration on the amount of cyclohexane produced was examined by using a number of benzene–cyclohexane concentrations as the reactant. Results at 0.00 V, typical of the reducing potentials, are shown in Figure 3. The amount of cyclohexane produced is seen to be independent of the initial benzene concentra-

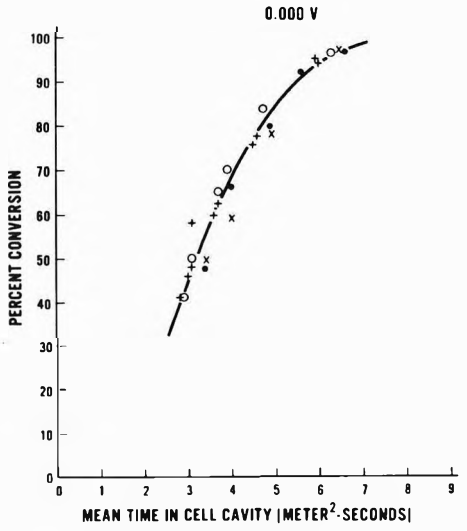

Figure 3. Per cent conversion at 80° of benzene to cyclohexane for various benzene–cyclohexane mixtures (in mol % benzene): 55, O; 78, +; 91, ×; 100, ●.

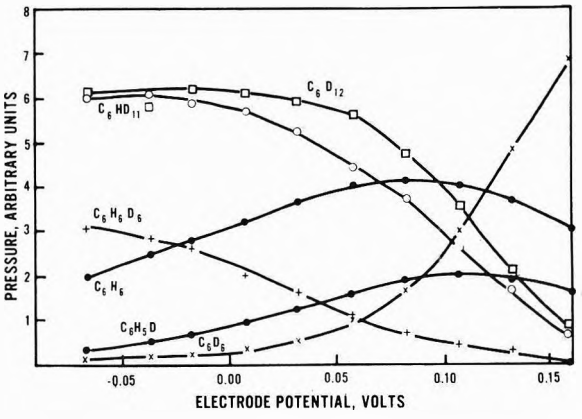

Figure 4. Effect of adsorption potential on the relative concentrations of selected species.

tion which means the reaction occurs on the catalyst surface rather than in the gas phase.

With this background, we studied the exchange and reduction of benzene using C_6D_6 in H_3PO_4 electrolyte and C_6H_6 in D_3PO_4 electrolyte. The experiments in D_3PO_4 are discussed first. Table I gives distributions for all compounds and deuterio isomers at several potentials and flow rates. The potentials are representative of regions where reduction is the predominant reaction, 0.00 V and below; where comparable amounts of exchange and reduction products are produced, 0.05 V; and where exchange is more important, 0.15 V. Flow rate is seen to have an important effect on product distribution. At the slowest flow rate, more than 95% of the reactant molecules exposed to the catalyst underwent some type of reaction. For a given potential, the trend toward the highly deuterated compounds at the slow flow indicates a portion of the molecules readsorbed on the catalyst surface after undergoing exchange or reduction. Note the small amounts of highly deuterated cyclohexanes which were always present at 0.15 V even at the fast flow rates. These results, obtained at 70°, are typical of those obtained over the range 60–110°. Figure 4 shows the relative concentrations of C_6H_6, C_6H_5D, C_6D_6, $C_6H_6D_6$, C_6HD_{11}, and C_6D_{12} as a function of adsorption potential at 70° and a flow rate of 1.73 ml/sec which computes to a mean time in the cell cavity of 0.614

TABLE I: Distribution of Benzene and Cyclohexane Isotopic Species from the Exchange and Reduction of Benzene with D_3PO_4 Electrolyte at Various Potentials and Mean Cavity Times at 80°

Mean time in cavity, m^2 sec	Electrode potential, V	Mass numbers															
		78	79	80	81	82	83	84	88	89	90	91	92	93	94	95	96
5.47	0.15	2.3	1.3	1.5	1.8	4.4	15.6	54.3							1.4	5.5	11.8
	0.05	3.0	0.9	0.6	0.5	0.5	0.6	7.0			8.2	5.5	5.1	4.9	12.8	22.9	27.5
	0.00	2.1	0.8							4.8	9.4	7.9	7.4	7.9	10.3	25.2	24.2
	−0.05	1.7	0.5						2.3	5.7	13.5	9.7	7.4	7.1	11.7	18.2	22.2
3.58	0.15	14.9	7.5	6.8	6.9	9.0	16.5	31.2							1.5	2.4	3.4
	0.05	14.8	5.9	3.8	2.6	2.1	2.4	3.3		1.9	3.9	4.2	4.2	5.3	8.1	16.6	20.8
	0.00	11.0	3.2	1.5	0.9	0.6	0.8	1.1	1.1	3.5	6.9	6.2	5.8	6.8	10.6	19.4	20.6
	−0.05	8.1	1.6	0.7	0.3	0.3	0.4	0.5	1.4	4.7	9.4	7.3	6.5	6.9	11.8	20.5	19.6
2.68	0.15	21.5	7.5	6.4	6.5	8.9	16.5	26.8	0.9						1.1	2.0	1.8
	0.05	22.5	7.6	5.3	4.1	3.7	4.2	5.0		1.5	2.3	2.8	3.5	4.6	7.7	12.6	12.7
	0.00	20.6	5.7	3.2	2.1	1.6	1.6	1.9	1.0	2.5	5.1	5.0	4.9	5.9	9.6	14.6	14.5
	−0.05	15.4	3.4	1.6	0.9	0.6	0.7	0.9	1.3	4.1	8.2	6.8	6.3	6.7	10.6	16.2	16.3

TABLE II: Distribution of Benzene and Cyclohexane Isotopic Species from the Exchange and Reduction of C_6D_6 in H_3PO_4 Electrolyte at Various Flow Rates and Electrode Potentials at 80°

Mean time in cavity, m^2 sec	Electrode potential, V *vs.* dhe	Mass numbers														
		78	79	80	81	82	83	84	84[a]	85	86	87	88	89	90	91
6.45	0.09	22.8	6.5	3.2	2.7	3.2	4.5	16.5	28.6	6.6	2.0	1.2	0.7	0.8	0.7	
	0.05	4.7	1.8	0.8	0.8	1.3	2.6	12.6	44.3	12.1	4.4	2.7	2.9	3.8	5.2	
	0.00	1.4	0.5	0.2	0.2	0.5	1.3	10.5	40.7	13.0	5.1	3.6	4.3	6.5	12.2	
	−0.05	0.6	0.2	0.0	0.0	0.2	0.8	9.5	36.8	12.5	5.5	3.9	4.9	8.0	17.1	
3.87	0.09	17.1	4.7	2.4	2.2	3.0	4.7	29.1	26.3	5.2	1.6	1.2	0.8	0.8	0.9	
	0.05	6.3	2.0	0.9	0.8	1.7	3.3	27.3	35.5	8.6	2.9	1.9	1.8	2.9	4.1	
	0.00	2.5	0.7	0.4	0.4	0.9	2.2	25.0	34.8	9.7	3.9	3.2	3.3	4.7	8.2	
	−0.05	1.5	0.4	0.2	0.2	0.6	1.7	23.5	32.6	9.7	4.1	3.6	3.9	6.1	11.9	
3.01	0.09	15.7	4.2	2.4	2.3	3.2	5.2	39.5	19.9	3.9	1.4	0.5	0.7	0.5	0.6	
	0.05	6.3	1.8	1.1	1.0	1.8	3.8	36.0	28.5	6.7	2.4	2.1	2.0	2.7	3.8	
	0.00	2.9	0.8	0.5	0.4	1.2	2.7	33.8	29.5	8.2	3.2	2.3	2.8	4.1	7.6	
	−0.05	1.6	0.6	0.4	0.3	1.1	2.1	32.9	28.5	8.0	3.3	1.8	3.4	5.3	10.6	

[a] This m/e 84 represents C_6H_{12} while the former is C_6D_6.

sec. Although the reactant input to the cell was held constant during the course of the experiment, the concentration of C_6H_6 in the effluent increased as the electrode potential was lowered from 0.15 tc about 0.07 V and then declined with a further decrease in adsorption potential. The concentration of C_6D_6 in the effluent falls to a barely detectable level as the potential is reduced from 0.15 to −0.05 V. While the concentration of C_6D_6 is falling, the amount of C_6HD_{11} and C_6D_{12} in the effluent are increasing. Beyond 0.00 V, these concentrations become constant. The behavior of $C_6H_6D_6$ is different from that of the other compounds in Figure 4. Its concentration remains low to about 0.07 V and then increases at a moderate rate as the potential is lowered further.

Although there are no distinct breaks over the voltage range studied (Figure 4) these results are discussed in terms of three regions: 0.15 to 0.07 V, 0.07 to 0.00 V, and potentials below 0.00 V. Considering the more anodic range first, hydrocarbon adsorption is not as favored on the electrode as between 0.20 and 0.30 V.[8] This is shown by the increasing concentration of unreacted benzene in the effluent. Benzene that does adsorb ungoes single or multiple exchange in the manner described previously.[9] A few active sites are available for reduction. Most of the molecules reaching these sites have already undergone exchange which results in highly deuterated cyclohexanes. This latter reaction is sensitive to flow rates as noted in the discussion of the reduction of C_6H_6 in H_3PO_4 above. In the intermediate potential range, both exchange and exchange with reduction are occurring although the former is much less favored as shown by the rapidly decreasing concentration of C_6D_6. Reduction sites are apparently numerous in this region. $C_6H_6D_6$, which probably results from the reduction of reactant benzene without prior exchange, increases as the potential is lowered. Thus reduction alone is becoming comparable to exchange alone. Below 0.00 V the great majority of intermediates on the catalyst are reduced prior to emerging from the cell. The lower cyclohexanes, $C_6H_5D_7$ (91) to C_6HD_{11} (95), are formed in appreciable concentrations as a result of reduction of partially exchanged benzene.

A few experiments were conducted using H_3PO_4 as the electrolyte and C_6D_6 as the reactant. In general, the data produced were in agreement with the above discussion. Selected results at several potentials and flow rates are shown in Table II. Again the isomer or isomers comprising peak 90 ($C_6H_6D_6$) increased as the adsorption potential was lowered as in Figure 4, indicating that reduction without prior exchange was occurring. No compounds were detected with masses higher than m/e 90 which means that reduction of reactant C_6D_6 with HD or D_2 (from exchanged deuterium on the catalyst) was not an

TABLE III: Isotopic Distribution of Deuteriocyclohexanes for the Exchange of C_6H_{12} in D_3PO_4 Electrolyte at Various Flow Rates and Electrode Potentials at 80°

Mean time in cavity, m^2 sec	Electrode potential, V vs. dhe	Isotopic species												
		d_0	d_1	d_2	d_3	d_4	d_5	d_6	d_7	d_8	d_9	d_{10}	d_{11}	d_{12}
5.72	0.095	73.5	4.7	1.8	1.6	1.6	2.2	3.5	1.8	1.4	1.3	1.5	2.2	3.0
	0.050	58.7	6.2	2.4	2.5	2.6	3.5	6.1	3.2	2.2	2.2	2.5	3.6	4.3
	0.000	54.5	6.8	2.8	2.7	1.6	4.5	6.8	3.6	2.6	2.6	3.0	4.0	4.4
4.14	0.095	81.4	3.8	2.2	1.1	1.2	1.5	2.2	1.1	1.0	0.8	1.0	1.0	1.7
	0.050	73.5	4.9	1.8	1.6	1.7	2.3	3.7	2.0	1.3	1.4	1.4	2.1	2.3
	0.000	67.9	5.7	2.1	1.9	2.2	3.0	4.7	2.4	1.8	1.7	1.8	2.2	2.6
3.35	0.095	85.3	3.3	1.4	0.9	1.0	1.1	1.6	0.9	0.7	0.7	0.8	0.9	1.2
	0.050	78.6	4.1	1.4	1.5	1.4	1.9	2.8	1.6	1.4	1.0	1.2	1.4	1.7
	0.000	75.1	4.9	1.7	1.6	1.7	2.4	3.6	1.8	1.2	1.2	1.5	1.6	1.7
2.73	0.095	89.3	2.8	1.0	0.8	0.6	1.0	1.3	0.7	0.5	0.0	0.5	0.7	0.9
	0.050	84.7	3.4	1.3	0.9	1.1	1.3	1.8	1.0	0.9	0.9	1.0	1.0	0.9
	0.000	80.8	4.1	1.5	1.2	1.4	1.7	2.6	1.4	1.0	1.0	1.1	1.0	1.2

important factor. Thus the small peaks at m/e 88 and 89, Table I, are probably derived from the fragmentation of higher molecular ion peaks.

The magnitude of the trend toward completely exchanged cyclohexanes observed in these experiments was surprising and caused us to wonder whether or not further exchange of product cyclohexanes occurred so as to skew the isotopic distribution. To test this possibility, cyclohexane (C_6H_{12}) was passed across the electrode in the presence of D_3PO_4 at a number of different flow rates and adsorption potentials. Temperatures in the 60–100° range had little effect on the reaction. Parravano[10] in studying the transfer of hydrogen between benzene and cyclohexane also observed that temperature had little effect on the reaction. Typical distributions are shown in Table III. These results indicate that cyclohexane can undergo exchange although the reaction is not prevalent, especially at fast and moderate flow rates. Therefore the further exchange of product cyclohexanes is not a major factor in the distribution of the deuteriocyclohexanes in Table I.

Considering again the data in Table III, the isotopic distribution of the exchange products shows a maximum at mass number 85 corresponding to a single hydrogen exchange and other maxima at 90 and 96 which result from the exchange of 6 and 12 hydrogen atoms, respectively. These results offer an insight into the nature of the reaction intermediates. It appears there are two types of reactions, one involving single exchange and the other in which six hydrogens are exchanged. The intermediate in this latter reaction may be very similar to one derived from the parallel adsorption of benzene on to the catalyst.[9] The stability of this intermediate which probably has some aromatic character could provide the driving force for the dehydrogenation of cyclohexane. Thus to form $C_6H_6D_6$ and C_6D_{12}, peaks 90 and 96, respectively, we suggest that reactant cyclohexane adsorbs on the electrode, positions itself on the catalyst so that it dehydrogenates to a C_6H_6 intermediate, is reduced to $C_6H_6D_6$ at the low adsorption potentials, desorbs, and passes out in the cell effluent or readsorbs after flipping over to expose the six hydrogen atoms to the electrode, whereupon the above steps would be repeated producing C_6D_{12}.

Over the past 35 years, the hydrogen–deuterium exchange of cyclohexane has been studied under a variety of nonelectrochemical conditions. The concentrations of $C_6H_{11}D$, $C_6H_6D_6$, and C_6D_{12} were often found to be higher than those of other deuterio isomers. A number of investigators have speculated about reaction intermediates and reaction mechanisms.[11-14] The scheme suggested by Rooney[13] is similar to our suggestions above except that we believe the π bound intermediate can lead to multiple exchange. A test for our hypothesis would be to compare under electrochemical conditions the relative exchange tendency of cyclopentane, which could not form an aromatic intermediate, to that of cyclohexane.

References and Notes

(1) H. J. Barger, Jr., and A. J. Coleman, *J. Phys. Chem.*, **75**, 3175 (1971).
(2) J. Giner, *J. Electrochem. Soc.*, **111**, 376 (1964).
(3) H. J. Barger, Jr., and M. L. Savitz, *J. Electrochem. Soc.*, **115**, 686 (1968).
(4) S. B. Brummer and M. J. Turner, *J. Phys. Chem.*, **71**, 2825 (1967).
(5) See J. R. Anderson and C. Kemball, *Advan. Catal.*, **9**, 51 (1957), for an alternate procedure.
(6) S. H. Langer and S. Yurchak, *J. Electrochem. Soc.*, **116**, 1228 (1969).
(7) (a) A. Misono, T. Osa, T. Yamagishi, and T. Kodama, *J. Electrochem. Soc.*, **115**, 226 (1968); (b) H. W. Steinberg, R. E. Markby, I. Wender, and D. M. Mohilner, *J. Amer. Chem. Soc.*, **89**, 186 (1967).
(8) M. L. Savitz and R. L. Carreras, *Advan. Chem Ser.*, **No. 90**, 188 (1969).
(9) (a) J. L. Garnett and W. A. Sollich-Baumgartner, *J. Phys. Chem.*, **68**, 3177 (1964); (b) H. J. Barger, Jr., and A. J. Coleman, *ibid.*, **74**, 880 (1970).
(10) G. Parravano, *J. Catal.*, **16**, 1 (1970).
(11) A. A. Balandin and B. S. Gudkov, *Probl. Kinet. Katal. Akad. Nauk SSSR*, **12**, 130 (1968); *Chem. Abstr.*, **69**, 90515Y (1968).
(12) R. L. Burwell, Jr., B. K. C. Shim, and H. C. Rowlinson, *J. Amer. Chem. Soc.*, **79**, 5142 (1957).
(13) J. J. Rooney, *Chem. Brit.*, **2**, 242 (1966).
(14) C. Kemball, *Advan. Catal.*, **11**, 223 (1959).

Immersion Method for the Potential of Zero Charge Determination. An Electrode Pretreatment

Sang Hyung Kim[1]

Department of Chemistry, University of Pennsylvania, Philadelphia, Pennsylvania 19104 *(Received November 6, 1972; Revised Manuscript Received July 9, 1973)*

We describe experimental details of an attempt to improve obtaining a *zero charge* state of the electrode in the immersion method for the potential of zero charge (E_z) determination. The attempt utilizes a preimmersion treatment in a dry space separated from the solution by a thin Teflon tape, through which the rapid immersion takes place. The treatment in the dry space consists of heat treatment with hydrogen and argon, and washing with water as well as drying with argon. The present method with *dry* electrodes yields more negative E_z values for gold and nickel than the earlier immersion methods with *wet* electrodes.

Introduction

The immersion method has been developed by Jakuszewski and Kozlowski[2-6] to determine the potentials of zero charge (E_z)[7] of solid metal electrodes. This method has been studied further by Jendrasic[8] to determine the surface charge of the electrodes. Matsuda, Damjanovic, and Bockris[9] have recently applied a rapid immersion technique to the ionic adsorption measurements at solid metal–solution interfaces.

The immersion technique involves rapid immersion of a clean and dry electrode into an electrolyte solution and measurement of the charging current required to form the electric double layer at the preset electrode potential. E_z of the electrode corresponds to the potential at which no charging current flows. The interference of faradaic reactions in the charging current measurement can be minimized by immersing the electrode as rapidly as possible. At the preimmersion state the electrode should have *zero charge* condition. Therefore, the adsorbed gas from the preimmersion environment should not interact with the electrode or alter natural electrode–solution double layer structure.[7]

In the previous studies[2-6,8,9] the electrode was dried in an inert gas atmosphere above the test solution before immersion. The electrode dried in this way could be covered by moisture films, which might cause some local cell reactions on the surface and thus result in a departure from *zero charge* at the preimmersion state especially in the case of active metals. Such uncertainties of the preimmersion environment of the electrodes leave doubt in the previous immersion methods.[7,10] It is probably due to some cathodic faradaic reactions of adsorbed films that the E_z values by earlier immersion methods[2,8] are more positive than those by other methods for gold[11-19] and nickel[15,20] electrodes. In this paper we report an attempt to improve obtaining *zero charge* state of the electrode before immersion. The electrode is prepared in a dry space separated from the test solution by a thin Teflon tape, through which the rapid immersion is performed without any prior contact with water vapor or air. The attempts were applied for gold and nickel electrodes.

Experimental Section

An one-compartment cell and an electrode preparation column above the cell shown in Figure 1 were separated by a thin Teflon tape, M (Almac plastics of Penna., 0.005 in. thick[21]), between "O" ring glass joints (18/9) with a Viton "O" ring sitting on the upper side of the tape. The preelectrolyzed solution, S, was filled up to the tape. About 50-cm long test electrode, T, made of ground glass precision bore tubing (0.25 in. o.d.) was prepared above the tape in inert atmosphere and then immersed through the tape, M. The rapid immersion of the test electrode was obtained with a speed of 100 ~ 200 cm/sec by the application of magnetic field from a solenoid (Model 149-1, Dormeyer Industries, Ill.) on a metal bar holding the upper end of the test electrode.[9] The potential of the test electrode, controlled by a potentiostat (Tacussel PIT 20-2X) with a platinum counter electrode, C, was measured by a Keithley electrometer with respect to a palladium–hydrogen electrode, R. The charging current at a given preset electrode potential was recorded on a Tektronix 564 storage oscilloscope with 3B3 time base and 3A3 amplifier. A standard resistor (1 kΩ) was connected in the platinum counter electrode circuit. The surface charge of the electrode was obtained by graphical integration of the current–time curve by means of a planimeter (Keuffel and Esser).

The nickel and gold wire electrodes (1 mm diameter, 2 cm long) were prepared in the following ways. Nickel wire[22] was spot welded to a thick tungsten wire connected to a long copper wire. The tungsten wire was sealed to the Pyrex glass first, then the nickel–tungsten joint was slightly covered by a Pyrex glass (a few mm), and finally a long ground glass precision bore tubing was connected. The nickel electrode was dipped in dilute HCl to remove nickel oxides, and washed with conductivity water. Then the electrode was placed in the furnace, F, and heated in argon for 5 to 60 min at 300° to remove moisture, then in hydrogen for 5 to 15 min at 300° to reduce the oxides if any, then again, in argon for 20 min at 450° to diffuse the absorbed hydrogen, and finally in cold argon in the cooling compartment, U, with water-cooled condenser for 10 min.[23] Gold wire[22] electrode was made by a "house-keeper" seal.[24] The gold electrode, initially cleaned with hot 1 *M* HCl, hot 2 *M* H_2SO_4, and distilled water, was placed in F, and was heated in argon for 20 min at 300°, in hydrogen for 15 min at 300°, in argon for 20 min at 450°, and then in cold argon in U for 10 min.[23] Once the electrode

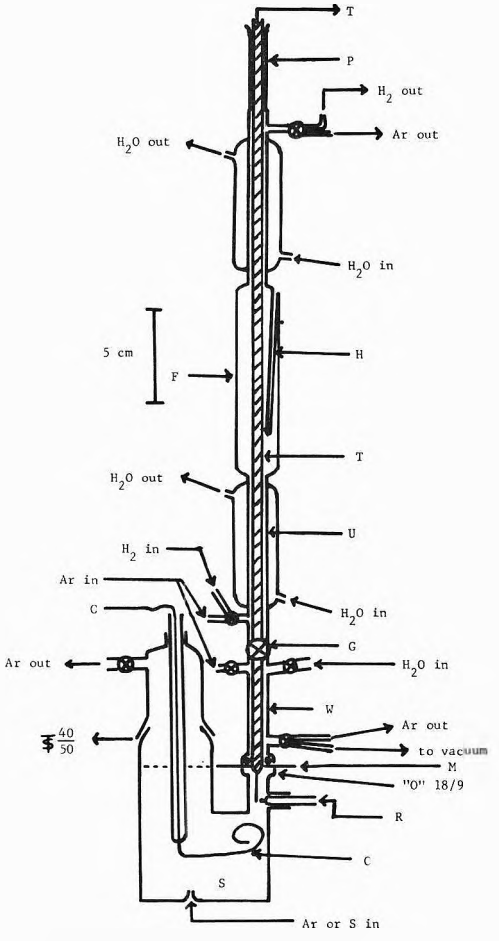

Figure 1. Cell and electrode preparation column.

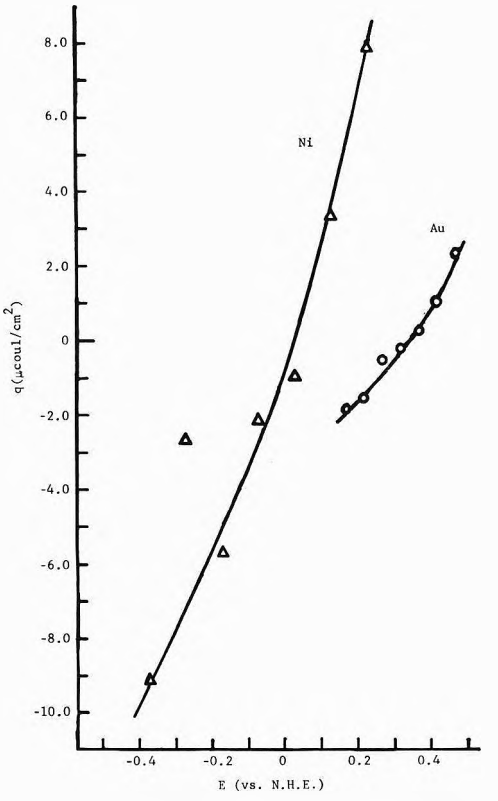

Figure 2. The measured charge (q) of the electrode *vs.* electrode potential (E *vs.* nHe): gold in 10^{-3} M $HClO_4$ (pH 3) and nickel in 10^{-4} M $HClO_4$ (pH 12). The charge, q ($\mu C/cm^2$) is based on geometric area.

was purified in the above ways, the 6-mm Teflon stopcock, G (widened to 8-mm bore), was opened and the electrode was immersed through the tape, M, into the solution. Precision bore tubing, P (0.25 in. i.d.), provided a dynamic seal. The end of the electrodes was pointed by grinding on silicone carbide paper so that it could punch through the tape easily.

After each measurement a new tape was placed by pulling the punched tape. While replacing it, argon was blown around the tape and cell in addition to the positive pressure applied inside the cell. The electrode was washed with predeaerated conductivity water in the washing compartment, W, a few times and dried in a cold argon stream in U. Then the above heating procedure was repeated so that the electrodes were prepared with identical treatments. The stopcock, G, was closed, and the water in the washing compartment, W, was removed and evacuated by using a duo-seal vacuum pump (0.1 μ) through a Dry Ice–acetone trap. The furnace, F, was made of flexible heating tape wrapped around Pyrex tubing and insulated by an asbestos sheet and insulating cloth. The temperature of the furnace was regulated by a powerstat and measured by a clomel–alumel thermocouple inserted in a housing inside furnace, H. All connections were made of Fisher solv-seal joints and Teflon stopcocks.

Prepurified argon gas (5 ppm O_2) was further purified by passing over two copper turning tubings, two molecular sieve columns (Linde 13X), and further molecular sieve columns cooled down to −75° by a Dry Ice–acetone mixture. Prepurified hydrogen was also further purified by passing it through a Surfass hydrogen purifier (Milton Roy Co., Model CH-A). Solutions were made of reagent grade chemicals and with conductivity water. All glassware was cleaned with 1:1 concentrated HNO_3–concentrated H_2SO_4 mixture and rinsed with conductivity water. The measurements were performed in an open laboratory (28 ± 3°).

Results and Discussion

The charging current measurements were performed for the gold electrode in 10^{-3} M $HClO_4$ (pH 3) and the nickel electrode in 10^{-4} M $HClO_4$ (pH 12). The measured excess charges (q) of the electrodes were averaged from two (for Au) and two to nine (for Ni) measurements at each potential. The ranges of error in q are up to ±0.3 and ±2.5 $\mu C/cm^2$ for Au and Ni, respectively. The worse reproducibility for Ni may be due to its high reactivity with water vapor at high temperature and a fast faradaic reaction such as dissolution of Ni.[25] Figure 2 shows the measured q of gold and nickel electrodes as a function of electrode potential. The measured potentials at q = 0 of gold (0.34 V) and nickel (0.03 V) may correspond to the respective E_z's in the absence of specific adsorption (all potentials are *vs.* nHe). The E_z's are estimated to be ±0.05 V.

The reported values of E_z for gold from the least adsorbing solutions vary from 0 to 0.4 V.[11-19] The present result for gold is in good agreement with capacitance[18,19] and organic adsorption[12,15] methods. By an immersion method, however, Jendrasic[8] reported more positive E_z than our value and the failure of the E_z measurement of gold in 0.1 M $HClO_4$ due to the nonequilibrium between the solution and the electrode surface.

The measured E_z of nickel is about 0.3 V more positive than other data from capacitance,[15,20] organic adsorption,[15] and friction[15] methods from neutral and alkaline solutions. By an immersion method, Jakuszewski and Kozlowski[2] however obtained +0.193 V for 0.01 *M* KCl solution. Due to the specific adsorption of the Cl^- ions,[7,26] their value may be more positive than our result by more than 200 mV.

The present method with *dry* electrodes gives more negative E_z's for both gold and nickel than the earlier immersion methods[2,8] with wet electrodes. This is in good agreement with the expectation that the *dry* immersion method minimizes some cathodic faradaic reactions probably due to adsorbed films on the *wet* electrode. However, the E_z values by the present method are also more positive than those by other *in situ* methods[11,13-17,20] determining E_z especially for the case of nickel. It seems unlikely that the adsorbed argon on the electrode in the present method may alter the natural electrode–solution double layer structure. The cause of the above discrepancy between our method and other *in situ* methods may be due to differences in preparation methods of the electrode, electrode surface conditions due to different duration of contact of the electrode with solution (the latter methods employ a prolonged contact), etc. At present, the exact cause of the positive shift of our E_z values from the other *in situ* methods[11,13-17,20] is not well understood. Nevertheless, since we are more likely to remove spurious faradaic reactions, it is desirable to work with *dry* electrodes rather than *wet* electrodes in the immersion method; however, there still may be a remaining cathodic faradaic process of unknown origin.

The present pretreatment of the electrode at each potential takes more than 1.5 hr. This shortcoming weakens the immersion method whose advantage is the rapidity of the measurements. Other faster pretreatment than ours, if any, should be employed. The present method with *dry* electrodes provides the E_z's of gold and nickel to be closer to the other methods[11-20] and more negative than the earlier immersion methods[2,8] with *wet* electrodes.

Acknowledgment. The author wishes to express his appreciation to Dr. J. O'M. Bockris for his suggestions, discussions, and support of this work. The author is indebted to Drs. Y. Matsuda and A. Damjanovic for their help, suggestions, and discussions during the beginning period of this work. The author also wishes to thank the members of the Electrochemistry Laboratory of University of Pennsylvania for useful discussions. This work was supported by the Office of Naval Research.

References and Notes

(1) Present address, Biomedical Engineering Center, Technological Institute, Northwestern University, Evanston, Ill. 60201
(2) B. Jakuszewski and Z. Kozlowski, *Rocz. Chem.*, **36**, 1873 (1962).
(3) B. Jakuszewski and Z. Kozlowski, *Rocz. Chem.*, **38**, 93 (1964).
(4) B. Jakuszewski and Z. Kozlowski, *Soc. Sci. Lodz. Acta Chim.*, **9**, 25 (1964).
(5) B. Jakuszewski and Z. Kozlowski, *Soc. Sci. Lodz. Acta Chim.*, **10**, 5 (1965).
(6) Z. Kozlowski and B. Jakuszewski, *Soc. Sci. Lodz. Acta Chim.*, **11**, 5 (1966).
(7) R. S. Perkins and T. N. Andersen in "Modern Aspects of Electrochemistry," Vol. 5, J. O'M. Bockris and B. E. Conway, Ed., Plenum Press, New York, N. Y., 1969. This review includes a complete reference on the potentials of zero charge.
(8) V. Jendrasic, *J. Electroanal. Chem.*, **22**, 157 (1969).
(9) Y. Matsuda, A. Damjanovic, and J. O'M. Bockris, unpublished work.
(10) R. S. Perkins, R. C. Livingston, T. N. Andersen, and H. Eyring, *J. Phys. Chem.*, **69**, 3329 (1965).
(11) G. M. Schmid and N. Hackerman, *J. Electrochem. Soc.*, **109**, 243 (1962); **110**, 440 (1963).
(12) M. Green and H. Dahms, *J. Electrochem. Soc.*, **110**, 466, 1075 (1963).
(13) D. D. Bode, T. N. Andersen, and H. Eyring, *J. Phys. Chem.*, **71**, 792 (1967).
(14) M. Petit and J. Clavilier, *C. R. Acad. Sci., Ser. C.*, **265**, 145 (1967).
(15) J. O'M. Bockris, S. D. Argade, and E. Gileadi, *Electrochim. Acta*, **14**, 1259 (1969).
(16) I. Morcos, *J. Colloid Interface Sci.*, **37**, 410 (1971).
(17) M. Shimokawa and T. Takamura, *J. Electroanal. Chem.*, **32**, 314 (1971).
(18) A. Hamellin and J. Lecoeur, *Collect. Czech. Chem. Commun.*, **36**, 714 (1971).
(19) J. P. Carr and N. A. Hampson, *J. Electrochem. Soc.*, **119**, 325 (1972).
(20) L. V. Volkov, A. F. Ponomarev, and B. P. Yurev, *Tr. Leningrad Politekh. Inst.*, **304**, 94 (1970); *Chem. Abstr.*, **73**, 83099v (1970).
(21) The per cent absorption of water for 24 hr is nil for the Teflon film with thickness up to 0.125 in. ("Modern Plastics Encyclopedia," 1972–1973, p 343.) The tapes thinner than 0.005 in. could not hold the vacuum we used.
(22) 99.99% pure gold and 99.95% pure nickel wires were obtained from A. D. McKay, Inc., New York, N. Y.
(23) S. D. Argade, Ph.D. Dissertation, University of Pennsylvania, 1968. Heating time in argon at 450° in this work is shorter than Argade's. However the same calculation as Argade's showed a negligible amount of hydrogen ($\sim 5 \times 10^{-8}$ g atom/cm^3) present in nickel after heat treatment. Rough calculation gave about 0.1 μC/cm^2 error in actual measurements which is within the error range of the present data.
(24) B. Cahan, Ph.D. Dissertation, University of Pennsylvania, 1968.
(25) T. N. Andersen, J. L. Anderson, D. D. Bode, Jr., and H. Eyring, *J. Res. Inst. Catal. Hokkaido Univ.*, **16**, 449 (1968).
(26) E. I. Mikhailova and Z. A. Iofa, *Elektrokhimiya*, **6**, 231 (1970).

Mean Activity Coefficients for the Simple Electrolyte in Aqueous Mixtures of Polyelectrolyte and Simple Electrolyte. The System Sodium Polystyrenesulfonate–Sodium Chloride

Jan C. T. Kwak

Department of Chemistry, Dalhousie University, Halifax, Nova Scotia, Canada *(Received June 18, 1973)*

Publication costs assisted by the National Research Council of Canada

Mean ionic activity measurements of NaCl are reported in the aqueous system Na polystyrenesulfonate–NaCl. An emf method with AgCl electrodes and a cation-exchange membrane or sodium ion glass sensitive electrode was used. NaPSA concentrations range from 0.004 to 0.06 *m*, NaPSA/NaCl ratios from 33 to 0.09. The results for log $\gamma_{\pm}$(NaCl) are compared to a form of the additivity rule relating log $\gamma_{\pm}$ to ϕ_p (osmotic coefficient of the pure polyelectrolyte) and to a theoretical "limiting law" derived by Manning. The experimental data can be described by one form of the additivity rule, using ϕ_p from vapor pressure data reported in the literature. Up to X ($= m_{NaPSA}/m_{NaCl}$) = 8 the theoretical value of $\gamma_{\pm}$ calculated with Manning's equation compares well to the data, if an extrapolation to zero ionic strength is made. In mixtures with a large excess of polyelectrolyte $\gamma_{\pm}$ is larger than the theoretical value.

Activity data for the simple electrolyte in the presence of a polyelectrolyte are needed, *e.g.*, to describe transport properties of ion-exchange membranes,[1] or to calculate salt activities in biological fluids. The additivity rule, originally formulated for hydrogen ion activities in mixtures of poly(vinyltoluene)styrenesulfonic acid and HCl[2] has been extended to all polyelectrolyte–simple electrolyte mixtures to describe counterion activity,[3-6] osmotic pressure and osmotic coefficients,[7,8] and mean ionic activity of the simple electrolyte.[5,7] A number of reviews discuss applications and short comings of the additivity rule.[9-12] In the case of relating the mean ionic activity of the added salt, $\gamma_{\pm}$, to the osmotic coefficient of the pure polyelectrolyte, ϕ_p, and the activity coefficient of the pure simple electrolyte, $\gamma_{\pm}^0$, the extrathermodynamic assumption equating ϕ_p to the counterion activity coefficient, γ_+, of the pure polyelectrolyte is not well justified,[9,13] and the choice for the ionic strength used in calculating $\gamma_{\pm}^0$ is ambiguous. Oosawa,[11] for example, does not include the polyelectrolyte contribution in the total ionic strength employed to calculate $\gamma_{\pm}^0$; Alexandrowicz[7] and Marinsky[10] include a fraction $\phi_p m_p$ of the polyelectrolyte molality m_p in the total ionic strength. Experimental justification for equating ϕ_p to γ_+ has come from comparison of "single ion activity" data for the counterion with ϕ_p measurements,[9] and from experimental verification of the additivity rule. Even if we neglect the problems inherent in single-ion activity determinations, especially in systems containing colloids or polyions,[5,14-16] the data quoted in Figure 3 of ref 9 are hardly convincing. Significant deviations from additivity for γ_+ have been found by Lyons and Kotin[4] and by Podlas and Ander.[6] The last authors find deviations in the region of excess polyelectrolyte. In this concentration region the osmotic coefficient of the mixture of course becomes insensitive to the activity of the added electrolyte, and osmotic or vapor pressure measurements can no longer yield accurate information on the activity of the simple electrolyte, or on the validity of the additivity rule. Donnan exclusion measurements in this concentration region are hampered by poor reproducibility of the salt concentration determinations, caused by interference of the polyelectrolyte or simply by the low salt concentration to be determined. This leaves emf measurements as the most suitable technique in mixtures with excess polyelectrolyte as well as in the region of low total concentration.

Manning[13] has derived a relation between log $\gamma_{\pm}$ of the simple electrolyte and the polyelectrolyte–simple electrolyte concentration ratio X. His relation is a limiting law in the sense that it applies to a hypothetical system of fully stretched polyions at low mobile ion concentrations, neglecting interactions between the fixed ionic groups on different parts of the polymer backbone. In reality, as the mobile ion concentration is decreased, interactions between the polyion fixed charges will become important, and the infinite cylinder model may no longer apply. The mean ionic activity measurements of the added electrolyte described in this paper, allow us to compare the results for log $\gamma_{\pm}$ to ϕ_p. The emf method used can provide data for log $\gamma_{\pm}$ in the low total concentration region as well as in mixtures with a large excess of polyelectrolyte, without relying on single ion activities.

High-quality data for the osmotic coefficient of sodium polystyrenesulfonate, NaPSA, and several other cationic forms of this polyelectrolyte anion have been published[17-20] and counterion activities have been studied.[4] Polystyrenesulfonic acid can be fully converted to the salt without hydrolysis problems. These considerations make salts of this polyion especially suited for further investigations of thermodynamic properties. The following electrochemical cell is used

Ag/AgCl	NaPSA + NaCl	cation exchange membrane or Na^+ selective glass	NaCl reference solution	AgCl/Ag

Measurements using the Na^+ selective ion electrode are used as a check for the generally more accurate measurements using a cation exchange membrane strip. In both cases the NaCl activity in the mixture is obtained by comparing the measured potential to a reference curve obtained with a solution of NaCl only.

Experimental Section

Sodium polystyrenesulfonate was kindly supplied by the Dow Chemical Co., Midland, Mich. (designation NC-1585, average molecular weight given as 500,000). Recrystallization with 2-propanol, dialysis, and ion exchange were tried to purify the original sample. The purification procedure finally adopted consisted of running an impure NaPSA solution through cation and anion exchange columns in series (Dowex 50W-X8 cation exchange resin and Dowex ANGA542 anion resin, respectively). Then the HPSA is titrated with NaOH to pH 7, using small samples of the solution for pH determinations. The resulting NaPSA solution is dialyzed for 2 days and freeze dried from a rotary evaporator to a stock solution of about 0.25 *m*. Water content of the stock solution was determined by drying a sample to constant weight. The Na^+ concentration was determined by ion exchanging a preweighed sample to HPSA followed by titration with NaOH. Repeatability of the equivalent weight of NaPSA determined from samples of the same stock solution was within 1% maximum deviation.

Complete removal of electrolyte impurities, especially halides, is crucially important in this work. No halide impurities could be detected in the NaPSA stock solution using $AgNO_3$ directly in the solution or in the ethanol extract after the solid NaPSA had been removed. Spiking the solution with small amounts of NaCl and NaBr again failed to detect halide impurity but established a detection limit of 0.1 mol % halide impurity. This means that in the mixture with the largest excess of polyelectrolyte (m_{PSA}/m_{NaCl} = 33) the halide impurity could at maximum contribute 3% to the NaCl concentration. Conductance measurements on NaPSA–NaCl mixtures performed in this laboratory[21] indicate that the simple electrolyte impurity is well below this upper limit. Contamination by nonionic low molecular weight material, important in osmotic measurements, is not very important in emf measurements, but should still be largely removed during the dialysis and freeze drying steps.

Double distilled water was used in all solutions. Ultrapure NaCl (Ventron Corp., Beverly, Mass.) was dried at 600°. Mixtures of NaPSA and NaCl were made by weight from the NaPSA stock solution and a 0.1 *m* NaCl stock solution. Maximum error in the NaPSA molality is estimated at ±0.3% (based on the repeatability of the concentration determinations), the NaCl molality is accurate to ±0.1%. This means that the uncertainty in log $\gamma_\pm$ caused by the uncertainty in the Na^+ and Cl^- concentration generally is about ±0.005.

In order to obtain a measurement series at constant $X(= m_{NaPSA}/m_{NaCl})$ and with decreasing ionic strength, a series of seven NaPSA–NaCl mixtures with m_{NaPSA} = 0.062 and X ranging from 33 to 1 was diluted with water (weight method) in successive steps.

AgCl electrodes of the conventional thermoelectrolytic type were used.[22] Electrodes were made up in batches of six. Asymmetry potentials within a batch were less than 50 μV. The electrodes show a slightly longer equilibration period when transferred from a NaCl solution to a NaPSA containing solution. The electrodes generally behave well in the relatively dilute polyelectrolyte solutions used. In more concentrated solutions (above 0.1 *m* NaPSA) an increased light sensitivity was noticed, which seemed to be reversible. For this reason the membrane cell described below was taped and contained in a black box. Upon returning an AgCl electrode to NaCl after use in a measurement series with polyelectrolyte solutions, the potential difference measured against an aged AgCl reference electrode was generally less than 200 μV. The membrane strip cell, described in detail in an earlier communication,[23] basically consists of two electrode wells separated by a membrane strip of 4 × 1 cm. The membrane is a C-322 (American Machine and Foundry Comp., Stamford, Conn.) fluorocarbon base cation-exchange membrane (sulfonate active group). One well is filled with 0.01 *m* NaCl, the other with the appropriate NaCl solutions to obtain a calibration curve, or with the NaPSA–NaCl mixture. With this arrangement problems arising from concentration polarization across a thin membrane are eliminated. Reproducibilities are well within 0.4 mV, normally only one calibration curve is necessary for a complete measurement series. In order to check results with the ion-exchange membrane, all measurements were repeated with a Na^+ selective glass electrode (Corning Glassworks, Corning, N. Y.) instead of the membrane. Reproducibilities with this electrode are less than with the ion-exchange membrane, resulting in a larger uncertainty in the log $\gamma_\pm$ values. Good agreement between the two cells was obtained over the whole concentration range. One typical series is shown in Table II. All other results given are measured with the ion-exchange membrane cell.

Potentials were measured using a K-4 potentiometer (Leeds and Northrup, North Wales, Pa.) and a 150-B null detector (Keithley Instruments, Cleveland, Ohio). The glass electrode potential was measured on the potentiometer as well, using the unity gain output of a 134 electrometer (Princeton Applied Research Corp., Princeton, N. J.).

Results and Discussion

Results for log $\gamma_\pm$(NaCl) in 58 mixtures of NaPSA and NaCl, with m_{NaPSA} ranging from 4×10^{-3} to 6.3×10^{-2} and X ($= m_{NaPSA}/m_{NaCl}$) from 33 to 0.09 are given in Table I.[24]

All results given are from measurements using the ion-exchange membrane as Na^+ electrode. Because of the importance of polyelectrolyte purity and accuracy of the molality determinations, two NaPSA stock solutions A and B were used for two different measurement series. Solution A was purified by exhaustive dialysis only, solution B by ion-exchange followed by 48-hr dialysis. Equivalent weight for solution A was determined at 236.5 ± 2.5, for solution B at 230.6 ± 2.0 g/equiv. This difference may be caused by the purification procedures. Results for log $\gamma_\pm$ of the two solution series can best be compared at the same NaPSA/NaCl ratio and the same total ionic strength.[13] With only two slight exceptions all results with mixtures from the two stock solutions duplicate each other within measurement and concentration error.

In Figure 2 measurement series from the two stock solutions essentially cannot be distinguished. Table II shows a comparison between log $\gamma_\pm$(NaCl) determined with an ion-exchange membrane or with a Na^+ selective glass electrode as Na^+ electrode, and serves as an example for the general agreement between these two measurements, in spite of the lower reproducibility of the glass electrode measurements. No literature data for mean ionic activities in the systems studied here exist. Comparison with the Na^+ activity data measured by Lyons and Kotin, also using a cation-exchange membrane as Na^+ electrode, can be made if certain assumptions concerning $\gamma(Cl^-)$ are made. For instance, at $m_{NaPSA} = 9.1 \times 10^{-3}$ and m_{NaCl} =

TABLE II: Comparison of Log $\gamma_{\pm}$(NaCl) Measured with a Cation-Exchange Membrane (CEM) and with a Na^+ Selective Glass as Na^+ Electrode[a]

$m_{NaPSA} \times 10^2$	$m_{NaCl} \times 10^2$	log $\gamma_{\pm}$ CEM	log $\gamma_{\pm}$ Na^+ glass
1.56	0.0468	-0.30^4	−0.31
1.56	0.0746	-0.29^9	−0.30
1.56	0.147	-0.28^2	−0.28
1.56	0.286	-0.25^6	−0.26
1.56	0.735	-0.19^5	−0.19
1.56	1.48	-0.15^5	−0.15

[a] Last digits given as superscript indicate an estimated precision of 5 in that digit.

3.34×10^{-3} Lyons and Kotin find $\gamma(Na^+) = 0.46$. This can be compared with our measurement series with $m_{NaPSA} = 9.39 \times 10^{-3}$; at the same X we find by interpolation $\gamma_{\pm}(NaCl) = 0.62$. Assuming $\gamma(Cl^-) = \gamma_{\pm}^0$, where $\gamma_{\pm}^0$ is the activity coefficient of NaCl in a pure NaCl solution of concentration $(\phi_p m_{NaPSA}/2 + m_{NaCl})$ we find $\gamma(Cl^-) = 0.93$, and $\gamma(Na^+) = 0.41$. This value is significantly lower than Lyons and Kotin's $\gamma(Na^+) = 0.46$. On the other hand, if for $\gamma(Cl^-)$ in the mixture we use Manning's limiting law value (ref 13, eq 47) we find $\gamma(Cl^-) = 0.83$ and consequently $\gamma(Na^+) = 0.46$, in excellent agreement with Lyons and Kotin's value! Indeed one of the major difficulties in comparing thermodynamic and transport data of polyelectrolyte solutions is the lack of material uniformity. The single-ion activity coefficients measured by Lyons and Kotin for pure NaPSA are lower than comparable data by Oman and Dolar[25] but higher than ϕ_p measured by vapor pressure and isopiestic methods.[17] The additivity rule can be formulated as[7,10]

$$\log \gamma_{\pm} = \log \gamma_{\pm}^0 + 1/2 \log \left(\frac{\phi_p m_p + m_s}{m_p + m_s} \right) \quad (1)$$

where, in our case of mixtures of NaPSA and NaCl, m_p and m_s are the monomolalities of NaPSA and of NaCl in the mixture, and ϕ_p is the osmotic coefficient of pure NaPSA at a monomolality m_p. Alexandrowicz employs $\gamma_{\pm}^0$ at a concentration of pure NaCl equal to $\phi_p m_p/2 + m_s$. There is no theoretical justification for this choice, and if we formulate additivity for the counterion activity as[3,5,11]

$$\gamma_+ m_+ = \gamma_+^p m_p + \gamma_+^0 m_s$$

where $\gamma_+ m_+$ is the counterion activity in the mixture and γ_+^p and γ_+^0 the counterion activity coefficient in the pure polyelectrolyte (concentration m_p) and pure simple electrolyte (concentration m_s), respectively, we arrive at

$$\log \gamma_{\pm} = 1/2 \log \gamma_{\pm}^0 + 1/2 \log \left(\frac{\phi_p m_p + \gamma_{\pm}^0 m_s}{m_p + m_s} \right) \quad (2)$$

where $\gamma_{\pm}^0$ is now taken at a concentration of pure electrolyte equal to m_s, and γ_+^p is assumed equal to ϕ_p.

Only in the region of excess polyelectrolyte, and at higher polyelectrolyte concentrations, is there a significant difference between (1) and (2). In Figure 1 measured values for log $\gamma_{\pm}$(NaCl) are plotted against log m_s for four representative NaPSA concentrations. Other series of mixtures follow a similar pattern. Solid lines (eq 1) and broken lines (eq 2) are calculated using an empirical relation for ϕ_p obtained from vapor pressure and isopiestic measurements: $\phi_p = 0.24 + 0.24 m_{NaPSA}$.[17]

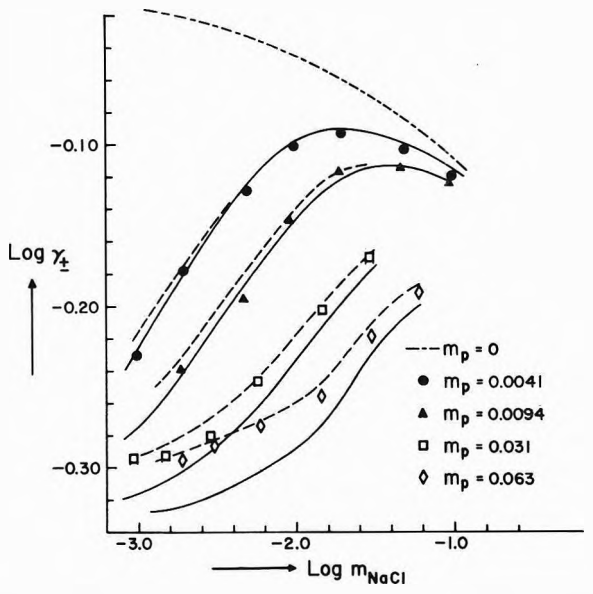

Figure 1. Log $\gamma_{\pm}$(NaCl) *vs.* log m_{NaCl} in mixtures of NaPSA and NaCl: solid line, additivity rule, eq 1; dashed line, additivity rule, eq 2.

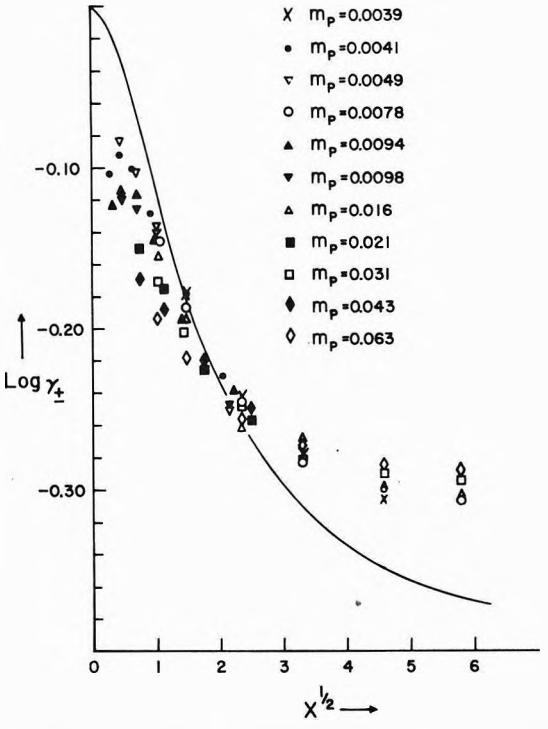

Figure 2. Log $\gamma_{\pm}$(NaCl) *vs.* $X^{1/2}$ ($X = m_{NaPSA}/m_{NaCl}$): solid line, theoretical curve, ref 13, eq 48.

Figure 1 shows that for $X < 5$ both forms of the additivity rule represent the present data adequately. However, at larger excess of polyelectrolyte eq 1 falls significantly below the experimental values for log $\gamma_{\pm}$, whereas eq 2 still gives reasonable agreement with the data. The purely empirical character of the additivity rule does not allow for any preference for eq 2 over eq 1 on theoretical grounds. It is significant, however, that this agreement is obtained using the well-defined mean ionic activity of the added electrolyte, and the osmotic coefficient of the pure polyelectrolyte obtained by a different research group using a different NaPSA sample from the same manufacturer.

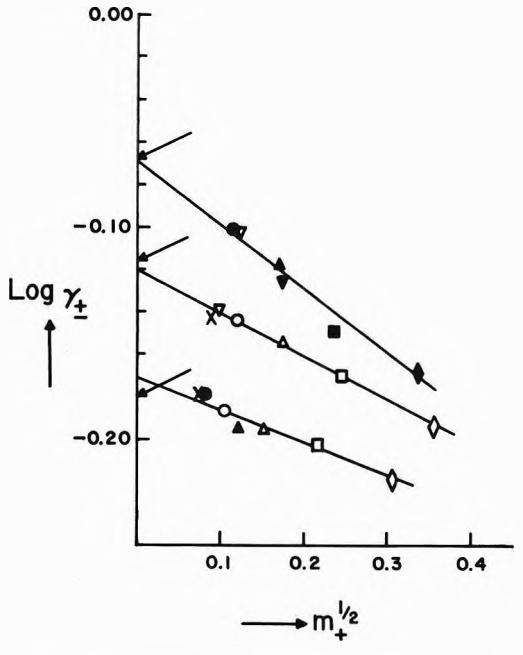

Figure 3. Log $\gamma_{\pm}$(NaCl) *vs.* $(m_{Na+})^{1/2}$ for mixtures at constant X: upper line, $X^{1/2} = 0.7$; middle line, $X^{1/2} = 1.03$; lower line, $X^{1/2} = 1.46$. Experimental points and symbols are the same as in Figure 2. Arrows indicate limiting law values.

Our results can be compared directly to a "limiting law" derived by Manning.[13] In Figure 2 log $\gamma_{\pm}$ is plotted *vs.* $X^{1/2}$ for all mixtures studied. The solid line is calculated from eq 48 of ref 13, with $\xi = 2.34$ (corresponding to 82% sulfonate substitution on the polymer repetitive unit). In interpreting this figure, it should be kept in mind that within a series of mixtures with constant m_p, the total ionic strength increases as X decreases, *i.e.*, for one m_p series the points to the right of the graph are the points of lowest ionic strength. Taking into account an estimated experimental error of ±0.005 in log $\gamma_{\pm}$ the deviations of log $\gamma_{\pm}$ from Manning's curve show a very regular behavior depending on total ionic strength and on X. The influence of the ionic strength is very clear especially at low X. In this region the additivity rule in either form is closely satisfied (Figure 1); the negative deviation of $\gamma_{\pm}$ from Manning's limiting law strongly increases with increasing ionic strength, as can be seen from the points for different m_p, *e.g.*, at $X^{1/2}$ approximately equal to 0.7, 1.03, and 1.46. It should be stressed that Debye-Hückel type interactions for the noncondensed ions are taken into account by Manning, and no obvious theoretical relation exists to extrapolate to zero ionic strength. Yet, as was suggested by Manning,[13] an empirical extrapolation to zero ionic strength leads to values for log $\gamma_{\pm}$ which are surprisingly close to the limiting law results. Such an extrapolation is shown in Figure 3. A different situation exists in the region of excess polyelectrolyte. Here we find $\gamma_{\pm}$ appreciably larger than the value predicted from the limiting law. The variation with ionic strength at constant X is much smaller than in the case of low X, although it seems that here too the deviation from the limiting law is largest for mixtures with the highest ionic strength. In Figure 2, the difference between log $\gamma_{\pm}$ at the lowest and highest m_p values at $X^{1/2} = 4.6$ and $X^{1/2} = 5.8$ is well outside experimental error. Lyons and Kotin find values for $\gamma_{\pm}$ in the system NaPVS-NaCl extending up to $X = 9$ which are close to the value predicted by Manning (ref 13, Figure 4); these authors report one value for $Na(PO_3)_x$-NaCl at $X = 6.4$ which is significantly higher than the limiting law value. Up to $X = 8$ our data for log $\gamma_{\pm}$ show a close agreement with the calculated values as well.

Manning's limiting law provides an excellent justification, born out by our experimental results, for comparison of activity and osmotic coefficient data in polyelectrolyte-simple electrolyte mixtures on the basis of two parameters only, the charge density parameter ξ and the polyelectrolyte-simple electrolyte ratio X, taking into account the ionic strength of the mixture. This gives us an excellent tool for estimating colligative properties of mixtures for which no experimental data exist. In the region of large excess of polyelectrolyte more experimental data are needed to establish a definite trend for the deviation from the theoretical equation. It is of course this region which is most important for model studies on ion-exchange membranes.

Acknowledgment. The author is grateful to the Dow Chemical Co., Midland, Mich., and to the National Starch and Chemical Corporation, New York, N. Y., for providing samples of NaPSA, and to Drs J. A. Marinsky and G. S. Manning for stimulating discussions.

This research was supported by the National Research Council of Canada.

Supplementary Material Available. Table I will appear following these pages in the microfilm edition of this volume of the journal. Photocopies of the supplementary material from this paper only or microfiche (105 × 148 mm, 20× reduction, negatives) containing all of the supplementary material for the papers in this issue may be obtained from the Journals Department, American Chemical Society, 1155 16th St., N.W., Washington, D. C. 20036. Remit check or money order for $3.00 for photocopy or $2.00 for microfiche, referring to code number JPC-73-2790.

References and Notes

(1) P. Meares in "Diffusion in Polymers," J. Crank, and G. S. Park, Ed., Academic Press, London, 1968.
(2) R. A. Mock and C. A. Marshall, *J. Polym. Sci.*, **13**, 263 (1954).
(3) M. Nagasawa, M. Izumi, and I. Kagawa, *J. Polym. Sci.*, **37**, 375 (1959).
(4) J. W. Lyons and L. Kotin, *J. Amer. Chem. Soc.*, **87**, 1670 (1965).
(5) D. O. Jordan, T. Kurucsev, and M. L. Martin, *Trans. Faraday Soc.*, **65**, 598 (1969).
(6) T. J. Podlas and P. Ander, *Macromolecules*, **3**, 154 (1970).
(7) Z. Alexandrowicz, *J. Polym. Sci.*, **56**, 115 (1962).
(8) J. A. Marinsky, *J. Phys. Chem.*, **75**, 3890 (1971).
(9) A. Katchalsky, Z. Alexandrowicz, and O. Kedem in "Chemical Physics of Ionic Solutions," B. E. Conway, and R. G. Barradas, Ed., Wiley, New York, N. Y., 1966, p 361.
(10) J. A. Marinsky in "Ion Exchange," Vol. I, J. A. Marinsky, Ed., Marcel Dekker, New York, N. Y., 1966, p 353.
(11) F. Oosawa, "Polyelectrolytes," Marcel Dekker, New York, N. Y., 1971.
(12) G. S. Manning, *Ann. Rev. Phys. Chem.*, **23**, 117 (1972).
(13) G. S. Manning, *J. Chem. Phys.*, **51**, 924 (1969).
(14) J. Th. G. Overbeek, *J. Colloid Sci.*, **8**, 593 (1953).
(15) J. W. Th. Lichtenbelt, *J. Electroanal. Chem.*, **37**, 283 (1972).
(16) N. Ise, *Advan. Polym. Sci.*, **7**, 536 (1971).
(17) M. Reddy and J. A. Marinsky, *J. Phys. Chem.*, **74**, 3884 (1970).
(18) M. Reddy, J. A. Marinsky, and A. Sarkar, *J. Phys. Chem.*, **74**, 3891 (1970).
(19) A. Takahashi, T. Kato, and M. Nagasawa, *J. Phys. Chem.*, **74**, 944 (1970).
(20) D. Kozak, J. Kristan, and D. Dolar, *Z. Phys. Chem. (Frankfurt am Main)*, **76**, 85 (1971).
(21) R. C. Hayes and J. C. T. Kwak, to be submitted for publication.
(22) D. J. G. Ives, G. J. Janz, "Reference Electrodes," Academic Press, New York, N. Y., 1961.
(23) J. C. T. Kwak, *Desalination*, **11**, 61 (1972).
(24) See paragraph at end of paper regarding supplementary material.
(25) S. Oman and D. Dolar, *Z. Phys. Chem.*, **56**, 1 (1967).

Internal Pressures of Liquids and Their Relationship to the Enthalpies and Entropies of Mixing in Nonelectrolyte Solutions

E. B. Bagley,*[1]

The Arcadia Institute for Scientific Research, Inc., Morton, Illinois 61550

T. P. Nelson,

Esso Research and Engineering Co., Florham Park, New Jersey 07932

and J. M. Scigliano

Monsanto Company, St. Louis, Missouri 63166 *(Received May 25, 1973)*

For a number of liquids it has been shown previously that an unambiguous and physically reasonable free volume can be evaluated from internal pressure, $P_i = (\partial E/\partial V)_T$, measurements. The free volume is given as $v_f = V - b = RT/(P + P_i)$, the b representing a quasilattice occupied volume. This approach to free volume has now been extended to solutions for which P_i of both the pure components and the mixtures are available. It is found experimentally that the occupied volume of the mixture, b_m, is the mole fraction average of the occupied volume of the components. The excess entropy and excess enthalpy of mixing are shown experimentally to be given by $-S^E = R\{x_1 \ln v_{f1} + x_2 \ln v_{f2} - \ln v_{fm}\}$ and $H^E = P_{im}V_m - x_1P_{i1}V_1 - x_2P_{i2}V_2$ for all nonelectrolyte systems tested. Since internal pressure measurements for mixtures are rare, an equivalent approach is to compute P_{im} from the P_i values for the pure components and the measured excess volumes, V^E, through the relation $P_{im} = [RT/(x_1v_{f1} + x_2v_{f2} + V^E)] - P$. Excellent agreement is found between calculated and measured excess properties. As always with such solution calculations, the results are very sensitive to input data and hence more complicated methods than those proposed here would appear to be unwarranted.

Introduction

The internal pressure, P_i, of a material is defined through the thermodynamic equation of state

$$P_i = \left(\frac{\partial E}{\partial V}\right)_T = T\left(\frac{\partial P}{\partial T}\right)_V - P \qquad (1)$$

and can be determined directly by measurement of the thermal pressure coefficient $(\partial P/\partial T)_V$.[2a] In comparing internal pressures for liquids with the cohesive energy density, $(\Delta E^V/V)$, where ΔE^V is the energy of vaporization and V the molar volume of the liquid, due account must be taken of the effects of both internal and external modes of motion of the molecule. When this is done, it is found that for organic liquids in general, even for systems showing polar and hydrogen bonding effects, liquid state energies are additive and, further, that the contributions of both nonpolar and polar forces to the total liquid state energy go as V^{-1} at total pressures lower than 500 psi.[2b-4]

The justification for these statements is experimental and has been discussed in detail in ref 2b, 3, and 4. Although the approach appears to be general for nonelectrolyte systems, the argument can be briefly summarized with reference to the experimental results obtained for small organic molecules such as carbon tetrachloride and cyclohexane. For such systems, it is found that[2b,3]

$$\Delta E^V = P_iV - (3RT/2) \qquad (2)$$

or, stated alternately, the internal pressure of such liquids is greater than the cohesive energy density by an amount $(3RT/2V)$. The difference, of course, is affected by polar and hydrogen bond effects, as well as by molecular complexity and temperature as described in earlier work.[4] In the simplest cases such as cyclohexane the result, eq 2, follows if the total liquid state energy can be written as

$$E_{TL} = E_{np} + E_{INT} + E_{PE} + E_{KE} \qquad (3)$$

Here E_{np} represents the equilibrium energy of a molecule in a nonpolar liquid due to all the other molecules in the liquid. This energy is the result of the London dispersion forces between molecules. E_{INT} represents the energy due to internal molecular modes of motion, such as carbon–carbon vibrations and depends only on temperature at the low pressures considered in this work. E_{PE} and E_{KE} represent the potential and kinetic energies of molecules vibrating as a whole in the liquid about their equilibrium position associated with E_{np}. An extension of the law of Dulong and Petit to the liquid state implies the classical result that both E_{PE} and E_{KE} will be given by $(3RT/2)$. Thus

$$E_{TL} = E_{np}(T,V) + E_{INT}(T) + (6RT/2) \qquad (4)$$

where E_{INT} depends only on temperature. For the vapor in equilibrium with the liquid

$$E_{TG} = E_{INT}(T) + (3RT/2) \qquad (5)$$

and subtracting eq 5 from 4 leads immediately to

$$\Delta E^V = E_{TG} - E_{TL} \qquad (6)$$

$$\Delta E^V = -E_{np} - (3RT/2) \qquad (7)$$

Combining eq 7 with the observation described by eq 2 leads immediately to the van der Waals' type relation

$$E_{np} = -a(T)/V \qquad (8)$$

The view has recently been expressed by Scott and van Konynenburg that the van der Waals equation of state

provides an excellent description of the static properties of the liquid state. As they note, "We are surprised and gratified that the unrefined van der Waals model is so successful and informative."[5] Our experimental results lend further support to this view and suggest rewriting a generalized van der Waals equation of state for liquids and solutions as

$$\left[P + \left(\frac{\partial E}{\partial V}\right)_T\right][V - b] = RT \quad (9)$$

$$V - b = v_f = RT/(P + P_i) \quad (10)$$

In eq 9, b is to be regarded as an occupied quasilattice volume in the liquid or solution. The justification for this is strictly experimental.[6] By direct measurement of $(\partial E/\partial V)_T$ values of b can be obtained for liquids at various temperatures above the melting point. When these values are plotted against temperature, it is found that b for the liquid at the melting point is nearly equal to the volume of the solid, V_S, at the melting point. In many cases, the b *vs.* T curve above the melting point is continuous with the V_S *vs.* T curve below the melting point.[6] This is shown also in Table I for a series of pure liquids, where the occupied volume at the melting point, b, evaluated from eq 10 using measured values of $(\partial E/\partial V)_T$, is tabulated along with V_S values at the melting point.[7] In this series benzene stands out, not unexpectedly, in the magnitude of the difference between V_S and b.

The purpose of this paper is to show that this free volume concept can be very effectively applied to nonelectrolyte solutions in the quantitative evaluation of the excess thermodynamic properties.

Free Volumes of Liquids and Liquid Mixtures. Bondi[10] has emphasized that the literature definitions of free volume, v_f, are ambiguous since "each author defines these volumes as what he wants them to mean." The range of free volumes calculated by different methods has been demonstrated by Hildebrand and Scott.[11] They tabulate v_f values for a series of liquids by three different methods: from ΔH^V, the enthalpy of vaporization; from P_i, essentially from eq 10; and from a cage model of the liquid state. For acetone the v_f values so calculated were 0.13, 7.5, and 0.42 cm^3/mol at 20°.

The calculation of free volume from a cage model is open to serious objection and hence will not be considered further here. The free volume calculated from ΔH^V is very sensitive to the assumptions involved in deriving the relation between v_f and liquid and gas properties. Free volume computed from internal pressures, however, is based solely on the assumption of the validity of the generalized van der Waals equation (eq 9 and 10) and has the further distinct advantage that P_i can be precisely and accurately determined not only on pure liquids but also on liquid mixtures. The experimental procedures are basically those of Westwater, *et al.*,[2a] but more modern techniques permit the determination of P_i of both liquids and solutions to better than 0.1% as described by Bagley, *et al.*[2b-4] (This accuracy is essential in computing excess thermodynamic properties of solutions as will be discussed later.) The method involves a constant volume bomb. Temperature is changed and the hydrostatic pressure required to maintain constant liquid volume is measured. A plot of pressure *vs.* temperature yields the thermal pressure coefficient, $(\partial P/\partial T)_V$, and the internal pressure is computed from $[T(\partial P/\partial T)_V - P]$. In the work reported here the pressure range covered is only from 1 to 20 atm, and P_i is not a function of pressure in this range.

TABLE I: Comparison of Occupied Volume, b, with Solid Volume, $\bar{V}_S$, at the Melting Point, T_f[a]

Material	T_f, °K	$\bar{V}_S$, cc/mol	b, cc/mol	Difference, cc/mol	% difference
Argon	83.8	24.61	24.34	−0.27	−1.05
Nitrogen	63.2	29.15	28.78	−0.37	−1.27
Methane	90.7	30.94	31.31	+0.37	+1.23
Carbon tetrachloride	250.2	87.9	86.2	−1.70	−1.94
Benzene	278.7	77.28	81.39	+4.11	+5.32
Acetone	177.6	60.0	59.6	−0.40	−0.67
Methanol	173.2	31.49	31.40	−0.09	−0.28
Ethanol	154.2	45.7	45.4	−0.30	−0.66
1-Butanol	193.3	76.3	77.6	+1.30	+1.71
n-Hexane	171.2	101.4	102.0	+0.60	+0.59

[a] Data from Rowlinson[9] and Nelson.[8]

TABLE II: Experimental and Calculated Excluded Volumes of Equimolar Mixtures at 20°[a]

System	Exptl b_m from eq 12, cc/mol	Calcd b_m from eq 11, cc/mol	Difference, cc/mol
Heptane–acetone	101.34	101.79	+0.45
Heptane–carbon tetrachloride	113.31[b]	113.25	−0.06
Heptane–benzene	110.04[b]	109.74	−0.30
Heptane–bromoform	109.33	109.65	+0.32
Benzene–carbon tetrachloride	85.93[b]	85.82	−0.11
Benzene–bromoform	82.31	82.21	−0.10
Benzene–carbon disulfide	67.96[b]	68.04	+0.08
Acetone–carbon disulfide	60.12[b]	60.09	−0.03

[a] Data of Westwater, *et al.*[2] [b] Corrected for volume of mixing.

In dealing with mixtures, the occupied volume of the mixture, b_m, would be expected to be the mole fraction average of the occupied volumes of the components, b_1 and b_2, so that

$$b_m = x_1 b_1 + x_2 b_2 \quad (11)$$

This can be confirmed experimentally by measuring the internal pressure of the mixture, P_{im}, and, where necessary, the volume of the mixture, V_m, so that

$$b_m = V_m - \frac{RT}{P + P_{im}} \quad (12)$$

The validity of the mixing rule (eq 11) is illustrated in Table II where b_m from eq 11 is compared with b_m from eq 12. Agreement between the calculated and experimental b_m values is superficially excellent with an average error of ±0.2% in these eight equimolar mixtures. It must be pointed out that the errors involved here are of the order of magnitude of the excess volumes. These errors, though numerically small, can be critical in evaluation of other excess thermodynamic properties.

There must be a close relation between P_{im}, the internal pressure of a mixture, and the excess volume of mixing, $V^E = \Delta V^M$. The volume change on mixing is defined as

$$\Delta V^M = V_m - x_1 V_1 - x_2 V_2 \quad (13)$$

where V_m is the volume of the mixture and V_1 and V_2 the molar volumes of the components. Since eq 11 holds eq 13

TABLE III: Comparison of Calculated and Experimental Excess Volumes (ΔV^M) for Equimolar Mixtures[a]

System	Temp, °C	ΔV^M (calcd) eq 15, cc/mol	ΔV^M (exptl), cc/mol	Difference, cc/mol	Data source (ref)
Benzene–heptane	20	+0.398	+0.620 ± 0.02	−0.222	12
Benzene–carbon disulfide	20	+0.161	+0.073 ± 0.02	+0.088	13
Acetone–carbon disulfide	20	+0.077	+0.095 ± 0.02	−0.018	13
Benzene–carbon tetrachloride	25	+0.015	+0.014 ± 0.03	+0.001	12
Heptane–carbon tetrachloride	20	+0.218	+0.220 ± 0.01	−0.002	14
Hexane–octane	25	−0.074	−0.050 ± 0.02	+0.024	15
Hexane–cyclohexane	25	+0.062	+0.150 ± 0.05	−0.088	16
Ethanol–cyclohexane	25	−0.244	+0.570 ± 0.01	−0.800	17
Ethanol–*n*-heptane	25	−0.160	+0.450 ± 0.01	−0.610	18

[a] Internal pressure data from ref 2a and 8.

reduces to

$$\Delta V^M = v_{fm} - x_1 v_{f1} - x_2 v_{f2} \quad (14)$$

where the v_f values refer to the mixture and the pure components, respectively, as defined by eq 10. This leads to

$$\Delta V^M = RT\left[\frac{1}{P_{im}} - \frac{x_1}{P_{i1}} - \frac{x_2}{P_{i2}}\right] \quad (15)$$

where P_{im}, P_{i1}, and P_{i2} are the measured internal pressures of the mixture and the two pure components, respectively and $P_i \gg P$.

A comparison of calculated ΔV^M values from eq 15 and experimental ΔV^M values for nine equimolar mixtures are shown in Table III. The agreement is only fair. Part of the problem arises because of the extreme sensitivity of eq 15 to small errors in P_i determinations. Thus, if P_i is in error by only 1%, then the v_f values, which are in the 5 to 10 cc/mol range, are in error by 0.05 to 0.10 cc/mol, errors of the order of magnitude of ΔV^M itself. This sensitivity of excess thermodynamic properties to input data is of frequent occurrence in solution studies and has been discussed by Bagley, *et al.*,[4] in reference to heats of mixing and excess Gibbs free energy calculations. Whatever the cause such deviations must be carefully considered in any approach to solution thermodynamic behavior.

In general, there seems little hope of solving the geometrically difficult problem of calculating V^E for a mixture from pure component properties, but these excess volume effects cannot be ignored in any theoretical calculation of excess enthalpies and entropies of mixing. Hence, the excess volume of mixing must presently be regarded as a vital parameter which must be evaluated experimentally.

Excess Thermodynamic Properties and Internal Pressure. The relationship between pressure and Helmholtz free energy, A, is

$$-P = (\partial A/\partial V)_T \quad (16)$$

For a van der Waals fluid (eq 9) the relation

$$A = -RT \ln(V - b) - \frac{a(T)}{V} + A'(T) \quad (17)$$

immediately follows. With the experimental observations relating P_i to both v_f and to an $a(T)/V$ van der Waals term, the excess Gibbs free energy of mixing at constant pressure can be written as[7,20,21]

$$G_p^E \doteq A_p^E = RT[x_1 \ln v_{f1} + x_2 \ln v_{f2} - \ln v_{fm}] - \left[\frac{a_m}{V_m} - x_1\frac{a_1}{V_1} - x_2\frac{a_2}{V_2}\right] \quad (18)$$

Since the integration constants, $A'(T)$, depend only on T, $A_m' - x_1A_1' - x_2A_2'$ has been taken as zero. The excess entropy of mixing at constant pressure is thus equivalent to the Hildebrand form[21]

$$-S_p^E = R[x_1 \ln v_{f1} + x_2 \ln v_{f2} - \ln v_{fm}] \quad (19)$$

The excess enthalpy of mixing at constant pressure, H_p^E, can be taken as approximately equal to the excess energy of mixing at constant pressure, E_p^E, so

$$-H_p^E \doteq -E_p^E = \frac{a_m}{V_m} - x_1\frac{a_1}{V_1} - x_2\frac{a_2}{V_2} \quad (20)$$

These equations can be rewritten in terms of the internal pressure so that the excess enthalpy is given as

$$H_p^E = P_{im}V_m - x_1P_{i1}V_1 - x_2P_{i2}V_2 \quad (21)$$

It is further known[11] that the excess energy of mixing at constant volume, E_V^E, is related to H_p^E through

$$H_p^E = E_V^E + P_{im}V^E \quad (22)$$

The correction term, $P_{im}V^E$, can easily be of the order of magnitude of 50 cal/mol for equimolar mixtures of organic solvents. This is of the order of magnitude of both E_V^E and H_p^E and hence excess volume effects can be critical in comparing constant volume theories with constant pressure experiments. Combining eq 21 and 22 leads to

$$E_V^E = (x_1V_1 + x_2V_2)(P_{im} - \phi_1P_{i1} - \phi_2P_{i2}) \quad (23)$$

where ϕ_1 and ϕ_2 are volume fractions of the two components. This reduces under certain conditions[7] to the regular solution equation for E_V^E as given in Hildebrand and Scott.[11]

Calculated and experimental H_p^E values are compared in Table IV for five equimolar mixtures for which P_{im}, H^E, and V^E data are available. P_i data for the four organic mixtures are from the direct measurements of Nelson[8] and Westwater, *et al.*[2a] The P_i data for argon–nitrogen are from compressibility data given by Eyring and Jhon.[22] The validity of the analysis is clearly demonstrated by the accuracy of the predictions, without the use of fitting parameters.

For the alcohol solutions, an additional term accounting for the heat of mixing due to H-bond breaking is required. The theoretical expression for this contribution, which is based on work by Wiehe[25,27] and Chen,[28] is

$$H_h^E = x_1H_h\left(\frac{1}{p_m} - \frac{1}{p}\right) \quad (24)$$

where H_h is the H-bond enthalpy, x_1 is the alcohol mole fraction, p_m is the degree of alcohol polymerization in the

TABLE IV: Calculated and Experimental Heats of Mixing of Equimolar Mixtures at 25°

System	V^E, cc/mol	P_{im}, cal/cc	E_v^E, cal/mol	$P_{im}V^E$, cal/mol	H_h^E, cal/mol	H_p^E, cal/mol	H_p^E (exptl), cal/mol	H^E data source (ref)
Cyclohexane–hexane	0.152	65.68	37.8	10.0		47.8	51.5	19
Argon–nitrogen, 83°K	−0.179	38.50	22.0	−6.9		15.1	12.1	22
Benzene–carbon tetrachloride	0.014	84.68	28.3	1.2		29.5	30.2	23
Ethanol–cyclohexane	0.556	73.53	6.0	47.6	126.8	180.4	172.0	24
Ethanol–*n*-heptane	0.453	63.63	2.4	28.8	130.5	161.7	158.0	18

TABLE V: Calculated and Experimental Excess Properties of the *n*-Hexane–Cyclohexane System at 25°

Property	Mole fraction *n*-hexane 0.2711	0.4886	0.7240	Data source (ref)
V^E (calcd)[a]	0.067	0.063	0.041	
V^E (exptl)	0.150	0.152	0.088	16
E^E (calcd)[b]	31.2	37.8	29.0	
H^E (calcd)	43.3	48.3	34.4	
H^E (exptl)	47.6	51.5	36.9	19
TS^E (calcd)[b]	27.5	27.7	17.7	
TS^E (exptl) (20°)	34.1	34.4	23.6	26
G^E (calcd)[b]	15.8	20.1	16.7	
G^E (exptl) (20°)	13.5	17.1	13.3	26
P_{im}* (V^E)[c]	69.11	65.08	61.55	
P_{im}* (H^E)	71.06	66.85	62.66	
P_{im}* (TS^E)	68.38	64.33	61.50	
P_{im}* (av)	69.52	65.42	61.90	
P_{im} (exptl)	69.84	65.68	61.85	8

[a] Values in cc/mol. [b] Values in cal/mol. [c] Values in cal/cc, calculated as described in the text.

TABLE VI: Comparison of Calculated Excess Properties Using V^E and P_{im} for *n*-Hexane–Cyclohexane

Property	Mole fraction *n*-hexane 0.2711	0.4886	0.7240
H^E (calcd w/ V^E)[a]	47.4	54.1	37.1
H^E (calcd w/ P_{im})	43.3	48.3	34.4
H^E (exptl)	47.6 ± 2	51.5 ± 2	36.9 ± 2
TS^E (calcd w/ V^E)[a]	33.4	33.0	20.3
TS^E (calcd w/ P_{im})	27.5	27.7	17.7
TS^E (exptl)	34.1 ± 2	34.4 ± 2	23.6 ± 2
G^E (calcd w/ V^E)[a]	14.0	21.0	16.8
G^E (calcd w/ P_{im})	15.8	20.1	16.7
G^E (exptl)	13.5 ± 0.5	17.1 ± 0.5	13.3 ± 0.5

[a] Values in cal/mol.

mixture, and p is the degree of polymerization for the pure alcohol. The sum of eq 22 and 24 gives H^E results in excellent agreement with experiment for the two alcohol–alkane solutions.

The argon–nitrogen system is included to illustrate the importance of good P_i data in these calculations. The P_i data for this system, which were obtained from compressibility measurements, lead to a calculated H^E value, which, while in fair agreement, is still 25% higher than the experimental value. On the other hand, use of directly measured P_i values for the organic systems gives results with an average difference of only 4.1%. Since the experimental error in H^E is 2–5% for these organic systems,[12] it is concluded that the free volume theory coupled with good P_i and V^E data can give excellent predictions of H^E. Further support for the approach is given when the excess free energy and entropy are examined.

The *n*-hexane–cyclohexane system is considered in detail since the excess properties and the P_{im} data are available for a range of concentrations. Calculated and experimental values of V^E, H^E, TS^E, and G^E for three different compositions are compared in Table V. Also given are the P_{im}* values required to give the experimental value of V^E, H^E, and TS^E (assuming the pure component P_i's are correct) and the experimental P_{im}.

The calculated values of V^E are all low, but the difference between the $P_{im}(V^E)$'s and the experimental results is less than 1%. (From Table IV, recall that this system has one of the largest errors in the calculated V^E.) Similarly, the calculated values of H^E are low by average of 7.4% while P_{im}*(H^E) averages about 1.5% higher than experimental values. Note the significance of the $P_{im}V^E$ correction. Calculated values of TS^E are in greatest disagreement with experiment with an average error of 21.4%. This, of course, reflects the error in the calculated V^E. Once again P_i*(TS^E) is within 1.5% of the experimental value. Considering how small the experimental G^E values are, the agreement between calculated and experimental values is reasonably good. Finally, note the small differences between P_{im}*(av) (average of the other three) and the experimental P_{im}.

The conclusion from the foregoing is that while the simple free volume theory gives excess properties as accurately as more complex theories, as always with solutions it is extremely sensitive to the input data used, in this case P_i values. It is indeed remarkable that the P_{im}*(av) values are so close to the experimental values when we consider that all errors in the pure component P_i's and molar volumes and the excess properties are combined into one parameter.

Pursuing this further, it would appear that measurement of V^E (which is simple experimentally) combined with pure component P_i's could be used to predict the other excess properties. This approach is tested on the *n*-hexane–cyclohexane system. From the results in Table VI, it is seen that significant improvement in the calculated G^E's is found in only one case using V^E. For the other two concentrations the calculated values are essentially equal for the two approaches. However, estimates of H^E and TS^E are in much better agreement with experimental values using V^E instead of P_{im}. In fact, two out of three calculated values for both H^E and TS^E are within experimental error. Based on these results, the measurement of V^E in lieu of P_{im} seems indicated not only because of better predictions but because of experimental simplicity.

Conclusions

Previous experimental studies of the internal pressure of pure liquids indicated that they behaved as generalized van der Waals fluids with b as a quasilattice occupied volume. Values of P_i can thus be used to evaluate both the free volumes of these liquids and to elucidate their ener-

getics. It has been shown here that these concepts can be extended to mixtures of nonelectrolytes. The analysis confirms, to the limits of the experimental data, the free volume theory of nonelectrolyte solutions. The excess enthalpies and entropies are given, essentially in the forms proposed by Hildebrand and coworkers, by

$$H^E = P_{im}V_m - x_1P_{i1}V_1 - x_2P_{i2}V_2$$
$$-S^E = R[x_1 \ln v_{f1} + x_2 \ln v_{f2} - \ln v_{fm}]$$

where the free volumes, v_f, are evaluated from internal pressures as

$$v_f = RT/(P + P_i)$$

These equations describe the thermodynamics of the mixing of nonelectrolytes to the accuracy of the data. Since measurements of mixture internal pressures are rare, however, it is important that equivalent results can be obtained from pure component internal pressure values coupled with excess volume measurements on the mixture. The expression for the internal pressure of the mixtures is given as

$$P_{im} = \frac{RT}{x_1v_{f1} + x_2v_{f2} + V^E} - P$$

Thus a measurement of V^E is equivalent to a measurement of the internal pressure of the liquid mixture. It should also be noted that, even for constant volume of mixing, H^E and S^E are not necessarily zero.

This work also serves to emphasize the need for extreme accuracy in solution work and especially in the determination of pure component physical properties. Since the excess properties depend on the small differences between the large numbers characterizing component properties, errors which might normally be regarded as trivial actually assume large proportions. This is well illustrated by the differences in V^E values calculated from the internal pressures of the mixture and components and the experimental V^E when P_i data are known only to 1%.

The fundamental concepts described here have also been applied successfully to polymer systems[7] and these will be discussed in a subsequent paper.

Acknowledgments. The authors gratefully acknowledge partial financial support from the Paint Research Institute and Monsanto Company and cooperation of the U. S. Department of Agriculture in preparing this manuscript.

References and Notes

(1) Address correspondence in care of the Northern Regional Research Laboratory, Agricultural Research Service, U. S. Department of Agriculture, Peoria, Ill. 61604.
(2) (a) W. Westwater, H. W. Frantz, and J. W. Hildebrand, *Phys. Rev.*, **31**, 135 (1928); (b) E. B. Bagley, T. P. Nelson, J. W. Barlow, and S. A. Chen, *Ind. Eng. Chem., Fundam.*, **9**, 93 (1970).
(3) E. B. Bagley, T. P. Nelson, J. W. Barlow, and S. A. Chen, *Ind. Eng. Chem., Fundam.*, **10**, 27 (1971).
(4) E. B. Bagley, T. P. Nelson, and J. M. Scigliano, *J. Paint Technol.*, **43**, 35 (1971).
(5) R. L. Scott and Peter H. van Konynenburg, *Discuss. Faraday Soc.*, **49**, 87 (1970).
(6) E. B. Bagley and J. M. Scigliano, *Polym. Eng. Sci.*, **11**, 177 (1971).
(7) J. M. Scigliano, Doctoral Dissertation, Washington University, St. Louis, Mo., 1972.
(8) T. P. Nelson, Doctoral Dissertation, Washington University, St. Louis, Mo., 1971.
(9) J. S. Rowlinson, "Liquids and Liquid Mixtures," Plenum Press, New York, N. Y., 1969.
(10) A. Bondi, "Physical Properties of Molecular Crystals, Liquids and Glasses," Wiley, New York, N. Y., 1968.
(11) J. L. Hildebrand and R. L. Scott, "The Solubility of Nonelectrolytes," Reinhold, New York, N. Y., 1950.
(12) A. Abe and P. J. Flory, *J. Amer. Chem. Soc.*, **87**, 1838 (1965).
(13) G. C. Schmidt, *Z. Phys. Chem.*, **121A**, 221 (1926).
(14) H. Dunken, *Z. Phys. Chem.*, **53**, 264 (1942).
(15) S. Young and E. C. Fortey, *J. Chem. Soc.*, **81**, 739 (1902).
(16) J. D. Gomez-Ibanez and C.-T. Liu, *J. Phys. Chem.*, **65**, 2148 (1961).
(17) F. Pardo and H. C. van Ness, *J. Chem. Eng. Data*, **10**, 163 (1965).
(18) H. C. van Ness, C. Soczek, and N. Kochar, *J. Chem. Eng. Data*, **12**, 346 (1967).
(19) H. Watts, E. C. W. Clarke, and D. N. Glew, *Can. J. Chem.*, **46**, 815 (1968).
(20) J. H. Hildebrand and R. L. Scott, "Regular Solutions," Prentice Hall, Englewood Cliffs, N. J., 1962.
(21) J. H. Hildebrand, *J. Chem. Phys.*, **15**, 225 (1947).
(22) H. Eyring and M. S. Jhon, "Significant Liquid Structure," Wiley, New York, N. Y., 1969.
(23) G. Scatchard, S. E. Wood, and J. M. Mochel, *J. Amer. Chem. Soc.*, **62**, 712 (1940).
(24) G. Scatchard and F. G. Satkiewicz, *J. Amer. Chem. Soc.*, **86**, 130 (1964).
(25) I. A. Wiehe, Doctoral Dissertation, Washington University, St. Louis, Mo., 1965.
(26) V. Mathot, *Bull. Soc. Chim. Belg.*, **59**, 111 (1950).
(27) I. A. Wiehe and E. B. Bagley, *Ind. Eng. Chem., Fundam.*, **6**, 209 (1967).
(28) E. B. Bagley and S. A. Chen, *J. Paint Technol.*, **41**, 494 (1969).

Temperature and Solvent Effects on the Equilibrium of Dilute Uranium Trifluoride Solutions Contained in Graphite[1]

L. M. Toth* and L. O. Gilpatrick

Reactor Chemistry Division, Oak Ridge National Laboratory, Oak Ridge, Tennessee 37830 *(Received May 29, 1973)*

Publication costs assisted by The Oak Ridge National Laboratory

The equilibrium of dilute UF_3–UF_4 molten fluoride solutions in contact with graphite and UC_2, $3UF_4 + UC_2 \rightleftarrows 4UF_3 + 2C$, has been studied as a function of temperature (370–700°) and melt composition. Equilibrium quotients, $Q = (UF_3)^4/(UF_4)^3$, for the reaction were determined by measuring the UF_3 and UF_4 concentrations spectrophotometrically. It has been found that the equilibrium quotient is sensitive to both temperature and solvent changes, increasing as either the temperature increases or the alkali-metal fluoride content of the solvent decreases. These results are explained by the tendency of UF_4 to form complexes of greater stability than UF_3. Differences in the heats of solution of these uranium solutes are estimated from these data.

Introduction

It has been previously recognized that the stability of UF_3 with regard to disproportionation

$$4UF_3 \rightleftarrows 3UF_4 + U \quad (1)$$

is decreased by dissolving it in a molten fluoride solution.[2] This decrease in stability has been attributed to the tendency of UF_4 to form complexes of greater stability in solution than does UF_3. The stability of UF_3 is decreased still further if these dilute solutions are contained in graphite because of the formation of uranium carbide

$$4UF_3 + 2C \rightleftarrows UF_4 + UC_2 \quad (2)$$

Long and Blankenship have studied the equilibrium[2] (eq 2) indirectly by measuring the hydrogen reduction of UF_4 (pure crystalline solid and in molten fluoride solution) according to the reaction

$$\tfrac{1}{2}H_2 + UF_4 \rightleftarrows UF_3 + HF \quad (3)$$

Equilibrium hydrogen and HF concentrations evolved from the reaction vessel were measured and from these data concentrations of UF_3 and UF_4 were calculated. They obtained the equilibrium constant for the reduction from the solid-phase UF_4 reduction and combined it with the equilibrium quotient for the dilute solution measurements to obtain the activity coefficient for UF_4 in the solutions. These data enabled them to calculate an equilibrium expression for eq 2. As a result of their investigation, they concluded that temperature and solvent changes should have little effect on the equilibrium of eq 2.

Since then our experience with these solutions has shown that temperature and solvent changes have a marked effect on the coordination chemistry of UF_4.[3a] It is therefore logical to assume that redox equilibria involving these ions are also strongly affected. In order to relate solvent effects on the coordination chemistry of ions to changes in their redox chemistry, we undertook an investigation of the equilibrium in eq 2. It is ideally suited for this study because the +3 and +4 valence states of uranium are relatively stable in molten fluoride solutions.

We have already identified UC_2 as the stable uranium carbide phase in equilibrium with UF_3–UF_4 solutions in graphite.[3b] The object of this report is to describe the effects of temperature and solvent changes on the equilibrium and to compare these measurements with previously established thermodynamic data.

Experimental Section

Equilibrium quotients for eq 2 were determined by measuring UF_3 and UF_4 concentrations spectrophotometrically with a Cary Model 14-H recording spectrometer. The sample system consisted of an inert atmosphere furnace shown in Figure 1 which held a diamond-windowed graphite spectrophotometric cell.[4] Molten fluoride salt solutions and reagent uranium carbides were contained in this cell. Absorption spectra of the molten salt solutions were measured against an air reference. Net spectra due to UF_3 and UF_4 were determined by subtracting independently determined solvent blank spectra using standard digital computer techniques. Spectra were measured in the near-infrared and visible regions from 4000 to 33,000 cm^{-1}. The absorption spectra of UF_3 and UF_4 served as the primary means of monitoring these components in solution.

Materials. Molten salt solvent compositions were prepared by mixing predetermined amounts of the pure component fluoride salts. Optical quality crystal fragments from the Harshaw Chemical Co. were the source of LiF. Beryllium fluoride was prepared by vacuum distillation of a large special purchase supplied by the Brush Beryllium Co. Uranium tetrafluoride was taken from a laboratory purified spectroscopic standard which contained less than 10 ppm total cation impurity. The uranium carbides used in this study were supplied by E. K. Storms and John Farr of the Los Alamos Scientific Laboratory. The analyses of these carbides were as follows: uranium dicarbide, "UC_2," wt % carbon = 8.83, O_2 = 200 ppm; uranium sesquicarbide, U_2C_3, wt % carbon = 6.99, O_2 = 50 ppm. These carbides were received sealed in glass ampoules and were stored afterwards in a helium filled drybox.

Procedure. All molten fluoride salts used in this study were pretreated while molten at 600° for oxide removal by sparging with reagent HF gas, or HF–H_2 gas mixtures. Residual HF was then stripped from the melt with helium prior to cooling. Clear portions of the recovered salt were crushed and used to charge the spectrophotometric cell. All handling of molten fluoride salt, reagent carbides and

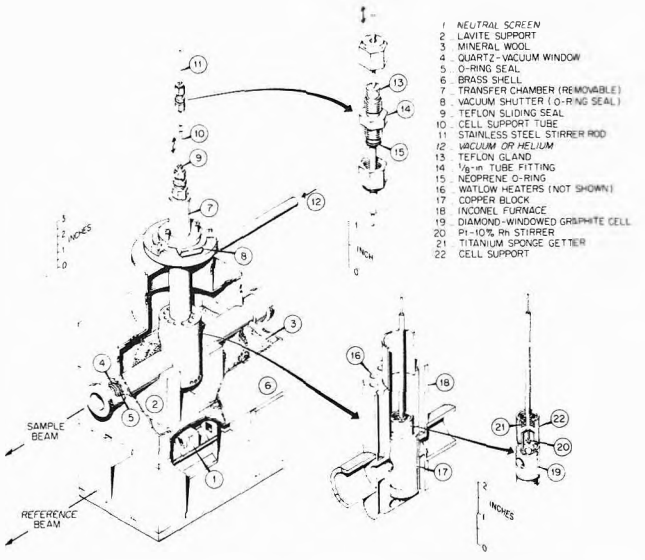

Figure 1. High-temperature furnace system for absorption spectra of molten fluorides.

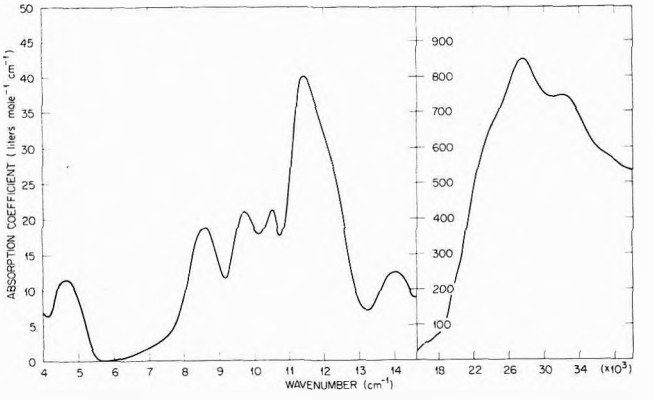

Figure 2. UF_3 spectrum (approximately 0.3 mol %) in $LiF-BeF_2$ (66–34 mol %).

spectrophotometric cell components was done in an inert atmosphere glove-box of less than 0.1 ppm water vapor content and less than 2 ppm O_2 content. Approximately 0.6 g of salt solvent made a convenient cell loading to which was added from 5 to as much as 100 mg of the uranium carbide. Poco AXF-5Q1 grade graphite spectrophotometric cells were used which were purified after fabrication by heating in an H_2 gas stream to 1000° and then flushed free of H_2 with helium. A "dashpot" stirrer made from platinum–10% rhodium was used to hasten the attainment of equilibrium which is otherwise dependent largely on diffusion in the molten fluoride solution.

Spectral Measurements. Molar concentrations of dissolved UF_3 and UF_4 were determined simultaneously in solution at a series of temperatures above the melting point by measuring optical densities at 9147 and 11,360 cm^{-1}. These wave numbers represent the maximum absorbance values for dissolved UF_4 and UF_3, respectively. Detailed absorption spectra for UF_4 in molten fluoride solutions have already been presented.[3a] A typical spectrum of UF_3 is shown in Figure 2. The strong band in the visible region from 16,000 to 33,000 cm^{-1} is too intense to be useful because the solutions studied had initial UF_4 molarities in the range of 0.04 to 0.10. Calibration curves for UF_3 and UF_4 at various temperatures and melt compositions showed that both uranium fluorides absorbed throughout the entire spectral region. In calculating molar absorption coefficients from the calibration curves, the solutions were adjusted for concentration changes due to thermal expansion. To determine the molar concentrations of each in a mixture containing the two, a set of Beer's law simultaneous equations representing the measured absorbances at the two frequency positions were solved. The molar concentrations were then converted to mole fractions for use in the equilibrium quotient calculations.

To attain equilibrium, the system was initially held at *ca.* 50° above the temperature desired until no change in UF_3 concentration was observed (UF_4 reacting with UC_2 *via* eq 2). Then the temperature was dropped 50° and the UF_3 concentration was allowed to fall by its reaction with graphite until no further change could be detected. The equilibrium could be shifted repeatedly in this manner by varying the temperature of the system.

Results

The back reaction of eq 2

$$3UF_4 + UC_2 \rightleftharpoons 4UF_3 + 2C \qquad (2a)$$

was more convenient for measurement of equilibrium quotients, $Q = (UF_3)^4/(UF_4)^3$, because excess uranium carbide could be added to ensure that the molten fluoride solution was always in contact with all the reactive solid phases. However, before quantitative data for the equilibrium quotient was collected, the validity of the expression in eq 2a was first examined to demonstrate that it represented the actual chemical process which was occurring in the system. This included (1) identification of all the reactive components, soluble UF_3 and UF_4 by their characteristic absorption spectra, and insoluble UC_2 and graphite by X-ray diffraction; (2) measurement of the stoichiometry of the solute components in the reaction; and (3) proof of the equilibrium reversibility by cycling the system temperature in order to approach the equilibrium from both directions.

An anomaly exists as a result of the UC_2 phase identification because its formation is contrary to the established phase diagram for the uranium–carbon system which shows UC_2 to be metastable with respect to U_2C_3 and graphite at temperatures less than 1500°.[5] On the basis of this phase diagram and the accepted free energies of formation for the uranium carbides at temperatures less than 1000°K, U_2C_3 is the carbide phase which was expected in this work. Nevertheless, UC_2 has been identified repeatedly at these temperatures and has been established as the stable carbide phase in the equilibrium of eq 2. The reader who is interested in the details of this identification is referred to an earlier paper.[3b] In the present paper we have included a series of experiments where excess U_2C_3 was used to reduce UF_4 solutions *via* a reaction similar to eq 2a. Results are compared with similar experiments where UC_2 was used as a reductant and they demonstrate that U_2C_3 has a slightly greater uranium activity than UC_2 in the systems studied.

Effect of Temperature on the Equilibrium. Previous results[2] from the hydrogen reduction of UF_4 in molten fluoride solutions had indicated that the temperature effect on the equilibrium of eq 2a should be small. However, when we measured the equilibrium by either the forward or the back reaction, we found it to be very sensitive to temperature. This can be seen qualitatively by examining the molten fluoride absorption spectra of Figure 3 for

TABLE I: Equilibrium Data for the Reaction of UF_4 with Uranium Carbides in Molten Fluoride Solutions of LiF–BeF_2

Run	Solvent	Carbide phase	Temp, °C	Measured absorbance 11,360 cm^{-1}	Measured absorbance 9170 cm^{-1}	Mole fraction × (10^4) UF_3	Mole fraction × (10^4) UF_4	Equilibrium quotient Q (× 10^8)
1	L_2B	UC_2	500	0.130	0.515	0.264	7.25	0.128
2	L_2B	UC_2	550	0.212	0.505	0.804	7.22	11.10
3	L_2B	UC_2	550	0.600	1.050	2.71	14.40	180
4	L_2B	UC_2	573	0.412	0.510	2.17	6.64	761
5	L_2B	UC_2	600	0.485	0.517	2.76	6.68	1,951
6	L_2B	UC_2	600	0.357	0.430	1.97	5.76	786
7	L_2B	UC_2	622	0.516	0.440	3.18	5.29	6,860
8	L_2B	UC_2	650	0.692	0.527	4.57	6.14	19,080
9	L_2B	UC_2	700	1.305	0.780	9.83	7.60	212,300
10	L_2B	U_2C_3	500	0.254	0.538	0.99	7.17	26
11	L_2B	U_2C_3	573	0.474	0.465	2.65	5.66	2,710
12	L_2B	U_2C_3	600	0.409	0.416	2.36	5.29	2,070
13	L_2B	U_2C_3	600	0.595	0.504	3.56	5.98	7,500
14	L_2B	U_2C_3	622	0.524	0.420	3.26	4.91	9,574
15	L_2B	U_2C_3	650	0.611	0.437	4.09	4.90	23,800
16	L_2B	U_2C_3	650	1.276	0.695	8.88	6.27	252,000
17	L_2B	U_2C_3	700	1.083	0.567	8.29	4.74	443,000
18	LB	UC_2	370	0.136	0.390	0.45	5.64	2.3
19	LB	UC_2	400	0.215	0.330	1.04	4.67	115
20	LB	UC_2	450	0.380	0.328	2.23	4.36	2,950
21	LB	UC_2	500	0.482	0.274	3.09	3.21	27,600

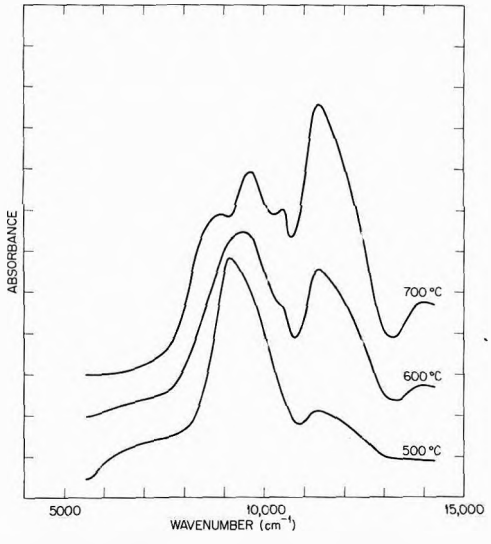

Figure 3. Spectra of dilute UF_3–UF_4 mixtures in LiF–BeF_2 (66–34 mol %) showing temperature effect on the equilibrium $3UF_4 + UC_2 \rightleftarrows 4UF_3 + 2C$.

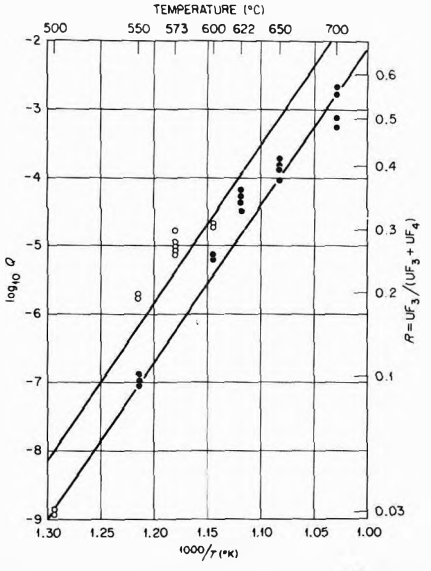

Figure 4. Equilibrium quotients, $Q = (UF_3)^4/(UF_4)^3$, *vs.* temperature for $UC_2 + 3UF_4 \rightleftarrows 4UF_3 + 2C$ in the solvent LiF–BeF_2 (66–34 mol %).

equilibrium mixtures of dilute UF_3 and UF_4 in LiF–BeF_2 (66–34 mol %), "L_2B," in contact with excess UC_2 at various temperatures. The spectra are due only to the UF_3 and UF_4 components of the solution. Therefore, by comparing these spectra with those of pure UF_4 and UF_3 (*cf.* Figure 2 for the UF_3 spectrum and ref 3a for UF_4 spectra) it can be seen that at 500°, most of the uranium in solution is present as UF_4 whereas at 700°, enough UF_3 is present to make the composite spectrum resemble that of UF_3. The composite spectrum at 600° resembles neither of the two pure component spectra but an intermediate mixture of the two.

The quantitative aspects of the temperature change can be seen by the data of Table I for the L_2B solvent. These data are plotted in Figure 4 as log Q *vs.* $(°K)^{-1}$ and show that the equilibrium quotient shifts by 10^6 in going from 500 to 700°. The two lines drawn through the data points represent the least-squares line including the experimental uncertainty of the data arising mainly from the baseline error in the absorption spectra. The point at 500° in Figure 5 was not used in the least-squares determination because it fell outside the experimental uncertainty and could be explained only on the basis that it represented a nonlinear trend in the data. Equilibria at various temperatures were approached from both the high (open circles) and low (closed circles) temperature directions. The train of points at any given temperature in the figure represents the approach to equilibrium with only the lowermost (for open circles) and uppermost (for closed circles) being the best measured equilibrium value. When the equilibrium was approached from the high-temperature side, the

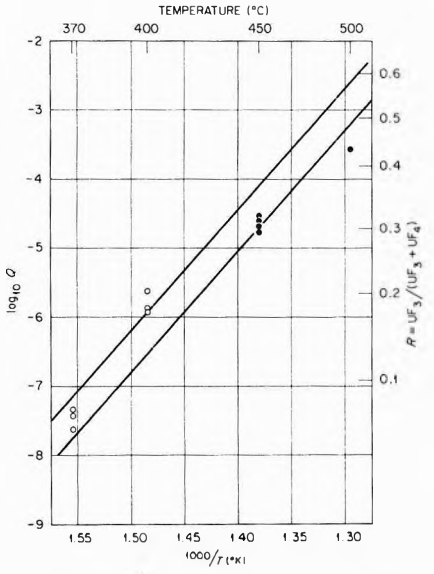

Figure 5. Equilibrium quotients, $Q = (UF_3)^4/(UF_4)^3$, *vs.* temperature for $UC_2 + 3UF_4 \rightleftarrows 4UF_3 + 2C$ in the solvent $LiF-BeF_2$ (48–52 mol %).

chemical reaction involved UF_3 and the graphite walls of the spectrophotometric cell. For ratios, R (*cf.* Figures 4 and 5), greater than 0.2, the amount of UF_3 reacting with the walls was great enough to coat the graphite surfaces with (presumably) UC_2 and slow the approach to equilibrium. Therefore the open circles did not always descend far enough to meet the closed circles. This is especially evident for the 550 and 573° values of Figure 4 and suggests that equilibrium was not achieved for these points. An attempt to alleviate this problem by adding graphite powder failed because the graphite invariably collected at the window sites and interfered with the absorption spectral measurements.

The same large temperature effect is found when U_2C_3 (in place of UC_2) is allowed to react with UF_4 solutions.[6] Some of these data are shown in Table I. The Q values are greater at a given temperature than those when UC_2 is used as the reductant, supporting the identification of the latter as the stable carbide phase of eq 2. These U_2C_3 experiments also demonstrate that the UF_3 stability in dilute fluoride solutions and the temperature effect on the equilibrium would not be far different from that presented in Figure 4 even if U_2C_3 were the stable carbide phase in these systems.

Effect of Solvent on the Equilibrium. In the same way that temperature shifted the equilibrium, changes in the solvent composition did also. The original purpose of this research was to demonstrate that changes in the fluoride ion concentration (which have already been shown[3a] to affect the coordination behavior of dilute UF_4 solutions) might be related to shifts in redox equilibria as well. The effect of changing the solvent composition on the equilibrium is exemplified by comparing the equilibrium quotients for L_2B with those for $LiF-BeF_2$ (48–52 mol %), "LB," in Table I. These data are shown in Figure 5 with the train of open and closed circles plotted under the same conditions as were described for Figure 4.

At any given temperature (*e.g.*, 500°), Q is larger in the LB composition than in the corresponding L_2B melt and is caused by the shift of the equilibrium in eq 2a to the right by increasing the concentration if BeF_2 in the solvent.

Discussion

Changes in solvent composition and temperature have been shown to shift the equilibrium of eq 2a significantly. Although our results compare favorably with previous unreported experimental observations of others in this laboratory, they are not always predictable using the limited thermodynamic data which are available for these systems.

For example, the change in enthalpy for the equilibrium of eq 2a in L_2B can be calculated from our data. Using Baes' standard state for UF_3 and UF_4 of 1 mol % in L_2B,[7a] the equilibrium quotients become equivalent to equilibrium constants, K. The change in enthalpy, ΔH, for the reaction in the 500–600° range can then be obtained from the least-squares slope of the line by the van't Hoff equation. This value is found to be 99.3 kcal and can be compared with the value calculated from enthalpies of formation for the pure, undiluted components at 800°K. These enthalpies of formation and other thermal data given in Table II yield $\Delta H = -12.90$ kcal for the reaction of the *undissolved components*. The process of solvation is not included in the latter calculation because heats of solution for UF_3 and UF_4 are unavailable. The discrepancy between the experimental and the thermodynamic values is therefore attributed to two factors: (1) the neglect of UF_3 and UF_4 heats of solution and (2) the cumulative effect of the uncertainties in these heats of formation.

An estimate in the maximum difference between the UF_3 and UF_4 heats of solution can be made assuming that the effect of cumulative errors in the thermodynamic data is insignificant. It is also assumed that the ΔH of solution for UF_3 is equivalent to the 17 kcal/mol value measured for CeF_3 from solubility studies[11] in the range 600–800°. Combining this with the experimental and calculated enthalpies of reaction from above yields −16 kcal/mol for the UF_4 heat of solution. The difference in the heats of solution for UF_3 and UF_4 would suggest that UF_4 forms complexes of greater stability than does UF_3, in agreement with previous predictions[2] based on the greater ionic potential of U(IV). This then accounts for the previously noted[2] decrease in stability of UF_3 when it is dissolved in fluoride solvents.

If the solutions are made F^- deficient by the addition of acidic constituents such as BeF_2 or ZrF_4, the solvation of UF_4 becomes more like that of UF_3 and an increase in the UF_3 stability is noted (*cf.* Figure 5 for the LB solution). The large solvent effect on the UF_3 stability in $LiF-BeF_2$ solutions also suggests, in agreement with previous coordination studies,[3a] that the L_2B solvent is more basic than would be estimated by Bredig's free-fluoride[11] concept.

It should be emphasized again that the above estimates only give maximum differences in the heats of solution for UF_3 and UF_4 because the errors in the enthalpies of formation were neglected. The availability of reliable solution data for quadrivalent ions would provide a check of this difference. Although considerable work has been reported for heats of mixing of mono- and divalent cations in molten salt solutions,[12] none is available for more highly charged cations such as the ones considered here.

A more direct comparison between our results and previously reported thermodynamic data can be made in considering the effect of solvent changes on the equilibrium. Realizing that the only difference in equilibrium quotients between the two melts L_2B and LB is the ratio of the respective activity coefficients, γ, for UF_3 and UF_4 raised to the appropriate powers, then

TABLE II: Enthalpy Data in kcal/mol[a]

	UC_2	UF_4	UF_3	C
ΔH°_{298}	−20 (1)[5]	−450 (5)[7b]	−345 (10)[7b]	0
$H^\circ_{800} - H^\circ_{298}$	8.79[5]	14.99[8]	11.8[9]	1.83[10]

[a] Sources are referenced as superscripts. Errors associated with each value are given in parentheses (in kcal/mol).

$$K = Q_{L_2B}(\gamma_{UF_3}{}^{L_2B})^4/(\gamma_{UF_4}{}^{L_2B})^3 = Q_{LB}(\gamma_{UF_3}{}^{LB})^4/(\gamma_{UF_4}{}^{LB})^3 \quad (4)$$

where L_2B and LB denote the solvent systems. Since Baes defines[7a] all activity coefficients as unity in the reference composition, L_2B, eq 4 becomes

$$Q_{LB}/Q_{L_2B} = (\gamma_{UF_4}{}^{LB})^3/(\gamma_{UF_3}{}^{LB})^4 \quad (5)$$

The right-hand term can be estimated from Baes' data at 600°[13] where $\lambda_{UF3} \approx \lambda_{CeF3} = 0.7$ and $\lambda_{UF4} \approx \lambda_{ThF4} = 10$ by extrapolating to $LiF-BeF_2$ (48–52 mol %). By this procedure Q_{LB}/Q_{L_2B} is estimated to be 4×10^3.

From our data, Q_{LB}/Q_{L_2B} at 600° can be determined by extrapolating the double lines of Figure 5 to 600° and comparing this value, Q_{LB}, with the value Q_{L_2B} read from Figure 4. We find $Q_{LB}/Q_{L_2B} \approx 5 \times 10^4$ in reasonable agreement with the estimate from Baes' data. The extrapolation of our data in Figure 5 is subject to much error, realizing the scatter in the data points. Better agreement would be anticipated if the comparison had been made at 500° instead, but activity coefficient data were not available.

The two comparisons with thermodynamic data are intended to demonstrate the gaps in the current data for these fluoride systems. The absolute values which were measured here involve a large experimental uncertainty due to the scatter of the data from the spectrophotometric procedure. A parallel study by electrochemical methods would undoubtedly give more precise data for this equilibrium.

In conclusion, the results of this study have shown that the equilibrium of eq 2a is very sensitive to both temperature and solvent changes. High temperature and fluoride-ion deficient solutions enhance the stability of UF_3 whereas low temperature, fluoride-rich solutions decrease it. Therefore, in the fluoride-ion rich solvent, LiF–NaF–KF (45–11.5–42 mol %), UF_3 should be very unstable in graphite, reacting with it to form UF_4 and UC_2. This is actually found to be the case although the interpretation is obscured by competing reactions.[14] The solvent effects described here are in agreement with the previously reported activity coefficients for UF_3 and UF_4 in these solutions. However, the temperature effects which have been measured cannot be adequately predicted from the enthalpies of formation alone; and, consequently, a measurable difference in the solvation energies of UF_3 and UF_4 is suggested.

References and Notes

(1) Research sponsored by the U. S. Atomic Energy Commission under contract with the Union Carbide Corporation.
(2) G. Long and F. F. Blankenship, "The Stability of Uranium Trifluoride," Part I and II, ORNL-TM-2065, 1969.
(3) (a) L. M. Toth, *J. Phys. Chem.*, **75**, 631 (1971); (b) L. M. Toth and L. O. Gilpatrick, *J. Inorg. Nucl. Chem.*, **35**, 1509 (1973).
(4) L. M. Toth, J. P. Young, and G. P. Smith, *Anal. Chem.*, **41**, 463 (1969).
(5) E. K. Storms, "Refractory Materials," Vol. 2, Academic Press, New York, N. Y., 1967.
(6) This metastable system converts so slowly to one involving UC_2 that within the initial time period (days), the higher uranium activity of the excess U_2C_3 determines the value of Q.
(7) (a) C. F. Baes, Jr., "The Chemistry and Thermodynamics of Molten-Salt Reactor Fluoride Solutions, Thermodynamics," International Atomic Energy Agency, Vienna, 1966, pp 409–433. (b) M. H. Rand and O. Kubaschewski, "The Thermochemical Properties of Uranium Compounds," Interscience, New York, N. Y., 1963.
(8) A. S. Dworkin, *J. Inorg. Nucl. Chem.*, **34**, 135 (1972).
(9) C. E. Wicks and F. E. Block, Bureau of Mines Bulletin No. 605 (1963).
(10) JANAF, "Interim Thermochemical Tables," Dow Chemical Co., Midland, Mich.
(11) C. J. Barton, M. A. Bredig, L. O. Gilpatrick, and J. A. Fredricksen, *Inorg. Chem.*, **9**, 307 (1970).
(12) (a) O. J. Kleppa and F. G. McCarty, *J. Phys. Chem.*, **70**, 1249 (1966); (b) G. N. Papatheodorou and O. J. Kleppa, *Inorg. Chem.*, **10**, 872 (1971).
(13) C. F. Baes, Jr., Molten Salt Reactor Semiannual Progress Report for Period Ending Feb 28, 1972, ORNL-4548, p 153.
(14) J. P. Young, *Inorg. Chem.*, **6**, 1486 (1967).

Diffusion of Hydrogen in Rhodium–Palladium Alloys

D. Artman and Ted B. Flanagan*

Chemistry Department, University of Vermont, Burlington, Vermont 05401 (Received April 20, 1973)

Diffusion constants have been determined for interstitial hydrogen in a series of random face-centered cubic rhodium–palladium alloys. Diffusion parameters were determined at small hydrogen contents where they are independent of hydrogen concentration. In contrast to data for gold- and silver–palladium alloys, the presence of small amounts of rhodium leads to a decrease in the diffusion constants. This decrease arises from an increase in the energy of activation for the diffusion of interstitial hydrogen in the alloys.

Introduction

This investigation represents a continuation of studies of how substitutional metals affect the diffusion constants of interstitial hydrogen in substitutional face-centered cubic (fcc) palladium alloys. The Ag–Pd[1-5] and Au–Pd[6] systems have been studied. The diffusion constants measured at H-to-metal, atomic ratio, $n \rightarrow 0$, show similar trends with substituted noble metal contents. The diffusion constants remain nearly invariant with substituted metal content to about 20 atom % and then they decline approximately logarithmically as a function of substituted metal content to the limit of the investigations, *i.e.*, approximately 60 atom % added metal. The closely logarithmic relationship cannot be obeyed over the whole range of contents because in both alloy systems the diffusion constants increase at the limit of pure noble metal.

These two noble metal–palladium alloy systems are similar. Both metals add s electrons to the collective d band of palladium[7] and they both increase the lattice parameter of the palladium host lattice.[8,9] There have been no published accounts of how the diffusion constant of palladium is affected by substituting metals which themselves have holes in their d bands and which decrease the lattice parameter of the host palladium lattice. The Rh–Pd alloy system falls into this category and because of recent interest in the Rh–Pd–H_2 system[10,11] it was selected for study. It was found that rhodium behaves as an absorber of hydrogen at high pressure of gaseous hydrogen when situated within the palladium lattice.[10,11]

Various macroscopic techniques have been employed for the determination of the diffusion constants of hydrogen in palladium and its alloys.[1-6,12-15] The selection of an appropriate technique depends upon the magnitudes of the diffusion constants to be expected and the solubilities of hydrogen in the alloys. In general, the electrochemical techniques[2,6,12-16] at their present stage of development are best suited for the temperature range from 0 to 100° and for those alloys which dissolve appreciable amounts of hydrogen. Gas-phase techniques are more widely applicable but suffer more readily from surface poisoning in the low-temperature range. In this study both techniques have been employed. The electrochemical breakthrough technique[6,12,15] has been employed for alloys of low rhodium content and the gas-phase technique[4] has been used over the entire range of alloys available.

Experimental Section

Apparatus. The electrochemical technique employed was that of Küssner[15] as modified by Maestas and Flanagan.[6] This technique involves electrochemically altering the hydrogen content of one face of a membrane and noting the time required for this perturbation to penetrate to the other side. It was found that this technique did not work well for Rh–Pd alloys with rhodium contents greater than about 10% because of the combination of difficulties in surface activation and low hydrogen solubilities. A gas-phase method similar to that employed by Holleck[4] was therefore employed. The membrane sample is mounted to separate two sides of a vacuum apparatus. Both sides are evacuated and then the appearance of H_2 is monitored on the other side (diffusion side). The pressure was measured on both sides of the membrane with Pirani gauges (LKB, AutoVac, Type 3294B). These were frequently calibrated against a McLeod gauge. The output of the Pirani gauge on the diffusion side of the membrane was recorded with a strip chart recorder (Moseley, Model 7101B) during a diffusion run. The volume of the entry side was large (~15 l.) so that the pressure on this side remained essentially constant during the run. Gold foil protected the membrane from contamination by mercury.

The membrane samples (2.5 cm diameter) were placed between two stainless steel flanges each of which had circular ridges which deformed the membrane in order to make a vacuum tight seal. This seal was the most likely source of leaks and the vacuum had to be carefully tested after mounting a fresh sample. A thermocouple was affixed to the flanges which held the sample. The sample and connecting tubing were sealed to Pyrex *via* a kovar seal. Each side of the connecting tubing contained a flexible bellows tube so that some flexibility was present. The sample and connecting tubing were inserted into an air furnace which was controlled to ±0.2°. The temperature range investigated was 10–270°.

Materials. Hydrogen was introduced into the apparatus by a sample of palladium which had been filled with hydrogen by electrolysis and then transferred to the apparatus, evacuated, and then heated to release its H_2. The Rh–Pd alloy samples were obtained from Engelhard Industries, Inc. Their thicknesses were carefully determined with a high-quality micrometer gauge and they were generally 0.01 ± 0.001 cm. It has been shown previously that these alloys have the expected lattice spacings and they are nonsegregated substitutional fcc alloys.[8]

Sample Preparation. The samples were roughened with very fine emery cloth, briefly immersed in concentrated nitric acid, and then cleaned anodically in sulfuric acid until fine bubbles formed uniformly over the entire surface. The samples were then charged cathodically with

hydrogen for 1–6 hr. The fully charged alloys were then rinsed in distilled water and immersed in a stirred solution of $PdCl_2$(1%). The absorbed hydrogen reduced a thin layer of palladium black onto the membrane surface. The Rh(30%)Pd and Rh(40%)Pd alloys were made cathodic (25 mA) during this plating (0.5 to 5 min) since they absorbed only small amounts of hydrogen during electrolysis. The coated samples were rinsed and stored in water prior to mounting. The samples were mounted wet and then the system was quickly evacuated in order to avoid contact of the dry surface with oxygen.

Method. In the gas-phase method the sample was thoroughly evacuated prior to a run so that the initial concentration of hydrogen was zero, $c_0 = 0$. H_2 was introduced to the entry side of the membrane at a constant pressure at values from 0.1 to 90 mm. Generally, however, the pressure was 2 to 5 mm. The exact time of initiation of a run was automatically indicated by a blip on the recording tracing.

This method differed from that employed by Holleck[4] because he evacuated continuously through a capillary on the diffusion side until a steady-state pressure was attained. In the method employed here H_2 accumulated on the diffusion side. All Pirani readings were converted to pressures *via* a calibration curve. The time lag was determined by extrapolation of the linear region of the pressure increase (steady-state permeation rate) to the time axis. The intercept gives the time lag, t_L.[4,12] If c_0 is zero, and if the pressures on the diffusion side are negligible compared to the entry side, then

$$D = s^2/6t_L \quad (1)$$

The pressure difference between the two sides was large, 10^2 to 10^3. Alternatively the time lag can be evaluated from the time at which the permeation rate is 0.6299 times its steady-state value.[12] Either procedure gave closely similar values of t_L. Time lags ranged from several seconds to about 1000 sec for the various alloys.

Diffusion constants can also be evaluated from the time behavior during the approach to the steady-state permeation rate. The slope of plots of ln $(J_\infty - J_t)/J_\infty$ against t give as the slope $1/t_0$, where t_0 is the rise time[12] and J_t and J_∞ are fixed at time t and at infinite time, respectively. The relationship between t_0 and D is

$$t_0 = s^2/\pi^2 D \quad (2)$$

If J_t is plotted against t, the intercept of the extrapolation of J_t to the time axis gives as the intercept t_b, the breakthrough time which is related to D[12] by

$$t_b = s^2/15.3D \quad (3)$$

Values of t_b can also be obtained from the time at which gas first appears on the diffusion side. In practice, the most convenient measurement of D was *via* t_L and data were determined from this diffusion parameter.

Details of the electrochemical method are given elsewhere.[6] Diffusion constants were determined from the electrochemical breakthrough time.

$$t_b = 0.755s^2/D\pi^2 \quad (4)$$

This differs somewhat from eq 3 because in the electrochemical method the concentration at the diffusion surface is monitored rather than the total gas evolved.[15]

Results

In order to check the experimental apparatus and the method, diffusion constants were determined for a sample whose diffusion behavior is well established, Ag(24%)Pd. Using values determined from the time lag a diffusion constant of $1.4 \pm 0.2 \times 10^{-6}$ cm^2 sec^{-1} (100°) was obtained compared to values in the literature of 1.4×10^{-6} and 1.21×10^{-6} at the same temperature.[4,5]

TABLE I: Values of *D* Corrected for Nonzero Concentrations of Hydrogen at the Diffusion Side (Ag(24%)–Pd, 245°)

p, mm (entry side)	*D*, cm^2 sec^{-1} (eq 1)	*D*, cm^2 sec^{-1} (eq 6)
0.3	0.86×10^{-5}	1.42×10^{-5}
0.4	0.96	1.49
2.3	1.26	1.54
2.7	1.17	1.39
3.0	1.19	1.41
4.5	1.26	1.44

Diffusion constants were determined for the Rh(5%)–Pd and Rh(10%)–Pd alloys with the electrochemical breakthrough technique using eq 4 with samples of the same composition and thickness as used in the gas-phase method, $D(25°) = 5.9 \times 10^{-8}$ (electrochemical) and 7.0×10^{-8} (gas phase) cm^2 sec^{-1} for the Rh(10%)–Pd and $D(25°) = 16.6 \times 10^{-8}$ (electrochemical) and 13.5×10^{-8} (gas phase) cm^2 sec^{-1} for the Rh(5%)–Pd. The agreement is not perfect but good enough to indicate the general validity of this gas-phase method.

A pressure dependence was noted in the values of t_L obtained, *i.e.*, they were shorter at higher pressures. Holleck[4] noted such a dependence of t_L on pressure and he corrected for this dependence with[17]

$$D = \frac{s^2(c_1 + 2c_2)}{6t_L(c_1 - c_2)} \quad (5)$$

where c_2 is the concentration of hydrogen at $x = 0$, the diffusion side of the membrane, and c_1 is the concentration at $x = s$, the entry side. Equation 5 allows for a nonzero concentration of hydrogen at the diffusion side in only an approximate way because the concentration on the diffusion side changes continually with time in both the present method and in Holleck's until the steady state is attained. Sieverts' law[18] should be applicable at these low H concentrations, *i.e.*, $c \alpha p^{1/2}$. The proportionality constant is the same for a given alloy, therefore, eq 5 can be given in terms of pressure

$$D = \frac{s^2(p_1^{1/2} + 2p_2^{1/2})}{6t_L(p_1^{1/2} - p_2^{1/2})} = \frac{s^2}{6t_L}F(p) \quad (6)$$

Holleck employed the final value for p_2 whereas the average value up to the development of the steady state is employed here. Both approaches are only approximate because p_2 is a function of t. Generally the average value of pressure on the diffusion side of the membrane was 0.01 mm. Typical values of $F(p)$ are then 1.67 (at $p_1 = 0.3$ mm), 1.22 (at $p_1 = 2.0$ mm), and 1.14 (at $p_1 = 5.0$ mm). Some values of D corrected in this way are shown in Table I.

It can be seen that the correction appears to give constant values of D to within experimental error. Between about 2 and 5 mm the uncorrected diffusion constants are nearly invariant and approximately 18% smaller than the corrected values. Most data have been obtained in this pressure range because smaller pressures require larger corrections and larger pressures are somewhat inconvenient for routine measurements. Data have been corrected

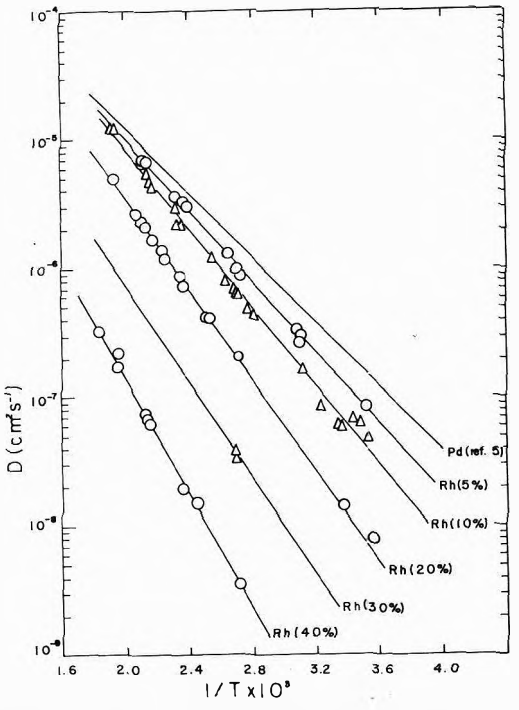

Figure 1. Arrhenius plots of log D against $1/T$ at $n \rightarrow 0$.

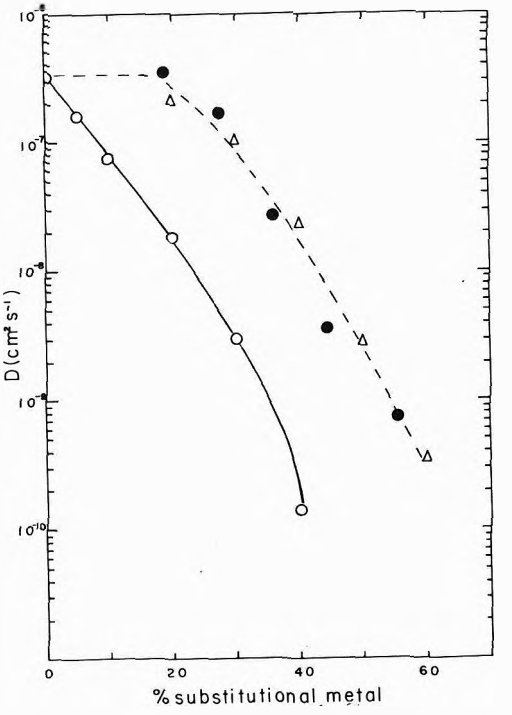

Figure 2. Comparison of D values for interstitial hydrogen at $n \rightarrow 0$ for a series of Au–Pd[6] and Ag–Pd[5] alloys with data for Rh–Pd alloys: O, Rh–Pd (25°); Δ, Ag–Pd (25°); ●, Au–Pd (37°).

TABLE II: Diffusion Parameters for Interstitial Hydrogen ($n \rightarrow 0$) in a Series of fcc Rhodium–Palladium Substitutional Alloys

Alloy	$D_0 \times 10^3$, cm²/sec	E_a, kcal/mol
Pd	5.25	5.76
Rh(5%)–Pd	$5.8 \pm 2.0 \times 10^{-3}$	6.3 ± 0.3
Rh(10%)–Pd	6.5	6.7
Rh(10%)–Pd[a]	10.4	6.8
Rh(20%)–Pd	8.0	7.7
Rh(30%)–Pd	(6.6)[b]	(8.8)[b]
Rh(40%)–Pd	5.2	10.4

[a] Electrochemically determined. [b] D_0 taken as the average value of the Rh(20%)- and Rh(40%)–Pd alloys and E_a calculated from the measured, most reproducible, value of D (92°).

by a factor of 1.18 for the pressure buildup on the diffusion side of the membrane.

Runs were made over a 20-fold pressure change for the Rh(10%)–Pd alloy, 3 to 90 mm (95°). Values of D were approximately 20% greater for this alloy at 90 mm than at 3 mm even after the correction *via* eq 6 was applied. No explanation is offered for this behavior.

Values of t_b were generally too large compared to t_L; this may have been due to the sensitivity of the Pirani gauge in the very low-pressure range. It was not related to problems due to possible slow surface steps because the same behavior was noted for both very long and very short diffusion times measured at the same temperature and pressure for different alloy compositions. Values of t_0, on the other hand, were too small compared to t_L. (Interestingly, despite the discrepancy, $t_0 + t_b$ still was equal to t_L.) This inconsistency of the values of t_0, t_b, and t_L leads to the result that values of D evaluated *via* t_b or t_0 were about 15–20% smaller or 15–20% larger, respectively, than those obtained from t_L. Results based on t_L are believed to give correct values of D and they are the ones reported here. These agree with the literature values for the Ag(24%)–Pd and the electrochemical results obtained here for the 5 and 10% rhodium samples agree with the gas-phase measurements based on the time-lag evaluation of the diffusion constants. In addition, time lags can be more accurately evaluated than t_0 and t_b which require obtaining values of J_t from the slopes of the p–t plots.

Diffusion constants were determined *via* t_L values for the Rh–Pd alloys and are shown in Table II and Figure 1 expressed as $D = D_0 \exp(-E_a/RT)$. These all refer to conditions of $n \rightarrow 0$. In Figure 2 these data are compared with those of other alloys.[4-6] A marked contrast in behavior can be seen with the alloys in which the substituted metal is to the right of palladium in the periodic table. The decline in values of D is caused by the increase in energy of activation for mobility of the interstitial hydrogen.

Discussion

In contrast to the Au–Pd[19] and Ag–Pd[20] systems, substitution of rhodium for palladium results in a greater endothermicity for solution of H_2 at small hydrogen contents.[21,22] This presumably arises from the decrease in size of the interstitial site and the smaller compressibility of rhodium as compared to pure palladium.[21] The decrease in values of D cannot be explained simply by the decrease in size of the interstitial site because a decrease in D is also observed in the other type of alloy and in that case the interstitial site increases in size with added metal.

Beck and coworkers[23] have carried out electrochemical diffusion constant determinations for a series of Fe–Ni alloys over a limited temperature range. In the composition range from 40 wt % nickel to pure nickel fcc substitutional alloys are formed in this alloy system. The diffusion constant increases slightly as the percentage of nickel increases from 40 to 100% (27°). The energy of activation declines slightly with nickel content over the same composition range.[23] They have assigned the principal varia-

tion in D to changes in E_a as was observed in the present research. Changes of E_a are, on the other hand, attributed to corresponding changes of the heat of solution of H_2 with alloy composition, *i.e.*

$$D_{alloy} = D_{Ni} \exp(-\Delta[\Delta H_s]/2RT) \quad (7)$$

the factor ½ arises from a symmetry factor[23] and $\Delta[\Delta H_s]$ is the change in the heat of solution of H_2. This interpretation of interstitial diffusion in fcc alloys cannot be generally valid, however, because such a linear correlation does not exist for palladium alloys. $\Delta[\Delta H_s]$ changes in different directions for Rh–Pd alloys and the Ag–Pd and Au–Pd alloys. It is not clear why the top of the energy barrier should remain nearly unaltered by alloying as implied by eq 7.

It must be concluded that there is at present no adequate theory to account for the behavior of the diffusion constants of interstitial hydrogen with substitutional metals in fcc palladium matrices. It is hoped that a theory along the lines of the Flynn–Stoneham theory[24] for pure metals will be extended to fcc alloys.

Acknowledgments. We thank Miss Geraldine Gross for helpful discussions.

References and Notes

(1) G. Bohmholdt and E. Wicke, *Z. Phys. Chem.* (*Frankfurt am Main*), **56**, 133 (1967).
(2) G. Holleck and E. Wicke, *Z. Phys. Chem.* (*Frankfurt am Main*), **56**, 155 (1967).
(3) D. N. Jewett and A. C. Makrides, *Trans. Faraday Soc.*, 61, 932 (1965).
(4) G. L. Holleck, *J. Phys. Chem.*, **74**, 503 (1970).
(5) H. Züchner, *Z. Naturforsch. A*, **25**, 1490 (1970).
(6) S. Maestas and T. B. Flanagan, *J. Phys. Chem.*, **77**, 850 (1973).
(7) N. F. Mott and H. Jones, "Theory of the Properties of Metals and Alloys," Oxford University Press, London, 1936.
(8) B. R. Coles, *J. Inst. Metals*, **84**, 346 (1956).
(9) A. Maeland and T. B. Flanagan, *Can. J. Phys.*, **42**, 2364 (1964).
(10) T. B. Flanagan, B. Baranowski, and S. Majchrzak, *J. Phys. Chem.*, **74**, 4299 (1970).
(11) B. Baranowski, S. Majchrzak, and T. B. Flanagan, *J. Phys. Chem.*, **77**, 850 (1973).
(12) M. A. V. Devanathan and Z. Stachurski, *Proc. Roy. Soc., Ser. A*, **270**, 90 (1962).
(13) J. W. Simons and T. B. Flanagan, *J. Phys. Chem.*, **69**, 3581 (1965).
(14) M. von Stackelberg and P. Ludwig, *Z. Naturforsch. A*, **19**, 93 (1964).
(15) A. Küssner, *Z. Naturforsch. A*, **21**, 515 (1966).
(16) K. Allard, T. B. Flanagan, and E. Wicke, *J. Phys. Chem.*, **74**, 298 (1970).
(17) J. D. Crank, "Mathematics of Diffusion," Clarencon Press, Oxford, 1956.
(18) *E.g.*, see F. A. Lewis, "The Palladium/Hydrogen System," Academic Press, New York, N. Y., 1967.
(19) K. Allard, A. Maeland, J. W. Simons, and T. B. Flanagan, *J. Phys. Chem.*, **72**, 136 (1968).
(20) H. Brodowsky and E. Poeschel, *Z. Phys. Chem.* (*Frankfurt am Main*), **44**, 143 (1965).
(21) H. Brodowsky and H. Husemann, *Ber. Bunsenges. Phys. Chem.*, **70**, 626 (1966).
(22) J. F. Lynch, J. D. Clewley, and T. B. Flanagan, to be submitted for publication.
(23) W. Beck, J. O'M. Bockris, M. A. Genshaw, and P. K. Subramanyan, *Met. Trans.*, **2**, 883 (1971).
(24) C. P. Flynn and A. M. Stoneham, *Phys. Rev. B*, **1**, 3966 (1970).

Quantitative Biphotonic Chemistry by a Fluorescence Loss Method. The Photodissociation and Photoionization of Durene in a Rigid Solution[1]

F. P. Schwarz and A. C. Albrecht*

Department of Chemistry, Cornell University, Ithaca, New York 14850 *(Received January 26, 1973; Revised Manuscript Received August 1, 1973)*

Publication costs assisted by the National Institutes of Health

Two simultaneous biphotonic chemistries in a rigid organic solution are treated quantitatively. The fractional "fluorescence loss" of the parent solute molecule is monitored as the key experimental parameter for quantifying the photochemistry. The fluorescence loss results both from the depletion of the parent molecule as well as competitive light absorption by the photoproducts. Furthermore the photoproducts are not homogeneously distributed in the sample because of its high viscosity. A general formalism is developed for handling this problem with the aim of obtaining quantum yields or cross sections for the several elementary steps. Durene as the solute in 3-methylpentane at 77°K is the example studied. Here the two photochemistries are β-bond scission to give the duryl radical, and a one-electron ionization to give the durene cation. Both photochemistries proceed *via* a one-photon excitation from the lowest durene triplet state. The two simultaneous photochemical channels are differentiated by reversing the ionization step through infrared-induced charge recombination and measuring a fractional "fluorescence recovery" of durene. Perdeuterated durene is studied as well. The β-bond cleavage shows a strong isotope effect. The quantitative results, though crude, yield the following results. The quantum yields for the second photon step at 275 nm out of the triplet state are $\sim$0.4 (β-bond scission) and $\sim$0.6 (ionization). Thus every excitation appears to lead to photochemistry. Molar decadic extinction coefficients at 270 nm in nonpolar solution at 77°K are found to be 1.3×10^4 for the triplet state, 2.5×10^3 for the duryl radical, and $\sim 0.5 \times 10^3$ for the durene cation. The efficiency for the infrared-induced charge recombination to generate durene *via* its excited singlet and triplet states is found to be of the order of unity. Finally, a previously discovered one-photon channel for the β-bond cleavage *via* upper vibrational levels of the first excited singlet state is seen to proceed with a quantum yield of $\sim 10^{-4}$.

I. Introduction

The methylated benzenes are representative of a class of molecules which undergo β-bond photodissociation and one-electron photoionization when dissolved in dilute, rigid 3-methylpentane (3MP) solutions at 77°K.[2a] These two elementary photochemical processes are mutually competitive; they both appear to proceed biphotonically *via* a near continuum of triplet states with energies very close to the ionization potential of the methylated benzene in 3MP.[2b] These highly excited molecular states are reached from the ground state by radiative excitation into the excited singlet manifold followed by intersystem crossing to populate the lowest triplet level; a second photon then excites this triplet state into upper levels of the triplet manifold. At this point the system enters the radiationless channels which lead to each of the two elementary chemical changes. Tsubomura[3] has published a brief survey of molecules which undergo either photoionization, photodissociation, or both processes as in the case of the methylated benzenes. He has shown that one can predict from the energy available for the second photon step whether a molecule would belong to the photoionizable class, to the photodissociative class, or to both classes. To our knowledge no detailed quantitative study of both processes occurring within a single molecule has been made.

We have undertaken such a study in a model system of a 10^{-3} *M* solution of durene (1,2,4,5-tetramethylbenzene) in 3MP at 77°K. The β-bond cleavage yields a 2,4,5-trimethylbenzyl radical which emits a bright green fluorescence.[2a] Photoionization of the durene in this system is demonstrated by photoconductometric measurements[4] and infrared-stimulated charge recombination (ISCR) luminescence.[2b,5] (Infrared stimulation of the sample following ionization mobilizes the matrix trapped electrons, the majority of which recombines with the durene cations resulting in durene luminescence.) A preliminary result[6] of this study is the discovery of two additional mechanisms for β-bond cleavage in durene. (1) At low photosensitization intensities ($\sim 10^{13}$ photons/cm^2 sec) and at energies $\geq$4.6 eV, β-bond cleavage proceeds by a one-photon mechanism. (2) Upon infrared-stimulated charge recombination the production of duryl radical is observed. The present report is concerned with the quantitative study of both monophotonic and biphotonic β-bond cleavage and of photoionization. The duryl radical production *via* ISCR has been reported elsewhere.[7]

While it is not difficult to follow the two photochemistries with good sensitivity by observing properties of the product molecules such as luminescence or recombination luminescence, these are not immediately quantitative since quantum yields and/or extinction coefficients belonging to these molecules are not known. Instead, in this work the basic approach is to follow the total photochemistry by observing the fractional decline of the parent molecule fluorescence with time. This must be quantitatively related to the fraction of the known initial concentration of parent molecule which has been destroyed through the photochemical channels. The two observed photochem-

istries (we assume no other) are then separated by forcing the reversal of only the ionization component through ISCR which results in a partial recovery of the durene fluorescence. The quantifying of this technique is fraught with complications such as the competitive light absorption by photoproducts, and the polychromatic nature of the photosensitizing light compounded by the fact that the photoproducts are biphotonically (or monophotonically) produced in a nonfluid and optically dense medium and are thereby sharply distributed in a depth. Photoproducts may be orientationally distributed as well, a complication that will not be considered here. A principal effort of this work is to develop the analysis which converts properties observed from the bulk sample to their "front surface" equivalents where the separation of the various interferences is relatively straightforward. The analysis is then applied to the experimental data which provides the first quantitative estimate of yields in the two biphotonic chemistries, as well as estimates of the quantum yields for the monophotonic β-bond scission and the ISCR process. Following the Experimental Section comes a section which outlines the principles of the "fluorescence loss" techniques and presents the equations needed for the "front surface" analysis. The introduction of the experimental data then appears followed by a brief discussion of the results. It will be seen how not only are quantitative estimates obtained of the quantum yields for four different processes, but, accompanying these determinations are estimates of (1) an extinction coefficient for the triplet–triplet transition involved in the second photon step, (2) an estimate of the duryl radical extinction coefficient, and (3) a more complete description of the events which carry the system from the "super excited" states (generated by the infrared stimulation of the ionized system) to its ground state.

II. Experimental Section

A. Materials. The durene was purified Puriss Grade from the Aldrich Chemical Company. Purification consisted of many passes through a zone refiner. Perdeuterated durene was kindly supplied by A. Kalantar of the University of Alberta. The 3MP was purified MCB Chromatography Grade 3 and it was purified by keeping the solvent over Linde Molecular Sieves for several days prior to its usage.

B. Apparatus. The apparatus shown schematically in Figure 1 consisted of four components: (1) a sample holder containing liquid N_2; (2) an AH-6 lamp passing light through an Aminco monochromator for excitation and photosensitization of the sample; (3) an infrared source to photostimulate charge recombination in the photosensitized samples; and (4) a detection system to monitor the exciting light intensity and to detect luminescence emitted by the solution. The monochromator was equipped with a 1200 grooves/mm grating blazed at 300 nm. It had a dispersion of 33 A/mm and an $F/4.4$ gathering power. The uv light emerging from the monochromator was passed through a Corning 9863 filter, a cobalt–nickel chloride solution, and a quartz plate which deflected 10% of the light into the monitoring photomultiplier.

This light was focused into the sample by an 8-in. focal length Suprasil lens. The sample was contained within a 0.5-cm (i.d.) square quartz cell which was immersed in liquid nitrogen contained in a Suprasil quartz optical dewar. The dewar was placed in a special housing to minimize the scattering of light into the detection system.

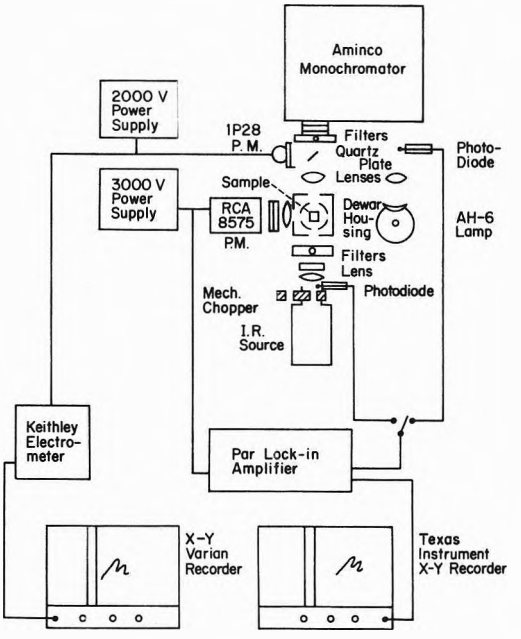

Figure 1. Schematic diagram of the experimental arrangement.

Luminescence from the sample was detected through suitable filters by an RCA 8575 photomultiplier operated at 2500 V. Its output was fed into either a Keithley Model 610 electrometer or a P.A.R. lock-in amplifier. This amplifier was tuned to the 120-Hz modulation of the AH-6 lamp by means of a photodiode. The output from either amplifier was recorded on a Texas Instrument X–Y recorder. The monitoring photomultiplier consisted of a sodium salycilate screen which has a constant quantum yield[8] from 350 nm to the vacuum uv for a blue fluorescence which was passed through appropriate filters and detected by an RCA 1-P28 photomultiplier. The 1-P28 was operated at 1000 V and its output was amplified by a Keithley Model 610 electrometer and recorded on a Varian X–Y recorder. Use of both photomultipliers allowed simultaneous detection of the exciting light intensity and the luminescence intensity.

The infrared stimulation system consisted of 300-V Bell and Howell slide projector in which the infrared absorbing lens was replaced by several Corning 2504 filters. To avoid absorption of infrared light by the solvent in the sample, a 1-cm cell of 3MP was used to filter the infrared light. The infrared stimulation took place from a position 180° with respect to the exciting beam.

Whenever optical density measurements of the duryl radical were made, a 1-P28 photomultiplier was placed before the 3MP solvent filter in a position to receive the transmitted exciting light beam. Its output was amplified by the Keithley electrometer and recorded by an X–Y recorder. Since the discontinuous wavelength output of the AH-6 could induce additional error in the absorption spectrum, it was replaced by a Bausch and Lomb H_2 lamp which was inserted in between the AH-6 lamp and the entrance slit of the Aminco monochromator.

The samples were prepared and deoxygenated in the following manner. Accurate amounts of the solute were measured by a Cahn electrobalance to make a 1.30×10^{-3} M solution (or 1.66×10^{-3} M at 77°K because of a 22% contraction of the sample). A sample was deoxygenated by purging the sample with helium just before immersing it in the liquid nitrogen. The helium-purging technique

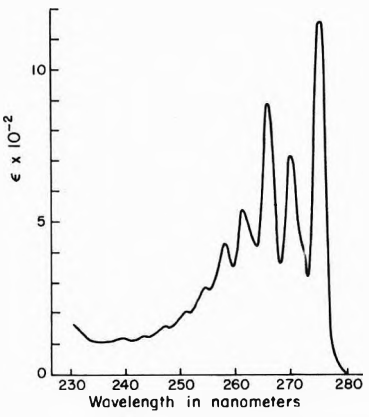

Figure 2. Absorption spectrum of durene in 3-MP at 77°K (from ref 2) (molar decadic absorptivity).

gave results indistinguishable from the more tedious freeze–pump–thaw method. Each sample was discarded after a photosensitization since the duryl radicals were irreversibly formed.

C. Low-Temperature Absorption Spectrum of Durene. The absorbancy of the 10^{-3} *M* durene 3MP solutions at 77°K has been measured previously.[2a] To obtain the corresponding absorbtivity (extinction coefficients) we have used an approach based on the fact that the electronic transition probability is to first-order independent of temperature.[9]

Thus, for any given pair of temperatures, T_1 and T_2, we may write

$$\int \epsilon_{T_1} \, d\nu = \int \epsilon_{T_2} \, d\nu$$

If at T_2, we have the absorbancy of the sample, A_T, in arbitrary units and at T_1 we know the absorbtivity of the sample, ϵ_{T_1} (a Cary 14 spectrophotometer was used), then we may determine the proportionality constant, K, in the relation $\epsilon_{T_2} = KA_{T_2}$, thus permitting a conversion of absorbancy measurements to absorbtivity values without directly determining the concentration-cell thickness factor under conditions prevailing at T_2.

Thus

$$K = \int \epsilon_{T_2} \, d\nu / \int A_{T_2} \, d\nu = \int \epsilon_{T_1} \, d\nu / \int A_{T_2} \, d\nu$$

where the first equality follows from the definition of K, the second equality from the assumed temperature independence of the oscillator strength, and where the factors in the last quotient are experimentally available (T_1 is room temperature and $T_2 = 77$°K).

In Figure 2 we present the absorptivity *vs.* λ of a durene–3MP solution at 77°K thus determined. (Henceforth, the symbols T_1, T_2 shall exclusively refer to triplet levels and not temperatures.)

D. Actinometry Measurements. For the actinometry measurements we used the potassium ferrioxalate actinometry method developed by Hatchard and Parker.[10] All the solutions and the calibration curve were kindly supplied by Dr. R. A. Caldwell. The actinometric solutions were exposed to the same intense photon flux as was used in photosensitization of the sample and at various lengths of time. The typical photon flux under these conditions is $\sim 10^{15}$ photons/cm^2 sec. We used the reading of the monitor photomultiplier as the standard for comparing the photon flux in the actinometric measurements to that of the photosensitization experiments.

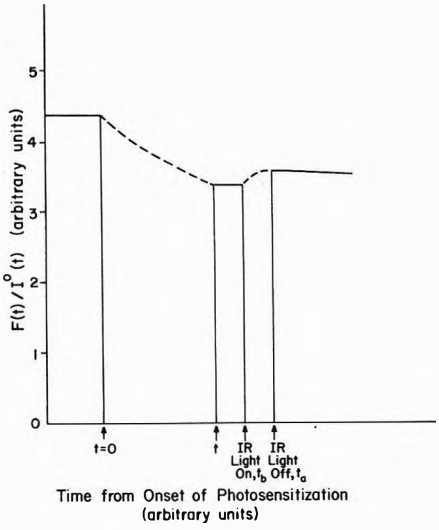

Figure 3. Observed "fluorescence loss" (relative to I^0) of durene as a result of photosensitization. A "fluorescence recovery" is seen following infrared-induced reversal of the ionization channel.

III. The Fluorescence Loss Technique in a Rigid Medium

The method of using the fluorescence loss of the parent molecule as a quantitative indicator of photoproduct formation when performing photochemistry in a rigid, optically thick, sample is now examined using the rigid durene–3MP system as the working example.

For sake of brevity the actual details of the analysis are offered elsewhere.[11] Here only the notation and the salient features of the analysis are presented.

A. Preliminary Observations on the Changes of Durene Luminescence. Prolonged intense photosensitization in the durene absorption region of the rigid durene–3MP solutions results in a luminescence color change from the violet durene phosphorescence to a whitish green luminescence. This conspicuous change of the luminescence properties of the sample is principally due to the growth of duryl radical fluorescence as the durene luminescence itself diminishes. The change in durene fluorescence is conveniently monitored by using a weak beam of 270-nm exciting light and viewing the sample emission in the near ultraviolet. Thus, to check the durene level before and after intense photosensitization (done at 5-mm slit widths centered at 275 nm), the slits are narrowed to 0.1 mm and the monochromator is set to 270 nm to excite the durene fluorescence, F. Next, the sample is stimulated with infrared light. This bleaches the durene cation interference and restores some of the durene. Accordingly, a partial recovery of the durene fluorescence is observed. Such changes in the level of durene fluorescence in a typical experiment are shown in Figure 3. The actual parameter used is $(F/I^0)_t$, the ratio (at point t in the experiment) of the fluorescence signal to the exciting light intensity at 270 nm, since I^0 would vary at different points in the experiment.

From data of the sort shown in Figure 3 we can extract two important parameters. One is the apparent fractional conversion of durene to duryl radical

$$\Delta\Phi_R = [(F/I^0)_0 - (F/I^0)_a]/(F/I^0)_0 \qquad (1)$$

where $(F/I^0)_a$ is the (F/I^0) ratio after reconversion to durene of the cation by ISCR. $(F/I^0)_0$ is the fluorescence to

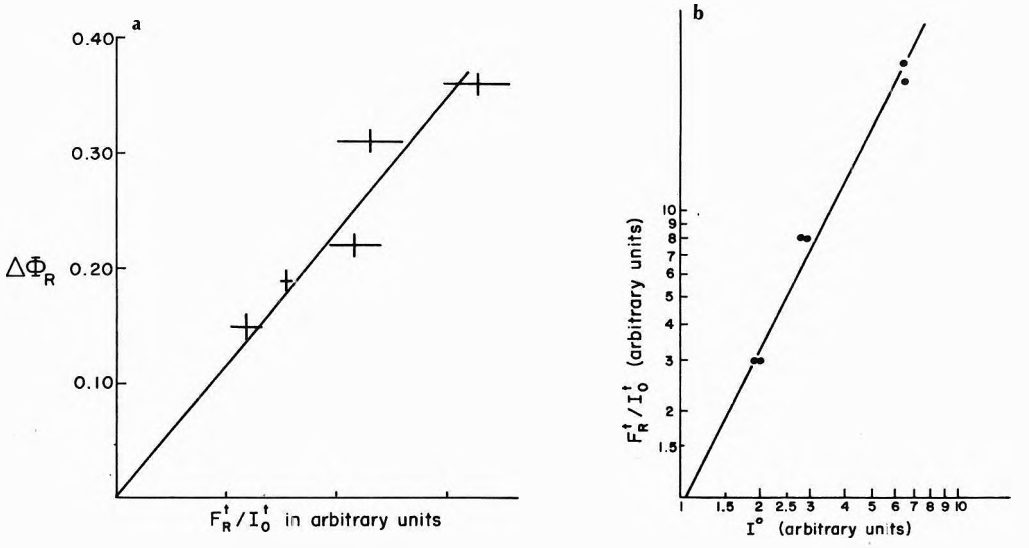

Figure 4. (a) The apparent fractional conversion of durene to duryl radical ($\Delta\Phi_R$ of eq 1) plotted against the duryl radical fluorescence (normalized) excited at 329 nm. (b) The logarithm of the duryl radical fluorescence (normalized) excited at 329 nm *vs.* the photosensitization light intensity.

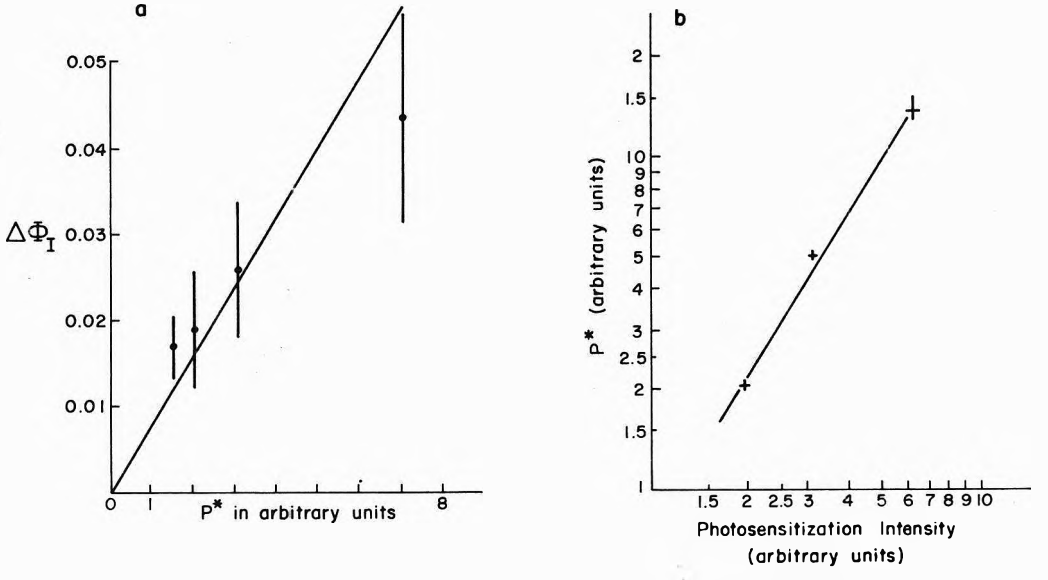

Figure 5. (a) The apparent fractional conversion of durene to the durene cation ($\Delta\Phi_I$ of eq 2) plotted against the infrared-induced charge recombination durene phosphoresence P^*. A straight line is forced through the data points. (b) The logarithm of the recombination phosphorescence *vs.* the intensity of the photosensitization light.

incident light ratio prior to any photosensitization. This is the observed loss of durene fluorescence (excluding that due to ionization) divided by the initial level of durene fluorescence.

The second parameter is the apparent fractional conversion of durene to the durene cation

$$\Delta\Phi_I = [(F/I_0)_a - (F/I_0)_b]/(F/I^0)_0 \qquad (2)$$

where a refers to the time after complete ISCR (as just stated) while b refers to the time just before ISCR. This is the increase of the durene fluorescence seen upon reversing (with ISCR) the ionization step, normalized to the initial fluorescence level.

The parameter $\Delta\Phi_R$ does, roughly, correlate with radical production. Thus, (a) $\Delta\Phi_R$ observed under different conditions, such as a variation of the photosensitization intensity, follows the fluorescence level of the duryl radical itself (given as $F_R^\dagger/I_0^\dagger$, the superscript indicating that the radical luminescence is excited at 329 nm), see Figure 4a; and (b), values of $\Delta\Phi_R$ correlate qualitatively with the observed absorbancy of the duryl radical in the near ultraviolet region. A logarithmic plot of $(F_R^\dagger/I_0^\dagger)$ *vs.* the intensity, I^0, of the photosensitization light is shown in Figure 4b and an essentially quadratic dependence is seen.

A direct independent measure of durene cation level is, of course, the intensity of the recombination luminescence, measured here as a recombination phosphorescence, P^*. A plot of $\Delta\Phi_I$ *vs.* P^* is given in Figure 5a and a close correlation between these parameters is seen. In Figure 5b a logarithmic plot of P^* *vs.* intensity reveals a superlinear dependence on the photosensitizing light intensity of 1.5.

The distinctly different light exponents shown by the two different biphotonic chemistries reflects another important feature distinguishing the two processes. On the time scale of this work it is found that the buildup of the duryl radical is essentially *linear* in photoexcitation time (the buildup is in the initial slope region of the process

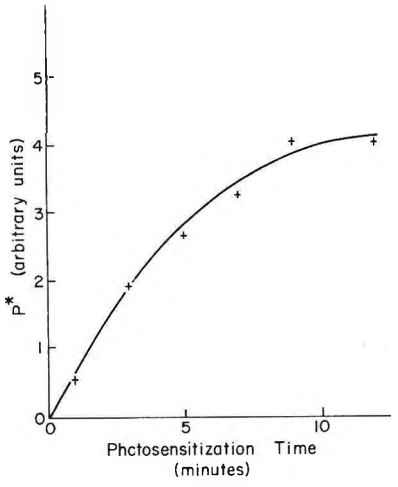

Figure 6. Recombination phosphorescence, P^*, *vs.* the photosensitization time.

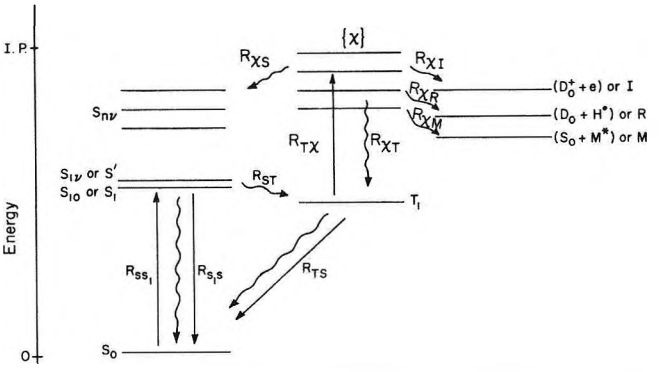

Figure 7. Energy level diagram illustrating most of the elementary steps discussed in the text. In particular the three channels leading from the $\{\chi\}$ states to the I (ionization), R (β-bond cleavage), and M (energy transfer to matrix) states are shown. Only four of the elementary steps are taken as radiative (solid arrows). The notation is defined in the text.

and the elementary quadratic dependence on light intensity is exhibited). However, on this same time scale the photoionization has approached a steady-state condition. This is shown in Figure 6 where a plot of P^* *vs.* time of photosensitization is given. This is because charge recombination (the complete reversal of the photoionization) is stimulated (the electron is detrapped) both thermally and by the incident ultraviolet photosensitizing beam. Under these conditions an effective power dependence on incident light between 1 and 2 can be expected (depending on the balance between thermally stimulated and radiatively stimulated charge recombination). Thus, because, in the ionization one of the photoproducts (the electron) can be mobilized to recombination, a pseudo-steady-state condition is achieved. (The steady conversion to duryl radical prevents a genuine steady state from being achieved.)

In order to avoid complications presented by this saturation of the photoionization (for example, the depth distribution of the ionization will differ from that of the radical), we shall use Figure 6 as a guide to extrapolate the $\Delta\Phi_I$'s observed at long times into the linear region where their direct measurement is difficult. In this extrapolation, the appropriate correction for differing intensity from trial to trial must be made.

In introducing the two durene fluorescence parameters, $\Delta\Phi_R$, $\Delta\Phi_I$, it is important having qualified them as "apparent" because of the interferences, which actually disallow their simple interpretation, particularly in the case of $\Delta\Phi_R$. Thus, some decrease in F is a result of competitive light absorption by the photoproduct. For example, the fractional loss of durene should not depend on the wavelength being used to excite the durene fluorescence yet when comparing the $\Delta\Phi_R$ obtained at 270 nm with that at 275 nm we find $\Delta\Phi_R$ (270 nm)/$\Delta\Phi_R$ (275 nm) = 1.84 ± 0.12, not unity. This reflects a considerable and variable interference due to absorption of the fluorescence excitation beam by photoproduct which turns out to be mainly the duryl radical.

The necessary task is to find the connection between those easily measured "fluorescence loss" parameters $\Delta\Phi_R$ and $\Delta\Phi_I$ (properties of a *bulk* sample which has been sensitized with *polychromatic* light) and the quantum yields for the three elementary processes: (1) the monophotonic duryl radical production; (2) duryl radical production by one photon absorption from the lowest triplet state of durene (overall biphotonic); (3) the ionization by one photon absorption from the lowest triplet state of durene (overall biphotonic). The second and third processes are of course the two *biphotonic* transformations since the triplet state must be radiatively formed from the ground state of durene. In order to achieve this connection in as straightforward a manner as possible it is necessary to develop a simple and efficient notation. This is done next within the context of presenting the general kinetic scheme.

B. Kinetic Model and Notation. The basic model involves a series of unimolecular type events occurring within any given solute molecule–solvent cluster domain. Figure 7 organizes around an energy level diagram the notation to be used in the kinetics treatment. They are as follows.

(*1*) *States.* S_0, S_1, ...; T_1, T_2 ... represent the usual notation for singlet and triplet states. Double subscripts are used when a vibrational sublevel is indicated, D_0^+ the ground (doublet) state of the cation, $D_0^\cdot$ the ground (doublet) state of the neutral radical product of the β-bond scission, $\{\chi\}$ the set of ill-defined states near the ionization continuum of the solute reached by excitation from T_1 and from which lead channels for the two chemistries, $\{\chi^*\}$ a set of similar states reached through ISCR, (D_0^+ + e) or I the ionization, ($D_0^\cdot$ + H) or R the β-bond scission, and also (S_0 + M*) the collapse to the parent ground state resulting in energy rich medium M*. All state symbols are simultaneously used as concentration variables at penetration depth, x, in the sample at time t following the onset of photosensitization. Whenever these various states are referred to in general, the symbols X and Y are used. The units are moles/liter (or millimoles/cc).

(*2*) *Rates, Rate Constants, and Quantum Yields.* All processes are divided into elementary steps coupling two states X → Y (X,Y can be any of the above-mentioned states). We have $R_{XY}(x,t)$ representing the rate in moles/liter (or millimoles/cc) per sec of passage from state X to state Y at position x in the sample after time t of photosensitization, k_{XY} the corresponding unimolecular rate constant (sec^{-1}), ϕ_{XY} the efficiency of the X → Y channel for the passage out of X with $\phi_{XY} = k_{XY}/\Sigma_Y k_{XY}$, τ_X the lifetime of state X(sec) where $\tau_X^{-1} = \Sigma_Y k_{XY}$. Because of the basic unimolecularity of the steps we have

$$R_{XY}(x,t) = k_{XY}X(x,t) = \phi_{XY}\tau^{-1}X(x,t)$$

Of all the elementary processes, three are induced radiatively. $R_{S_0S_1}$ refers to the rate of excitation of durene

from its ground state to its first excited singlet state; $R_{T\chi}$ shall indicate the rate of excitation from the lowest triplet state to the chemically active $\{\chi\}$ states; and $R_{I\chi^*}$ is the rate of exciting the ionized state (normally with near-infrared light) into the $\{\chi^*\}$ states from which ground-state durene is ultimately recovered.

All excited singlet and triplet states (except T_1) are taken to be sufficiently short-lived to represent a "steady-state" condition on time scales at least comparable to the 120-Hz modulation of the exciting lamp and longer. The lowest triplet state, while not responsive to the 120-Hz modulation will respond faithfully to changes occurring on the time scale of several seconds and longer corresponding to the photosensitization time scales.

(3) *Integrations.* The elementary parameters of the kinetic model are related to the observed properties of a macroscopic sample through three important integrations. There must be (a) an integration over the photosensitization time period, (b) an integration over the full sample thickness and, (c) a monochromatic statement must be integrated over a finite wavelength region. In general, these integrations are not separable; however, in the approximation employed here they prove to be so. The following notation is employed for each of the three integrations.

(a) To symbolize an integration of any property over photosensitization time from zero to t the symbol of that property is set in boldface. Thus, $\mathbf{R}_{XY}(x,t)$ is the moles/liter of Y made from X at position x in the sample after t seconds of photosensitization.

(b) To symbolize the integration of any property over the sample thickness (in cm) brackets will be used. Thus $\langle R_{XY}(t)\rangle$ is the millimoles of Y being made from X at time t in the full thickness of the sample per second per 1 cm^2 cross section. $\langle \mathbf{R}_{XY}(t)\rangle$ is the total Y made from X (millimoles) during the entire photosensitization period.

(c) The wavelength integrations normally involve products of photon capture cross sections, σ, light intensities, I, and quantum yields ϕ_{XY}. The effective wavelength spread is no more than between 10–20 nm so the ϕ_{XY} are taken as some average value for this range. This procedure is known not to be possible for the first photon cross section, which is simply related to the wavelength dependent extinction coefficient of the structured S_0–S_1 transition in durene. The "monochromatic" rate constants, the $\sigma I(x,t)$ products, when suitably integrated over wavelength will be given the symbol $J(x,t)$ with appropriate subscripts. These become effective polychromatic rate constants (sec^{-1}) for the elementary radiative steps. Wavelength integrations for biphotonic events are more complicated, but will also carry the symbol J appropriately identified. The problem of the wavelength integrations is handled in detail in the Appendix.

(4) *"Front Surface" Properties.* The complexities of the fluorescence loss method arise because of the necessity of working with samples which are not optically thin. The "front surface" behavior of the sample, however, suffers the least from complications. Thus, when determining quantum yields it is most convenient to express these in terms of "front surface" properties which are indicated with a superscript zero. For example $\mathbf{R}_{XY}{}^0(t)$ represents the "front surface" concentration of Y made from X after t seconds of photosensitization, etc. It then becomes convenient to express any bulk properties of the sample as its "front surface" value multiplied by depth integrals over appropriate dimensionless depth distribution functions. These depth distribution functions must indicate the distribution in depth of the incident light, or of the photoproducts and of durene, too.

Because of the approximations employed,[11] the depth distribution function for the photoproducts will be independent of time and fall into two types: the depth distribution function for photoproducts made monophotonically, $l_1(x)$; and $l_2(x)$ the depth distribution of the biphotonically generated photoproducts. Thus if X → Y amounts to the culmination of a biphotonic event we can write

$$\langle \mathbf{R}_{XY}(t)\rangle = \mathbf{R}_{XY}{}^0(t)\langle l_2\rangle$$

The depth distribution function for ground-state durene is, of course, constant at $t = 0$. However, already then its excited state is distributed exponentially (Beer's law), a depth distribution function assigned as $g_0(x)$. This is nothing more than the depth distribution of the monitoring light (at 270 nm). Once photoproduct develops the depth distribution of this monitoring light changes and in general is given by $g(x)$. Explicit forms of these depth distribution functions are found in the Appendix.

With the notation thus defined, it is possible to relate the various quantum yields of interest to the fluorescence loss parameters and other observables. This is outlined in the next section and more thoroughly presented elsewhere.[11]

C. Photochemical Quantum Yields. If it is assumed that the quantum yield for any given elementary process is independent of position in the sample and of the duration of the photosensitization, then there are several alternate ways to express these yields. Thus, for the biphotonic radical production, the principle quantum yield is $\phi_{\chi R}$. This is just the fraction of all radiative excitations from T_1 → $\{\chi\}$ which produces the duryl radical. Thus

$$\phi_{\chi R} = \frac{R_{\chi R}}{R_{T\chi}} = \frac{\mathbf{R}_{\chi R}}{\mathbf{R}_{T\chi}} = \frac{\mathbf{R}_{\chi R}{}^0}{\mathbf{R}_{T\chi}{}^0} \quad \text{etc.} \tag{3}$$

which, respectively, refers to (1) events momentarily occurring at any point in time and position in the sample, (2) the total events which have occurred after t seconds of photosensitization at any given position in the sample, or (3) the total events which have occurred after t second of photosensitization at the front surface. It is the front surface version which is of interest here. Thus, for the ionization we have

$$\phi_{\chi I} = \mathbf{R}_{\chi I}{}^0/\mathbf{R}_{T\chi}{}^0 \tag{4}$$

and the monophotonic radical production from a vibronic level of S_1 (S′ for short)

$$\phi_{S'R} = \mathbf{R}_{S'R}{}^0/\mathbf{R}_{SS'}{}^0 \tag{5}$$

and, finally, for the efficiency of the infrared-stimulated charge recombination step I → $\{\chi^*\}$

$$\phi_{I\chi^*} = \mathbf{R}_{I\chi^*}{}^0/\mathbf{R}_{\chi I}{}^0 \tag{6}$$

In each case, the numerator gives the moles/liter (or mmoles/cc) of the given elementary process which has taken place after t seconds of the photosensitization. The denominator is just the total concentration of radiative events leading to the given elementary process after t seconds of illuminating the sample. (In the case of the recombination process, eq 6, it is assumed that the totality of infrared-stimulated events giving ground-state durene is just the number of ionizations, $\mathbf{R}_{\chi I}{}^0$). Alternatively, these quantum yields could be converted to a ratio of pure numbers by dividing both numerator and denominator by the same element of volume.

In each case the numerator is to be obtained by the fluorescence loss technique. The denominator is obtained essentially by using extinction coefficients and actinometry. More directly, however, the number of $T_1 \rightarrow \{\chi\}$ excitations (in eq 3 and 4) is found *via* radiative lifetime shortening of the triplet state, as will be seen below.

The fluorescence loss parameters $\Delta\Phi_Y$(Y = R,I) may be expressed in terms of the fraction of durene converted to the given photoproduct on the front surface multiplied by a dimensionless function, L_Y, which explicitly accounts for the complications arising when passing from observations on the bulk sample (the fluorescence loss parameters) to its front-surface properties. Thus

$$\Delta\Phi_Y = (\mathbf{R}_{\chi Y}{}^0/S_0{}^0)L_Y \quad (Y = R,I) \tag{7}$$

where it is found,[11] under the simplifying conditions of low conversions, how

$$L_Y = \frac{\langle l_2 g_0\rangle}{\langle g_0\rangle} + (\epsilon_Y - \epsilon_0)S_0{}^0\frac{\langle g_0\langle l_2\rangle_x\rangle}{\langle g_0\rangle} \tag{8}$$

The various depth integrals in eq 8 have already been alluded to and are given explicitly in the Appendix. The extinction coefficients, ϵ_0 and ϵ_Y (Y = R,I), are the molar Naperian extinction coefficients at the fluorescence monitoring wavelength, 270 nm, of durene (S_0), the duryl radical ($D_R^{\cdot}$), and the cation of durene ($D_0{}^+$), respectively. $S_0{}^0$ is the initial concentration of durene in the sample. The two terms in eq 8 have the following physical significance. The first term, which is less than or equal to one, represents the fact that the fluorescence loss parameter reflects a depth-averaged conversion of durene to photoproduct and therefore is a weaker parameter than it would be if it reflected only the front-surface conversion where the photochemistry is strongest. In the limit of an infinitely thin sample this term would become unity. The second term results from the fact that the intensity of the 270-nm beam used to probe the durene fluorescence has a changing penetrating power as durene is converted to photoproduct. Thus if $\epsilon_Y > \epsilon_0$, the probing beam is less penetrating than it was in the absence of photochemistry and the apparent fluorescence loss is greater as a result. If, accidentally, $\epsilon_Y = \epsilon_0$, then the penetration of the probe beam is independent of photochemical conversion, and this term simply vanishes. Interestingly, were $\epsilon_Y < \epsilon_0$, this term becomes negative, allowing more penetration of the probing beam after photochemistry than before. This means that as durene is destroyed there is of course a fluorescence loss due to this, but there is a recovery as well, because the sample becomes more transparent and more of the remaining durene can be excited. In the limit of infinitely thin samples this competitive light absorption term vanishes, as it must, and then $L_Y = 1$. For the practical studies carried out here, both of these terms are significant and knowledge of ϵ_Y (Y = R,I) becomes important for determining the quantum yields.

Equation 7 is the direct source of the front-surface conversion to photoproduct needed in the quantum yield expressions for the two biphotonic photochemistries; thus, rearranging eq 7

$$\mathbf{R}_{\chi Y}{}^0(t) = S_0{}^0\Delta\Phi_Y(t)L_Y{}^{-1} \quad (Y = R,I) \tag{9}$$

The front-surface rate of exciting the triplet state into the $\{\chi\}$ states appearing in the denominators of the quantum yield expressions, is

$$R_{T\chi}{}^0 = \sigma_2 I^0 T_1{}^0 = J_2{}^0 T_1{}^0 \tag{10}$$

where $T_1{}^0$ is the steady-state triplet concentration at the front-surface of the sample and σ_2 is its average photon capture cross section for the $T_1 \rightarrow \{\chi\}$ event with I^0 the incident light intensity during the photochemistry. The product $\sigma_2 I^0$ is the radiative rate constant, $k_{T\chi}$ (sec^{-1}), for this excitation and is symbolized by $J_2{}^0$. The steady-state triplet concentration is the rate of its formation ($R_{SS_1}{}^0$ times the intersystem crossing efficiency, ϕ_{ST}), multiplied by its front-surface lifetime (with the light on). Thus

$$T_1{}^0 = R_{SS_1}{}^0\phi_{ST}\tau_T{}^0 \tag{11}$$

where $R_{SS_1}{}^0$ is known from actinometry and the durene concentration, and its extinction coefficient. It is given by the symbol $J_1{}^0S_0{}^0$ when properly averaged over exciting wavelengths (see the Appendix). The total moles/liter of front-surface triplet excited in t seconds is the time integral of $R_{T\chi}{}^0$. For the region of linear buildup of photoproducts,[11] $R_{T\chi}{}^0$ is a constant so that finally

$$\mathbf{R}_{T\chi}{}^0 = J_2{}^0(\tau_T{}^0\phi_{ST}J_1{}^0S_0{}^0)t \tag{12}$$

1. Final Form of Quantum Yields in the Biphotonic Photochemistries. Equations 3 and 4 with eq 9 and 12 give

$$\phi_{\chi R} = \Delta\Phi_R{}'L_R{}^{-1}/[\phi_{ST}J_1{}^0J_2{}^0\tau_T{}^0] \tag{3a}$$

and

$$\phi_{\chi I} = \Delta\Phi_I{}'L_I{}^{-1}/[\phi_{ST}J_1{}^0J_2{}^0\tau_T{}^0] \tag{4a}$$

whose ratio, incidentally, is

$$\phi_{\chi R}/\phi_{\chi I} = \frac{\Delta\Phi_R L_I}{\Delta\Phi_I L_R} \tag{13}$$

since common to both photochemistries is the $T_1 \rightarrow \{\chi\}$.

In eq 3a and 4a the quotient $\Delta\Phi_Y/t$ has been written as $\Delta\Phi_Y{}'$ (Y = R,I) which is the initial rate of growth of the fluorescence loss parameter. The method for finding the front-surface triplet lifetime in the presence of radiation, $\tau_T{}^0$, will be outlined below.

2. Quantum Yield in Monophotonic Radical Production. The method of "fluorescence loss" is applicable only when a reasonable fraction of parent molecule is converted to photoproducts. When the one-photon route to β-bond scission is investigated, weak photosensitization light is needed to force a relative reduction of the competing biphotonic channel which is simultaneously available. The direct application of the fluorescence loss technique is now difficult. The monitoring of photoproduct fluorescence is, of course, a far more sensitive method for following the kinetics but it does not directly contain a measure of the absolute concentration needed for yield measurements. What is possible, though, is to calibrate the photoproduct fluorescence through the "fluorescence loss" technique at high intensities and then use the sensitive photoproduct fluorescence method, now quantitive, for measurements of weak photoconversions. This is the approach applied for studying the monophotonic channel and it is an approach that could have been used advantageously for more refined studies on the biphotonic channels.

Formally we can treat eq 5 in a manner analogous to eq 3 and 4 to obtain for the monophotonic quantum yield

$$\phi_{S'R} = \Delta\Phi_R(t_1)L_R{}^{-1}/J_0{}^0t_1 \tag{5a}$$

where $\Delta\Phi_R(t_1)L_R{}^{-1}$ would be the fluorescence-loss parameter (times the depth function) seen after t_1 seconds of one-photon photosensitization, and $J_0{}^0$ is simply the number of times per second durene is being excited into an

TABLE I: Luminescence Parameters

Methylated benzene	ξ^a	$\phi\chi^*_T/\phi\chi^*_S{}^b$	$\phi_{ST}{}^c$	$\phi_F{}^e$	$\phi_{ST} + \phi_F{}^f$
p-Xylene	5.5	3.0	0.67[d]	0.42	1.09
Mesitylene	4.9 ± 0.3	3.0	0.78 ± 0.06[g]	0.16	0.94 ± 0.06
Durene	6.4	3.0	0.56	0.52	1.08

[a] ξ were measured at 77°K in 3-MP glasses.[2a] [b] Assumed. [c] Calculated using eq 15. [d] An experimental value of 0.53 for *p*-xylene in cyclohexane has been reported. See ref 12. [e] ϕ_F were measurec at 12° in O_2-free hexane solutions.[13] [f] This sum should not exceed unity. The slight discrepancy may be due to slight temperature dependence of ϕ_{ST} or ϕ_F. In fact, at 18° it has been found that with *p*-xylene in the gas phase, $\phi_{ST} + \phi_F = 1.0$ in the spectral region of interest.[14] Alternatively, the assumed values for $\phi\chi^*_T/\phi\chi^*_S$ may be in slight error. [g] The first more direct determination of ϕ_{ST} for mesitylene has just appeared (F. A. Carroll and F. H. Quina, *J. Amer. Chem. Soc.*, **94**, 6246 (1972)). The value found is 0.60 ± 0.03 at room temperature in a nonpolar solvent. Either there is a temperature dependence in this parameter or the branching ratio for mesitylene in 3-MP at 77°K is more nearly 2.3 than 3.

upper vibrational level of S_1, $S_{1\nu}$ (or S′), at the front surface. As stated, $\Delta\Phi_R(t_1)$ is too weak to measure. However, we can monitor the strength of the fluorescence, $F_R(t_2)$, of the duryl radical, produced after t_2 seconds of biphotonic photosensitization, where $\Delta\Phi_R(t_2)$ is measurable and also monitor the fluorescence, $F_R(t_1)$, of duryl radical produced after t_1 seconds of low-intensity (monophotonic) conditions. (These two fluorescences are normalized to the incident intensity of the probing beam at 329 nm, $I^{0\dagger}(t_2)$ and $I^{0\dagger}(t_1)$, respectively.) Using the fluorescence ratio, we can scale the observed $\Delta\Phi_R(t_2)L_R{}^{-1}$ to the desired $\Delta\Phi_R(t_1)L_R{}^{-1}$. A ratio of one- and two-photon depth integrals $\langle l_1\rangle$ and $\langle l_2\rangle$ is also needed to correct for the transformation from a two-photon depth distribution to the one-photon depth distribution. The details are offered elsewhere.[11] The quantum yield now becomes (from eq 5a)

$$\phi_{S'R} = \frac{\Delta\Phi_R(t_2)L_R{}^{-1}}{J_0{}^0 t_1}\frac{\langle l_2\rangle}{\langle l_1\rangle}\{[F_R(t_1)/I^{0\dagger}(t_1)]/[F_R(t_2)/I^{0\dagger}(t_2)]\} \tag{5b}$$

where the term in brackets is the scaling by radical fluorescence and all factors appearing are measured or calculated, in particular L_R now refers to the same two-photon depth correction discussed above.

3. Stimulated Recombination Luminescence Quantum Yield. When near-infrared light is used to stimulate the trapped electron to recombine with the durene cation, ground-state durene is formed. What fraction of these recombinations proceed *via* the set of ill-defined high-energy recombination levels of durene, $\{\chi^*\}$, which in turn lead to fluorescing and phosphorescing durene? The yield for this process is $\phi_{I\chi^*}$ and has been expressed through eq 6. The fraction of recombination events, $(1 - \phi_{I\chi})$, is that fraction which by-pass the ordinary available luminescing channels.

A common link between the number of front-surface luminescing recombination events $\mathbf{R}_{I\chi^*}{}^0$ and the total number of front-surface recombination (or ionizations) $\mathbf{R}_{\chi I}{}^0$ is the front-surface phosphorescence of the triplet state. On the one hand, luminescing recombination events lead to triplet state both *via* $\{\chi^*\} \rightarrow T_1$ channels and $\{\chi^*\} \rightarrow S_1 \rightarrow T_1$ channels; on the other hand, all ionizations proceed outwardly *via* the phosphorescing triplet state. When the analysis of this link is completed one obtains[11]

$$\phi_{I\chi^*} = \frac{1}{\phi_{\chi I}\tau_T J_2{}^0}\frac{\langle \mathbf{P}^*\rangle}{\langle \mathbf{P}\rangle}\frac{\langle l_0\rangle}{\langle l_2\rangle}\frac{1}{(\phi_{\chi^*S}\phi_{ST} + \phi_{\chi^*T})} \tag{6a}$$

where $\langle \mathbf{P}^*\rangle$ is the total area under the recombination phosphorescence pulse while $\langle \mathbf{P}\rangle$ is the total area under the (constant) phosphorescence signal observed under identical conditions during the photosensitization period. It is related to the number of ionization events, through the factors $\tau_T J_2{}^0$, an effective number of $T_1 \rightarrow \{\chi\}$ excitations, and the ionization quantum yield, $\phi_{\chi I}$. The reciprocal factor in quantum yields recognizes that in the recombination channel there are two routes, already mentioned, for reaching T_1. We shall define the $\{\chi^*\}$ states in a manner such that $\phi_{\chi^*T} + \phi_{\chi^*S} = 1$, that is, all transitions out of $\{\chi^*\}$ lead ultimately either to S_1 or T_1. The usual integrals over depth distribution functions are evident where l_0 refers to the depth distribution of T_1 which, of course, is monophotonically produced but under the broad band illumination conditions typical of the photosensitization step.

In previous recombination luminescence studies on the methylated benzenes[2a] an enhancement factor, ξ, has been determined. This factor expresses a comparison of the phosphorescence to fluorescence strength found in recombination luminescence to that seen in ordinary luminescence. Thus

$$\xi = \{\langle \mathbf{P}^*\rangle/\langle \mathbf{F}^*\rangle\}/\{\langle \mathbf{P}\rangle/\langle \mathbf{F}\rangle\} \tag{14}$$

The ratio of the quotients in eq 14 are readily written in terms of quantum yield expressions (the radiative yields and detector sensitivity factors all cancel) to give

$$\xi = 1 + [\phi_{\chi^*T}/(\phi_{\chi^*S}\phi_{ST})] \tag{15}$$

In Table I the observed ξ for three different methylated benzene systems are entered. In each case ϕ_{ST} is calculated under the assumption of the statistically expected 3/1 value for $(\phi_{\chi^*T}/\phi_{\chi^*})$. Observed quantum yields for fluorescence, ϕ_F (under other conditions), are then combined with the ϕ_{ST} to provide a check on this procedure for determining ϕ_{ST}. The fairly good conservation of efficiencies, especially for durene, suggests that the assumption of a 3/1 branching ratio and no internal conversion from S_1 is warranted. Furthermore in the case of *p*-xylene an experimental value for ϕ_{ST} of 0.63 has been reported which compares favorably with the predicted value of 0.67. With these assumptions eq 6a may now be written as

$$\phi_{I\chi^*} = 4(\phi_{ST}\xi\phi_{\chi I})^{-1}\frac{\langle \mathbf{P}^*\rangle}{\langle \mathbf{P}\rangle}\frac{\langle l_0\rangle}{\langle l_2\rangle\tau_T J_2{}^0} \tag{6b}$$

4. The Parameters $J_2{}^0$ and $\tau_T{}^0$ in the Second-Photon Step. Quantum yield eq 3a, 4a, and 6a,b each require the "frequency of $T_1 \rightarrow \{\chi\}$ excitation" parameter $J_2{}^0$ and the first two also require the front-surface lifetime of the triplet state in the presence of radiation. Now (eq 10) $J_2{}^0$ is the photon capture cross section, σ_2, times the front-surface light flux I^0 in the wavelength region of photosensitization. It is assumed (see Appendix) that σ_2 is a constant over this ~12-nm bandwidth of excitation. With I^0 known from actinometry it remains to determine σ_2 (equivalent-

ly, the T_1 extinction coefficient). The only available experimental approach to this is the observed triplet lifetime shortening in the presence of light. However, this records only those $T_1 \rightarrow \{\chi\}$ excitations which lead to a destruction of T_1 on the time scale of seconds or longer and cannot include those ordinary transition which quickly return to T_1. Let, therefore, the fraction of $T_1 \rightarrow \{\chi\}$ excitations which destroy T_1 be ϕ_2 (and $(1 - \phi_2)$ is the fraction of excitations which quickly recover T_1). The lifetime shortening kinetic parameter is then $\phi_2 J_2(x)$ and when averaged over sample depth[11] one finds

$$(1/\tau_T - 1/\tau_T^D) = \phi_2 J_2^0 \frac{\langle l_2 \rangle}{\langle l_0 \rangle} \quad (16)$$

The left-hand side is the lifetime (reciprocal) shortening of the bulk sample (τ_T^D is the dark lifetime) where τ_T is best measured as a phosphorescence risetime in the presence of photosensitizing radiation. Since the depth intergrals $\langle l_2 \rangle$ and $\langle l_0 \rangle$ are known (see Appendix), $\phi_2 J_2^0$ is determined. Thus we have for the cross section, scaled by ϕ_2

$$\phi_2 \sigma_2 = (\phi_2 J_2^0)/I^0 \quad (17)$$

Now for an infinitely thin sample $\langle l_2 \rangle = \langle l_0 \rangle$, the observed lifetime, τ_T, becomes the front-surface value τ_T^0, and $(1/\tau_T^0 - 1/\tau_T^D)$ is $\phi_2 J_2^0$. Thus τ_T^0 is determined.

Since J_2^0 itself (or σ_2, eq 17) has not been uniquely found, the quantum yields will carry with them the unknown ϕ_2. Fortunately, other considerations make it possible to bracket the value of σ_2 and ϕ_2 turns out to be close to unity (all $T_1 \rightarrow \{\chi\}$ excitations destroy T_1 in the photosensitization region).

In bracketing σ_2 (or ϵ_T) a fluorescence loss study is made on the time scale of the triplet lifetime under the conditions used for the biphotonic photosensitizations. In complete analogy to the fluorescence loss treatment in the photochemistry, eq 7 and 8, we also can expect a fluorescence loss due to the conversion of ground-state durene to its triplet level. Thus in terms of the front-surface fractional conversion to triplet, $\mathbf{R}_{ST}^0/S_0^0$, we have

$$\Delta\Phi_T = \frac{\mathbf{R}_{ST}^0}{S_0^0} L_T \quad (18a)$$

where

$$L_T = \frac{\langle l_0 g_0 \rangle}{\langle g_0 \rangle} + (\epsilon_T - \epsilon_0) S_0^0 \frac{\langle g_0 \langle l_0 \rangle_x \rangle}{\langle g_0 \rangle} \quad (18b)$$

As before, the second term in L_T represents the effect on fluorescence loss, $\Delta\Phi_T$, due to competitive light absorption by the "photoproduct" which now is T_1. (On the time scale of seconds the real photoproducts have not yet appeared.) The absence of an observable $\Delta\Phi_T$ will place an upper limit on L_T and therefore upon ϵ_T (or σ_2).

5. The Extinction Coefficient of the Radical, $\epsilon_R(\lambda)$. We have seen how a dimensionless depth function L_Y (Y = R,I) (eq 8) is vital in determining quantum yields, eq 3a, 4a. To evaluate it ϵ_Y (Y = R,I) must be determined. It has not been possible to make a direct determination of ϵ_I, the extinction coefficient of the durene cation. However, it will be seen how, accidentally, its value at 270 nm will be bracketted. On the other hand, a direct measure of ϵ_R the duryl radical extinction coefficient is possible. Its determination is, in any case, of general interest since the absorptivities of the benzyl radical are not well known. Suppose the (Naperian) absorbancy of the radical is measured at some wavelength, λ (such as 329 nm), where there is no interference from any other species. With the radical concentration known, an extinction coefficient is obtained, and the entire radical spectrum (from independent absorption and fluorescence excitation measurements) will have been placed on an extinction coefficient basis. Thus we have

$$A_e(\lambda) = \epsilon_R(\lambda)\langle \mathbf{R}_{\chi R} \rangle = \epsilon_R(\lambda)\mathbf{R}_{\chi R}^0 \langle l_2 \rangle \quad (19)$$

or, with eq 7 for Y = R

$$\epsilon_R(\lambda) = A_e(\lambda) L_R / S_0^0 \Delta\Phi_R \langle l_2 \rangle \quad (20)$$

where L_R depends on ϵ_R (270 nm) whose relation to ϵ_R (329 nm) is known from the radical fluorescence excitation spectrum itself. It now remains to present the data and to apply them to the equations developed in this section.

IV. Results and Discussion

In the left-hand portion of Table II experimental data are assembled for seven experiments carried out under biphotonic conditions, the last two of which are performed using perdeuterated durene. The last four columns on the right represent the conversion of these data to properties of the system using the equations just developed. Table III similarly deals with the experiments performed under monophotonic conditions. The crucial fluorescence loss parameters, $\Delta\Phi_R$ and $\Delta\Phi_I$, were normally measured over time periods of about 30 min. Typical values found for $\Delta\Phi_R$ were $\sim$0.2. These are converted to an initial slope value (in sec^{-1}), $\Delta\Phi_R'$, as found in Table II for each of the seven trials. $\Delta\Phi_I$, on the other hand, has reached saturation after only a few minutes of photosensitization (see Figure 6) and values considerably smaller than 0.2 were measured. These were converted to the initial slope values $\Delta\Phi_I$ reported in Table II with the aid of the P^* *vs.* t behavior displayed in Figure 6 and the fact that the saturation level varies with a light exponent of 1.5. This procedure amounts to a fluorescence loss calibration of P^* at saturation, where $\Delta\Phi_I$ is measurable, and applying this calibration to the initial slope of the P^* *vs.* t plot in a manner more explicitly done for the monophotonic experiments (Table III).

It is clear that the reproducibility, in general, is rather disappointing. It is conceivable that photochemical efficiencies actually vary from sample to sample. Nonetheless, we have no independent suggestion of this in general and, in fact, when the standard *N,N,N′,N′*-tetramethyl-*p*-phenylenediamine (TMPD) is used as the solute in 3-MP the extent of ionization has always been reproducible, to within a few per cent from freezing to freezing. Matters might be different for the monophotonic β-bond scission, however, we are not ready to suggest this in the biphotonic case given that these experiments represent only the first effort at determining quantum yields for such photochemistry. Instead it will be the qualitative nature of the results which will be emphasized and which can be regarded as probably the main significance of this work. In order to calculate quantum yields by this fluorescence loss technique the dimensionless factors L_R and L_I must be known. This requires knowledge of the extinction coefficients of the duryl radical and the durene cation respectively at 270 nm. This problem will be dealt with shortly. First it is worth exploring evidence for isotope effects in each of the photochemistries since this question can be formulated in a way that does not depend on L_R and L_I. Next L_R and L_I will be treated and the calculation of the quantum yields in the biphotonic photochem-

TABLE II: Data and Results for the Biphotonic Experiments

	Data							Results			
Trial	J_1^0, 10^{-3} sec^{-1}	J_2^0, $\phi_2^{-1} \times$ 10^{-2} sec^{-1}	$\Delta\phi_R'$, $\times$ 10^{-4} sec^{-1}	$\Delta\phi_I'$, $\times$ 10^{-4} sec^{-1}	τ_T, sec	τ_T^0, sec	$\langle P^* \rangle / \langle P \rangle$, 10^{-2}	σ_2^b, $\phi_2^{-1} \times$ 10^{-17} cm^2	$\phi_{\chi R}$, ϕ_2	$\phi_{\chi I}$, ϕ_2	$\phi_{I\chi^*}$
1	2.3	4.3	1.1	0.8	5.08	4.89	6.2	6.0	0.3	0.6	0.6
2	2.1	3.0	1.0	0.5	5.37	5.22	7.5	4.6	0.4	0.6	1.1
3	2.9	3.5	1.1	0.7	5.26	5.09	5.9	3.9	0.3	0.5	0.9
4	2.0	2.9	1.3	0.5	5.40	5.25	13.8	4.6	0.5	0.6	1.9
5	2.9	4.9	1.3	1.8	4.96	4.75	7.4	4.8	0.2	1.0	0.4
6[a]	2.2	3.2	0.5	0.8	5.33	5.17	7.4	4.4	0.2	0.8	0.7
7[a]	3.0	4.7	0.6	1.6	5.00	4.80	10.7	4.6	0.1	0.9	0.7

[a] Perdeuterated durene is used. [b] Naperian cross sections at 270 nm from T_1. Taken from eq 17 with average $I^0 = 7.1 \times 10^{14}$ photons/cm^2 sec.

TABLE III: One-Photon Results

Trial	$\lambda_{ex}(\Delta\lambda)$,[a] nm	t_1, sec $\times 10^3$	J_0^0, $sec^{-1} \times$ 10^{-4}	$\Delta\phi_R(t_2)$[b]	F ratio,[c] 10^{-4}	$\phi_{S'R}$, 10^{-4}
1	266.5(3.3)	1.8	1.2	0.15	1.55	0.7
2	266.5(1.5)	1.2	1.9	0.21	0.49	0.3
3	266.5(3.3)	0.6	2.1	0.20	4.69	5
4	266.5(0.8)	1.2	1.9	0.24	0.39	0.3
5	266.5(0.8)	0.6	1.6	0.21	0.60	0.8
6	252.0(1.5)	1.2	1.6	0.33	1.34	0.9
7	252.0(1.5)	1.2	1.4	0.22	0.55	0.3
8[d]	266.5(0.8)	1.2	1.7	0.36	0.50	0.5
9[d]	266.5(0.8)	0.9	9.9	0.04	9.47	0.3

[a] Bandwidth of monophotonic excitation. [b] The two-photon calibration fluorescence loss. [c] The "fluorescence ratio" for the one-photon produced radical to that produced in the high-intensity calibration experiment. See eq 5b. [d] Perdeuterated durene is used.

istries discussed. Lastly, the calculation of the low-intensity, monophotonic yields for β-bond scission will be presented.

A. Isotope Effects. Let the isotope effect in a given elementary step, $X \rightarrow Y$, be defined as Ψ_{XY} (the quotient of the quantum yield for the fully protonated durene to that of perdeuterated durene). More explicitly, the four possible isotope effects read $\Psi_{\chi R} = (\phi_{\chi R})_H/(\phi_{\chi R})_D$, $\Psi_{\chi I} = (\phi_{\chi I})_H/(\phi_{\chi R})_D$, $\Psi_{I\chi^*} = (\phi_{I\chi^*})_H/(\phi_{I\chi^*})_D$, and $\Psi_{S'R} = (\phi_{S'R})_H/(\phi_{S'R})_D$. It will be assumed that the remaining elementary steps have no isotope effects. These include all light absorption and light emission steps. Absorption spectra exhibit at most only slight wavelength shifts (shifts we shall regard as not significant in this work) and, as allowed transitions, should show no significant change in their extinction coefficients. This immediately says that L_R and L_I cannot carry any isotope sensitivity and will therefore cancel in the quantum yield ratios. Isotope effects are seen in triplet state lifetimes when radiationless decay channels are dominant. This appears not to be true for durene (the triplet decay is apparently predominantly radiative).

Finally, the $S_1 \rightarrow T_1$ crossing efficiency, ϕ_{ST}, will be taken as isotope independent, as one might expect when intersystem crossing is not controlled by Frank-Condon factors of the hydrogen normal modes. Even this assumption is not necessary if one focusses on the $\Psi_{\chi R}/\Psi_{\chi I}$ ratio which represents the relative isotope effect of the two photochemistries. From eq 13 we have for this ratio very simply $\Psi_{\chi R}/\Psi_{\chi I} = (\Delta\Phi_R'/\Delta\Phi_I')_H/(\Delta\Phi_R'/\Delta\Phi_I')_D$ which can be quickly taken from Table II. The average value of $(\Delta\Phi_R'/\Delta\Phi_I')_H$ is 1.7 ± 0.5. For the average $(\Delta\Phi_R'/\Delta\Phi_I')_D$ we have 0.5 ± 0.1. Thus, the *relative* isotope effect in the two photochemistries is ~3.4 ± 1. In fact, this represents primarily an isotope effect in β-bond scission alone. Individual calculations of the $\Psi_{\chi R}$ and $\Psi_{\chi I}$ (trials 1–5 against 6 and 7) give the ten values: $\Psi_{\chi R}$ = 1.7, 2.4, 2.4, 3.3, 1.7, 2.4, 3.3, 4.7, 1.5, 2.2 and $\Psi_{\chi I}$ = 0.8, 0.7, 0.7, 0.7, 0.6, 0.6, 0.8, 0.7, 1.3, 1.2). These ratios of quantum yields carry a great deal of error given the imprecision of the yields themselves. Still the pattern illustrates the point. A most direct demonstration of the isotope effect in β-bond scission is shown in Figure 8 where F_R excited at 329 nm after different photosensitization times is plotted for the two durenes in experiments carried out under as identical conditions as possible. In these two experiments the intensity of the recombination durene fluorescence was the same, indicating identical yields for the ionization channel. The ratio of the slopes from this figure gives $\Psi_{\chi R}$ = 3.3 in excellent agreement with values based on the fluorescence loss techniques. Not only does this confirm an isotope effect in the β-bond cleavage,[15] and very little or none in the ionization, but the quantitative agreement of the results derived from these two different techniques indicates that there is no significant isotope effect in the fluorescence lifetime of the duryl radical (not an unexpected result).[16]

In the monophotonic β-bond scission the quantum yields are very low and appear to vary erratically from freezing to freezing (see Table III). If there is an isotope effect here, it is obscured by the nearly order-of-magnitude variation in $\phi_{S'R}$ for the fully protonated durene itself.

B. Quantum Yields in the Biphotonic Chemistries. The evaluation of the photochemical quantum yields in the biphotonic chemistries through eq 3a, 13, and 6b requires, among other things, the dimensionless factors L_R and L_I. As already indicated, in the limit of low conversions these are true constants and, as determined in the Appendix, are given by

$$L_{R,I} = 0.599 + (\epsilon_{R,I} - \epsilon_0)0.218 \times 10^{-3} \qquad (21)$$

in which ϵ_R, ϵ_I, and ϵ_0 are molar Naperian extinction coefficients at 270 nm (the monitoring wavelength). From the known absorption spectrum of durene $\epsilon_0 = 1.65 \times 10^3$ M^{-1} cm^{-1}, but ϵ_R and ϵ_I are unknown. Since ϵ's are normally of the order of 10^3 at least, eq 21 makes clear how competitive light absorption (the second term) can be a variable and highly significant factor in determining quantum yields. Now eq 20 permits a determination of $\epsilon_R(\lambda)$ which, however, depends on L_R. A Naperian optical density of 0.14 for D_0 was measured at 329 nm in an experiment where $\Delta\Phi_R$ = 0.39. Equation 20 then gives (see

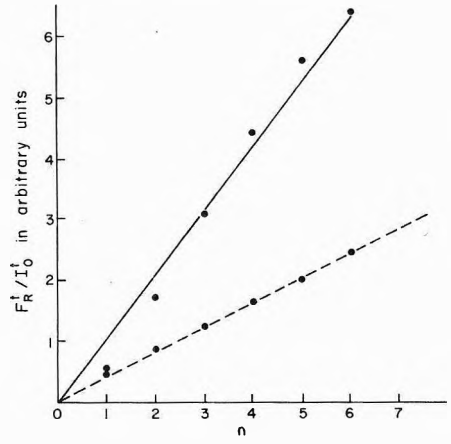

Figure 8. The growth of duryl radical fluorescence for protonated (——) and fully deuterated (----) durene photosensitized under identical conditions. *n* represents the number of uv photosensitization exposures.

Appendix for other parameters) ϵ_R (329 nm) = 0.84 × $10^3 L_R$. It is necessary to convert this to the duryl radical extinction coefficient at 270 nm. An ultraviolet absorption spectrum of the duryl radical has been obtained by Johnson.[2a] In that spectrum a correction was made for parent optical density in the region of overlap but the correction was explicitly made as a subtraction of the *undepleted* parent spectrum. It is easy to show that the ratio of the "duryl radical" optical density (thus corrected) at 270 nm to that at 329 nm, which is found to be 3.3/1, actually is equivalent to $(\epsilon_R(270\text{ nm}) - \epsilon_0)/\epsilon_R(329\text{ nm})$. This gives $\epsilon_R(270\text{ nm}) = \epsilon_0 + 2.77 \times 10^3 L_R$ and, with eq 21, L_R = 1.51, and $\epsilon_R = 5.8 \times 10^3$. Equation 3a can now be used, with the data reported in Table II, to calculate $\phi_{\chi R}$ for each trial. It must be noted that the lifetime shortening gives directly $\phi_2 J_2^0$, not J_2^0, thus J_2^0 and σ_2, as found in Table II, are given in units of ϕ_2^{-1}. Similarly, the quantum yields $\phi_{\chi R}$ (and $\phi_{\chi I}$) are given in units of ϕ_2.

Unfortunately, no direct spectroscopic signs of the radical cation, D_0^+, are seen in this work so that it is not possible to obtain the necessary ϵ_I at 270 nm. Judging from reported absorption spectra of the radical anions and theoretical predictions for the cations of benzene, toluene, and *p*-xylene and allowing for methyl shifts for durene it appears that 270 nm should lie distinctly to the blue of the two lowest transitions but well to the red of the next, strong, transition. The radical cation ought not to absorb strongly at the monitoring wavelength. One approach to this dilemma is to recognize that $\phi_{\chi I}$ can never *exceed* (1 − $\phi_{\chi R}$) when given in units of ϕ_2, and in fact must be equal should the two photochemistries be the only channels for the long-term destruction of T_1 ($\phi_{\chi I} + \phi_{\chi R} = \phi_2$ or $(\phi_{\chi I} + \phi_{\chi R})\phi_2^{-1} = 1$). One can then compute a *lower* limit to L_I for each trial using the firm $\phi_{\chi R}$ data from Table II with eq 13 and $\phi_{\chi I} = 1 - \phi_{\chi R}$ (in units of ϕ_2). Each L_I then determines an ϵ_I (eq 21) which represents a lower limit to the cation extinction coefficient at 270 nm. An average value is taken, since L_I, in zeroth order, must be independent of each experiment, and one obtains L_I = 0.47 ± 0.08 or $\epsilon_I = 1.1 \times 10^3$ (±30%). This value for L_I is then taken with eq 13 to compute the $\phi_{\chi I}$ entered in Table II (in units of ϕ_2). The lower limit to the molar decadic extinction coefficient of the durene cation at 270 nm is then about 500 M^{-1} cm.$^{-1}$ Shortly it will be found that the $\phi_{\chi I}$ thus calculated must represent *lower* limits as well, and furthermore, $\phi_2 \cong 1$. Thus these figures (within their considerable experimental limits) must represent correct absolute values. It is because the competitive light absorption appears to the same order of photoconversion as does the depletion effect that it has been possible to bracket an extinction coefficient of a species otherwise undetected by a direct absorption measurement. Conservation of quantum yields together with more definite knowledge of the β-bond scission ($\phi_{\chi R}$ and ϵ_R) has made this possible.

It remains to discuss the calculation of the quantum yields for the radiatively stimulated charge recombination step, $\phi_{I\chi^*}$. The calculation is straightforward through eq 6b and requires only the additional $\langle \mathbf{P}^* \rangle / \langle \mathbf{P} \rangle$ data appearing in Table II. Since $\phi_{\chi I}$ is available in units of ϕ_2, while J_2^0 is in units of ϕ_2, $\phi_{I\chi^*}$ is independent of ϕ_2 and the results appearing in the last column of Table II represent absolute values. Reproducibility from experiment to experiment is certainly lacking, if it is to be expected. Furthermore, one of the yields is considerably above unity so that experimental error is certainly rather large. The most definitive statement possible is to say that the yields appear to be on the order of unity. This is a crucial point, for it imposes a new condition on the $\phi_{\chi I}$ (in units of ϕ_2), namely, that they represent *lower* limits. Until now they appeared as upper limits, but now were their true values to be significantly smaller, than the $\phi_{I\chi^*}$ (depending on $\phi_{\chi I}^{-1}$) would seriously exceed unity. Thus the $\phi_{\chi I}$ entries must be fairly representative of the actual $\phi_{\chi I}$ (in units of ϕ_2) and this leaves the previously determined lower limit $\epsilon_I \cong 500$ (molar decadic) as, in fact, an upper limit as well. The experimental errors involved throughout must considerably soften these quantitative conclusions, of course.

Finally it is to be noted how ϕ_2 must be on the order of unity. In Table II the capture cross-section for the second photon, σ_2, given in units of ϕ_2^{-1}, is therefore a lower limit. The average value is 4.6 ± 0.2 × 10^{-17} cm^2 units of ϕ_2^{-1}, or $\sigma_2 \geq 4.6 \times 10^{-17}$ cm^2. Now it is an experimental fact that no detectable fluorescence loss is seen as the triplet state builds up over the first several seconds of photosensitization. Thus, $\Delta\Phi_T < 0.05$ (an upper limit to the experimental uncertainty in a fluorescence loss measurement). The front surface fractional conversion to triplet state, $\mathbf{R}_{ST}^0/S_0^0$, is $J_1^0 \phi_{ST} \tau_T^0$ since $\mathbf{R}_{ST}^0 = T_1^0$, the front surface steady-state triplet concentration. According to Table II a typical value for $J_1^0 \phi_{ST} \tau_T$ is ≈0.006. Equation 18a with $\Delta\Phi_T < 0.05$ and this front surface fractional conversion gives $L_T \gtrsim 8$. With eq 18b and the integrals from the Appendix we have $L_T = 0.697 + (\epsilon_T - \epsilon_0)0.245 \times 10^{-3}$ and therefore $\epsilon_T \gtrsim 3.1 \times 10^4$. Thus an *upper* limit for σ_2 becomes 5.1 × 10^{-17} cm^2. *With σ_2 now rather tightly bracketed, the units of ϕ_2^{-1} must be on the order of unity or $\phi_2 \approx 1$.* This means that the major radiative channels for destroying T_1 are just the very two photochemical processes being discussed: $\phi_{\chi T} + \phi_{\chi R} \cong 1$. Neither energy transfer to the solvent nor intersystem crossing from the {χ} states appears to be an important channel at these wavelengths. *Furthermore, all entries in Table II (scaled by ϕ_2 or ϕ_2^{-1}) now turn out, in fact, to be representative of their absolute values.* The molar decadic extinction coefficient of T_1 in the photosensitization wavelength region is about 13,000 M^{-1} cm^{-1}. This transition is presumably related to the intense, in-plane polarized, $^3B_{1u} \rightarrow {}^3E_{2g}$ transition expected for benzene in this same region according to theory.[17] However, since the $T_1 \rightarrow$ {χ} step seems to be isotropic (unpolarized),[2b] this re-

mark needs some qualification. Godfrey and Porter[18] have estimated the lower limit to the molar decadic extinction coefficient of T_1 in benzene in the uv region to be $\epsilon_T > 1.5 \times 10^3$. All ISCR events appear to reenter through $\{\chi^*\}$ states of durene which fully lead to T_1 and S_1 without any loss and with the expected statistical 3/1 ratio ($\phi_{I_{\chi^*}} \approx 1$). The two photochemistries proceed with similar efficiencies: $\phi_{\chi R} \simeq 0.4$ and $\phi_{\chi I} \simeq 0.6$. This general behavior of the biphotonic system is summarized in Figure 9.

Of special interest is the fact that the $\{\chi\}$ states display high photochemical yields, while the $\{\chi^*\}$ states reached during ISCR do not. Decay from the latter, as previously assumed, appears to leave durene intact in its S_1 and T_1 states. One expected difference between the $\{\chi\}$ and $\{\chi^*\}$ states is their nuclear geometries. The $\{\chi\}$ states should momentarily exhibit the configuration of the T_1 state from which they are radiatively generated. The $\{\chi^*\}$ states ought to initially carry the nuclear configuration of the cation of durene. Whether this is sufficient, or even significant, in explaining the utterly different photochemical behavior of the $\{\chi\}$ and $\{\chi^*\}$ is not clear, for there does not appear to be any serious Frank–Condon block in the passage from $\{\chi\} \rightarrow I$ in which durene must pass from a T_1 geometry to the geometry of its cation. An alternative factor might be the energy of the $\{\chi\}$ states *vs.* that of the $\{\chi^*\}$ states, the latter being reached from the ionized condition with the aid of a near-infrared photon. It is possible that the $\{\chi^*\}$ states lie above the $\{\chi\}$ states by as much as several tenths of an electron volt. On the other hand, there may be some decay of stored energy prior to the last step of the recombination event. Until careful wavelength dependence studies are made this question will remain unresolved. The fact that ISCR does not bypass the S_1 and T_1 states in making durene is interesting enough.

C. Monophotonic Quantum Yields. The data for nine photosensitization experiments carried out under "monochromatic" conditions appear in Table III. Two wavelengths have been selected (266 nm and 252 nm) using varying bandwidths as indicated. The times, t_1, employed for the monophotonic photosensitizations were varied as well. The important calibration fluorescence loss parameter $\Delta\Phi_R$ for each trial appears and the ratio of the 329 nm excited duryl radical fluorescence generated after the monophotonic experiment to that seen after the biphotonic calibration experiment is listed too. This radical fluorescence ratio, as has been said, helps to convert the observed $\Delta\Phi_R(t_2)$ to a hypothetical monophotonic fluorescence loss, $\Delta\Phi_R(t_1)$. This fluorescence loss is on the order of 10^{-5} and is much too weak to measure directly. It is noteworthy how the front surface frequency of excitation, J_0^0, is at least one order of magnitude lower than that in the studies carried out at 275 nm (see J_1^0 in Table II), a condition necessary to permit the one-photon route to dominate over the biphotonic path. Equation 5b provides the means for computing the $\phi_{S'R}$ and the results appear in the last column of Table III. The variation of $\phi_{S'R}$ from experiment to experiment is as much as one order of magnitude and this may quite possibly reflect a genuine variation of $\phi_{S'R}$ with each preparation. Nevertheless, the principal result is that the quantum yield is on the order of 10^{-4}. Thus, only about one out of every 10^4 $S_0 \rightarrow S_1$ excitations leads to β-bond scission of durene in this rigid solution. As already noted an isotope effect, if present at all, is obscured by the variation of $\phi_{S'R}$ from trial to trial.

Actually many years ago Hentz and Burton[19] examined the mercury photolysis products of liquid and gaseous toluene, mesitylene, and ethylbenzene. The major photochemical channel observed was β-bond scission and that was with a quantum yield on the order of 10^{-4}. It is almost certain that this 2537-Å photolysis is monophotonic. Not only is the energy sufficient but the triplet intermediate necessary for the biphotonic route is quenched in such systems. The agreement with present observations speaks strongly for a truly intramolecularly determined mechanism for the one-photon channel. Cage effects in the rigid sample, possibly varying from freezing to freezing, could permit some variations in the yield. The cage effect might similarly influence the biphotonic β-bond scission as well unless there, under the more energetic conditions, the H atom is more convincingly implanted in the surrounding solvent cage.

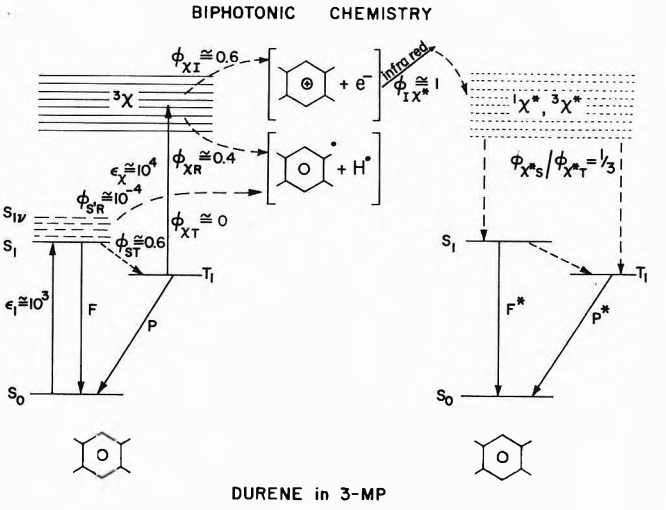

Figure 9. A summary of the results.

V. Conclusions

The basic results in this work are summarized in Figure 9. The quantum yields for two photochemistries *via* the lowest triplet state are similar and very high. In fact, it appears that all $T_1 \rightarrow \{\chi\}$ excitations lead to the two main chemical decay channels. The β-bond channel has shown a clear cut isotope effect. All of this, of course, refers only to the broad-band 275-nm excitation performed in this work, corresponding to very energetic $\{\chi\}$ triplets at ~8.0 eV above the ground state of durene (~3.5 eV for T_1 and ~4.5 eV for the $T_1 \rightarrow \{\chi\}$ excitation).

With regard to the $I \rightarrow \{\chi^*\}$ ISCR recombination event, it is remarkable, first of all, that the return of all electrons proceeds so efficiently into the excited triplet and singlet manifolds, and secondly that their return manages to avoid the highly efficient chemical channels out of the $\{\chi\}$ states.

A very important and obvious extension of these studies would be to perform a careful investigation of the wavelength dependence of the second photon for each of the two photochemistries as well as that of the charge recombination step.[20] With regard to technique for such studies, it seems that a great deal can be done using very thin (front-surface) samples and detecting only photoproduct luminescence signals (F^* or P^* for the cation and F_R for the radical). The complication of depth integrations,[21] though manageable, would be avoided. A quantitative fluorescence loss calibration need be done at only one wavelength and could be performed on thicker samples as

treated here. As a first approximation, the present fluorescence loss results at 275 nm could be used for durene. However, it would doubtlessly be wise to postpone further work until tunable lasers can be introduced, for the wavelength variations of intensity and the need for polychromatic conditions to obtain sufficient light from ordinary sources are a particular nuisance when studying biphotonic phenomena. In some favorable cases it is possible to use two beams, one for each photon, but this will not be a general possibility. The application of tunable lasers would also then offer a real chance to explore this fluorescence loss technique for determining extinction coefficient of photoproducts (such as crudely accomplished here for both the duryl radical and the duryl radical cation). An alternate method of quantifying such photochemistry is the use of esr to count the radical photoproducts. Just recently there has appeared work[22] on quantitative biphotonic chemistry of some aromatic compounds in rigid ethanol solutions at 77°K in which the essential quantifying feature was the use of esr. Also, a steady-state method was used to determine the rate of radiative depleting T_1 (our $\phi_2 J_2$) where we have used the transient method of lifetime shortening. Finally, in the case of carbazole these workers report an interesting wavelength dependence of the photochemical yield out of excited triplets (or $\{\chi\}$ states).

The original stimulus for this work was actually provided by the mechanistic question of how β-bond cleavage actually takes place. One guess was that this primary step involved ionization and then, by charge recombination, a dissociative electron attachment might occur at the β-bond position. However, according to this picture, ISCR should yield β-bond scission. In fact this was found to occur and this is discussed in another paper.[7] However, the yield is far too low to support this scheme for the very efficient channels found in this work. Still, the most intimate version of this mechanism would be passage from the $\{\chi\}$ states into a charge transfer state where the transferred electron takes on antibonding character at the β position and this cannot be excluded. The mystery of how the returning electron *via* ISCR bypasses such a state still remains.

There is a suggestion in the literature[23] that β-bond scission proceeds by energy transfer to a dissociative triplet state of the solvent. The radical solvent product then would abstract an H atom from the β position of the solute molecule. Our current results cannot exclude this possibility of course. In fact, after prolonged 275-nm photosensitization of durene in 3-MP, we have seen an esr signal from the solvent radical. However, the distinct isotope effect we have observed in this work suggests that the β-bond scission is the rate-determining step. It is not obvious that such would be the case were this step to be accomplished by H (D) atom abstraction by solvent radicals locked in the solute–solvent cage. Other observations suggest that a truly unimolecular route may be the major active channel. Thus, Johnson and Rice[24] report successful biphotonic β-bond scission of *p*-xylene in an argon matrix. And finally, an esr study[25] of β-bond scission of *N,N.N′,N′*-tetramethyl-*p*-phenylenediamine (TMPD) in perdeuterated 3-MP showed the biphotonic emergence of the fully protonated methyl radical.

Further insight into the mechanisms of these two dominant photochemistries at the very least must await careful wavelength dependent studies, supplemented by the use of isotopically substituted solute and solvents.

Appendix

The Wavelength Dependent Light Flux, the Extinction Coefficients, and the Depth Integrals. The measurement of light intensity involves detecting photons over a finite increment of wavelength with a detection function $s(\lambda)$. Thus, if $j(x,\lambda)$ is the photon flux per unit wavelength interval at λ and position x, the corresponding flux that would be measured, $I(x)$ is

$$I(x) = \int s(\lambda) j(x,\lambda)\, d\lambda \qquad \text{(A-1)}$$

If the integrand is a narrow enough function of λ centered at λ_0, then we can speak of a "monochromatic" intensity, $I(x,\lambda_0)$, which obeys Beer's law and for the monophotonic photochemistry this has been assumed. For the biphotonic work, polychromatic conditions are necessary where, in general, Beer's law cannot hold. It is convenient to work with the function $j(x,\lambda)$, which obeys Beer's law in the strictest of senses, and then integrate over wavelength after properly weighting it with a photon capture cross section $\sigma(\lambda)$ to determine the photons captured per second by a molecule under polychromatic conditions. Thus, Beer's law gives

$$j(x,\lambda) = j^0(\lambda) \exp\left(-\sum_r \epsilon_r \langle C_r \rangle_x\right) \qquad \text{(A-2)}$$

when different species, r, are present.

For the rate of photon capture, $J_i(x)$, in a polychromatic process having photon capture cross section $\sigma_i(\lambda)$, we have

$$J_i(x) = \int \sigma_i(\lambda) j(x,\lambda)\, d\lambda \qquad (i = 1,2) \qquad \text{(A-3)}$$

In this work there are two polychromatic steps, the first and second photon steps of the biphotonic photochemistries. It is necessary to determine $J_1(x)$ and $J_2(x)$, respectively.

In keeping with the previous limitations to low conversions, the depth dependence of $j(x,\lambda)$ will be simplified to its functional form in the absence of photochemistry

$$j(x,\lambda) = j^0(\lambda) \exp[-\epsilon(\lambda) S_0^0 x] \qquad \text{(A-4)}$$

It is found that the neglect of photoproduct and triplet state levels incorrectly estimates $j(x,\lambda)$ at most by about 6% in a typical photosensitization experiment. This assumption leaves $j(x,\lambda)$ time independent as well.

The wavelength dependence of the durene extinction coefficient $\epsilon(\lambda)$ (or $\sigma(\lambda)$) is of course well known. It is only necessary to determine the wavelength dependence of the front surface flux density $j^0(\lambda)$ before evaluating the $J_i(x)$ of eq A-3. For this purpose one simply uses an integrating screen monochromatically excited by the incident light using fixed, narrow slits. The viewing is now always in the blue fluorescence region of the integrating screen. The detection function $s(\lambda)$ in eq A-1 must therefore be the same for all wavelengths and is sufficiently narrow to regard j as a constant when integrating over this function at each λ setting. Thus, $I^0(\lambda) = s^* j^0(\lambda)$ where s^* represents the integral over $s(\lambda)$ at any λ. However, since s^* remains an undetermined constant, only the *relative* λ dependence of $I^0(\lambda)$ (or $j^0(\lambda)$) is thus determined. A convenient reference wavelength, λ_0, in this work has been 275 nm where the incident photon flux is $I^0(275) \equiv I_0^0$ and the incident photon flux density $j^0(275) \equiv j_0^0$. Thus, the integrating screen study gives simply a dimensionless wavelength distribution function of light, $q(\lambda)$, where

$$j^0(\lambda) = j_0^0 q(\lambda) \quad \text{or} \quad I^0(\lambda) = I_0^0 q(\lambda) \qquad \text{(A-5)}$$

TABLE IV: Summary of Extinction Coefficients in 3-MP at 77°K

Compound	Molar Naperian, ϵ, M^{-1} cm^{-1} × 10^3	Cross section, σ, cm^2 × 10^{-18}/mol	Molar Decadic, ϵ, M^{-1} cm^{-1} × 10^3
Durene[a]			
275 nm	2.66	4.41	1.15
270 nm	1.65	2.74	0.72
266 nm[b]	1.6	2.6	0.7
252 nm	0.48	0.80	0.21
Duryl radical[c]			
270 nm	5.8	9.7	2.5
Durene cation[c]			
270 nm	1.1	1.8	0.5
Durene triplet[c]			
270 nm	30	4.9	13

[a] Measured (see Figure 2). [b] A shoulder, therefore inaccurate. [c] Determined in this work (see text).

TABLE V: Commonly Used Depth Distributing Functions[a]

Meaning	Symbol and functional form
1. The depth distribution of biphotonically (broad band) produced photoproducts	$l_2(x) = \exp(-3.05x)$
2. The depth distribution of monophotonically produced photoproducts	
at 266.5 nm	$l_1(x) = \exp(-2.65x)$
at 252.0 nm	$l_1(x) = \exp(-0.80x)$
3. The depth distributior of the first photon in the biphotonic studies (same as the depth distribution of T_1)	$l_0(x) = \exp(-2.05x)$
4. The depth distributior of the monitoring light at 270 nm	$g_0(x) = \exp(-2.74x)$

[a] Based on methods just outlined and valid for the limit of the initial buildup of photoproducts.

Next it is necessary to determine the absolute flux at 275 nm. This is done with actinometry. Sufficiently sensitive actinometry required nonmonochromatic illumination (wide slits). The monochromator was set at 275 nm and the slits were opened, it happens, to the same setting used in the biphotonic photochemistry. A standard triangular slit function $s(\lambda)$ ($s(\lambda_0) = 1$) was introduced to give (with eq A-1) $\bar{I}_0^0$ the absolute photon flux measured at 275 nm with wide slits

$$\bar{I}_0^0 = \int_{\lambda_0-\Delta\lambda}^{\lambda_0+\Delta\lambda} s(\lambda) j^0(\lambda)\, d\lambda = j_0^0 \int_{\lambda_0-\Delta\lambda}^{\lambda_0+\Delta\lambda} s(\lambda) q(\lambda)\, d\lambda$$

where in the second equality the substitution $j^0(\lambda) = j_0^0 q(\lambda)$ has been introduced. The integral is carried out, $\bar{I}_0^0$ actinometrically measured, and j_0^0 is thereby absolutely determined. Through $q(\lambda)$, $j^0(\lambda)$ is now known at all λ. The durene photon capture cross section $\sigma_1(\lambda)$ is similarly referenced to its value (written as σ_1) at 275 nm and a λ distribution, $p(\lambda)$. Thus, $\sigma_1(\lambda) = \sigma_1 p(\lambda)$.

The photosensitization wavelength region 265–277.5 nm is partitioned into six parts 2-nm wide each. The spectrum of durene in this region is treated crudely analytically as triangularly shaped peaks. The $q(\lambda)$ function is similarly partitioned, and the integral for the first photon step of the biphotonic process becomes a sum of the separate integrals over the 2-nm regions, each of which is performed using the trapezoidal rule. Thus, eq A-3 for $i = 1$

$$J_1(x) = j_0^0 \sigma_1 \sum_{j=1}^{6} \int_{\lambda_j}^{\lambda_{j+1}} q(\lambda_j') p_1(\lambda_j') \exp\{-\epsilon(\lambda_j') S_0^0 x\}\, d\lambda_j'$$

The resulting complex function of x is plotted for values of x in the range $x = 0$ to 0.5 cm and it is found that a good empirical fit can be made to this plot with a single exponential function. Thus, it is found that

$$J_1(x) = 3.5 j_0^0 \sigma_1 \exp\{-2.05x\} \qquad \text{(A-6)}$$

The same approach is used for the second photon step of the two-photon process, only here an assumption of a *constant* photon capture cross section, σ_2, is made over the ~12-nm bandwidth of the photosensitization. This assumption is based on the expected monotonous λ dependence of the $T_1 \rightarrow \{X\}$ transition over such a narrow region. The threshold, where abrupt changes would occur, appears to be at considerably longer wavelengths. Thus, it is found that

$$J_2(x) = 6.2 j_0^0 \sigma_2 \exp\{-1.00x\} \qquad \text{(A-7)}$$

The front surface light flux density at 275 nm, j_0^0, is evaluated as just described. The calibrated sodium salicylate quantum counter is used in each trial.

The extinction coefficients or cross sections needed in this work are found in Table IV. The quantum yield weighted capture cross section for the second photon step, $\phi_2\sigma_2$, is approached by measuring the radiative triplet lifetime shorting $[(\tau_T^0)^{-1} - (\tau_T^D)^{-1}]$ on the front surface, which is $\phi_2 J_2^0 = \phi_2\sigma_2 I^0$, and dividing by the actinometrically measured I^0 (7.1×10^{14} photons/cm^2 sec).

The dimensionless depth distribution function for the photoproducts made biphotonically, in the limit of the initial buildup, is the product of the exponential factors in J_1 and J_2 (eq A-6 and A-7) or

$$l_2(x) = \exp\{-3.05x\} \qquad \text{(A-8)}$$

The depth distribution function for polychromatically produced T_1, l_0, is the exponential factor in J_1 (eq A-6) or

$$l_0 = \exp\{-2.05x\} \qquad \text{(A-9)}$$

The depth distribution function for the monochromatic monitoring beam at 270 nm and under the same initial conditions is (see g_0 in eq 8) $\exp\{-\epsilon_0 S_0^0 x\}$ where ϵ_0 refers to durene extinction at 270 nm. Or, with $S_0^0 = 1.66 \times 10^{-3}$ M at 77°K

$$g_0(x) = \exp\{-2.74x\} \qquad \text{(A-10)}$$

Finally, for the monochromatic photosensitizations the detailed wavelength integrations are unnecessary and $J_0^0(\lambda) = \sigma_1(\lambda) I^0(\lambda)$ where $I^0(\lambda)$ is obtained from actinometry. The subscript zero identifies the J as being that for the first (and only) photostep in the monochromatic, monophotonic experiments. The corresponding depth distribution functions are ($\exp(-\epsilon(\lambda) S_0^0 x)$)

$$l_1(266.5\text{ nm}) = \exp(-2.65x) \qquad \text{(A-10a)}$$

and

$$l_1(252.0\text{ nm}) = \exp(-0.80x) \qquad \text{(A-10b)}$$

These functions are summarized in Table V. Next the results of the various necessary depth integrations are presented in Table VI indicating where the given integral is needed.

The dimensionless factors L_R and L_I are especially important and for these we now obtain (eq 8) with $S_0^0 =$

TABLE VI: Depth Distribution Integrals

Integral	Value, cm	Where needed (eq)
$\langle g_0 \rangle$	0.272	L_R (8), L_I(8), L_T(18b)
$\langle I_2 g_0 \rangle$	0.163	L_R, L_I, L_T
$\langle g_0 \langle I_2 \rangle_x \rangle$	0.036	L_R, L_I
$\langle g_0 \langle I_0 \rangle_x \rangle$	0.040	L_T
$\langle I_0 g_0 \rangle$	0.190	L_T
$\langle I_1 \rangle$ at 266.2	0.277	$\phi_{S'R}$(5b)
$\langle I_1 \rangle$ at 252.0	0.412	
$\langle I_2 \rangle$	0.256	$\phi_{S'R}$, $\epsilon_R(\lambda)$ (20), $1/\tau_T^0$ (16), ϕ_{IX}*(6b)
$\langle I_0 \rangle$	0.313	$1/\tau_T^0$, ϕ_X*

$1.66 \times 10^{-3} M$ (at 77°K)

$$L_{R,I} = 0.599 + (\epsilon_{R,I} - \epsilon_0)(0.218 \times 10^{-3}) \quad \text{(A-11)}$$

which is eq 21 of the text. Were it necessary it would not be difficult to carry out L_R, and L_I, to higher order where new integrals of the type found in Table VI would appear.

Supplementary Material Available. A more comprehensive version of section III will appear following these pages in the microfilm edition of this volume of the journal. Photocopies of the supplementary material from this paper only or microfiche (105 × 148 mm, 20× reduction, negatives) containing all of the supplementary material for the papers in this issue may be obtained from the Journals Department, American Chemical Society, 1155 16th St., N.W., Washington, D.C. 20036. Remit check or money order for $5.00 for photocopy or $2.00 for microfiche, referring to code number JPC-73-2808.

References and Notes

(1) (a) Taken In part from the Ph.D. Thesis of F. P. S., Cornell University, 1970. (b) This work has been supported primarily by NIH Grant No. G.M. 10865. Additional support by the Materials Science Center at Cornell University is gratefully acknowledged.
(2) (a) P. M. Johnson, Ph.D. Thesis, Cornell University, Ithaca, N. Y., 1967; (b) P. M. Johnson and A. C. Albrecht *Chem. Ioniz. Excitation, Proc. Conf. Radiat. Chem. Photochem., 1966,* 91 (1967).
(3) H. Tsubomura, *Bull. Chem. Soc. Jap.*, **42,** 3604 (1969).
(4) G. E. Johnson and A. C. Albrecht, *J. Chem. Phys.*, **44,** 3162, 3179 (1966).
(5) A. C. Albrecht, P. M. Johnson, and W. M. McClain, *Proc. Int. Conf. Lumin., 1966,* B-2, 405 (1968).
(6) F. P. Schwarz and A. C. Albrecht, *Chem Phys. Lett.*, **9,** 163 (1971).
(7) F. P. Schwarz and A. C. Albrecht, *J. Phys. Chem.*, in press.
(8) M. Seya and F. Masuda, *Sci. Light (Tokyo),* **12,** 9 (1963).
(9) R. S. Mulliken and C. A. Rieke, *Rept. Progr. Phys.*, 8, 231 (1941).
(10) C. G. Hatchard and C. A. Parker, *Proc. Roy. Soc., Ser. A,* **235,** 518 (1956).
(11) See paragraph at end of paper regarding supplementary material.
(12) K. Sandros, *Acta Chem. Scand.*, **23,** 2815 (1969).
(13) E. J. Bowen and A. H. Williams, *Trans. Faraday Soc.*, **35,** 765 (1939).
(14) W. A. Noyes, Jr., and D. A. Harter, *J. Phys. Chem.*, **75,** 2741 (1971).
(15) Recently a strong isotope effect has been reported for a photodissociation out of a triplet state in another system: V. G. Plotnikov, Yu. I. Kozlov, V. A. Smirnov, M. V. Alfimov, and V. M. Gebel, *Opt. Spektrosk.*, **32,** 694 (1972).
(16) The lifetime of the fluorescence of the duryl radical in 3MP at 77°K for (H_{13}) and (D_{13}) is, respectively, 0.50 and 0.59 μsec as measured by A. Bromberg and D. Friedrich in this laboratory.
(17) R. Pariser, *J. Chem. Phys.*, **24,** 250 (1956).
(18) T. S. Godfrey and G. Porter, *Trans. Faraday Soc.*, **62,** 7 (1966).
(19) R. R. Hentz and M. Burton, *J. Amer. Chem. Soc.*, **73,** 532 (1951).
(20) An interesting report has just appeared on the detailed wavelength dependence of the second photon step in another system: V. A. Smirnov, V. G. Plotnikov, Yu. A. Zabyalov, and M. V. Alfimov, *Opt. Spektrosk.*, **33,** 230 (1972).
(21) Incidently, a study of the influence of a nonuniform distribution of photoproducts (one-photon produced) on kinetic parameters as measured by optical absorption is found in J. W. Boag, *Trans. Faraday Soc.*, **64,** 677 (1968).
(22) KH. S. Bagdasaryan, Yu. I. Kirjuknin, and Z. A. Sinitsina, *J. Photochem.*, **1,** 225 (1972).
(23) V. G. Venogradova, B. N. Shelimov, N. V. Fok, and V. V. Voevodskii, *Dokl. Akad. Nauk. SSR,* **154,** 188 (1964).
(24) P. M. Johnson and S. A. Rice, *Chem. Phys. Lett.*, **1,** 709 (1968).
(25) P. Bekowies and A. C. Albrecht, *J. Phys. Chem.*, **75,** 431 (1971).

From the borders of organic chemistry . . . To the borders of theoretical physics:

Inorganic Chemistry brings you a broad range of authoritative information presenting both experimental and theoretical studies in all phases of inorganic chemistry.

Each month, this rapidly growing journal brings you the data you need on synthesis and properties of new compounds, quantitative studies regarding structure, and thermodynamics of inorganic reactions.

When you've seen the 50 or more papers offered in each issue, you'll also want to look through the Notes and Correspondence sections for their concise exchange of scientific views and ideas.

To order INORGANIC CHEMISTRY today, just complete and return the form below.

. . anotner ACS service

Inorganic Chemistry

Inorganic Chemistry
American Chemical Society
1155 Sixteenth Street, N.W.
Washington, D.C. 20036

Yes, I would like to receive INORGANIC CHEMISTRY at the one-year rate checked below:

	U.S.	*Canada*	*Latin America*	*Other Nations*
ACS Member Personal-Use One-Year Rate	☐ $18.00	☐ $22.00	☐ $22.00	☐ $23.00
Nonmember	☐ $54.00	☐ $58.00	☐ $58.00	☐ $59.00

Bill me ☐ Bill company ☐ Payment enclosed ☐

Name _____

Street _____ Home ☐ Business ☐

City _____ State _____ Zip _____

P-73